University of Plymouth

PEARL **https://pearl.plymouth.ac.uk**

04 University of Plymouth Research Theses 01 Research Theses Main Collection

2010

Transformation of wave shape and spatial distribution of wave overtopping water over a coastal structure

Peng, Zhong

http://hdl.handle.net/10026.1/493

http://dx.doi.org/10.24382/4859
University of Plymouth

All content in PEARL is protected by copyright law. Author manuscripts are made available in accordance with publisher policies. Please cite only the published version using the details provided on the item record or document. In the absence of an open licence (e.g. Creative Commons), permissions for further reuse of content should be sought from the publisher or author.

This copy of the thesis has been supplied on condition that anyone who consults it understood to recognize that its copyright rests with its author and that no quotation from the thesis and no information derived from it may be published without the author's prior consent

Transformation of Wave Shape and Spatial Distribution of Wave Overtopping Water over a Coastal Structure

by

Zhong Peng

A thesis submitted to the University of Plymouth in partial fulfilment for the degree of

Doctor of Philosophy

School of Marine Science and Engineering

Faculty of Science and Technology

June 2010

70 2926091 9

STORE

University of Plymouth Library
Subject to status this item may be renewed
via your Voyager account
http://voyager.plymouth.ac.uk
Tel: (01752) 232323

Transformation of Wave Shape and Spatial Distribution of Wave Overtopping Water over a Coastal Structure by **Zhong Peng**

Abstract

This work investigates the transformation of wave shapes and the landward spatial distribution of overtopping water over coastal structures by experimental data and a numerical model based on the Reynolds Averaged Navier-Stokes (RANS) equations and Volume of Fluid (VOF) surface capturing scheme (RANS-VOF). The aim of this study is to understand the transformation of wave shapes and the landward spatial distribution of overtopping water in the presence of coastal structures. This work provides new insights on the role of wave skewness and asymmetry on the breakwaters stability and sediment transport around the structure and on the beaches behind it. Also it helps to establish the extent of hazardous zones behind coastal structures when overtopping is anticipated.

A set of practical empirical formulae, relating wave shapes to local Ursell number, are derived based on an analysis of measurements collected in wave basin transmission tests of the DELOS (Environmental Design of Low Crested Coastal Defence Structures) project. This work also introduces the relationship of wave skewness on both sides of Low-Crested Structures (LCS), as well as wave asymmetry. RANS-VOF model results show that in the presence of LCBs, wave skewness decreases in the seaward near-field region including the seaward slope and increases rapidly up to the maximum above the structural crest. It then decreases dramatically in the leeward near-field region covering the leeward slope. Wave asymmetry decreases in the seaward near-field region, down to the minimum value on the structural crest, and then increases up to positive value in the leeward near-field region of LCBs. Wave skewness retains a positive sign on both sides but asymmetry changes from negative on the incident side to positive on the transmission side.

Bispectral Analysis of experiment and model results suggest that sum interaction between wave components contributes positively to wave skewness but negatively to wave asymmetry, while difference interaction contributes negatively to wave skewness but positively to wave asymmetry. The underlying physics of large variations of wave shapes in the vicinity of coastal structures is that: both sum interactions and difference interactions are significant in the seaward near-field region, while the sum interactions dominate on the structural crest but difference interactions dominate in the leeward near-field region of LCBs.

A semi-analytical model is developed to relate the landward spatial distribution to the flow depth and flow velocities at the leeward end of structural crests and the landward ground levels. Model results indicate that for the same incident wave conditions, the proportion of wave overtopping water passing a landward location increases initially with the increase in the seaward slope of the structure from 1:8 to 1:3, but it subsequently decreases with steeper slopes (from 1:3 to vertical). It is also found that the proportion of wave overtopping water passing a location increases with Ursell number of the incident waves and landward ground level, but decreases with increasing relative structural freeboard and structural crest width. The effect of wave randomness is negligible on landward spatial distribution of wave overtopping water.

RANS-VOF model results of the transformation of wave shapes and spatial distribution of wave overtopping water are in good agreement with measurements collected in small scale wave channel tests of DELOS project and measurements collected in CLASH project ('Crest Level Assessment of coastal Structures by full scale monitoring, neural network prediction and Hazard analysis on permissible wave overtopping') respectively. RANS-VOF model is successful in reproducing the laboratory results and can therefore be used as well as laboratory experiments in the future.

LIST OF CONTENTS

CHAPTER 1 INTRODUCTION 1

1.1 Background 1

1.1 Rationale 3

1.1.1 Transformation of wave shapes over a coastal Structure 3

1.1.2 Wave overtopping and its landward distribution 8

1.1.3 Links between wave shapes and overtopping 12

1.1.4 Present approaches and methodologies 13

1.2 Aims and Objectives 17

CHAPTER 2 NUMERICAL MODEL 19

2.1 Introduction 19

2.2 RANS-VOF Model 28

2.2.1 Governing equation 28

2.2.2 Boundary condition: 32

2.2.3 Surface capturing scheme and Partial Cell Treatment 37

2.2.4 Internal wave maker 39

2.2.5 Computational mesh 43

2.2.6 Time Step Criteria 44

2.2.7 Computational procedure 45

2.3 Model Improvements 48

2.3.1 PLIC-VOF surface capturing scheme 48

2.3.2 Return flow system 52

2.3.3 Wave overtopping algorithm 55

2.3.4 Mass conservation of wave overtopping 59

CHAPTER 3 PARAMETERISATION AND TRANSFORMATION OF WAVE ASYMMETRIES OVER LOW-CRESTED STRUCTURES (LCS) 62

3.1 Introduction 63

3.2 Experimental data 67

3.3 Transformation of Wave Skewness and Asymmetry over LCS 68

3.3.1 Transformation of wave skewness and asymmetry over smooth LCS 75

3.3.2 Transformation of wave skewness and asymmetry over rubble mound LCS. 79

3.3.3 Relationships of wave asymmetries between both sides of LCS 82

3.4 Bispectral Analysis of Nonlinear Wave Interactions 85

3.5 Summary 91

CHAPTER 4 NUMERICAL MODELLING OF EVOLUTION OF WAVE ASYMMETIES OVER LOW-CRESTED STRUCTURES 94

4.1 Introduction 95

4.2 Experiment 98

4.3 RANS-VOF Model Implementation 100

4.3.1 Model set-up 101

4.3.2 Validation of generated waves 106

4.3.3 Velocity field around LCS 109

4.4 Comparisons of Model Results and Measurements 111

4.5 Relationships of Wave Asymmetries and Ursell number 114

4.6 Factors Affecting the Evolution of Wave Asymmetries 117

4.6.1 Incident wave height, period and water depth 117

4.6.2 Incident wave shapes 119

4.6.3 Randomness in incident waves 122

4.6.4 Relative crest width of LCS 123

4.6.5 Porosity of LCS 125

4.6.6 Relative freeboards of LCS 127

4.7 Discussions 129

4.8 Summary 134

CHAPTER 5 SPATIAL DISTRIBUTION OF WAVE OVERTOPPING WATER BEHIND COASTAL STRUCTURES 137

5.1 Introduction 138

5.2 RANS-VOF Model Implementation 141

5.2.1 Set-up of RANS-VOF model 141

5.2.2 Effect of mesh size 142

5.3 Model Validation 144

5.3.1 Surface elevation 144

5.3.2 Average overtopping discharge 145

5.3.3 Landward spatial distribution of overtopping water 148

5.4 Semi-Analytical Model 149

5.5 Parameter Analysis of Model Results 154

5.5.1 Incident wave condition 154

5.5.2 Randomness in incident waves 156

5.5.3 Seaward slope of the structure 157

5.5.4 Relative crest width of the structure 159

5.5.5 Relative freeboard of the structure 161

5.5.6 Landward ground level 162

5.6 Summary 164

CHAPTER 6 CONCLUSIONS AND FUTURE WORK 166

6.1 Conclusions 166

6.1.1 Main findings 166

6.1.2 Recommendations 170

6.2 Future Work 172

APPENDIX A EMPIRICAL FORMULAE FOR OVERTOPPING DISCHARGE 174

APPENDIX B TMA SPECTRUM 177

APPENDIX C BISPECTRAL ANALYSIS 181

APPENDIX D EXPERIMENTS 185

REFERENCES 196

LIST OF SYMBOLS

a	Wave amplitude	(m)
A	Wave asymmetry	(-)
A_i	Wave asymmetry on the incident side of breakwaters	(-)
A_t	Wave asymmetry on the transmission side of breakwaters	(-)
B	Crest width of coastal structure	(m)
D_{n50}	Nominal diameter of rocks with a percentage exceeding of 50%	(m)
f_O	VOF function	(-)
f	Ordinary frequency	(Hz)
h	Local water depth	(m)
h_A	Layer thickness at the structural crest	(m)
h_O	Water depth around the wave-maker	(m)
h_{meas}	Landward ground level	(m)
h_{toe}	Water depth at the toe of coastal structures	(m)
H_i	Incident significant wave height	(m)
H_{m0}	Energy-based significant wave height	(m)
H_s	Local significant wave height, equals to H_{m0} in this study	(m)

k	Turbulent kinetic energy	(m^2/s)
L_0	Deep water mean wave length, $L_0=gT_m^2/(2\pi)$	(m)
L_p	*Deep water peak wave length,* $L_p=gT_p^2/(2\pi)$	(m)
L_m	Local mean wave length calculated with T_{m01}	(m)
m_i	Local i-th moment of spectrum	
P	Pressure	(Pa)
q_{t0}	Average overtopping discharge between t=0 and t=t_0	($m^3/s/m$)
Q	Dimensionless overtopping discharge, $Q=q_{t_0}\sqrt{\tan(\alpha)}/(\xi_p\sqrt{gH_s^3})$	(-)
R	Dimensionless structural freeboard, $R=R_c/(H_s\xi_p)$	(-)
R_c	Structural freeboard	(m)
δ	Openness coefficient of structures	(-)
s'	Spreading parameter	(-)
s_0	Incident mean wave steepness, $s_0=H_i/L_0$	(-)
s_{op}	Incident peak wave steepness, $s_{op}=H_i/L_p$	(-)
S	Wave skewness.	(-)
S_i	Wave skewness on the incident side of breakwaters	(-)
$S_0(\omega)$	Power spectrum	(m^2/rad)

S_t	Wave skewness on the transmission side of breakwaters	(-)
$tan(a)$	Seaward slope of coastal structures	(-)
T_m	Incident wave mean period around the wavemaker	(s)
T_{m01}	Local wave mean period, $T_{m01}=2\pi m_0 / m_1$	(s)
T_{pi}	Incident wave peak period around the wavemaker	(s)
T_p	Local wave peak period	(s)
$u_{A,50\%}$	Velocity on the structural crest which 50% incident wave will exceed	(m/s)
$u_{i,j}$	Horizontal velocity in the cell (i, j)	(m/s)
U_r	Ursell number, $U_r = \frac{H_s L_m^2}{h^3}$	(-)
U_{ri}	Ursell number on the incident side of breakwaters	(-)
U_{rt}	Ursell number on the transmission side of breakwaters	(-)
$v_{i,j}$	Vertical velocity in the cell (i, j)	(m/s)
V_t	Cumulative overtopping volume at t	(m^3/ m)
$V(x)/V_t$	Proportion of overtopping water passing x	(-)
Δt	Time step in numerical simulations	(s)
Δx_i	Cell width in the cell (i, j)	(m)

Δy_j	Cell height in the cell (i, j)	(m)
β	Incident wave angle	(°)
γ	Porosity of the structure	(-)
η	Wave surface elevation	(m)
μ	Molecular dynamic viscosity	(kg/s/m)
ν	Molecular kinematic viscosity	(m^2/s)
ν_t	Eddy viscosity	(m^2/s)
ε	Turbulent dissipation rate	(m^2/s)
ω	Angular frequency	(/s)
ξ_m	Iribarren number with mean period, $\xi_m = \tan(\alpha) / s_0^{0.5}$	(-)
ξ_p	Iribarren number with peak period, $\xi_p = \tan(\alpha) / s_{op}^{0.5}$	(-)

LIST OF ABBREVIATIONS

LCS:	Low-Crested Structures
RANS:	Reynolds Averaged Navier-Stokes equations
VOF:	Volume of Fluid method
DELOS:	Environmental Design of Low Crested Coastal Defence Structures
CLASH:	Crest Level Assessment of coastal Structures by full scale monitoring, neural network prediction and Hazard analysis on permissible wave overtopping
LEACOAST	Effect of shore-parallel breakwaters in tidal conditions on coastal morphology
LEACOAST2	Larger-scale Morphodynamic Impacts of Segmented Shore-Parallel Breakwaters on Coasts and Beaches
PLIC:	Piecewise linear interface calculation
SPH:	Smooth Particle Hydrodynamics
WG:	Numerical wave gauge
G:	Wave gauge in experiments
NLSWE:	Nonlinear Shallow Water Equation
SWL	Still water level

LIST OF FIGURES

Figure 1.1.1 Beach changes in presence of coastal defences at Sea Palling, Norfolk 5

Figure 1.1.2 Definition of skewed wave and asymmetric wave. solid line: positive skewed wave, dashed line: positive asymmetric wave, η is the time series of surface elevations and t is time. 8

Figure 1.1.3 Newlyn: Damage to promenade due to wave overtopping (Source: Cornwall City Council) 9

Figure 1.1.4 the failure of a sea dike due to wave overtopping (photo: Zitscher, 1976) 9

Figure 1.1.5 Severe wave overtopping at Samphire Hoe sea wall (photo courtesy of WCCP/Eurotunnel Developments Ltd) 10

Figure 2.2.1 Finite difference meshes and cell classifications in the model, f_0: the ratio of cell occupied by the fluid to the whole cell area, δ: the ratio of cell not occupied by the solid object to the whole cell area. 39

Figure 2.2.2 Flow chart of computational processes of RANS-VOF model .. 47

Figure 2.3.1 Comparisons between Hirt and Nichols' VOF interface reconstruction, Youngs' PLIC interface reconstruction and actual interface (Delnoij et al., 1988) 49

Figure 2.3.2 Comparisons of the surface elevation calculated by Hirt and Nichols' VOF and by Youngs' VOF and measurements (a) on the incident side (b) on the transmission side of LCS. Wave height H=0.10m, wave period T=1.6s, water depth h=0.35m and freeboard R_c=0m. 52

Figure 2.3.3 Wave height envelopes and mean water level during time interval from *t=101s* to *t=120s with* R_c*=0m,* (a) without flow recirculation, (b) with flow recirculation. Arrows stand for the direction of the return flow. Symbols represent the experimental data: 'O' for maximum height; '□' for mean height; '◊' for minimum height. Spongy layer is

located from x=0m to x=4m..... 54

Figure 2.3.4 Hornsea's seawall along the Holderness coast, UK (Source: http://picasaweb.google.com/lh/photo/YCUHTs8PXbwdasEuIh9NRg). 56

Figure 2.3.5 Sketch of a sea wall and definitions of governing parameters involved in numerical simulations of wave overtopping. The rule of the cell indexes can be referred in Section2.2.5..... 57

Figure 2.3.6 (a) Mass fluctuations on the incident side of overtopping structure and (b) mass difference of overtopping water, Δm. m_0 is the initial mass and m is the mass at simulation time $t= n*\Delta t$..... 61

Figure 3.3.1 Surface elevation measured in (a) gauge 2 on the incident side and (b) gauge 7 on the transmission side of smooth LCS. Freeboard is 0 m, incident wave height is 0.14 m, wave period is 2.12 s, water depth is 0.3 m and incident angle is 0°..... 70

Figure 3.3.2 Definitions of governing parameters involved in wave transmission over LCS (Van der Meer et al., 2005). 71

Figure 3.3.3 Power spectrum of surface elevation on the incident side and transmission side 73

Figure 3.3.4 Comparison between Equations 4.10 (solid line) and 4.11 (dash-dotted line) in Doering and Bowen (1995) and DELOS data on the incident side of both smooth and rubble mound LCS. Note, the definition of Ursell number here is calculated by the peak period in order to keep the same as that in Doering and Bowen (1995). 74

Figure 3.3.5 Relationship between wave skewness (a and b) and asymmetry (c and d) and Ursell number on the incident side (left panel) and the transmission side (right panel) of smooth LCS. Solid line is predicted by Equations 3.3.4 for (a), Equations 3.3.5 for (c), Equations 3.3.6 for (b) and Equations 3.3.7 for (d). 78

Figure 3.3.6 Comparisons of the dependence of wave skewness on Ursell number with (a) peak wavelength and (b) mean wavelength on the

transmission side. Symbols represent the measurements; dashed lines stand for measurements equal predictions. Predictions are calculated by the best-fitted expressions in form of Equation 3.3.6. 79

Figure 3.3.7 Relationship between wave skewness (a and b) and asymmetry (c and d) and Ursell number on the incident side (left panel) and the transmission side (right panel) of rubble mound LCS. Solid line is predicted by Equation 3.3.8 for (a), Equation 3.3.9 for (c), Equation 3.3.10 for (b) and Equation 3.3.11 for (d). The dash-dotted lines are predicted using Equation 3.3.4 for (a), Equation 3.3.5 for (c), Equation 3.3.6 for (b) and Equation 3.3.7 for (d) respectively. 81

Figure 3.3.8 Relationships of wave asymmetries between both sides of LCS. (a) wave skewness of smooth LCS, (b) wave asymmetry of smooth LCS, (c) wave skewness of rubble mound LCS and (d) wave asymmetry of rubble mound LCS. Dotted line represents $S_i=S_t$ while Dashed line stands for $A_t=-A_i$. 84

Figure 3.4.1 Normalized Power spectra by the energy of peak wave component (a and b), contours of bicoherence (c and d), contours of real part (e and f) and imaginary part (g and h) of normalized bispectrum on the incident side (left column) and transmission side (right column) of smooth LCS (R_c=-0.05m, H_i=0.13m, h=0.35m, α=0°). The minimum levels of contour plots are (c) 0.15, (d) 0.15, (e) 2e-4, (f) 2e-4, (g) -11e-4 and (h) 0.6e-4. The corresponding intervals of contour levels are 0.1, 0.1, 3e-4, 3e-4, 3e-4, and 1.5e-4 respectively. Dashed contours are negative values and solid ones are positive values. 87

Figure 3.4.2 Normalized Power spectra by the energy of peak wave component (a and b), contours of bicoherence (c and d), contours of real part (e and f) and imaginary part (g and h) of normalized bispectrum on the incident side (left column) and transmission side (right column) of smooth LCS (R_c=0.05m, H_i=0.11m, h=0.25m, a=0°). The minimum levels of contour plots are (c) 0.15, (d) 0.15, (e) 1e-4, (f) 1e-4, (g) -13e-4 and (h) 2e-4. The corresponding intervals of contour levels are 0.1, 0.1, 2e-4,

3e-4, 3e-4, and 3e-4 respectively. Dashed contours are negative values and solid ones are positive values. 88

Figure 4.2.1 Installation of wave gauges in the experiments with (a) narrow crest tests and (b) wide crest tests. Unit: m. G1 to G11 represent the surface elevation gauges. 99

Figure 4.3.1 Sketch of the numerical setup and the computational meshes. Dashed line stands for still water level, SWL, and h represents the water depth. 102

Figure 4.3.2 Overview of 30 numerical gauges (WG1 to WG30). Water depth at x=11m is 0.4 m. Solid line represents calculated surface elevations at t=200 s; dash-dotted line stands for still water level. 105

Figure 4.3.3 Comparisons of predicted wave surface elevations and measurements (a) on the incident side, (b) on the seaward slope, (c) on the crest, (d) on the landward slope and (e) on the transmission side of LCS (Case No.1). Coordinates of WGs can be referred in Figure 4.3.2. 106

Figure 4.3.4 Comparisons of calculated power spectrum and measurements (Case No.8). Coordinates of WGs can be referred in Figure 4.3.2. 108

Figure 4.3.5 Snapshot of the flow pattern in the computational domain (shown in Figure 4.3.2). The grey area is the impermeable bottom, while the blue area represents the permeable obstacles. The wave conditions: H=0.07m, T=1.6s, h=0.4m and R_c=-0.05m 110

Figure 4.4.1 Comparisons of wave skewness (S) and asymmetry (A) of wave surface elevations between different (a, d) significant wave heights with T_{pi}=1.6s and h_0=0.4m, (b, e) peak wave periods with H_i=0.07m and h_0=0.4m (c, f) water depths at x=11m with H_i=0.10m and T_{pi}=1.6s under the same other wave conditions and structural geometry. Structural crest width B=1.0m. Lines represent numerical results and dots represent measurements. o: measurements associate with solid line, □: measurements associate with dashed line. Grey area represents the

LCB and bottom (scaled for aesthetic reason). 113

Figure 4.5.1 Relationships of U_r ($U_r=H_sL_m^2/h^3$) and (a) wave skewness and (b) asymmetry in front of LCS. o: the calculated results; Δ: measurements; solid lines: predictions by Equations 3.3.8-3.3.9. 115

Figure 4.5.2 Relationships of Ursell number, U_r, and (a) wave skewness, S, and (b) wave asymmetry, A, above the flat bottom on the transmission side of LCS. o: the calculated results; Δ: measurements; solid lines: predictions by Equations 3.3.10-3.3.11. 115

Figure 4.6.1 Effect of incident wave shapes on the evolutions of wave skewness and asymmetry across LCS. (a) Wave profiles at x=11m, (b) significant wave heights, H_s, (c) wave skewness, S, and (d) wave asymmetry, A, under the same wave parameters and structural properties. Grey area represents the LCB and bottom geometry (scaled for aesthetic reason). Negatively skewed wave: S=-0.23, A=-0.19; positively skewed wave: S=0.45, A=--0.35. Source region is located around x=10 m. B=1.0m, R_c= -0.05m. 121

Figure 4.6.2 Effect of the randomness in incident waves on the evolution of wave skewness (S) and asymmetry (A) over LCS, with the same significant wave height and peak period and structural geometry. (a) Power spectrum, $S_0(f)$, at x=11m and (b) wave skewness and asymmetry. The dotted line represents the 95% confidence levels of the mean skewness or asymmetry. Grey area represents the LCB and bottom geometry (scaled for aesthetic reason). B=0.25 m, R_c= -0.05 m. 122

Figure 4.6.3 Effect of relative crest width of LCS on (a) wave skewness (S) and (b) asymmetry (A) under the same wave conditions. Grey area represents the LCB and bottom geometry (scaled for aesthetic reason). Symbols represent measurements, ○: narrow crest with; □: wide crest with. R_c= -0.05m. 124

Figure 4.6.4 Effect of structural porosity on the evolution of (a) significant wave height (H_s), (b) wave skewness (S) and (c) wave asymmetry (A)

under the same wave conditions and structural geometry. Grey layer only represents the LCB and bottom geometry (scaled for aesthetic reason). ○: measurements of the case with large porosity. B=1.0m, R_c= -0.05m..... 126

Figure 4.6.5 Effect of relative freeboard on the evolution of (a) wave skewness (*S*) and (b) wave asymmetry (*A*) under the same wave conditions and structural geometry. Grey layer only represents the horizontal location of bottom geometry. B=1.0m. 129

Figure 4.7.1 Normalized power spectrum and bi-coherence, b2(f1, f2), of surface elevations (a) on the front slope (WG8), (b) on the crest (WG12), (c) on the rear slope (WG18) and (d) on the transmission side (WG21). The dotted lines represent the primary frequency and second harmonic. 131

Figure 5.2.1 Sketch of computational domain. G1 to G4 represent the locations of four wave gauges in the experiments; h_{toe} is water depth at the toe of structures; SWL is still water level; R_c, B and tan(α) are the structural freeboard, crest width and seaward slope respectively. The origin of coordinates is at the landward end of structural crest with x for horizontal axis and y for vertical axis. 141

Figure 5.2.2 Effect of mesh size on the predicted surface elevations. H=0.16m, T=2.0s, h=0.7m and R_c=0.1m. 143

Figure 5.3.1 Calculated surface elevations (solid line) and measured surface elevations of Li et al. (2007) (circles) at (a) G2 and (b) G4. H=0.16m, T=2.0s, h=0.7m and R_c=0.1m..... 145

Figure 5.3.2 Comparisons of dimensionless overtopping discharge, $Q=q_0*\sqrt{\tan(\alpha)}/(\xi_p*\sqrt{g*H_s^3})$, against the dimensionless freeboards, $R=R_c/(H_s*\xi_p)$ (ξ_p is surf similarity with the peak period at the toe of structures), between numerical results and empirical formulae. 147

Figure 5.3.3 Comparisons of landward spatial distribution of overtopping water between numerical results and measurements for (a) a vertical

wall and (b) a sea dike with the seaward slope of 1:2. $V(x)/V_t$ is the proportion of overtopping volume passing x; V_t is the cumulative overtopping volume; L_0 is deep water wave length with the mean period and H_i is significant wave height at the toe of sea dike; landward ground level h_{meas}=0 for both cases..... 149

Figure 5.4.1 Comparisons of landward spatial distribution of overtopping water over (a) a 1:6 dike and (b) a 1:2 dike between semi-analytical results, numerical results and measurements. H_i=0.12m. 153

Figure 5.5.1 Effect of Ursell number of incident waves on landward spatial distribution of overtopping water, h_{toe}=0.7m, B=0.3m, $tan(a)$=1:6, R_c=0.1m and h_{meas}=0m. 155

Figure 5.5.2 Effect of wave randomness on (a) cumulative overtopping volume (V_t) and (b) landward spatial distribution of overtopping water. Solid line represents the expected value and the dashed lines show the 95% confidence levels of the expected value. H_i=0.12m, T_{pi}=1.6s, h_{toe}=0.7m, R_c=0.1m, B=0.3m and h_{meas}=0m..... 156

Figure 5.5.3 Effect of structural seaward slope, tan(α), on the landward spatial distribution of overtopping water. H_i=0.12m, T_{pi}=1.6s, h_{toe}=0.7m, R_c=0.1m, B=0.3m and h_{meas}=0m. 158

Figure 5.5.4 Effect of the relative structural crest width, B/L_p, on the landward spatial distribution of overtopping water. H_i=0.12m, T_{pi}=1.6s, h_{toe}=0.7m, $tan(a)$=1:6, R_c=0.1m and h_{meas}=0m. 160

Figure 5.5.5 Effect of relative structural freeboard, R_c/H_i, on landward spatial distribution of overtopping water. H_i=0.16m, T_{pi}=2.0s, h_{toe}=0.7m, h_{meas}=0m, B=0.3m and tan(a)=1:6. 162

Figure 5.5.6 Effect of landward ground level, h_{meas}, on the landward spatial distribution of wave overtopping water. H_i=0.12m, T_{pi}=1.6s, h_{toe}=0.7m, R_c=0.1m, tan(α)=1:6 and B=0.3m..... 163

LIST OF TABLES

Table 3.2.1 Overall view of test program in wave basin transmission tests. 68

Table 4.2.1 Overall view of test programmes in wave channel tests..... 100

Table 4.3.1 Overall view of numerical simulations of the transformation of wave shapes over LCS..... 104

Table 5.3.1 Overall view of numerical simulations of spatial distribution of overtopping water..... 146

ACKNOWLEDGEMENT

First and foremost, I owe my deepest gratitude to my Director of Studies, Qingping Zou for her patience, her expressed commitment and for her thoughtful guidance and support throughout its development; sincere thanks also to Dominic Reeve for his warm encouragement and insightful comments on this work.

I am grateful to Morten Kramer from Aalborg University offering the data of small scale wave channel tests, along with Baoxing Wang formerly from University of Plymouth providing the data of wave basin transmission tests. The authors would like to thank Pengzhi Lin from Sichuan University, who generously supplied his RANS-VOF code for the present work. I would also like to thank Johan Vandamme, Kieran Monk for the language helps, and other friends in the University of Plymouth who contributed to my success. Thank the examiners, Professor Ping Dong and Dr Deborah Greaves, for their insightful comments on this work leading to significant improvement of the thesis.

I would like to express my thanks to the University of Plymouth postgraduate research scholarship for financing my study and research. Also, thanks to the Royal Academic of Engineering, the German Port Technology Association, the ENCORA project, Plymouth Marine Science Education Fund and Challenger Society for Marine Science for the financial support for attending conferences.

Lastly, grateful thanks to ALL my family back in China, in particular to my parents and my brother, for their love and support. Special thanks to my wife, Tong Sun, for her love and caring support and for sharing this special time.

AUTHOR'S DECLARATION

At no time during the registration for the degree of Doctor of Philosophy has the author been registered for any other University award without prior agreement of the Graduate Committee.

This study was financed with the aid of the University of Plymouth postgraduate research scholarship. Additional support was provided by the Faculty of Technology.

The author presented two internal seminars to members of the academic staff of the School of Marine Science and Engineering, also attended a summer school on Mathematical methods for Coastal Engineering run by the University of Plymouth. Parts of materials in this thesis have also been submitted for publications to the journal of Coastal Engineering (Elsevier). One has been published and the other two are now under the examination of international referees. The publications related to the present work as listed on next page. In addition, three international conferences were attended and work from this thesis was presented.

CONFERENCE ATTENDED:

- International Conference on Coastal Dynamics, Tokyo, Japan, Sep 7th-12th, 2009, presenting paper.
- International Conference on Coastal engineering, Hamburg, Germany, Aug 31st-Sep 5th, 2008, presenting paper.
- IMA 2nd Conference on Flood Risk Assessment, Plymouth, UK, Sep 2007, presenting poster

Word count of main body of thesis: 36941

Signed

Date 30 July 2010

RELEVANT PUBLICATIONS

Journal papers:

- **Zhong Peng**, Qingping Zou. Evolutions of wave shape over low-crested breakwaters. Coastal Engineering (Under review).
- **Zhong Peng**, Qingping Zou. Spatial distribution of wave overtopping water behind impermeable coastal structures. Coastal Engineering (Under review).
- **Zhong Peng**, Qingping Zou, Dominic Reeve, Baoxing Wang, 2009. Parameterisation and transformation of wave asymmetries over a low-crested breakwater. Coastal engineering, 53-54.

Conference papers:

- **Zhong Peng**, Qingping Zou, 2010. An investigation on spatial distributions of wave overtopping water using RANS-VOF model, the 32nd International Conference on Coastal Engineering. Shanghai, China, 30th June to 5th July, 2010. Abstract accepted.
- **Zhong Peng**, Qingping Zou, 2009. Model-Data Comparisons of Wave Shape Changes over Low-Crested Breakwaters, the 6th International Conference on Coastal Dynamics, Tokyo, Japan, 7th August to 11th September, 2009.
- Zou, Q., Chen, Y., Cluckie, I., Hewston, R., Lv, X., Pan, S., **Peng, Z**. and Reeve, D., 2009. EPIRUS: an integrated "clouds-to-coast": ensemble modelling framework of coastal flood risk, 11th International Workshop on wave hindcasting and forecasting and coastal hazard symposium, Halifax, Canada.
- **Zhong Peng**, Qingping Zou, Baoxing Wang and Dominic Reeve, 2008. Transformation of wave skewness and asymmetry over low-crested breakwaters, the 31st International Conference on Coastal Engineering, Hamburg, Germany, 31st August to 5th September, 2008.
- Jonathan Pearson, Qingping Zou, Ian Guymer and **Zhong Peng**, 2008. Horizontal and vertical tracer dispersion in the nearshore: Laboratory and numerical results, the 31st International Conference on Coastal Engineering, Hamburg, Germany, 31st August to 5th September, 2008.
- **Zhong Peng**, Qingping Zou, 2008. Numerical analysis of wave transformation over low-crested impermeable breakwater, the 18th International Offshore and Polar Engineering Conference, Vancouver, Canada, pp. 672-677.
- **Zhong Peng**, Qingping Zou and Dominic Reeve, 2007. Transformation of wave skewness and asymmetry over smooth low-crested breakwaters, Flood Risk Assessment II. the Institute of Mathematics and its Applications, Plymouth, UK, pp. 205-210.

CHAPTER 1

INTRODUCTION

1.1 Background

Ocean waves are usually formed by the local atmosphere conditions, such as pressure, and a complex process of wind-water interactions, including the resonance and the shearing action. As waves travel toward beaches, they will gradually enter a nearshore coastal region where the local water depth starts to influence the waves. In this region, wave amplitudes increase, wavelengths decrease, and wave incident direction refracts toward the normal of the beach. These linear propagation effects are observed readily and understood well. In addition, pronounced nonlinear effects in shallow water cause a dramatic transformation of wave shapes from initially symmetric, nearly sinusoidal profiles, to asymmetric, pitched forward profiles characteristic of near-breaking waves. Once waves have broken, bore formation starts and broken waves pour water into the surf zone, where complex energy dissipation, energy transfer and turbulent processes occur.

Waves with these characteristics lead to nearshore fluid motions (e.g., long-shore currents, rip currents, and undertow) and sediment transport (e.g., erosion and accretion of beaches, and the formation of bars and cusps).

The shoaling waves in a nearshore coastal zone exhibit high nonlinearity and large wave energy densities, represented by large wave heights. If there are insufficient sea defences or other human interventions, waves can cause enormous damage to beach morphology, cliffs, farmland and coastal properties. Of prime concern is the safety of people living by the coastlines especially to those strolling along promenades during wave overtopping events. As a result, coastal structures, such as seawalls, groynes, armoured breakwaters, perforated-wall breakwaters and low-crested breakwaters, are constructed. These structures are employed to prevent or reduce erosion and flooding of coastal stretches of high value, to stabilize and retain beaches and reclaimed land, and to increase the amenity value of the coast (e.g. beach use, surfing). Their hydrodynamic function is to dissipate high waves by forcing the waves to break, consequently causing substantial wave attenuation and reflection, and reducing transmission and overtopping energy.

However, in the presence of coastal structures, wave transformation inevitably involves more complex processes, such as wave reflection, wave refraction, wave transmission, wave overtopping and structural stability. When the incident wave train impinges on the structure, part of the energy is reflected back to the sea and part is transmitted in the leeside zone. Most

of the incident wave energy is lost on the structure's crest, essentially by breaking. Part of the energy is also dissipated by air entrainment and friction at the solid skeleton interface and within the porous media. Most of the previous work has been oriented towards the functional design of coastal structures to evaluate reflection (Zanuttigh and van der Meer, 2008), structural stability (Van der Meer, 1987; Burcharth et al., 2006) and transmission (Van der Meer et al., 2005; Wang et al., 2007), run-up (Van der Meer and Stam, 1992), overtopping (EurOtop, 2008), scour (Sumer et al., 2001; Sumer et al., 2005) and velocity and turbulence fields (Sakakiyama and Liu, 2001; Losada et al., 2005). These complex processes present a big challenge to coastal engineers in maintaining the structural stability and protecting the beaches and landward properties that are sheltered by those coastal structures.

1.1 Rationale

1.1.1 Transformation of wave shapes over a coastal Structure

The sediment transport in front of a toe of coastal structures can lead to severe toe scour. Toe scour can compromise the structural stability, and is known as one of the most common causes of failure for coastal structures. There have been many evidences indicating that the failure of many coastal structures was due to the toe erosion of these structures (Shiraishi et al., 1960; Ichikawa, 1967; Gunbak et al., 1990; Lillycrop and Hughes, 1993; Oumeraci, 1994a, b). For example, Ichikawa (1967) studied the collapse of

breakwater of Tagonoura Harbour in Japan. Its failure took place in 1964 when the Typhoon No.24 hit that region. The investigation found that the base of the structure had been scoured to a depth of up to 8 meters. More recently, Silvester and Hsu (1997) have provided a variety of examples of the collapse of coastal structures due to toe scour around the world. In general, the toe failure occurs because of scour and the collapse of the stones at the toe into the same scour hole. Markle (1986) indicated that after major storms bedding layers slough off into the scour holes, and this damage migrates back to the toe of the primary armour. The resulting instability of a toe will also trigger or accelerate the instability of the main armour and the eventual deterioration of the structures. Recently, the accumulated knowledge about scouring around various coastal structures had been reviewed by Sumer and Fredsøe (2002). Sediment transport also significantly affects the morphology of the beaches that are sheltered by the coastal structures (Figure 1.1.1). This was extensively studied by EPSRC funded research projects LEACOAST (Effect of shore-parallel breakwaters in tidal conditions on coastal morphology) and LEACOAST2 (Larger-scale Morphodynamic Impacts of Segmented Shore-Parallel Breakwaters on Coasts and Beaches). For example, Pan et al. (2005) found that during storm events, large beach slope and wide gaps between salient and breakwater may be formed due to the effects of sediment transport. Johnson et al. (2010) also showed that sediment transport results in the tombolo at low tide level and the salient at higher tide levels in Sea Palling, Norfolk. Furthermore, they have also noticed obvious bulges in the shoreline platform at Elmer, West Sussex and Jaywick,

Essex.

Figure 1.1.1 Beach changes in presence of coastal defences at Sea Palling, Norfolk

A key parameter for cross-shore sediment transport under breaking and near-breaking waves is the shape of waves and associated near-bed orbital velocity. Cornish (1898) observed that the onshore velocity under wave crests was more effective at moving coarse sediment than the seaward velocity related to wave troughs. This observation was consistent with the theory of Stokes (1847): the onshore velocity related to a wave crest is larger and of shorter duration than the seaward velocity associated with a wave trough, arising from the skewed wave shape characterised by peaked crests and flat troughs. It is generally believed that skewed near-bed velocities are directly related to the net sediment transport (Inman and Bagnold, 1963; Bowen, 1980; Bailard and Inman, 1981; Elfrink et al., 1999; Doering et al., 2000; Haas et al., 2008; Fuhrman et al., 2009). This is mainly because the onshore velocity related to a wave crest is larger, but of shorter duration and

consequently more effective at dislodging coarse sediment than the seaward velocity associated with a wave trough. Nielsen (1992) identified the importance of fluid acceleration in asymmetric waves. For a pitching forward wave, the onshore velocity increases in magnitude faster than the offshore velocity, and the associated boundary layer has a shorter time to develop. Thus, the onshore velocity generates a thinner boundary layer and therefore a larger bed shear stress. Janssen et al. (1997) concluded that an asymmetric free-stream flow can result in different settling speeds of particles during its increasing and decreasing phases. This is conclusively supported by numerical results of Dong and Zhang (2002). Flow acceleration in asymmetric waves, which serves as a proxy for horizontal pressure gradient in the coastal bottom boundary layer, has significant effect on sediment transport (Drake and Calantoni, 2001; Hoefel and Elgar, 2003; Nielsen and Callaghan, 2003; Hsu and Hanes, 2004; Nielsen, 2006; Gonzalez-Rodriguez and Madsen, 2007; Austin et al., 2009; Ruessink et al., 2009; van der A et al., 2010). This effect is validated with U-tube experiments (e.g., King, 1990) and field measurements in the surf zone (e.g.,Gallagher et al., 1998) and in the swash (e.g.,Puleo et al., 2003). Therefore, the transformation of wave shapes, related to sediment transport, is believed to be important to structural stability and to the morphology of the beach which is sheltered by coastal structures.

Better understanding of the transformation of wave shapes over coastal structures is crucial in the assessment of functionality and stability of coastal and flood defence schemes. It is also of key importance to the

application and development of physically-based models of sediment transport that aim to simulate the evolution of cross-shore beach profiles. Previous studies, however, have mainly been on wave transmission, reflection and wave spectral change over coastal structures (Van der Meer et al., 2000; Van der Meer et al., 2005; Wang et al., 2007), and the cross-shore evolution of wave skewness and asymmetries on the natural beaches (Elgar and Guza, 1985; Doering and Bowen, 1995; Herbers et al., 2003). Work on wave energy transfer in the presence of coastal structures or sandy bars has also been done by previous researchers (e.g., Beji and Battjes, 1993; Losada et al., 1997; Masselink, 1998; Brossard and Chagdali, 2001; Brossard et al., 2009). Currently, literature on the transformation of wave skewness and asymmetry over coastal structures is sparse. A direct relationship between wave skewness, wave asymmetry and wave conditions, such as the relative water depth and relative wave height, will enable engineers to apply wave skewness and asymmetry to sediment transport models easily and accurately. Moreover, it would be helpful to look at the whole picture of wave evolution, from the incident side, over the structural crest to the transmission side of coastal structures. This work helps to enhance our understanding of wave-structure interactions and provides a guideline in designing and assessing the functionality and stability of coastal and flood defence schemes.

In this thesis, third moments of wave surface elevations, such as wave skewness and asymmetry, are employed to describe wave shapes. Wave skewness describes the lack of symmetry of a wave profile relative to the

horizontal axis, and wave asymmetry describes the lack of symmetry of a wave profile relative to the vertical axis. For example, a wave with positive skewness has peaky, narrow crests and flat, wide troughs, while a wave with positive asymmetry has a pitch backward shape, with a steep rear face and a gentle frontal face (Figure 1.1.2).

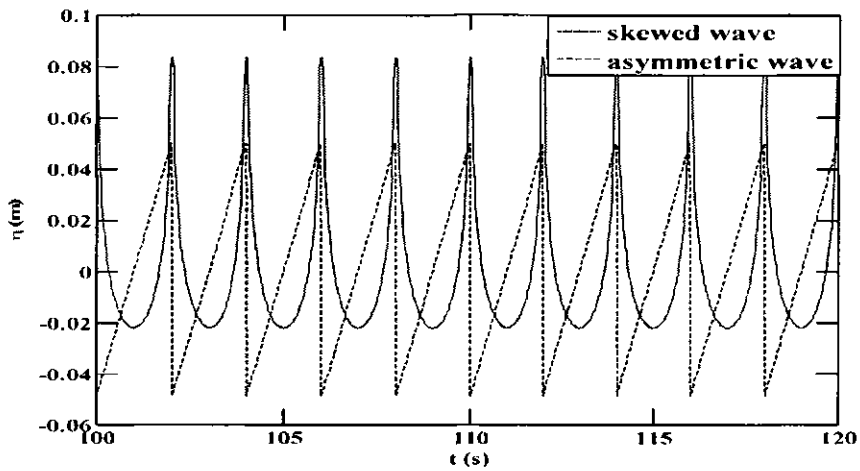

Figure 1.1.2 Definition of skewed wave and asymmetric wave. solid line: positive skewed wave, dashed line: positive asymmetric wave, η is the time series of surface elevations and t is time.

1.1.2 Wave overtopping and its landward distribution

It has long been recognized that the erosion due to wave overtopping is another one of the possible mechanisms of structural failure. For example, Figure 1.1.3 shows a section of the tarmac promenade backing the damaged seawall section that collapsed at Newlyn due to wave overtopping during a storm in October 2004. The damage is probably due to the overtopping downfall and the loss of fill from beneath/behind the wall. Figure 1.1.4

shows a sea dike failure due to wave overtopping in a storm. This failure may be due to the erosions of the clays by the overtopping flow. Minikin (1950) also provided a description of the seaward collapse of the Mustapha breakwater due to wave overtopping in a severe storm in Algeria in 1934.

Figure 1.1.3 Newlyn: Damage to promenade due to wave overtopping (Source: Cornwall City Council)

Figure 1.1.4 the failure of a sea dike due to wave overtopping (photo: Zitscher, 1976)

Wave overtopping over coastal structures significantly affects morphological changes of the beaches sheltered by coastal structures. Du et al. (2010) found that wave overtopping alters the current circulation and sediment transport patterns under storms and macro-tide conditions, consequently leading to the formation of tombolos and salients. Wave overtopping can also cause damages to the properties landward of the coastal structures. The landward spatial distribution of overtopping water determines the risk of damages and sets restrictions on the use of areas behind the coastal defences. It ultimately affects the placement of roads, walkways, railways, buildings and other infrastructure (Figure 1.1.5). Along

developed coasts, the safety of people using the coastline is of particular concern. In the UK, the safety issue of developed coasts is of particular concern. According to statistics, approximately two to four people die every year because of accidents happening at seawalls, breakwaters, natural rock outcrops or beaches (Allsop et al., 2003). Evidence of damages to properties behind coastal structures due to wave overtopping, was most graphically given by the trainload of pig iron washed off Dover East Breakwater in the 1940s and by the destruction of seafront shelters at Sidmouth in 1992 (Allsop et al., 2005).

Figure 1.1.5 Severe wave overtopping at Samphire Hoe sea wall (photo courtesy of WCCP/Eurotunnel Developments Ltd)

The purpose of a coastal or shoreline structure is to reduce the frequency and severity of wave overtopping, and hence the risks or extent of flooding. The UK government spends approximately £100 million per annum on new or refurbished coastal defences (Allsop et al., 2005). An important criterion for the design of a sea wall is the allowable degree of wave overtopping,

which depends on the activities normally performed on the leeside of the structure, the need to prevent erosion of the rear face of the sea wall, and the economic consequences of flooding (Hedges and Reis, 1998). A mean overtopping discharge smaller than 0.03 l/s/m is recommended for the safety of the public close behind a seawall (Beseley, 1999; Allsop et al., 2003). To achieve this low level of overtopping requires significant confidence in the analysis of the overtopping characteristics of urban seawalls. Many coastal engineers and scientists have dedicated great efforts to investigating wave overtopping (Jensen and Sorensen, 1979; Schüttrumpf and Oumeraci, 2005; Pullen et al., 2008; Hughes and Nadal, 2009; Lykke Andersen and Burcharth, 2009; van der Meer et al., 2009). Most of the existing research has been directed towards the evaluation of the mean overtopping discharge.

However, average overtopping discharge is apparently not an appropriate parameter for describing the overtopping flow away from the overtopping point (Schüttrumpf and Oumeraci, 2005) and the landward spatial distribution of overtopping water (EurOtop, 2008). Moreover, better understanding of the spatial distribution of wave overtopping water is of key importance to the design of the sea defences and the placement of roads, walkways, railways, buildings and other infrastructure, even the safety of people. It is anticipated that the spatial distribution of overtopping water is related to flow depth and flow velocities. Therefore, researches have been carried out recently to investigate the overtopping flow velocities and the related flow depth on the seaward slope, the dike crest and the landward slope (Schuttrumpf and van Gent, 2003; Schüttrumpf and Oumeraci, 2005).

Preliminary studies on the spatial distribution of overtopping water on a vertical wall (Jensen and Sorensen, 1979; Bruce et al., 2005; Pullen et al., 2008) and permeable structures with a seaward slope of 1:2 (Lykke Andersen and Burcharth, 2006; Lykke Andersen et al., 2007; EurOtop, 2008) have been done based on experimental data.

Previous studies depend mainly on limited experimental data, which is also restricted to low data resolution of the spatial distribution, a few geometries and a small amount of wave conditions. As a result there is little guidance on how to parameterize the landward spatial distribution of overtopping water across coastal structures. A better understanding of spatial distribution of wave overtopping discharge will enable engineers to establish the location and area of hazardous zones behind a structure when overtopping is anticipated. Therefore, it is of importance to understand the effects of wave conditions and structural geometries on the spatial distribution of overtopping water, as well as the physics behind the landward spatial distribution. For example, the governing parameters involved in landward spatial distribution and the trajectory of overtopping water.

1.1.3 Links between wave shapes and overtopping

As mentioned above, the transformation of wave shapes directly affects the sediment transport around coastal structures. It consequently leads to significant scour in front of the toe of the coastal structures, and affects morphological changes to the beaches behind the coastal structure. On the

other hand, the landward spatial distribution of wave overtopping determines the risk of damages to landward properties and is therefore crucial in the assessment of structural functionality. Wave overtopping also brings erosion on the landward side, occasionally resulting in the structure failure. Thus, both the transformation of wave shapes and landward spatial distribution of overtopping water are crucial in the assessment of functionality and stability of coastal and flood defence schemes. In addition, Elgar and Guza (1985), Doering and Bowen (1995) and Ruessink (1998) concluded that the transformation of wave shapes arises from nonlinear triad interactions in which two primary wave components with frequencies f_1 and f_2 excite a secondary wave component with the sum (f_1+f_2) or difference $(f_1-f_2,\ f_1>f_2)$ frequency. The incident waves and the nonlinearly excited higher frequency waves are predominantly dissipated around the coastal structures. The nonlinearly excited lower frequency (infra-gravity) wave components are reflected from the structure and often dominate wave run-up at the seaward slope of coastal structures. Once the highest run-up levels exceed the structure crown, wave overtopping occurs.

1.1.4 Present approaches and methodologies

Low-Crested Structures (hereinafter LCS) are increasingly being used to manage coastal erosion globally because they are economical and there is no visual impact to coastal landscape. The objective of the European project DELOS ('Environmental Design of Low Crested Coastal Defence Structures', www.delos.unibo.it) is to develop effective and environmentally compatible

design of LCS as a method of shoreline defence which also preserved the littoral environment (e.g. prevent high-energy wave action and intermittent periods of flooding within the region or zone between the limits of high and low tides) and coast economic development. A new database, made up of 2337 tests, concerning experiments on wave transmission over low-crested structures in wave flumes has been collected within the DELOS project by Van der Meer et al. (2005). On the other hand, The EU project CLASH ('Crest Level Assessment of coastal Structures by full scale monitoring, neural network prediction and hazard analysis on permissible wave overtopping', www.clash.ugent.be) aims to produce practical prediction methods on the required crest height of most coastal structure types, based on permissible wave overtopping and hazard analysis. A database on wave overtopping, consisting of more than 10,000 irregular wave overtopping tests collected from more than 160 independent projects or test series, was created in the EU project CLASH by van der Meer et al. (2009). These two databases in wave transformation and wave overtopping over coastal structures are state of the art and both available to be downloaded. Therefore, a part of two databases is used in this study to explore the underlying physics of the transformation of wave asymmetries over coastal structures and validate the numerical results of wave transformation and wave overtopping.

Rather than laboratory experiments or field measurements of wave-structure interactions covering a limited number of setups and devices, a numerical model provides a means to obtain high spatial and time resolution information of magnitudes which are difficult or impossible to measure in a

physical experiment and therefore is a popular method for investigating wave-structure interactions. Lin and Liu (1998) developed a numerical model based on the Reynolds Averaged Navier-Stokes (RANS) equations and Volume of Fluid (VOF) surface capturing scheme (hereinafter RANS-VOF). The RANS-VOF model solves the Reynolds Averaged Navier-Stokes equation for the mean flow field and the nonlinear k–ε equations for the turbulent kinetic energy, k, and the turbulence dissipation rate, ε. The Volume of Fluid method is employed to capture the free surface. In contrast with Boussinesq model and Nonlinear Shallow Water Equation models, the RANS-VOF model is able to describe the complex free surface, as well as nearshore wave-structure interactions without assuming hydrostatic pressure (pressure exerted by a fluid at equilibrium due to the force of gravity). It allows the calculation of the velocity field in the whole computational domain for both rotational and irrotational flow. This model also takes into account mechanisms of turbulence generation/dissipation in the wave breaking process by employing more advanced turbulence models, such as nonlinear k-ε model. It also has the advantage of being able to simulate the flow inside porous structures and requires less computational resources compared with the 3D Large Eddy Simulation model and Particle method models. As a result, the RANS-VOF model is employed in the present work.

Several improvements to the RANS-VOF model are needed in order to obtain more accurate results of wave transformations and to simulate wave overtopping. Firstly, the piecewise constant interface algorithm of VOF method, which was originally developed by Hirt and Nichos (1981), always

orientates free surface interfaces parallel to horizontal or vertical boundary of cells. This method cannot obtain the accurate locations of surface interfaces if mesh level is not fine enough. A piecewise linear interface calculation (PLIC) reconstruction algorithm, developed by Youngs (1982), will be employed in this study. This algorithm can orientate free surface interfaces in a direction perpendicular to the locally evaluated VOF gradient, thus giving a more accurate capturing of the free surface. Secondly, the overtopping and transmission give rise to a piling-up of water in the leeside region of the structure if the water is irreversible. In the experiments of DELOS project and real cases of shore protected by coastal structures, this pilling-up of water is not observed, as the potential piling-up behind the breakwater is relieved by a circulation system and through the sides of the breakwater respectively. In general, the piling-up of water will lead to inaccurate surface elevations and flow conditions on the transmission side and even perturb the wave breaking process on the structure by forcing a strong return flow over the structure (Garcia et al., 2004). Therefore, a flow recirculation system will be built in order to avoid the fluid piling-up in the leeside of the breakwater (Diskin et al., 1970; Garcia et al., 2004). Finally, the RANS-VOF model calculates wave transformation over coastal structures, but there is no module dealing with the wave overtopping discharge and its spatial distribution. Within a small computational domain, the cumulative overtopping mass will lead to the instability of numerical simulations due to the non-conserved mass in front of overtopping structures. Therefore, new modules will be developed into the RANS-VOF model to calculate wave

overtopping discharge, to recirculate overtopping water back to the incident side of structure, and to evaluate the landward spatial distribution of overtopping water. These improvements will be done before applying the RANS-VOF model to the transformation of wave shapes and to the landward spatial distribution of overtopping water over coastal structures.

1.2 Aims and Objectives

The aim of this work is to understand the transformation of wave shapes and landward spatial distribution of wave-overtopping water in the presence of coastal structures.

In particular the objectives of this work are to:

- parameterize the relationship between wave asymmetries and local wave conditions,
- model the evolution of wave asymmetries over coastal structures, and examine the contribution of wave conditions and geometries to the evolution,
- interpret the underlying physics of the transformation of wave asymmetries over coastal structures,
- investigate spatial distribution of overtopping water behind impermeable coastal structures, paying special attention to the effects of wave conditions, structural geometries, and landward ground level on spatial distribution of wave-overtopping water,

- improve the RANS-VOF model and validated the numerical results by measurements,

The organization of this thesis is as follows: **Chapter 2** presents a comparison of potential numerical models in simulating wave-structure interactions, a description of the RANS-VOF model and model improvements for the present work. **Chapter 3** gives the parameterization and transformation of wave asymmetries over Low-Crested Structures based on measurements. **Chapter 4** presents numerical simulations and interpretations of the evolution of wave asymmetries over Low-Crested Structures, paying special attention to the area above the structure. The underlying physics is also given at the end. **Chapter 5** investigates landward spatial distribution of overtopping water using the RANS-VOF model, along with a semi-analytical model and parameter analysis of numerical results. **Chapter 6** summarizes conclusions and future points of investigation that have been identified through the development of this study.

CHAPTER 2

NUMERICAL MODEL

In this chapter, the comparison of some potential numerical models in simulating wave-structure interactions is presented, along with the justification of selecting RANS-VOF model in this study. It is then followed by a brief description of the selected RANS-VOF model. Some model improvements that have been done during this work are introduced at the end of this chapter.

2.1 Introduction

Since an accurate description of wave transformation processes is necessary to assess correctly the performance of LCS, a series of previous studies have let to a deeper knowledge of wave-structure interaction, based on experimental and numerical investigation. Experimental study mainly focused on the wave transmission, wave reflection and energy dissipation (e.g. Seelig, 1980; Seabrook and Hall, 1998; Sakakiyama and Liu, 2001;

Kramer et al., 2005; Van der Meer et al., 2005). However, experimental investigations on wave-structure interactions have two main disadvantages: first, the imperfection of experimental setups and device limitations; second, small-scale experiments are influenced by scale effects, large-scale models are expensive to be built. As a consequence, numerical modelling has gained great popularity in recent decades for studying the wave-structure interaction. It provides a means to obtain information of magnitudes in a high spatial and time resolution, as well as the flexibility in setups of numerical simulations.

The traditional numerical model is nonlinear shallow water equation (NLSWE) model, which is derived from the Navier-Stokes equations with the assumptions of hydrostatic pressure distribution, a depth-uniform velocity profile and negligible vertical accelerations. Kobayashi et al. (1987) employed it to study wave run-up and reflection from structures, but only for impermeable boundaries. Kobayashi and Wurjanto (1989) then investigated the normally incident irregular waves on a rough permeable slope and within a thin permeable under-layer. It was extended to irregular waves interacting with thick permeable under-layers by Kobayashi and Wurjanto (1990). Numerical Results were validated by Cox et al. (1994) with the swash zone measurements of irregular waves from the SUPERTANK Laboratory Data Collection. Van Gent (1994) applied the nonlinear shallow water equation model to wave motion inside the permeable structures. Satisfactory results were obtained for modelling surface elevations and wave velocities. This kind of model was also employed to simulate the propagation and run-up of one-

dimensional long waves by Titov and Synolakis (1995) and long-shore and onshore wave propagation by Titov and Synolakis (1998). Results showed that the model describes the evolution and run-up of nonbreaking waves very well. To consider wave breaking, one dimensional depth-averaged NLSWE with bore-like dissipation and quadratic bottom friction was widely used for the study of the surf zone (Raubenheimer et al., 1995; Elgar et al., 1997) and swash zone (Raubenheimer et al., 1996). They found that this kind of model described well the combined effect of reflection and dissipation. More recently, such models have been used to simulate wave overtopping (Causon et al., 2000; Hu et al., 2000; Hubbard and Dodd, 2002). Model results are in good agreement with analytical solutions and laboratory data for wave overtopping at sloping and vertical seawalls, although the detailed structure of wave breaking is ignored. However, NLSWE model is restricted to small relative water depth. It requires locating the offshore boundary condition of the numerical model close to the structure. NLSWE model is suitable for relative long waves, therefore cannot reproduce the nonlinear interactions between peak frequency and its higher harmonics. In addition, restrictions of NLSWE model are associated with the semi-empirical introduction of breaking, porous flow modelling or the difficulty in simulating complicated free surfaces.

The Boussinesq model can be thought as an extension of the NLSWE model with larger ranges of frequencies and water depths, by adding extra terms to account for the dispersion and the nonlinearity. Peregrine (1967) firstly introduced the standard Boussinesq equations into coastal

engineering using the depth-averaged velocity as a dependent variable. The Boussinesq model is able to predict the nonlinear wave transformation in varying depth by integrating the momentum and conservation of mass equations over depth reducing the three-dimensional problem to a two-dimensional one. After that, Boussinesq equations were developed over many decades and applied widely to the simulations of wave-structure interactions. Beji and Battjes (1994) improved the Boussinesq model with improved dispersion properties to simulate propagations of regular and irregular waves over a submerged trapezoidal bar. Comparisons for non-breaking waves show good agreement between numerical results and measurements. Boussinesq models simulate wave breaking process by adding a dissipation term to the depth-integrated momentum equations. For instance, Karambas and Koutitas (1992) used the eddy viscosity model and Schäfer et al. (1993) employed a more complicated 'roller' model to incorporate the velocity distribution in the aerated region. Results of these models showed reasonable agreement with measurements for free-surface profiles, but are unlikely to produce accurate solutions for the velocity field. Karambas and Koutitas (2002) developed a higher-order Boussinesq model, with improved linear dispersion characteristics to describe wave motion in the regions upstream and downstream of the breakwaters. Numerical results show very good agreement with experimental data. Taking account of the bed or structural permeability, Flaten & Rygg (1991) used the Darcy's flow approximation to model the flow inside the permeable bed, while Cruz et al. (1997) introduced a fictitious potential function to linearize the problem.

Hsiao et al. (2002) presented a fully nonlinear 2D Boussinesq-type model for regular waves propagating over a permeable bed and a porous submerged breakwater. Since the linear Darcy's law fails due to the turbulence effect for flows with a high Reynolds number, Forchheimer extended Darcy's law to include a quadratic term for the frictional force induced by turbulence (Bear, 1972). Avgeris et al. (2004) introduced the Forchheimer terms instead of a depth-averaged Darcy equation to account for the flow inside the submerged permeable breakwaters. Johnson et al. (2005) incorporated a depth-averaged Darcy-Forchheimer equation describing the flow inside the porous medium into the model derived by Karambas and Koutitas (2002) with an eddy viscosity formulation. These numerical results of waves and currents in the vicinity of submerged porous breakwater are in good agreements with the laboratory data. Fuhrman et al. (2005) improved the highly accurate Boussinesq-type model by Madsen et al. (2002; 2003) to allow domains with arbitrary piecewise-rectangular bottom-mounted (surface-piercing) structures. Numerical simulations include cases of linear wave diffraction around a semi-infinite breakwater, linear and nonlinear gap diffraction, and highly nonlinear deep water wave run-up on a vertical plate. However, Boussinesq theory accommodates only moderate curvature of the free surface and is unable to provide a full description of wave breaking (Reeve et al., 2008). Moreover, Boussinesq models also lack the capability to determine spatial distribution of the turbulent kinetic energy due to its depth-integrated momentum equations.

It is well known that models with the Navier-Stokes solver are able to

describe nearshore wave-structure interactions without assuming the hydrostatic pressure. They also can predict the initiation of wave breaking with a more advanced turbulence model, such as nonlinear k-ε model. Lin and Liu (1998) developed the RANS-VOF model to study the evolution of a wave train, shoaling and breaking in the surf zone. The mean flow field is governed by the Reynolds equations with a nonlinear Reynolds stress model. Further turbulence closure assumptions lead to a set of transport equations for the turbulent kinetic energy, k, and the turbulence dissipation rate, ε. The volume of fluid (VOF) method, which was originally developed by Hirt & Nichols (1981), was employed to track the free surface. It is a front capturing method and can be used for modelling large-scale deformations of the interface including break up and merging. In order to consider the structural permeability, Liu et al. (1999) applied this model to porous structures with the assumption of no turbulence inside the porous media. The turbulence boundary layer adjacent to the porous wall was modified by including the effects of percolation velocity along the porous boundary. This assumption is not valid if the permeability of the medium is large, since there is strong experimental evidence that turbulence inside the protective armour layer could be significant under breaking waves when the size of the armour unit is relatively large (Sakakiyama and Liu, 2001). Hsu et al. (2002) applies the volume averaged method into the RANS-VOF model, developed by Lin and Liu (1998), in order to consider the fluid in the porous media and outside fluid simultaneously. This model was supported by the experiment data on wave propagating over a trapezoidal structure with permeable armour

(Sakakiyama and Liu, 2001). Garcia et al. (2004) applied the RANS-VOF model to investigate the near-field flow around the permeable structure under only regular waves. Losada et al. (2005) investigated the velocity and turbulence distribution around and inside the permeable structure. Lara et al. (2006) extended the application of RANS-VOF model to irregular wave cases, by using an internal wave-maker. The model performs well on different incident wave spectra, validated successfully by small-scale laboratory tests. Losada et al. (2008) employed the RANS-VOF model to investigate the functionality of rubble mound breakwaters with special attention focused on wave overtopping processes. The computed surface elevation and pressure under regular and irregular waves were compared with the experimental data, reaching a very good agreement. The model also reproduced the instantaneous and average wave overtopping discharge well. Another kind of Navier-Stokes-VOF model was also developed by Greaves (2004) and Greaves (2006) and Greaves (2007) with adapting quadtree grids and a Compressive Interface Capturing Scheme for Arbitrary Meshes (CICSAM) interface advection scheme. Model Results of interactions between viscous waves and a submerged cylinder in a stationary tank are in good agreement with experimental and other numerical data. In addition, model results showed the sufficient ability in simulating large-scale deformation of the free surface. Previous work proved the sufficient capability of simulating the complex wave-structure interactions, consisting of wave reflection, transmission, overtopping, breaking due to transient nonlinear waves and turbulence in the fluid domain.

In order to reproduce three dimensional processes including a better turbulence description of wave-structure interactions, A 3D Large Eddy Simulation (LES) model with a Smagorinsky sub-grid scale turbulence mode was employed by Christensen and Deigaard (2001) to simulate wave breaking, the large scale water motions and turbulence induced by the breaking process. The application of this model was extended to the investigation of flow rate over and through the gap of submerged breakwaters by Losada et al. (2005) and the free surface flow over a semi-circular obstruction by Lu et al. (2008). Results showed good agreement with measurements of wave basin experiments for instantaneous free surface and turbulence properties. However, computational efforts for LES approximations are still time consuming nowadays. There are few applications of LES on simulating porous flow as well.

Being a Lagrangian approach, particle methods such as the Moving Particle Semi-Implicit (MPS) method of Koshizuka et al. (1995) or the Smooth Particle Hydrodynamics (SPH) method (Dalrymple et al., 2001; Gotoh et al., 2004; Shao et al., 2006) have become very popular, by accurately tracking large deformations of the free surface. However, the high number of particles required, the limited validations available and very low computational efficiency are some of the issues that need to be resolved before considering SPH for complex wave-structure interactions. In addition, although Shao et al.(2006) demonstrated that SPH model can be used for wave overtopping, the RANS-VOF simulations of Reeve et al. (2008) gave slightly better results in comparison to experiments than the SPH model.

The justification of selecting RANS-VOF model is based on the consideration of three main aspects in wave-structure interactions. Firstly, when wave interacts with coastal structures, there is strong 3-D effect near these structures, where vertical variations of velocities and turbulence are significant. RANS-VOF model is depth-resolved model and therefore it can reproduce the vertical variations but the same does not hold for the depth-averaged Boussinesq model. Secondly, wave overtopping over coastal structure is a violent natural phenomena and always associates with complex free surface, such as the overtopping jet. RANS-VOF model is able to consider large free surface deformations with the Volume of Fluid capturing scheme, but Boussinesq model accommodates only moderate curvature of the free surface. Thirdly, wave breaking and wave overtopping over coastal structures associates with strong turbulence. RANS-VOF model captures the turbulence well with a k-ε turbulence model, while Boussinesq model lacks the capability to determine distribution of turbulent kinetic energy due to depth-integrated equations.

To date, RANS-VOF model is possibly the most adapted to the study of wave-structure interaction for engineering purposes, as computational efforts are reasonable and the number of simplifying assumptions is considerably reduced compared to Boussinesq models. RANS-VOF model is also probably most extensively validated for the simulations of wave-structure interaction. As a result, the RANS-VOF model is employed in the present work.

2.2 RANS-VOF Model

This study employs the RANS-VOF model that was developed by Lin and Liu (1998), Liu et al. (1999) and Lin and Liu (1999). It consists of a Reynolds-Averaged Navier-Stokes solver, a two equations k-ε turbulence model and a Volume of Fluid surface capturing scheme.

2.2.1 Governing equation

Turbulence flow

The Reynolds-Averaged Navier-Stokes (RANS) equations for an incompressible fluid are:

$$\frac{\partial \langle u_i \rangle}{\partial x_i} = 0 \tag{2.2.1}$$

$$\frac{\partial \langle u_i \rangle}{\partial t} + \langle u_j \rangle \frac{\partial \langle u_i \rangle}{\partial x_j} = -\frac{1}{\langle \rho \rangle}\frac{\partial \langle P \rangle}{\partial x_i} + \frac{1}{\langle \rho \rangle}\frac{\partial}{\partial x_j}\left(\mu\left(\frac{\partial \langle u_i \rangle}{\partial x_j} + \frac{\partial \langle u_j \rangle}{\partial x_i}\right) - \langle \rho \rangle \langle u_i' u_j' \rangle \right) + g_i \tag{2.2.2}$$

Where '< >' represents the ensemble average, "'" represents the turbulent fluctuation, $<u_i>$ is the i-th component of the velocity vector (i, j=1, 2 for a two dimensional problem), ρ is the fluid density, $<P>$ the mean pressure, g_i is the i-th component of the gravitational acceleration, μ the molecular dynamic viscosity, and $\langle u_i' u_j' \rangle$ is the Reynolds stress.

Flows in the porous media

Due to the complex structures of porous materials, it is not feasible to

resolve the intrinsic flow field and solve the N-S equations directly inside pores. Instead, Liu et al. (1999) and Hsu et al. (2002) suggested that the flow equations are averaged over a length scale l_p, which is larger than the characteristic pore size and is much smaller than the scale of the spatial variation of the physical variables in the flow domain. Therefore, the fluid variables can be decomposed into two parts, spatially averaged and spatially fluctuated quantities, i.e. $u_i = (\overline{u_i} + u_i'')/n$, n is the structural porosity.

The mean flow in porous media is governed by the following equations as described by Liu et al., (1999):

$$\frac{\partial \overline{u_i}}{\partial x_i} = 0 \tag{2.2.3}$$

$$\frac{1+c_A}{n}\frac{\partial \overline{u_i}}{\partial t} + \frac{\overline{u_j}}{n^2}\frac{\partial \overline{u_i}}{\partial x_j} = -\frac{1}{\rho}\frac{\partial \overline{P}}{\partial x_i} + g_i + \frac{\nu}{n}\frac{\partial^2 \overline{u_i}}{\partial x_j \partial x_j} - g a_p \overline{u_i} - g b_p \overline{u_i} \tag{2.2.4}$$

$$c_A = \gamma_p \frac{1-n}{n} \tag{2.2.5}$$

$$a_p = \alpha_p \frac{(1-n)^2}{n^3}\frac{\nu}{g D_{50}^2} \tag{2.2.6}$$

$$b_p = \beta_p (1 + \frac{7.5}{KC})\frac{1-n}{n^3}\frac{1}{g D_{50}} \tag{2.2.7}$$

where $u_c = \sqrt{\overline{u_i}\,\overline{u_i}}$; ν is the molecular kinematic viscosity; n is the effective porosity of porous materials; van Gent (1995) proposed that γ_p=0.34, α_p=1000 for both the armour layer and the core and β_p=0.8 and 1.2 respectively for negative or null freeboard structures. Losada et al. (2005)

argued that β_p=0.4 instead of 1.2 for positive freeboard without wave overtopping. KC is the Keulegan-Carpenter (Keulegan and Carpenter, 1958) number representing the ratio of the characteristic length scale of fluid particle motion to that of porous media, i.e., $KC=u_cT/(nD_{50})$, where T is the typical wave period and D_{50} is the characteristic diameter of porous materials.

In the equation (2.2.4), the third term on the right hand side is responsible for transferring shear force and may become increasingly important near the interface between porous media and outside flow for smaller scale problems; the fourth term is the frictional force induced by viscous effect (surface friction); and the fifth term represents the turbulence effect (form drag). However, formulations above for flows in the porous media have not considered the shape, orientation, and surface roughness of porous materials, which also affect the added mass and friction characteristics.

Turbulence model

As can be seen in Equation (2.2.2), Reynolds stresses should be related to the mean velocities in order to solve the Reynolds equations for the mean flow. Extensive research work has been done to seek the proper closure model for the Reynolds stresses in the 1970s (e.g. Launder and Spalding, 1974; Launder et al., 1975). An alternative to Reynolds stress closure model is the so-called k-ε model in which Reynolds stress tensor is assumed to be related to the strain rate of the mean flow and and the characteristic scales of turbulence through the algebraic nonlinear Reynolds stress model (Shih et

al., 1996).

$$\begin{aligned}\left\langle u_i'u_j'\right\rangle = &\frac{2}{3}k\delta_{ij} - C_d\rho\frac{k^2}{\varepsilon}\left(\frac{\partial\langle u_i\rangle}{\partial x_j}+\frac{\partial\langle u_j\rangle}{\partial x_i}\right)\\ &-\rho\frac{k^3}{\varepsilon^2}\left[C_1\left(\frac{\partial\langle u_i\rangle}{\partial x_l}\frac{\partial\langle u_l\rangle}{\partial x_j}+\frac{\partial\langle u_j\rangle}{\partial x_l}\frac{\partial\langle u_l\rangle}{\partial x_i}-\frac{2}{3}\frac{\partial\langle u_l\rangle}{\partial x_k}\frac{\partial\langle u_k\rangle}{\partial x_l}\delta_{ij}\right)\right.\\ &+C_2\left(\frac{\partial\langle u_i\rangle}{\partial x_k}\frac{\partial\langle u_l\rangle}{\partial x_k}-\frac{1}{3}\frac{\partial\langle u_l\rangle}{\partial x_k}\frac{\partial\langle u_l\rangle}{\partial x_k}\delta_{ij}\right)\\ &\left.+C_3\left(\frac{\partial\langle u_k\rangle}{\partial x_i}\frac{\partial\langle u_k\rangle}{\partial x_j}-\frac{1}{3}\frac{\partial\langle u_l\rangle}{\partial x_k}\frac{\partial\langle u_l\rangle}{\partial x_k}\delta_{ij}\right)\right]\end{aligned} \tag{2.2.8}$$

$$k=\frac{1}{2}\left\langle u_i'u_j'\right\rangle,\ \varepsilon=\nu\left\langle\left(\frac{\partial u_i'}{\partial x_j}\right)^2\right\rangle \tag{2.2.9}$$

where C_1, C_2, C_3 and C_d are empirical coefficients, k is the turbulent kinetic energy and ε is the turbulent dissipation rate, δ_{ij} is the Kronecker delta (equals 1 if i=j, and 0 otherwise) and ν is the molecular kinematic viscosity.

The conventional eddy viscosity model can be derived with $C_1=C_2=C_3=0$ and it is in the expression:

$$\left\langle u_i'u_j'\right\rangle=\frac{2}{3}k\delta_{ij}-2\nu_t\left\langle\sigma_{ij}\right\rangle \tag{2.2.10}$$

in which σ_{ij} is the rate of strain tensor, ν_t is the eddy viscosity $\nu_t=C_dk^2/\varepsilon,\ C_d=0.09$.

Recommended by Shih et al. (1996) and Lin and Liu (1998), the empirical coefficients are:

$$\left.\begin{aligned} C_d &= \frac{2}{3}\left(\frac{1}{7.4+S_{\max}}\right) \quad C_1 = \frac{1}{185.2+D_{\max}^2} \\ C_2 &= -\frac{1}{58.5+D_{\max}^2} \quad C_3 = \frac{1}{370.4+D_{\max}^2} \end{aligned}\right\} \qquad (2.2.11)$$

Where $S_{\max} = (k/\varepsilon)\max(|\partial u_i/\partial x_i|)$ and $D_{\max} = (k/\varepsilon)\max(|\partial u_i/\partial x_j|)$.

Two equations k-ε turbulence model are:

$$\frac{\partial k}{\partial t} + \langle u_j \rangle \frac{\partial k}{\partial x_j} = + \frac{\partial}{\partial x_j}\left[\left(\nu + \frac{\langle \nu_t \rangle}{\sigma_k}\right)\frac{\partial k}{\partial x_j}\right] - \langle u_i' u_j' \rangle \frac{\partial \langle u_i \rangle}{\partial x_j} - \varepsilon \qquad (2.2.12)$$

$$\frac{\partial \varepsilon}{\partial t} + \langle u_j \rangle \frac{\partial \varepsilon}{\partial x_j} = C_{1\varepsilon}\frac{\varepsilon}{k}\nu_t\left(\frac{\partial \langle u_i \rangle}{\partial x_j} + \frac{\partial \langle u_j \rangle}{\partial x_i}\right)\frac{\partial \langle u_i \rangle}{\partial x_j} + \frac{\partial}{\partial x_j}\left[\left(\nu + \frac{\nu_t}{\sigma_\varepsilon}\right)\frac{\partial \varepsilon}{\partial x_j}\right] - C_{2\varepsilon}\frac{\varepsilon^2}{k} \qquad (2.2.13)$$

The empirical coefficients that appear in the model are surprisingly universal. The recommended values for these coefficients are (Rodi, 1980): C_d =0.09; $C_{1\varepsilon}$=1.44; $C_{2\varepsilon}$=1.92; σ_k=1.0 and σ_ε=1.3.

2.2.2 Boundary condition:

Free surface:

For the dynamic boundary condition, denoting $\vec{n}$ as the unit normal on the free surface and n_i as the projection of $\vec{n}$ on the x_i, the continuity of the normal stress component is:

$$\langle P \rangle - \mu\left(\frac{\partial \langle u_i \rangle}{\partial x_j} + \frac{\partial \langle u_j \rangle}{\partial x_i}\right) n_i n_j = \langle \tau_n \rangle \qquad (2.2.14)$$

in which $<\tau_n>$ is a prescribed normal stress applied on the free surface and the surface tension has been ignored. If external tangential stress component is applied on the free surface $<\tau_t>$, the continuity of tangential stress component becomes:

$$\mu\left(\frac{\partial\langle u_i\rangle}{\partial x_j}+\frac{\partial\langle u_j\rangle}{\partial x_i}\right)n_i t_j=\langle\tau_t\rangle \tag{2.2.15}$$

Kinematic boundary condition is:

$$\frac{\partial F}{\partial t}+u_i\frac{\partial F}{\partial x_i}=0 \tag{2.2.16}$$

where F is any physical property associated with the free surface particles.

The exchange of turbulent kinetic energy and the turbulent dissipation rate at the free surface are assumed to be zero, that is,

$$\frac{\partial\langle\varepsilon\rangle}{\partial x_i}n_i=0 \tag{2.2.17}$$

$$\frac{\partial\langle k\rangle}{\partial x_i}n_i=0 \tag{2.2.18}$$

Solid boundary:

For solid boundary, such as impermeable bottom and structure interface, it is difficult to resolve the viscous layer for practical computation. Alternatively, the free-slip boundary condition and the turbulent boundary theory are applied:

$$\langle u_i \rangle \cdot n = 0 \quad in\ \Omega \tag{2.2.19}$$

$$\frac{\partial \langle u_i \rangle \cdot \tau}{\partial n} = 0 \quad in\ \Omega \tag{2.2.20}$$

where Ω is the part of the fluid domain boundary where the slip occurs; $<u_i>$ (i=1,2 for a two dimension problem) is the velocity vector in Ω; n and τ are the outward unit normal vector and a tangent unit vector in Ω.

For the turbulence field, near the solid boundary, the log-law distribution of mean tangential velocity in the turbulent boundary layer is applied, where the values of k and ε can be expressed as functions of distance from the boundary and the mean tangential velocity outside of the viscous sub-layer:

$$\frac{\langle u \rangle}{u^*} = \frac{1}{\kappa} \ln(E \frac{u^* y}{\nu}) \tag{2.2.21}$$

$$k = \frac{u^{*2}}{\sqrt{C_d}} \tag{2.2.22}$$

$$\varepsilon = -\langle u'v' \rangle \frac{d\langle u \rangle}{dy} = \frac{u^{*3}}{\kappa y} \tag{2.2.23}$$

$$\nu_t = -\frac{\langle u'v' \rangle}{\frac{\partial \langle u \rangle}{\partial y}} = \kappa u^* y \tag{2.2.24}$$

Inlet and outlet boundary

The open boundary, composed of the radiation boundary condition and sponge layer, is employed at the inlet and outlet of the computational

domain.

The radiation boundary is:

$$\frac{\partial C}{\partial t} \pm c_i \frac{\partial C}{\partial x_i} = 0 \qquad (2.2.25)$$

where i=1, 2, representing the x- and y- coordinates; $c_i=\sqrt{g(h+\eta)}$ is the analytic wave velocity of the wave train that is positive at the right boundary and negative at the left boundary. For irregular wave only the peak component of irregular waves was considered; C could represent both surface elevation and velocity vectors.

Inside the sponge layer, an additional friction term is added to the original momentum equation in RANS equations (Equation 2.2.2) and this term takes the form of $-f_f(x)*\langle u_i\rangle$, where $f_f(x)$ is the friction factor and $\langle u_i\rangle$ is the ensemble-averaged velocity in the i-th direction. Based on Wei and Kirby (1995), the function $f_f(x)$ has the form:

$$f_f(x) = \alpha \frac{\exp\left[\left(\frac{x_s - x}{x_s}\right)^n\right] - 1}{\exp(1) - 1} \quad for\ x_0 - x_s \le x \le x_0 \qquad (2.2.26)$$

where x_o is the coordinate of the right edge of the sponge layer, x_s the length of the sponge layer, α=200 and n=20 in present work.

As mentioned by Lin et al. (1998), the model will produce no turbulent energy if there is no turbulent kinetic energy initially. Both the initial condition and inflow boundary condition for k and ε are defined as:

$k = \frac{1}{2}(\zeta c)^2$ and $\varepsilon = C_d k^2/(\xi \nu)$, where c is the wave celerity on the inflow boundary, ζ=2.5e-3, ξ=0.1. Lin et al. (1998) found there is little impact on the numerical solutions for both ζ and ξ, except the breaking point.

Interface between fluid and porous media

In reality, the flow just outside of the porous surface is in the form of jets and wakes, which are turbulent and quickly mixed within a short distance in order of characteristic pore size D_{n50}. However, present work mainly concerns wave transformations and overtopping outside of the porous materials, which is not significantly influenced by the approximation of the mean flow field just outside of the porous media (Liu et al. 1999). The turbulence model is not solved in the porous media either.

Ilegbusi (1989) suggested the formulation to calculate the wall shear stress near a porous surface:

$$\frac{\langle u_t \rangle - \overline{u_t}}{(\tau_w/\rho)^{1/2}} = \frac{1}{k} \ln\left\{\frac{Ey\left[(\tau_w + \tau_m)/\rho\right]^{1/2}}{\nu}\right\} \qquad (2.2.27)$$

$$\tau_m = \frac{c_n \overline{v_n} \langle u_t \rangle}{1 + (\tau_w/\rho)^{1/2}/(k\langle u_t \rangle)} \qquad (2.2.28)$$

Where <u_t> is the tangential velocity outside of the turbulent boundary layer; $\overline{u_t}$ is tangential averaged velocity along the porous bed; von Karman constant k=0.41; E is roughness coefficient and equals 9.0 for smooth wall; τ_w is wall shear stress; τ_m is additional shear stress caused by flow suction or

injection through the porous bed; $\overline{v_n}$ is normal averaged velocity across the porous bed and c_n=0.01 suggested by Liu et al. (1999).

With known $\langle u_t \rangle$, $\overline{u_t}$ and $\overline{v_n}$, τ_w can be calculated using the Newton-Raphson method. The friction velocity u* can be calculated subsequently by $u^{*2} = |\tau_w| / \rho$, which can be employed to define both the turbulent kinetic energy, k, and dissipative rate, ε near the porous surface.

2.2.3 Surface capturing scheme and Partial Cell Treatment

The volume of fluid (VOF) method is a convenient and powerful tool for modelling fluid flows that contain a free surface. It is used to identify different types of computational cells and thus can be used to track the free surface motion. The VOF concept achieves this by defining a fractional volume or a VOF function, $f_0(x, y, t)$, which specifies the fraction of a computational cell filled with fluid (Figure 2.2.1). For simplicity the time and space varying function $f_0(x, y, t)$ is described by f_0. For example:

$$f_0 = \begin{Bmatrix} 0 & empty\ cell \\ 1 & full\ cell \\ other & surface\ cell \end{Bmatrix} \qquad (2.2.29)$$

The transport equation for the VOF function, f_0, is:

$$\frac{\partial f_0}{\partial t} + \left(\langle u_i \rangle \nabla\right) f_0 = 0 \qquad (2.2.30)$$

where u_i (i=1,2) is the fluid velocity vector.

When calculating these convective fluxes special care must be taken to avoid computational smearing of the air-fluid interface because this causes considerable inaccuracy in the interface representation. Hirt and Nichols (1981) proposed a simple way to track the fluid interface by introducing the volume of fluid (VOF) concept and a scheme for the advection of the VOF fraction function, which is called the Donor–acceptor method. Their VOF method shows the effectiveness for tracking a fluid interface. The algorithm of Hirt and Nichols (1981), known as 'piecewise constant scheme', is that the interface was forced to align with one of the coordinate axes (horizontal or vertical) depending on the prevailing direction of the interface normal. Fluxes in a direction perpendicular to the reconstructed interface are estimated using a Donor – Acceptor method.

The basic idea of partial cell treatment is that the obstacle can be modelled as a special case of two-phase flow with infinite density. Partial cell treatment partially blocks the cell face and cell itself according to the real geometry of the boundary. The openness coefficient, δ, is defined as the ratio of the fluid volume to the total volume in a cell (Figure 2.2.1). The variables in cells or cell faces are redefined as the multiplication of openness coefficients with original variables representing the mean values there. Near the obstacle openness coefficients are less than unity that makes the mean quantities smaller than their original values. When openness coefficients equal zero (obstacle), the numerical calculation is skipped in this cell.

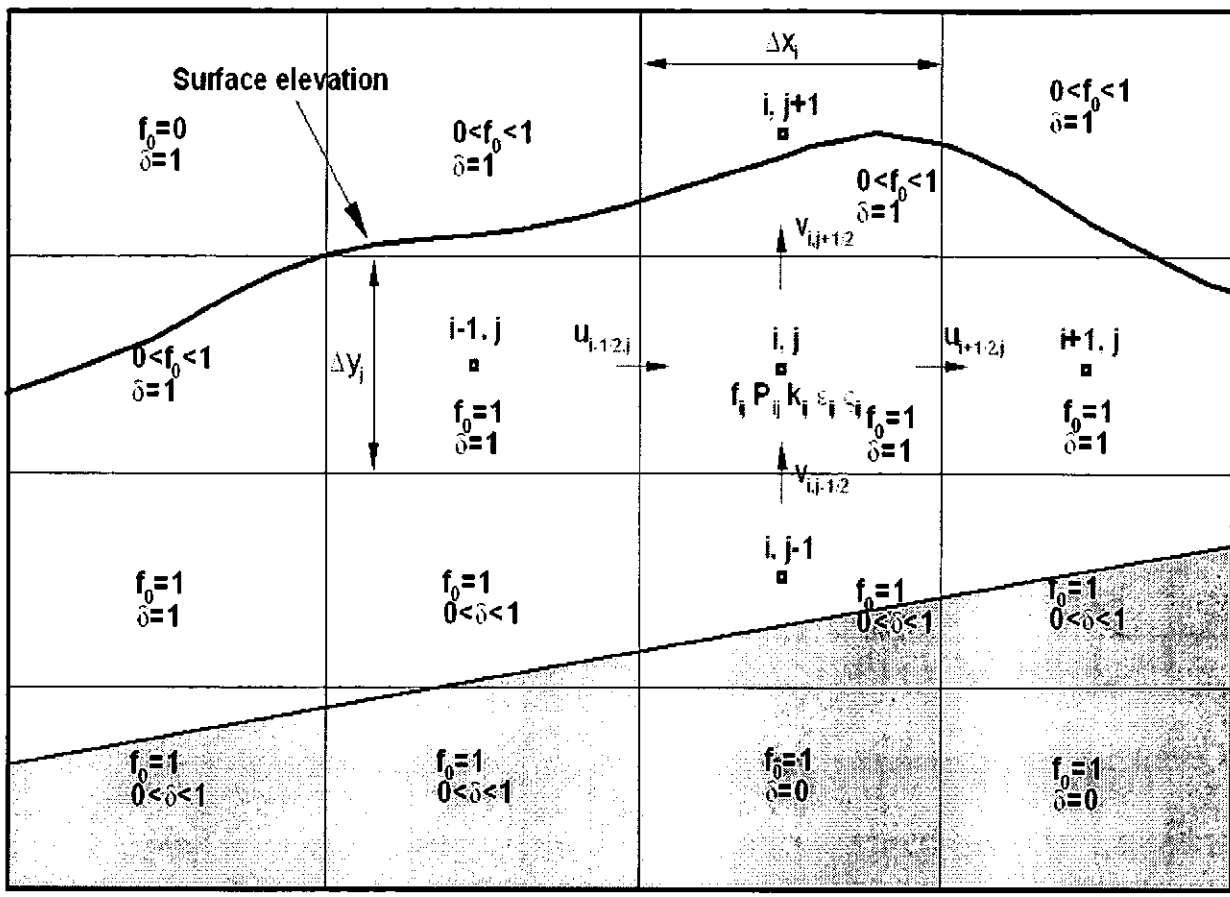

Figure 2.2.1 Finite difference meshes and cell classifications in the model, f_o: the ratio of cell occupied by the fluid to the whole cell area, δ: the ratio of cell not occupied by the solid object to the whole cell area.

2.2.4 Internal wave maker

It is a challenging work to generate the incident waves from inlet boundary and at the same time absorb the reflected waves from obstacles or beaches in the computational domain. For depth-averaged equations models, only the surface elevations are needed at the inlet boundary. Previous researchers (e.g. Kobayashi et al., 1987; Dongeren and Svendsen, 1997) developed the generating-absorbing boundary conditions based on the assumption of linear superposition of incident and reflected waves. However,

this type of boundary condition can only be applied to small amplitude waves and may lead to cumulative errors, which may contaminate numerical results in the entire domain eventually (Wei et al., 1999).

RANS-VOF model requires the velocity information along with the free surface elevations at the inlet boundary. Thus, the model is more sensitive to the errors from the boundary than other depth-averaged equations models. Although Petit et al. (1994) employed the weakly reflecting boundary conditions that send the incident wave and absorb the weakly reflected wave simultaneously, this method again can only be applied to small amplitude waves due to the linear theory assumption.

Based on the idea of Larsen and Dancy (1983) that a source function inside the computational region is used to generate waves, Lin and Liu (1999) employed this internal source function in the RANS-VOF model to generate the linear monochromatic waves and irregular waves (hereinafter internal wave maker). The validated relative wave height (H/h) is up to 0.3. The internal wave generator is not interacting with reflected waves, but leads to considerable increase of computational domain.

The brief description of the internal wave maker is (Lin and Liu, 1999):

$$\frac{\partial u}{\partial x}+\frac{\partial v}{\partial y}=s(x,y,t) \ in \ \Omega \qquad (2.2.31)$$

Where s(x, y, t) is nonzero mass source function within the source region Ω, the free surface directly above the source function will respond

immediately to the mass change induced by this source. A train of surface gravity waves will be generated due to the restoring force by the gravity.

The source region used in present work is a rectangle with the width (horizontal) of w_s and the height (vertical) of d_s, where $w_s << \lambda$, λ is the target wavelength. With the assumption that all of the mass increase or decrease introduced by the mass source function contributes to the generation of the target wave, the source function s(x, y, t) should satisfy the following relationship:

$$\int_0 \int_\Omega s(x,y,t)\, d\Omega dt = 2\int_0 C\eta(t) dt \qquad (2.2.32)$$

Where C is phase velocity of the target wave. The factor 2 is used since waves are generated on both sides of the source region. The spatial varying mass source function is not considered here.

The source function s(x, y, t) can be easily derived depending on the wave theory, Equation 2.2.32 and the assumption of the area A for rectangular source region Ω. In the present study, the source functions s(x, y, t) are:

For sinusoidal wave: $$s(t) = \frac{CH}{A}\sin(\omega t) \qquad (2.2.33)$$

For 2nd-order stokes wave:

$$s(t) = \frac{CH}{A}\cos(\omega t + P_s) + \frac{CkH^2}{8A}\frac{\cosh(kh)\left[2+\cosh(2kh)\right]}{\sinh^3(kh)}\cos(2\omega t + 2P_s) \qquad (2.2.34)$$

To maintain the numerical stability, the source function s(t) must start

from zero, therefore, $$P_s = \arccos\left(\frac{-1+\sqrt{1+8b_0^2}}{4b_0}\right) \quad (2.2.35)$$

In which, k is wave number, C is phase velocity of the target wave, H is wave height and $b_0 = \frac{kH}{8}\frac{\cosh(kh)\left[2+\cosh(2kh)\right]}{\sinh^3(kh)}$.

An irregular wave is composed of a series of sinusoidal waves with different wave frequency and amplitude. For a known energy spectrum of an irregular wave, the wave train can be reconstructed through the inverse Fourier transformation with a finite number of wave components. Therefore, an irregular wave can be generated by superposing different wave components:

$$s(t) = \sum_{i=1}^{n} \frac{2C_i a_i}{A} \sin(\omega_i t + p_{si}) \quad (2.2.36)$$

Where a_i, ω_i, p_{si} and C_i are the amplitude, angular frequency, phase and phase velocity of the i-th target wave component respectively; h is water depth at the source region; A is the area for rectangular source region.

In sum, internal wave maker is implemented in following steps: Firstly, setup the source region in a rectangular with the width far smaller than the target wavelength. Secondly, calculate the source function with the assumption that all of the mass increase or decrease introduced by the mass source function contributes to the generation of the target wave. Thirdly, add this source function within the source region into the right hand side of the continuity equation, to generate surface elevations.

2.2.5 Computational mesh

A staggered mesh finite difference scheme is used in the present model. At the beginning the whole computational domain is discretized by the i_{max}*j_{max} rectangular cells as sketched in Figure 2.2.1. The i-index of cells increases from the left boundary to the right boundary and j-index of cells increases from the bottom boundary to the top boundary of the computational domain. i_{max} and j_{max} are the maximum index of cells in the horizontal and vertical directions respectively. All scalar quantities, i.e. $P_{i,j}$, $k_{i,j}$, $\varepsilon_{i,j}$, the VOF function, $f_{i,j}$, and the openness function, $\delta_{i,j}$, in the cell (i, j) are defined in the centre of the cells, while the vector and vector-related quantities, such as mean velocities $u_{i,j}$ and $v_{i,j}$ are defined in the cell faces.

The present model is able to generate a non-uniform mesh. When a variable mesh is to be specified, the model uses the linear divergent function to make a smooth grid change (Lin and Liu, 2000). Although the use of uniform meshes can produce more accurate results than the use of variable meshes, in some practical computations, the variable size of mesh is necessary to reduce the computational cost. For example, when the case of wave breaking is simulated, the resolution near the breaking point must be rather fine in comparison to what needed to resolve the wave itself. However, it is necessary to deploy the constant size mesh around the free surface and both inlet and outlet boundary to ensure the high accuracy of free surface computation and the stability of numerical simulations.

The aspect ratio of the mesh size in the cell (i, j), $\Delta x_i/\Delta y_j$, is of great

importance for accurately capturing the free surface by VOF method. Normally, $\Delta x_i/\Delta y_j=1$ is preferred but Δx_i can be an order of magnitude greater than Δy_j for some small amplitude long waves. For breaking wave simulation, the aspect ratio should be smaller than or equal 2.5 to avoid inaccuracy arising from false breaking (Lin and Liu, 2000).

2.2.6 Time Step Criteria

The explicit finite difference form for transient advection-diffusion equations (Equations 2.2.1, 2.2.2, 2.2.3, 2.2.4, 2.2.12 and 2.2.13) is subject to the numerical instability unless certain stability criteria are satisfied. The standard von Neumann stability analysis was employed to obtain the stability criteria for the linear approximation:

$$\Delta t \le \min\left\{\frac{\langle u\rangle}{\Delta x_{i,j}}, \frac{\langle v\rangle}{\Delta y_{i,j}}\right\} \tag{2.2.37}$$

$$\Delta t \le \min\left\{\frac{1}{2(\nu+\nu_t)}\left[\frac{(\Delta x_{i,j})^2(\Delta y_{i,j})^2}{(\Delta x_{i,j})^2+(\Delta y_{i,j})^2}\right]\right\} \tag{2.2.38}$$

The criteria are obtained with the assumption that the advection term is discretized by upwind scheme. The first criterion is from the stability requirement for the advection term and the second one arises from the diffusion term. However, due to the intrinsic nonlinearity in the governing equations and the combination of central difference method and upwind scheme for the advection term in the present model, two coefficients of 3/10

for Equation 2.2.37 and 2/3 for Equation 2.2.38 (Lin and Liu 1998) were employed to ensure the practical stability in the computation.

2.2.7 Computational procedure

By decomposing the instantaneous velocity and pressure fields into the mean and turbulent components, the RANS-VOF model solves the 2D Reynolds Averaged Navier–Stokes equations with the finite difference two-step projection method (Chorin, 1968, 1969). The first step is to introduce a tentative velocity without the pressure gradient term.

$$\frac{\tilde{u}_i^{n+1}-u_i^n}{\Delta t}=-u_j^n\frac{\partial u_j^n}{\partial x_j}+\frac{1}{\rho^n}\frac{\partial}{\partial x_j}\left(\mu(\frac{\partial u_i^n}{\partial x_j}+\frac{\partial u_j^n}{\partial x_i})-\rho\left\langle u_i'u_j'\right\rangle^n\right)+g_i \qquad (2.2.39)$$

In the second step, the tentative velocity is projected onto a divergence-free plane to obtain the final velocity.

$$\frac{u_i^{n+1}-\tilde{u}_i^{n+1}}{\Delta t}=-\frac{1}{\rho^n}\frac{\partial p^{n+1}}{\partial x_i} \qquad (2.2.40)$$

Since the pressure field is unknown in equation (2.2.40), the final velocity is obtained by solving the pressure Poisson equation (2.2.41). The pressure Poisson equation is derived by taking the divergence of equation (2.2.40) and applying equation (2.2.1) to the resulting equation.

$$\frac{1}{\Delta t}\frac{\partial \tilde{u}_i^{n+1}}{\partial x_i}=-\frac{\partial}{\partial x_i}\left(\frac{1}{\rho^n}\frac{\partial p^{n+1}}{\partial x_i}\right) \qquad (2.2.41)$$

Both the Reynolds equations and the k-ε transport equations are solved by discretizing the convection terms with the combined central difference method and upwind method. The central difference method is used for the diffusion, production, and dissipation terms. The time derivatives are discretized by using forward time difference. The time step scheme was usually adopted the explicit scheme in previous work (Lin and Liu, 1998; Liu et al., 1999; Hsu et al., 2002; Garcia et al., 2004; Hieu and Tanimoto, 2006; Karim and Tingsanchali, 2006; Lara et al., 2006). The complete processes of RANS-VOF model are summarized in Figure 2.2.2.

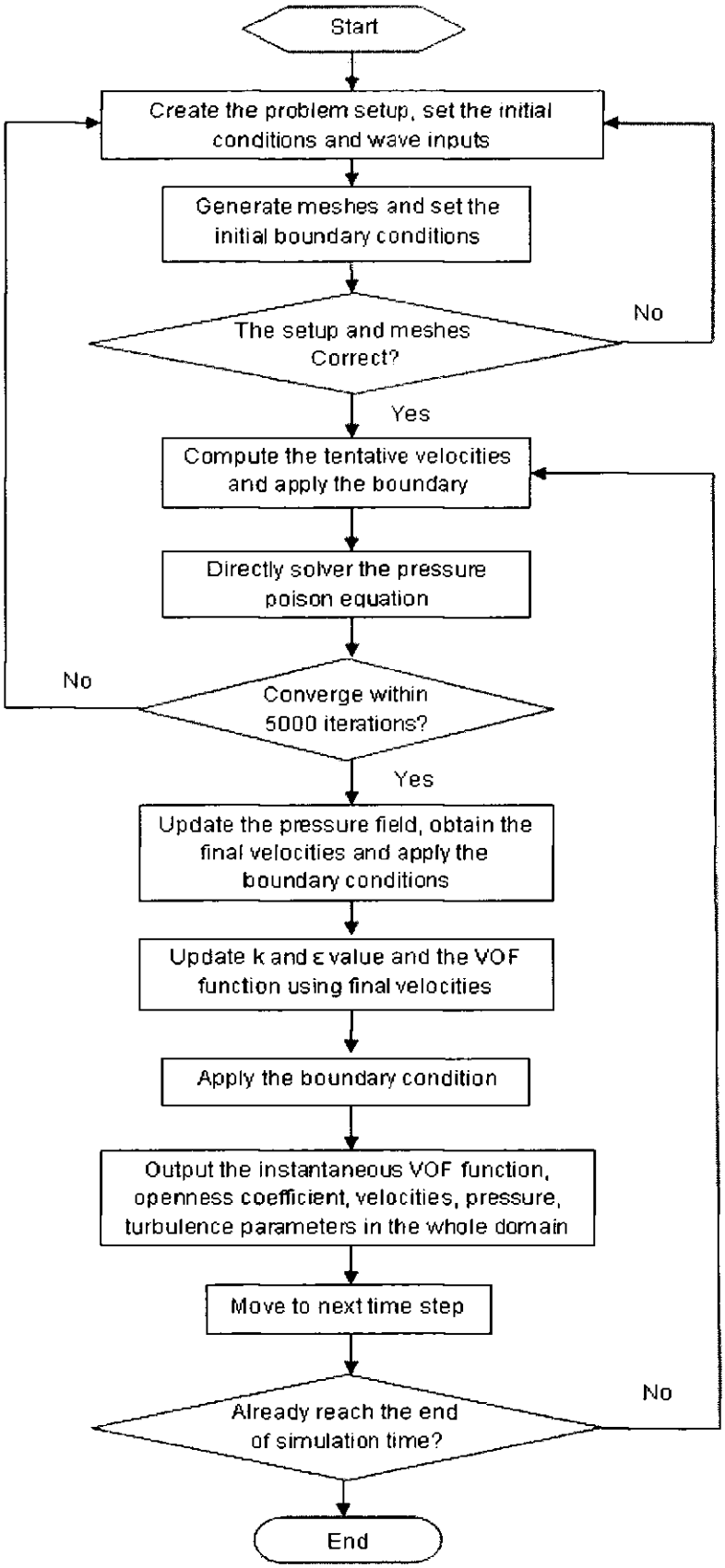

Figure 2.2.2 Flow chart of computational processes of RANS-VOF model

2.3 Model Improvements

The RANS-VOF model described above is widely used in coastal engineering. Although this model is capable of simulating wave-structure interactions, several aspects could be improved to increase the accuracy of numerical results and capability in handling the simulations of wave overtopping.

2.3.1 PLIC-VOF surface capturing scheme

The VOF method in the RANS-VOF model used the piecewise constant reconstruction algorithm of Hirt and Nichols (1981). This algorithm is not able to obtain the accurate locations of surface interfaces, which directly affect the computation of the pressure and the tangential velocities on the free surface. The main reason is that it always orientates free surface interfaces parallel to horizontal or vertical boundary of cells. The alternative is to orientate free surface interfaces in a direction perpendicular to the locally evaluated VOF gradient. Such method is known as piecewise linear interface calculation (PLIC) (Youngs, 1982; Ashgriz and Poo, 1991; Rider and Kothe, 1998; Lópeza et al., 2005). Thus, free surface interfaces within each cell can acquire any orientation, and the geometrical profile of the fluid can more closely represent the actual fluid geometry (Figure 2.3.1).

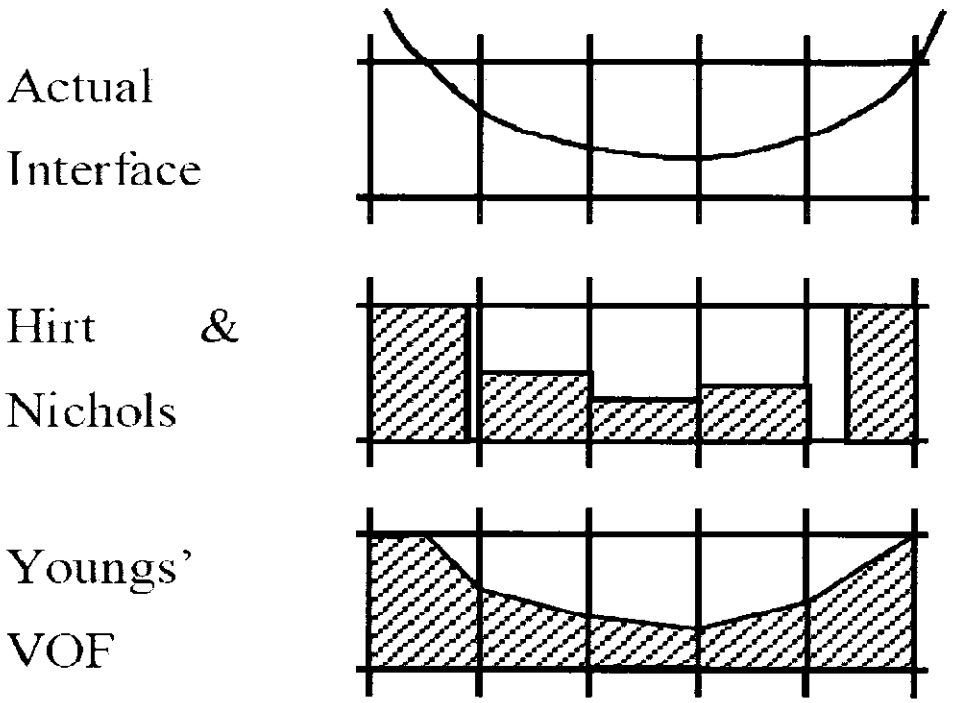

Figure 2.3.1 Comparisons between Hirt and Nichols' VOF interface reconstruction, Youngs' PLIC interface reconstruction and actual interface (Delnoij et al., 1988).

Most VOF advection algorithms are not derived directly from Equations 2.2.2, 2.2.4 and 2.2.13 but are based on a two-stage process. Firstly, free surface interfaces are 'reconstructed' from the VOF data; secondly, changes in VOF values are calculated by integrating fluid fluxes over cell boundaries, using the geometrical profile to indicate the location of fluid regions. In order to advance the solution of Equation 2.2.30 in time, it is first necessary to construct an approximation to the interface given the values of the volume fractions f_{ij}^n at time $t^n=n\Delta t$. This is referred to as the interface reconstruction algorithm.

An interface reconstruction algorithm in Youngs (1982) is used. Youngs' VOF method approximates the interface within a cell by a straight line

segment with a slope determined from the interface normal. This normal, in turn, is calculated from the gradient of the volume fraction using a nine point stencil:

$$\vec{n} = (n_x, n_y) = \frac{\nabla f}{|\nabla f|} = -(\frac{\partial f}{\partial x}, \frac{\partial f}{\partial y}) / \sqrt{\left(\frac{\partial f}{\partial x}\right)^2 + \left(\frac{\partial f}{\partial y}\right)^2} \tag{2.3.42}$$

The gradient of the volume fractions can be discretized by finite difference method as following:

$$\frac{\partial f}{\partial x} = \frac{f_E - f_w}{2} \tag{2.3.43}$$

$$\frac{\partial f}{\partial y} = \frac{f_N - f_S}{2} \tag{2.3.44}$$

$$f_E = \frac{1}{2+\alpha_0}(f_{i+1,j-1} + \alpha_0 f_{i+1,j} + f_{i+1,j+1}) \tag{2.3.45}$$

$$f_W = \frac{1}{2+\alpha_0}(f_{i-1,j-1} + \alpha_0 f_{i-1,j} + f_{i-1,j+1}) \tag{2.3.46}$$

$$f_N = \frac{1}{2+\alpha_0}(f_{i-1,j+1} + \alpha_0 f_{i,j+1} + f_{i+1,j+1}) \tag{2.3.47}$$

$$f_S = \frac{1}{2+\alpha_0}(f_{i-1,j-1} + \alpha_0 f_{i,j-1} + f_{i+1,j-1}) \tag{2.3.48}$$

where α_0 is a free parameter. Parker and Youngs (1992) proposed that $\alpha_0 = 2$ seems to give the best results.

The line segment cuts the computational cell under consideration in such a way that the fractional fluid volume is equal to f_{ij}. The interface normal computed in Youngs' 2D algorithm will reproduce a line, regardless of its orientation on an orthogonal mesh, and is, therefore, second-order accurate. The resulting fluid polygon is then used to determine the fluxes through any cell face with an outwards directed velocity. The method described above is used in this study because of its sufficient accuracy and rigorous volume (mass) conservation, especially in flow fields with appreciable spatial and temporal variations.

In order to examine the efficiency of Youngs' VOF interface reconstruction, a case with regular waves was simulated by the RANS-VOF model. Figure 2.3.2 shows on the incident side, calculated surface elevation of Hirt and Nichols' VOF is close to that of Youngs' VOF. Both of them are in a good agreement with the measurements. This may be because waves are relatively stable and do not break, consequently the free surface is regular and easy to be captured. On the transmission side, wave breaking and overtopping occurs above the structure, resulting in more turbulence generated and transported in the fluid. Therefore, the fluid became more and more unstable and free surface becomes irregular and complex. Figure 2.3.2b shows that model results calculated by Youngs' VOF are in better agreement with measurements than those by Hirt and Nichols' VOF, in particular at the harmonics. This is because that free surface interfaces within each cell by Youngs' VOF can be reconstructed in any orientation rather than only horizontal or vertical directions. The geometrical profile of the fluid can,

therefore, closely represent the actual free surface. Therefore, Youngs' VOF is able to provide more accurate numerical results than Hirt and Nichols' VOF.

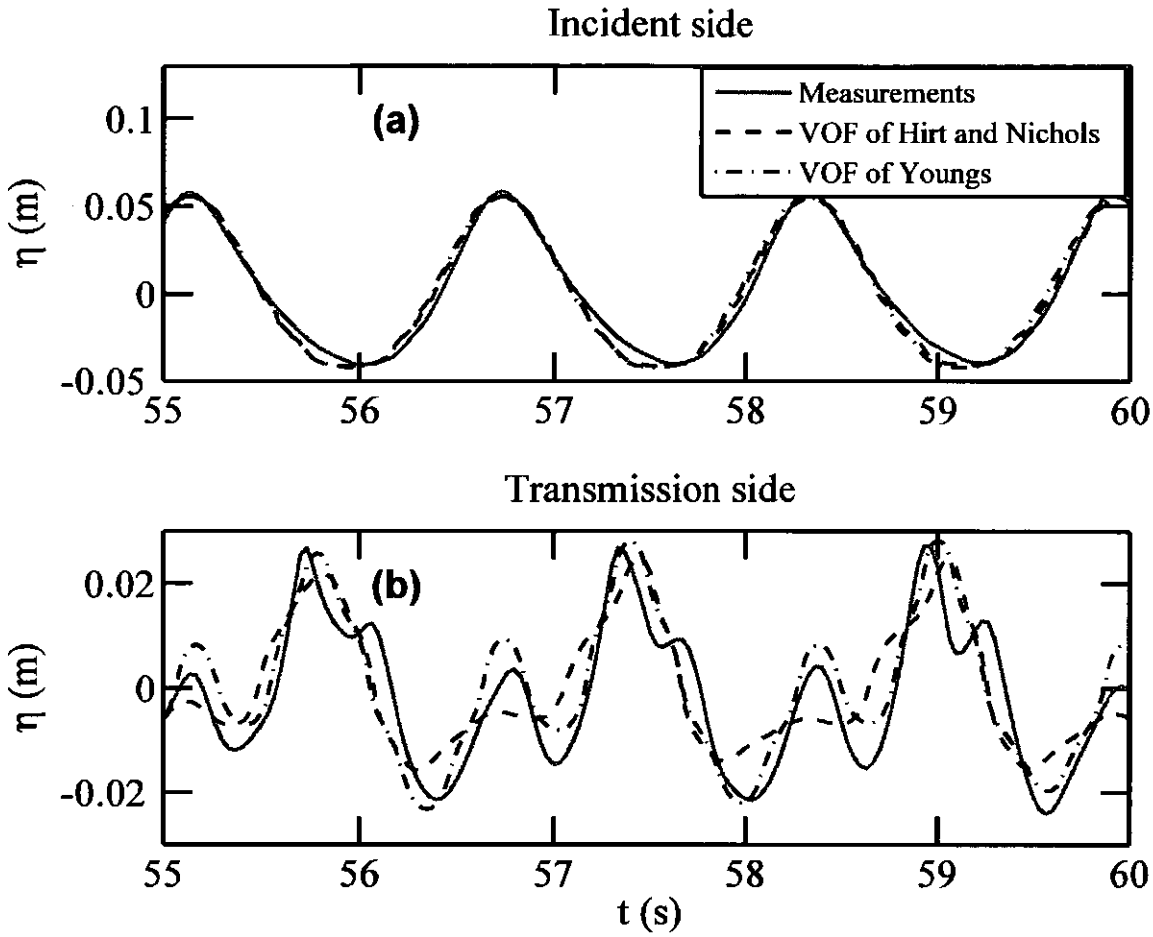

Figure 2.3.2 Comparisons of the surface elevation calculated by Hirt and Nichols' VOF and by Youngs' VOF and measurements (a) on the incident side (b) on the transmission side of LCS. Wave height H=0.10m, wave period T=1.6s, water depth h=0.35m and freeboard R_c=0m.

2.3.2 Return flow system

Coastal structures are designed to allow the transmission and overtopping of a certain amount of the incident wave energy to the

transmission side. In most 2D laboratory experiments of coastal structures, the overtopping and transmission give rise to a piling-up of water in the leeside region of the structure and hence to an increase of the mean water level. This setup on the transmission side modifies the dynamics of the waves in this region and the flow conditions in the vicinity of the breakwater. It forces a strong return flow over the structure which perturbs the wave breaking process on the structure seaward slope and crest, influencing the breaker type, position and height. In real cases of shore protected by coastal structures, this phenomenon is not observed, as the potential piling-up behind the breakwater is relieved by 3D circulation systems. Part of the flow is transmitted back to the seaward side through the permeable structure, but a greater proportion returns to the open sea by the sides of the breakwater, following pathways of lesser resistance (open areas with no breakwaters). In the experiments of DELOS project, a recirculation system was designed for preventing this usual shortcoming consisting of a non-realistic set-up on the transmission side of the coastal structures.

The numerical simulations also need to setup the configuration of the recirculation system the same as experiments. The return flow system consists of several small apertures on the bottom of computational domain (Figure 2.3.3). These apertures allow the excess of water in the leeward zone due to wave overtopping to flow back to the seaward zone, but do not disturb the flow pattern on either side of structures. The direction of this return flow is shown by the arrows in the figure. The returning flow in the numerical flume is exclusively forced by the difference of water level between the

seaside and leeside parts of the breakwater, and therefore has a nature-like pattern. This design is similar to that of Garcia et al. (2004).

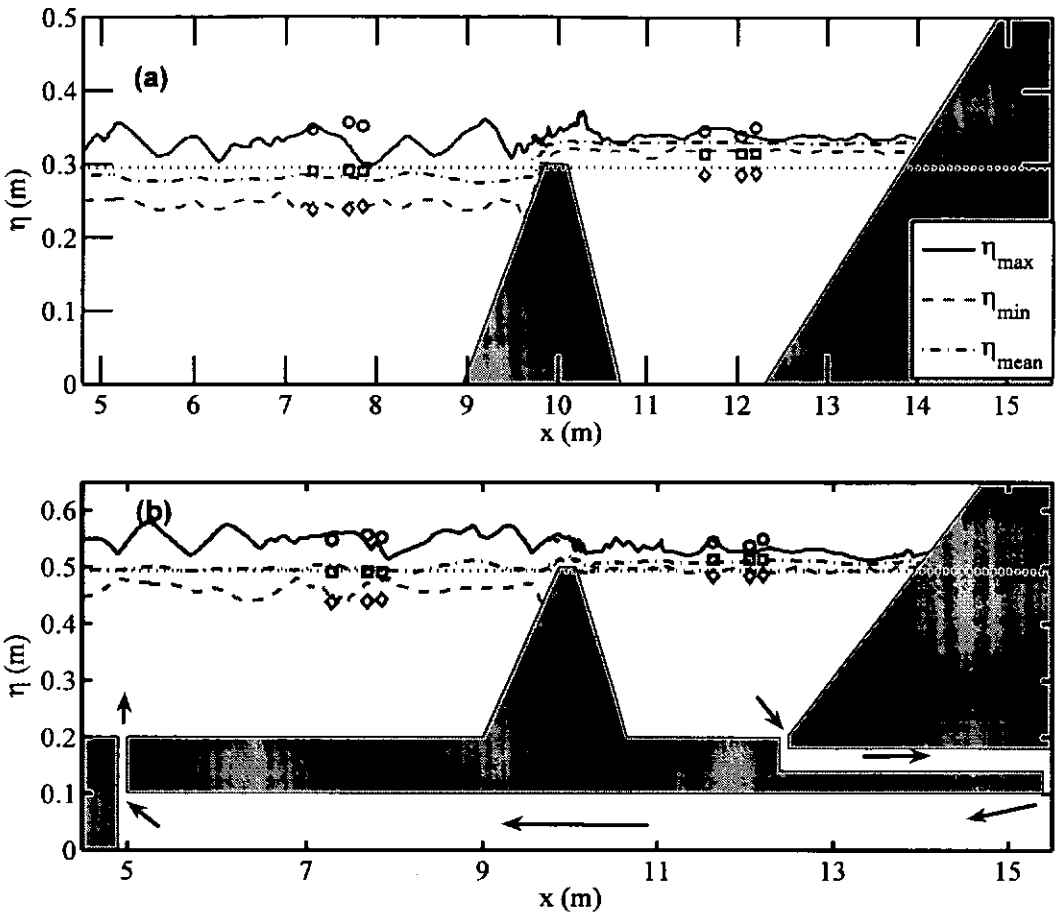

Figure 2.3.3 Wave height envelopes and mean water level during time interval from *t=101s* to *t=120s* with R_c=0m, (a) without flow recirculation, (b) with flow recirculation. Arrows stand for the direction of the return flow. Symbols represent the experimental data: '○' for maximum height; '□' for mean height; '◊' for minimum height. Spongy layer is located from x=0m to x=4m.

In order to examine the efficiency of this return flow pipe, case 2 in Table D2 was simulated by the RANS-VOF model. Figure 2.3.3 shows the maximum and minimum wave height envelopes and the mean water level measured in the laboratory (dots) and calculated with the numerical model

(lines). Numerical data result from a 10-wave phase-averaging, counted from 100s of simulation to ensure stable flow conditions. As can be seen in this figure, in the case without a recirculation system, the agreement between experimental and numerical data on the incident side is good. However, on the transmission side, the minimum and mean wave heights are overestimated significantly (Figure 2.3.3a). This is mainly due to the increasing pile-up of water level coming from the overtopping and transmission processes. Without a recirculation system, the increasing fluid volume cannot be drained until the water level is higher than the crest of structures, when the fluid can flow back to the incident side.

On the other hand, in the case with a recirculation system, the model is able to simulate adequately the main features of the propagation of a wave train passing over a zero freeboard breakwater (Figure 2.3.3b). The breaking induced mean water level decreases at the offshore side of the breaking point and then increases at the onshore side. Besides, in the leeward zone, overtopping of the structure can induce an increase of the mean water level. As can be seen in the Figure 2.3.3b, this set-up is correctly computed. As a result, a conclusion can be drawn that the return flow system improves the capability of RANS-VOF model in reproducing the waves and flow around coastal structures.

2.3.3 Wave overtopping algorithm

The governing parameters involved in wave overtopping over coastal

structures, such as significant wave height and peak period at the seaward toe of structure, the landward ground level, structural freeboard, structural crest width and structural slope, the layer thickness and velocity on the structural crest, were found to be important in wave overtopping process (Schüttrumpf and Oumeraci, 2005; Lykke Andersen and Burcharth, 2006; van der Meer et al., 2009). Historically, sloping sea dikes or sea walls (Figure 2.3.4) have been the most widely used option for sea defences along the coasts of the Netherland, Denmark, Germany and many parts of the UK (EurOtop, 2008). By changing the seaward slope, tan(α), the wave overtopping may exist following key processes: non-breaking or breaking waves overtopping over a sea wall, even a sloping sea dike or a vertical sea wall.

Figure 2.3.4 Hornsea's seawall along the Holderness coast, UK (Source: http://picasaweb.google.com/lh/photo/YCUHTs8PXbwdasEuIh9NRg).

A definition sketch of the embankment is given in Figure 2.3.5. The origin

of coordinates is at the landward end of structural crest with x for horizontal axis and y for vertical axis; H_i and T_{pi} are incident significant wave height and peak period at the seaward toe of structures; R_c, B and tan(a) are the structural freeboard, crest width and slope respectively. $u_{i,j}$, $v_{i,j}$, Δx_i, Δy_j are horizontal velocity, vertical velocity, cell width and cell height in the cell (i, j) respectively. $u_{A,50\%}$ is wave velocity at the crest of the structure, exceeded by 50% of the incoming waves; h_A is the layer thickness at the crest of the structure. h_{meas} represents the landward ground level.

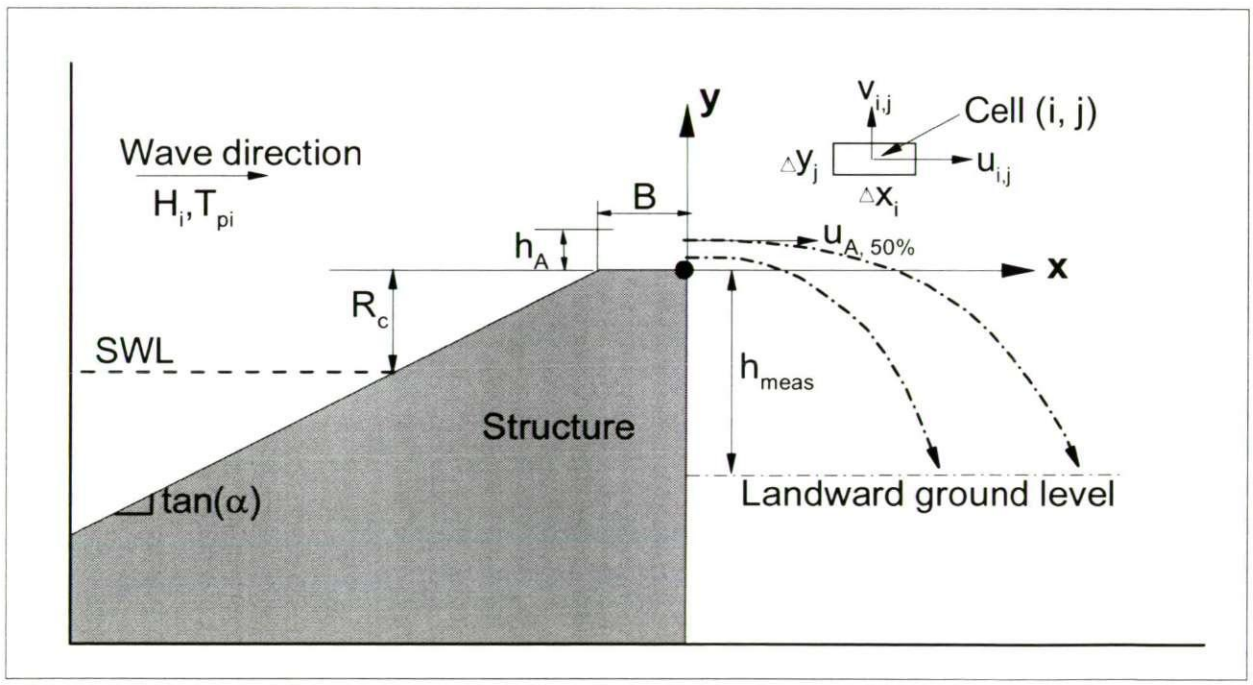

Figure 2.3.5 Sketch of a sea wall and definitions of governing parameters involved in numerical simulations of wave overtopping. The rule of the cell indexes can be referred in Section2.2.5.

The average overtopping discharge is usually calculated as the ratio of

cumulative overtopping volumes to the simulation time. However, the error in calculating overtopping volumes from VOF values may accumulate and become significant in numerical modelling. Instead, the overtopping rate *q(t)* per unit length of the dike is calculated as the product of layer thickness and overtopping velocity at the overtopping point (*x*=-*B*) (Schüttrumpf and Oumeraci, 2005). The average overtopping rate, q_{t_0} (x=-*B*), was calculated from *t*=0 to *t*=t_0 as:

$$q_{t_0} = \frac{\int_0^{t_0} \sum_{y(j)=0}^{y(j_{\max})} u_{i,j}(t) * \Delta y_j * f_{i,j} * dt}{t_0} \quad at\ x(i) = -B \qquad (2.3.49)$$

where $u_{i,j}(t)$ and Δy_j are the horizontal velocity and cell height in the cell (*i*, *j*) respectively (Figure 2.3.5). $f_{i,j}$ is the value of VOF function f_0 in the cell (i, j), j_{max} is the maximum index of cells in the vertical direction and t_0 is the simulation time.

In numerical modelling, the spatial distribution of overtopping water behind the structures can be calculated by:

$$\frac{V(x_0)}{V_t} = \frac{\int_0^{t_0} \sum_{x(i)=x_0}^{x(i_{\max})} v_{i,j}(t) * \Delta x_i * f_{i,j} * dt}{\int_0^{t_0} \sum_{x(i)=0}^{x(i_{\max})} v_{i,j}(t) * \Delta x_i * f_{i,j} * dt} \quad at\ y(j) = -h_{meas} \qquad (2.3.50)$$

where $V(x_0)/V_t$ is the proportion of overtopping volume passing x_0. $v_{i,j}(t)$ and Δx_i are the horizontal velocity and cell width in the cell (*i*, *j*) respectively. i_{max} is the maximum index of cells in the horizontal direction. t_0 is the

simulation time and h_{meas} is the landward ground level (Figure 2.3.5).

2.3.4 Mass conservation of wave overtopping

Wave overtopping water is usually in the forms of jets and splash behind the structures and these jets and splash are irreversible back to the incident side. In the experiments, the mean water level remains nearly constant since the length of flume in front of overtopping structures is large enough, and the overtopping volume is, therefore, relatively trivial to the initial water volume in front of overtopping structures. In numerical simulations, the irreversible overtopping water will cause the non-conserved mass on the incident side of the simulation domain. This non-conserved mass will accumulate as increasing simulation time up to a large value, leading to the decreasing mean water level and instability of simulations finally. Although large computation domain in front of overtopping structures could mitigate the effect of non-conserved mass on the stability of simulations, it inevitably increases the computational time of numerical simulations.

The mass difference of overtopping water between calculation step n and previous calculation step n-1, $\Delta m(n^*\Delta t)$, is:

$$\Delta m(n^*\Delta t) = \sum_{x(i)=-B}^{imax} \sum_{j=1}^{jmax} \left(f^n(i,j) - f^{n-1}(i,j) \right) * dx_{i,j} * dy_{i,j} \qquad (2.3.51)$$

where Δt is time step of numerical simulations; $f^n(i,j)$ and $f^{n-1}(i,j)$ stand for the VOF function in the cell (i, j) at $t=n^*\Delta t$ and $t=(n-1)^*\Delta t$ respectively; i_{max} and j_{max} are the maximum indexes of cells in the horizontal and vertical

directions; coordinates can be referred in Figure 2.3.5.

Considering the numerical diffusions occurred behind the structures, the Δm(t) may be a negative value without the wave overtopping. In this situation, the Δm(t) will be artificially defined as zero to avoid the mass errors on the incident side. Therefore, adding this mass term Δm(t) into the source function in Equation (2.2.36), we can obtain the updated source function to generate next waves with mass conservation:

$$s(x,y,t)=\sum_{i=1}^{n}\frac{2C_i a_i}{A}\sin(\omega_i t+p_{si})+\frac{\Delta m(t)}{A*\Delta t} \qquad (2.3.52)$$

where C is phase velocity of the target wave and A is the area of internal source region.

A sample of this mass difference is shown in Figure 2.3.6. The mass difference is similar to the pulse impact, with zero difference at most of time but dramatic fluctuations at some times. This is mainly due to the fluctuating nature of waves and wave run-up on the structure. The mass difference is very small by considering the compensation of wave overtopping mass the incident side of coastal structures. The percentage of mass difference to the initial mass is smaller than 5%. Therefore, this technique improves the stability of numerical simulation, as well as the accuracy of surface elevations and flow parameters.

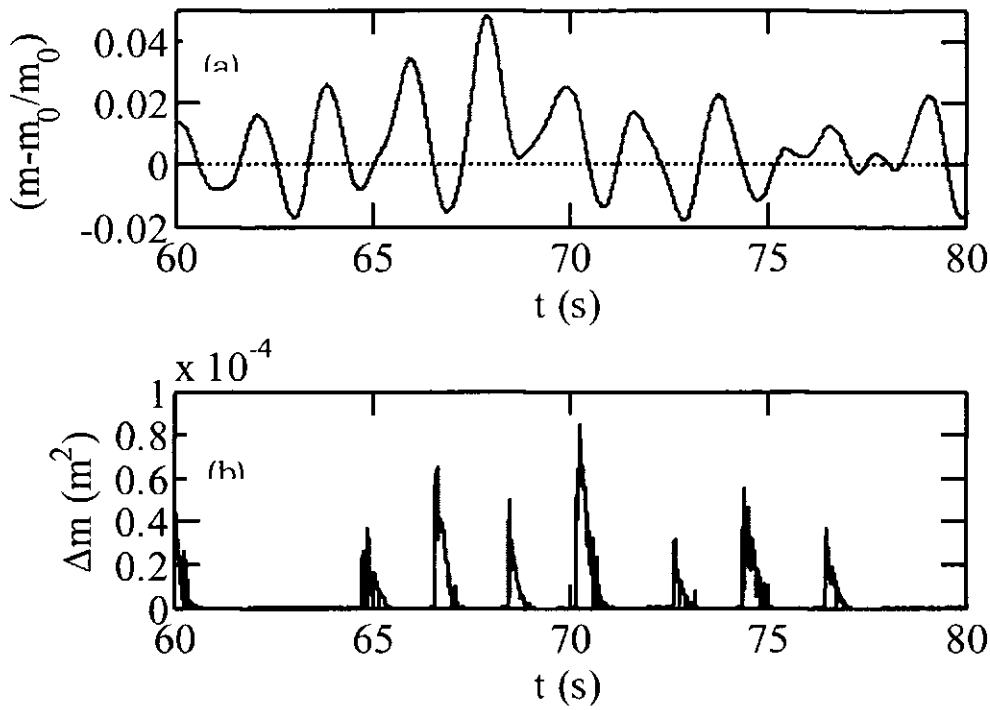

Figure 2.3.6 (a) Mass fluctuations on the incident side of overtopping structure and (b) mass difference of overtopping water, Δm. m_0 is the initial mass and m is the mass at simulation time t= n*Δt.

CHAPTER 3

PARAMETERISATION AND TRANSFORMATION OF WAVE ASYMMETRIES OVER LOW-CRESTED STRUCTURES (LCS)

Understanding the transformation of wave shapes, described by wave skewness and asymmetry, over coastal structures is crucial in the assessment of the functionality and stability of coastal and flood defence schemes. It is also central to the application and development of physically-based models of sediment transport that aim to simulate the evolution of cross-shore beach profiles.

The aim of this present work is to parameterize wave skewness and wave asymmetry and to understand their transformation over smooth and rubble mound Low-Crested Structures (LCS). A set of empirical formulae of wave asymmetries will be derived for practical use using laboratory data sets collected in the DELOS project. Bispectral analysis will be used to investigate

the contribution of nonlinear interactions between frequency components of wave spectrum to wave skewness and asymmetry.

This chapter includes four parts: firstly, the significance of wave skewness and wave asymmetry, and previous work are presented; followed by deriving a set of empirical formulae of wave asymmetries as functions of local wave parameters from laboratory data sets collected in the DELOS project; Bispectral Analysis is introduced next to investigate the main contribution of nonlinear interactions between frequency components of wave spectrum to wave skewness and asymmetry; finally a brief summary is given.

3.1 Introduction

It has long been recognised that wave skewness and asymmetry are directly related to sediment transport and subsequent changes in beach morphology. Inman and Bagnold (1963) were the first to apply the concept of a skewed velocity field to the modelling of beach equilibrium; Bagnold (1966) later applied this concept to predict the total bedload transport. Wilson (1966) showed that the net bed-load transport rate is proportional to the third moment of near-bed free-stream velocity. Subsequently, higher moments of the velocity field were incorporated into models of total bedload transport by Bowen (1980) and Bailard and Inman (1981). Elfrink et al. (1999) and Doering et al. (2000) analyzed the importance of velocity skewness on cross-shore sediment transport. Haas et al., (2008) found that the advection of sediment due to the skewed wave velocity is large and in the

direction of the waves. It is opposite to the results with sinusoidal wave velocities due to the increase in the bottom shear stress under the wave crests. Fuhrman et al. (2009) found that wave skewness has important onshore contributions outside the surf zone. Results of streaming induced within the wave boundary layer showed that skewness and asymmetry are demonstrated to promote largely offshore streaming velocities.

Nielsen (1992) noted that the onshore velocity of a pitch forward wave increases in magnitude faster than the offshore velocity, and the associated boundary layer has a shorter time to develop. Thus, the onshore velocity generates a thinner boundary layer and therefore a larger sediment transport. Drake and Calantoni (2001) found that differences in acceleration, between the front and the back of an asymmetric wave, yield horizontal pressure gradients in the boundary layer, which act on the near-bed fluid and sediment. This led Nielsen and Callaghan (2003) to conclude that the acceleration effects, associated with the saw-tooth asymmetry of the flume waves, account for the greatest part of the sediment transport. Hoefel and Elgar (2003) observed that onshore bar migration is related to cross-shore gradients in the skewness of velocity accelerations if mean currents are relatively weak. Hsu and Hanes (2004) employed a two-phase model to study the effects of wave shape on the transport of coarse-grained sediment in the sheet flow regime. Examinations of the sheet flow response to flow, forcing typical of asymmetric and skewed waves, indicated a net sediment transport in the direction of wave propagation. Gonzalez-Rodriguez and Madsen (2007)

parameterize the effects of wave shape on seabed shear stress and bedload transport.

Recently, Ruessink et al. (2009) found that sediments entrained into the flow during a particular wave half-cycle has not completely settled before flow reversal and tends to be transported during the next half-cycle. This phase-lag effect enhances net transport rates under oscillatory flow dominated by velocity asymmetry. Dong and Zhang (2002) found that the phase-lag between the free stream flow and particle can be simulated by two phase models described in Dong and Zhang (1999). Austin et al. (2009) found that onshore-directed flow accelerations under the steep front face of asymmetric waves were significantly correlated with sediment suspension, whilst the effects of flow skewness and bed-ventilation were discounted. Also van der A et al. (2010) confirmed that net transport in acceleration-skewed flow is non-zero, is always in the direction of the largest acceleration and increases with increasing acceleration skewness based on the experimental study.

Christou et al. (2008) concluded that highly nonlinear processes are involved in the evolution of waves propagating over a breakwater. The bispectrum can determine wave skewness and asymmetry arising from wave-wave nonlinear interactions. Bispectral analysis of previous studies showed that nonlinear interactions including self-interactions, sum and difference interactions determine the amplitude of wave skewness and asymmetry (Elgar and Guza, 1985; Crawford, 2000; Crawford and Hay,

2001). Based on the bispectral analysis of data sets for a natural beach, Doering and Bowen (1995) derived empirical relationships of wave skewness and asymmetry with Ursell number. Herbers *et al.* (2003) used a Boussinesq model to investigate the nonlinear transformation of the frequency-directional spectrum and bispectrum of surface gravity waves propagating over a submerged sand bar on a beach. Their Boussinesq model predicted surf zone skewness and asymmetry well. Zou et al. (2003) derived the analytical solutions of wave orbital velocity for the entire water column over a sloping bottom. Both their theory and observations showed that the skewness and asymmetry of the vertical velocity are subject to significant bottom slope effects, whereas those of horizontal velocity are not. However, these studies focused on wave skewness and asymmetry on natural beaches; the effect of coastal structures on wave skewness and asymmetry has not been investigated.

Low-Crested Structures (LCS) are increasingly regarded by coastal engineers and planners as a valuable alternative to more classical surface-piercing and/or high-crested structures. This is because the cost of the breakwater system increases with the increasing height of breakwaters. Furthermore, LCS are more aesthetic and do not spoil the coastal landscape, this being important in recreational and residential coastal development. Better understanding of the transformation of wave shapes over LCS is crucial in the assessment of the functionality and stability of coastal and flood defence schemes. Previous studies, however, have mainly been on wave

transmission, reflection and wave spectral change over LCS (Van der Meer et al., 2000; Van der Meer et al., 2005; Wang et al., 2007). Literature on the transformation of wave skewness and asymmetry over LCS is sparse.

3.2 Experimental data

Data was obtained from oblique three-dimensional wave transmission tests in the multidirectional wave basin (18.0 m × 12.0 m × 1.0 m) at Aalborg University, Denmark. Detailed descriptions about this project can be found in Appendix D2.

A smooth mound Low-Crested Breakwater, and a rubble mound Low-Crested Breakwater, were tested. The cross-section and layouts of smooth and rubble mound LCBs including positions of gauges are given in Figure D2. The target irregular 3-D waves were generated using the parameterised JONSWAP spectrum and spreading function of cosine distribution with spreading parameter s'=50. Layouts of breakwaters with 0°, 30° and 50° relative to the wave generator were used to cover a large range of wave incident angles.

Table 3.2.1 lists an overall view of 168 wave basin transmission tests under irregular waves. The observations were measured from ten fixed gauges, five of them located on the incident side of LCBs and the other five gauges located on the transmission side of LCBs. Each record was sampled at 40Hz and was 90-second long. A bandpass filtering (the upper and lower

cut-off frequencies are 5 and 0.2 times the peak frequency respectively) was applied to the measurements to remove the noise and signal which are separated in the temporal frequency domain.

Table 3.2.1 Overall view of test program in wave basin transmission tests

Parameters	Values
No of tests	168
Crest freeboard (m)	0.05, 0, -0.05
Water depth (m) (rubble mound LCS)	0.20,0.25,0.30
Water depth (m) (smooth LCS)	0.25,0.30,0.35
Wave height (m)	0.06 to 0.22
Wave steepness	0.02 to 0.058
Wave peak period (s)	1.06 to 2.33
Wave mean period (s)	0.9 to 1.8
Incidence angles (°)	0 to 60

3.3 Transformation of Wave Skewness and Asymmetry over LCS

Although the skewness and the asymmetry of near-bed velocities is directly related to the sediment transport rather than those of surface elevations, it is difficult to measure near-bed velocities and measurements have been done mainly for surface elevations. The skewness and asymmetry of near-bed velocities relate to those of surface elevations through a transfer function (Zou et al., 2003). The skewness, S, can be obtained from the third moment of surface elevation normalized by the second moment of surface

elevations to the power of 1.5:

$$S = \frac{E\left[\left(\eta_i - \overline{\eta_i}\right)^3\right]}{E\left[\left(\eta_i - \overline{\eta_i}\right)^2\right]^{\frac{3}{2}}} \tag{3.3.1}$$

where S represents wave skewness, η_i is the time series of surface elevations, $\overline{\eta}$ is the averaged surface elevations, E[ ] is the expected value.

Elgar and Guza (1985) proposed that wave asymmetry, A, can be calculated as the skewness of Hilbert transform (Oppenheim and Schafer, 1998) of surface elevations[1], ζ_i.

$$A = \frac{E\left[\left(\zeta_i - \overline{\zeta}\right)^3\right]}{E\left[\left(\zeta_i - \overline{\zeta}\right)^2\right]^{\frac{3}{2}}} \tag{3.3.2}$$

where A represents wave asymmetry, ζ_i is the Hilbert transform of surface elevations, $\overline{\zeta}$ is the mean of ζ_i.

A band pass filter (minimum frequency equals one fifth of peak frequency and maximum frequency equals five times of peak frequency) was applied to the calculated and measured time series of surface elevations.

[1] The Hilbert transform of surface elevations can be thought of as the convolution of $\eta(t)$ with the function $h(t) = 1/(\pi t)$

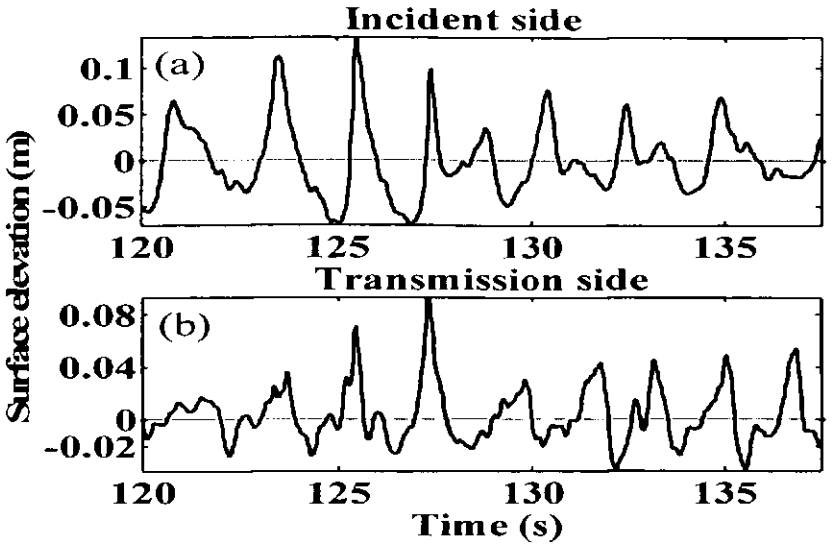

Figure 3.3.1 Surface elevation measured in (a) gauge 2 on the incident side and (b) gauge 7 on the transmission side of smooth LCS. Freeboard is 0 m, incident wave height is 0.14 m, wave period is 2.12 s, water depth is 0.3 m and incident angle is 0°.

As shown in Figure 3.3.1, waves are generally characterised by a gradual peaking of crests and flattening of troughs at both sides of breakwaters, a characteristic of positive wave skewness (Elgar and Guza, 1985). Also, most waves pitch forward on the incident side, but pitch backward on the transmission side, a characteristic of negative and positive asymmetries respectively. This change of wave shape from the seaward side to the leeward side of LCS was fully supported by the Bispectral analysis (Section 3.4) and numerical simulations (Section 4.4). The transmitted wave train has greater high frequency content than the incident wave train, as observed by Van der Meer et al (2005).

Parameters involved in wave transmission over LCS, such as incident wave height (preferably the value of H_s at the location of gauge 1), incident

wave angles (α), Iribarren number (ξ=tan(α)/(S_{op})$^{0.5}$, where tan(α) is the seaside slope of structures and S_{op} is the wave steepness in deep water), structural freeboards (R_c), crest width (B) and nominal diameters of rubbles (D_{n50}), were found to be important in wave transmission process (Van der Meer, *et al.*, 2005). A definition sketch is given in Figure 3.3.2.

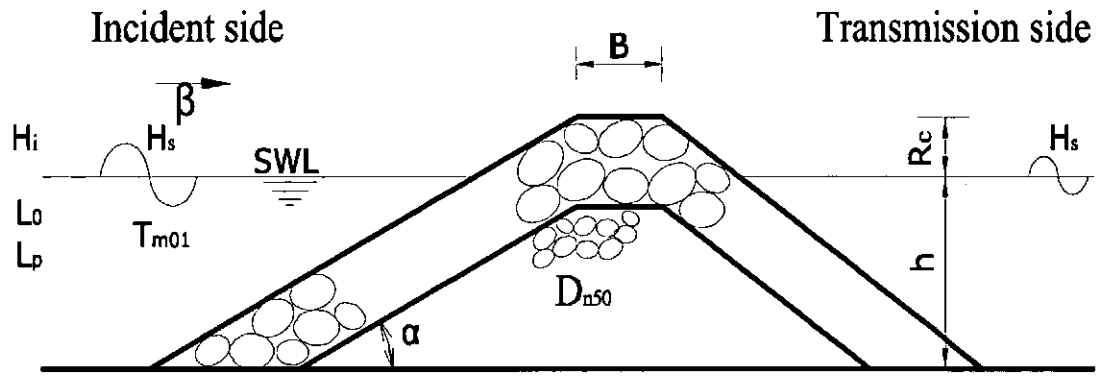

Figure 3.3.2 Definitions of governing parameters involved in wave transmission over LCS (Van der Meer et al., 2005).

However, parameters mentioned above are global and their effects on wave-structure interaction are reflected in the local wave parameters. For instance, the effect of incident wave angles is mainly on the transmission coefficient, and consequently the transmitted wave heights, which is consistent with the conclusions of Van der Meer et al. (2005). In addition, based on the bispectral analysis, Elgar et al. (1985) concluded that wave asymmetries were due to self-self interactions, sum frequency interactions

and different frequency interactions. Therefore, wave asymmetries are a measure of wave nonlinearity. The nonlinear interaction between two primary wave trains can induce a second-order Stokes wave train (Phillips, 1960), and Ursell number (the relative wave height times the relative wavelength squared) is the expansion parameter for a Stokes wave train. Thus the Ursell number indicates the wave nonlinearity. As a result, we will next look at the relationship between wave skewness or asymmetry and local Ursell number, which has been applied to parameterize orbital velocity asymmetries of shoaling and breaking waves on natural beaches in (Doering and Bowen, 1995; Doering et al., 2000). Although it has been observed that a gentler beach leads to more symmetric wave profile, this study does not consider the slope effect of LCS, since in the DELOS experiments the smooth LCB has only one seaside slope of 1:3, and the rubble mound LCB has only one seaside slope of 1:2 as well.

Van der Meer (2005) pointed out that more energy is distributed around higher frequencies than in the incident spectrum due to the effect of wave breaking over a low-crested breakwater. As a result, although the wave peak period on the transmission side (the reverse of peak frequency of wave spectrum) is close to wave peak period on the incident side, the mean period ($T_{m01}=2*\pi*m_0/m_1$, where m_0 is the zero order moment and m_1 is the first order moment of power spectrum) may decrease considerably. Taking case 17 in Table D2 for example, Figure 3.3.3 shows that the peak of power spectrum keeps the same ($f_p=2.23Hz$) when wave propagates from incident

side to the transmission side of LCS. However, the mean period T_{m01} changes from 1.54s on the incident side to 1.3s on the transmission side.

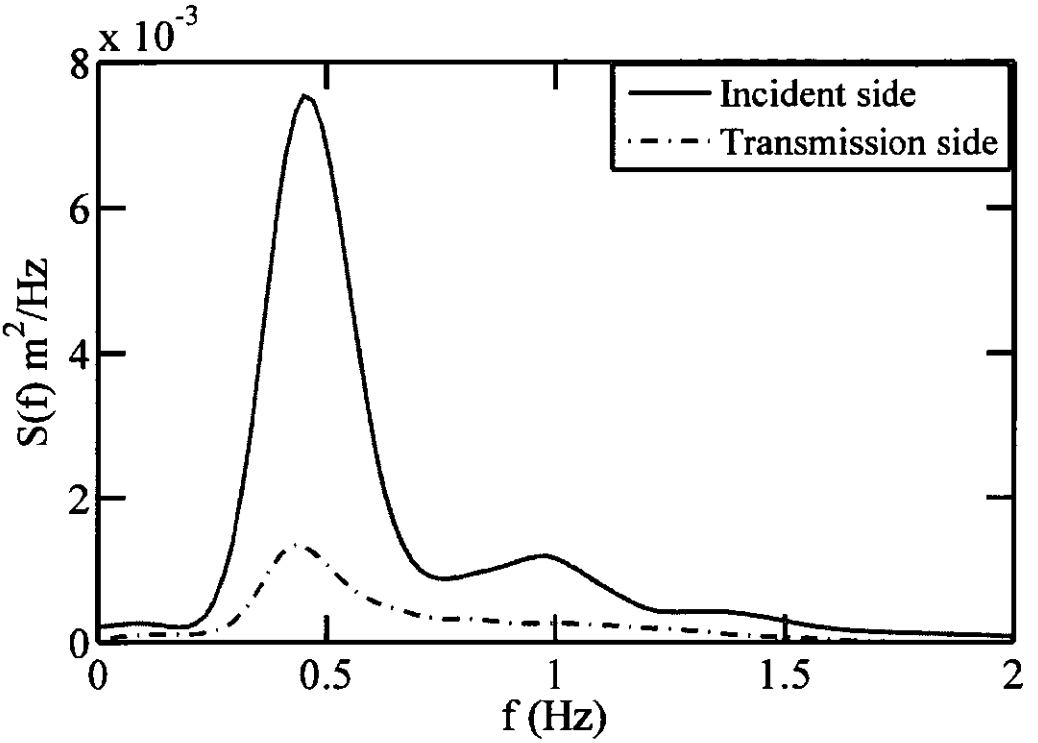

Figure 3.3.3 Power spectrum of surface elevation on the incident side and transmission side

Therefore, a local Ursell number calculated with peak period does not contain the information of wave period changes over LCS, which demonstrates the energy transferring from peak frequency to high frequencies over LCS (see Figure 3.4.2 and Figure 3.4.2). Wave mean period is used to calculate the local Ursell number instead. Thus, the definition of local Ursell number, U_r, in the present work is:

$$U_r = \frac{H_s L_m^2}{h^3} \tag{3.3.3}$$

where H_s is defined here as the average height of the highest one-third of the waves in 900 seconds for each gauge, L_m is the local mean wavelength calculated by the mean period and h is the local water depth.

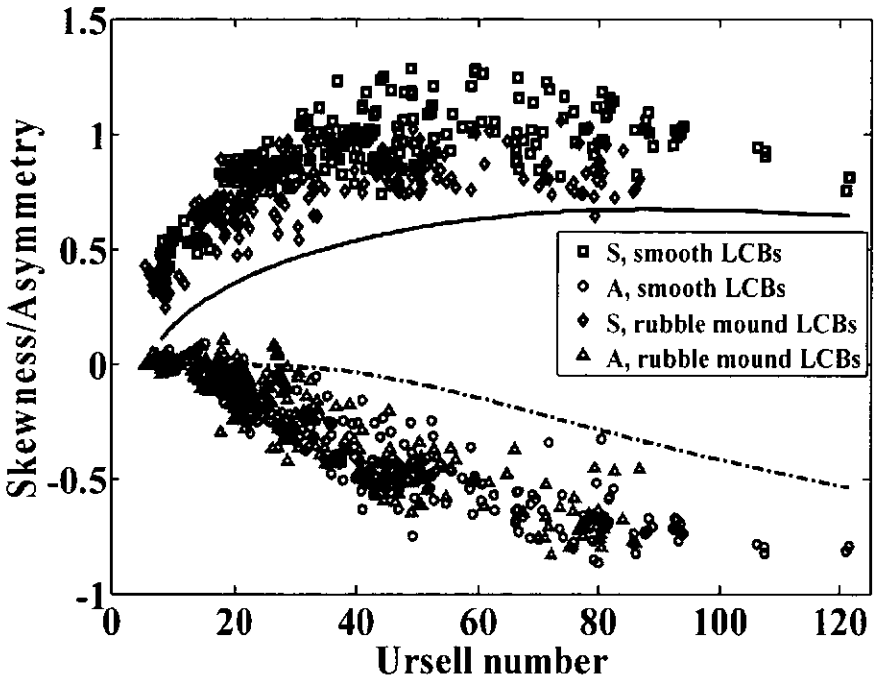

Figure 3.3.4 Comparison between Equations 4.10 (solid line) and 4.11 (dash-dotted line) in Doering and Bowen (1995) and DELOS data on the incident side of both smooth and rubble mound LCS. Note, the definition of Ursell number here is calculated by the peak period in order to keep the same as that in Doering and Bowen (1995).

It can be expected that wave skewness on the incident side (S_i) and asymmetry on the incident side (A_i) of LCS will show a similar relationship with respect to the Ursell number on the incident side (U_{ri}) as that of wave shoaling on a natural beach. Doering and Bowen (1995) obtained the relationship between wave asymmetries and the Ursell number, and argued

that the asymmetries at each depth are under strong local control. Figure 3.3.4 shows that the comparisons between Equations 4.10 and 4.11 in Doering and Bowen (1995) and DELOS data on the incident side of both smooth and rubble mound LCS. Note that the Ursell number in Doering and Bowen (1995) was calculated by peak period and also different from the present definition (Equation 3.3.3) by a factor 3/ (32π). Figure 3.3.4 shows that the Equations derived by Doering and Bowen (1995) underestimate wave skewness and absolute asymmetry. It is worth mentioning that Equations 4.10 and 4.11 in Doering and Bowen (1995) are empirical formulae derived from field measurements of a natural beach in the absence of coastal structures.

3.3.1 Transformation of wave skewness and asymmetry over smooth LCS

Figure 3.3.5a shows that wave skewness is positive and increases rapidly with increasing Ursell number, attains a maximum and then stays around the maximum. While wave asymmetry fluctuates around zero at small Ursell number, then becomes negative and decays with increasing Ursell number (Figure 3.3.5c). These results are similar to those of the natural beach (Doering and Bowen, 1995; Doering et al., 2000). Because of its similarity to saturation characteristics, the relationship between wave skewness and asymmetry and the Ursell number may be described by a hyperbolic tangent

law. Using the DELOS data, Equations 3.3.4 (the ratio of the regression sum of squares to the total sum of squares, R^2, is 0.69) and Equations 3.3.5 (R^2=0.84) are established from measurements on the incident side with least squares fitting and provide quantitative relationships between S_i and A_i in terms of U_{ri}. The range of Ursell number on the incident side is between 5 and 43.

$$S_i = 1.28 * \tanh(\frac{-3.17}{U_{ri}}) + 0.10 \qquad (3.3.4)$$

$$A_i = -1.53 * \tanh(\frac{-22.87}{U_{ri}}) - 1.52 \qquad (3.3.5)$$

It is expected that the relationship between wave skewness on the transmission side (S_t) and wave asymmetry on the transmission side (A_t) expressed in forms of the local Ursell number on the transmission side (U_{rt}) is not similar to that on the incident side due to the presence of LCS.

Figure 3.3.5b shows that wave skewness stays around zero at small Ursell number, then increases slowly up to a maximum value from zero, finally starts to decrease slowly. It is interesting to observe that wave skewness is larger than that on the incident side under the same Ursell number (Figure 3.3.5a and Figure 3.3.5b). Elgar and Guza (1985), Crawford (2000) and Crawford and Hay (2001) have suggested that wave energy at high frequencies enhances sum frequencies interactions, therefore generating more positive skewness, and this could be an explanation for our observation. As shown in Figure 3.3.5d, wave asymmetry increases rapidly

up to maximum value from zero then decays slowly with increasing Ursell number. Wave asymmetry on the transmission side also has a maximum value comparing with that on the incident side. The empirical Equations 3.3.6 and 3.3.7 are derived from the measurements on the transmission side using least squares fitting to relate S_t and A_t to U_{rt}. Predictions agree well with observations for wave skewness (R^2=0.70) and reasonably well for wave asymmetry (R^2=0.62). As seen in Figure 3.3.5, for large Ursell number on the transmission side of LCS, wave skewness for incident angle β=0° is smaller but wave asymmetry is larger than those for incident angles β=30° and 50°. These different wave skewness and asymmetry during oblique wave propagation over LCS cause scatters in the relationship between wave skewness and asymmetry and local Ursell number. This is mainly because normal incident wave energy is reduced by the strong reflected wave from LCS, while oblique waves face less resistance from reflected waves when they propagate over LCS. Therefore, the cases with normal incident wave have less transmitted wave energy and less sum nonlinear interactions, leading to small wave skewness and large positive asymmetry (Section 3.4). It should be stated that the range of Ursell number on the transmission side is between 0.05 and 12.5.

$$S_t = -1.25 * \tanh(\frac{3.19}{U_{rt}}) + 1.23 \qquad (3.3.6)$$

$$A_t = -0.015 * U_{rt}^{\ 2} + 0.19 * U_{rt} - 0.05 \qquad (3.3.7)$$

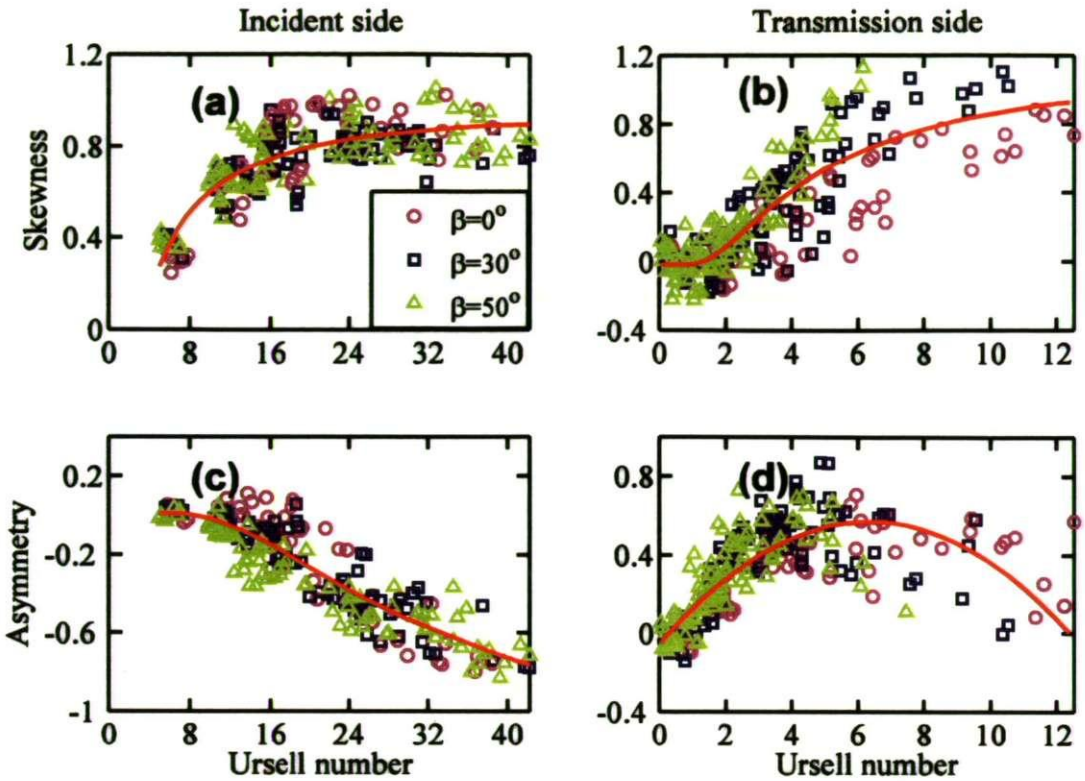

Figure 3.3.5 Relationship between wave skewness (a and b) and asymmetry (c and d) and Ursell number on the incident side (left panel) and the transmission side (right panel) of smooth LCS. Solid line is predicted by Equations 3.3.4 for (a), Equations 3.3.5 for (c), Equations 3.3.6 for (b) and Equations 3.3.7 for (d).

To demonstrate the validity the efficiency of Equation 3.3.3, a detailed comparison of the dependence of wave skewness on Ursell number with peak wavelength and mean wavelength can be found in Figure 3.3.6. Predictions are calculated by formulae in form of Equation 3.3.6 using the least squares regression. Regression results show that the R-square is 0.63 for Ursell number with peak wavelength, and R-square is 0.71 for Ursell number with mean wavelength. Therefore, a conclusion can be drawn that Ursell number with mean wavelength is a better governing parameter to describe wave

skewness and asymmetry on the transmission side of LCS, where there is a broad spectrum.

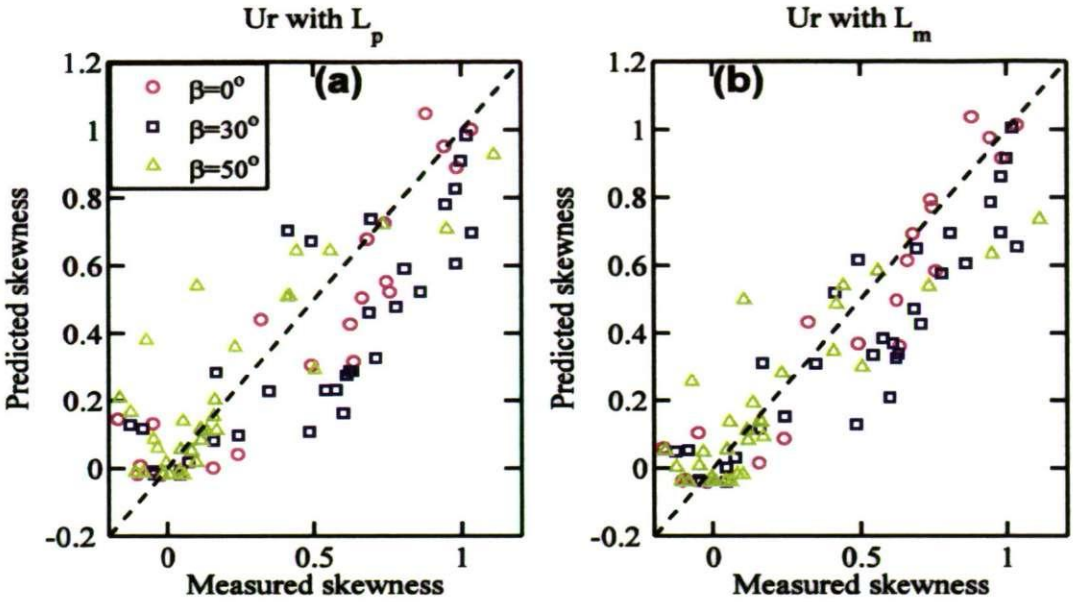

Figure 3.3.6 Comparisons of the dependence of wave skewness on Ursell number with (a) peak wavelength and (b) mean wavelength on the transmission side. Symbols represent the measurements; dashed lines stand for measurements equal predictions. Predictions are calculated by the best-fitted expressions in form of Equation 3.3.6.

3.3.2 Transformation of wave skewness and asymmetry over rubble mound LCS

The water depths used in the rubble mound LCS are 0.05m smaller than those of smooth LCS, the nominal diameter of the units in the rubble mound LCS is D_{n50}=0.047 m, and the seaside slope is 1:2 for rubble mound LCS, whereas it is 1:3 for smooth LCS.

Figure 3.3.7a and Figure 3.3.7c shows that the relationships of rubble

mound LCS between wave asymmetries and Ursell number are similar to those of smooth LCS on the incident side. This may be due to the reflection from both LCS is minimized with inclined structures in order to focus on wave transmission in the design of the DELOS project (Van der Meer, 2005; Kramer, 2005). Equations 3.3.8 and 3.3.9, derived by least squares fitting, specify these relationships with R^2 = 0.64 and R^2 = 0.84 for wave skewness and asymmetry respectively. The range of Ursell number on the incident side is between 6 and 66. Comparisons between Equations 3.3.8 and 3.3.9 of rubble mound LCS and Equations 3.3.4 and 3.3.5 of smooth LCS are shown in the Figure 3.3.7.

$$S_i = -11.32 * \tanh(\frac{0.42}{U_{ri}}) + 1.17 \qquad (3.3.8)$$

$$A_i = -1.23 * \tanh(\frac{-15.82}{U_{ri}}) - 1.16 \qquad (3.3.9)$$

We will next examine the relationships between wave skewness and asymmetry and Ursell number on the transmission side of rubble mound LCS. Figure 3.3.7b shows that wave skewness stays around zero at small Ursell number, then increases slowly up to a maximum value from zero, finally begins to decay. Wave asymmetry increases quadratically with increasing Ursell number from approximately zero, reaches the maximum of wave skewness, then decays quadratically low to negative values (Figure 3.3.7d). The recommended formulae for rubble mound LCS are:

$$S_t = 2.97 * \tanh(\frac{-9.16}{U_{rt}}) + 3.04 \qquad (3.3.10)$$

$$A_t = -0.015 * U_{rt}^{\ 2} + 0.22 * U_{rt} - 0.41 \qquad (3.3.11)$$

where R^2 is 0.72 for Equation 3.3.10 and 0.54 for Equation 3.3.11. The applicable range of Ursell number on the transmission side is 1.5 to 15. This applicable range of Ursell number is larger than that for smooth LCS, and it is due to smaller water depth at the same locations for rubble mound LCS.

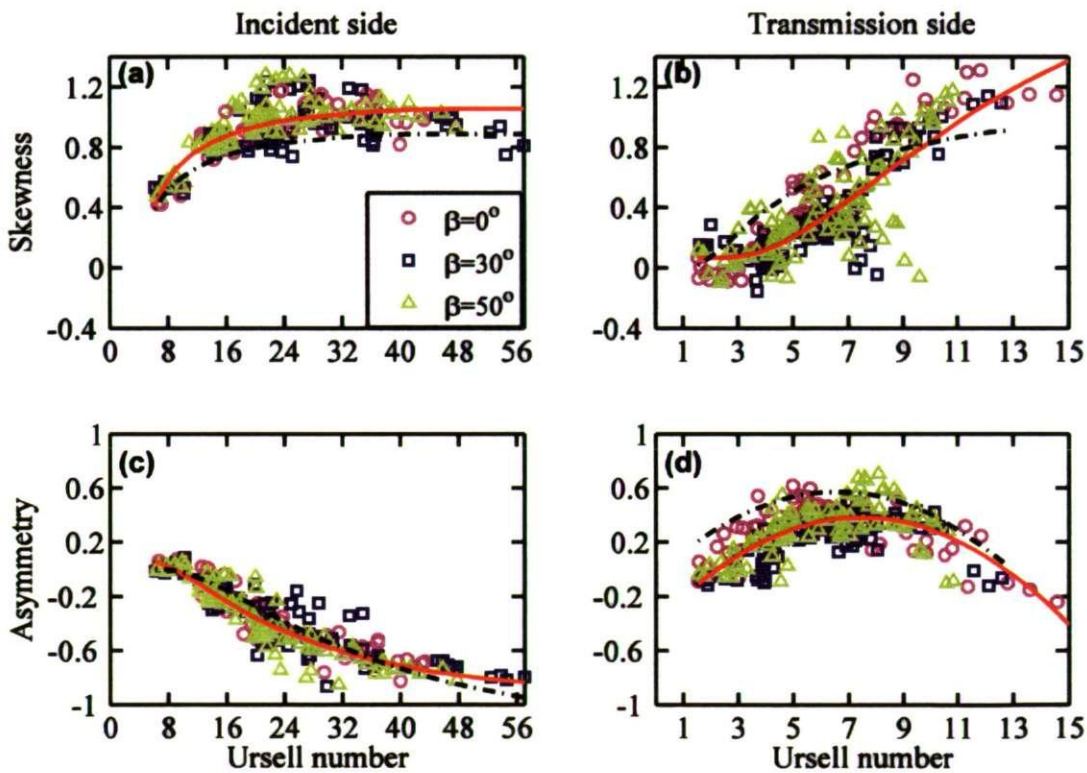

Figure 3.3.7 Relationship between wave skewness (a and b) and asymmetry (c and d) and Ursell number on the incident side (left panel) and the transmission side (right panel) of rubble mound LCS. Solid line is predicted by Equation 3.3.8 for (a), Equation 3.3.9 for (c), Equation 3.3.10 for (b) and Equation 3.3.11 for (d). The dash-dotted lines are predicted using Equation 3.3.4 for (a), Equation 3.3.5 for (c), Equation 3.3.6 for (b) and Equation 3.3.7 for (d) respectively.

Figure 3.3.7 shows comparisons between Equations 3.3.10 and 3.3.11 of rubble mound LCS and Equations 3.3.6 and 3.3.7 of smooth LCS. Predictions of wave asymmetries on the transmission side for rubble mound LCS are smaller than those of smooth LCS, although they are both around zero values at small Ursell numbers. This may be due to the roughness and porosity of the structure, causing energy dissipation, which consequently decreases wave nonlinear interactions and generates small wave asymmetries.

It is obvious to observe that wave skewness and asymmetry strongly depend on local Ursell number on the transmission side for rubble mound LCS, while there are some scatters for smooth LCS in Figure 3.3.5. This is because rubble mound LCS has small reflection coefficients due to its permeability. Since wave skewness and asymmetry are related to net sediment transport, the investigations above provide effective ways to predict wave asymmetries, which may help incorporate wave asymmetries into analytic or numerical models of the sediment transport, consequently may help improve the stability of breakwaters and decrease sediment transport.

3.3.3 Relationships of wave asymmetries between both sides of LCS

Although wave skewness and asymmetry are strongly related to local Ursell number as discussed above, it is worthwhile investigating the relationships of wave asymmetries between both sides of LCS. This helps understand the effect of the presence of LCS on wave transformation over

LCS.

Figure 3.3.8 shows that for smooth LCS, wave skewness on the transmission (S_t) side stays around zero, and then has weakly linear independent on wave skewness on the incident side (S_i), while wave asymmetry on the transmission side (A_t) has weakly quadratic independence on wave asymmetry on the incident side (A_i). The effect of the relative freeboard on the relationships of wave asymmetries between both sides of LCS is not significant. Wave skewness retains a positive sign on both sides but asymmetry changes from negative on the incident side to positive on the transmission side. For rubble mound LCS, wave skewness on the transmission side shows linear dependence on wave skewness on the incident side, and wave asymmetry on the transmission side displays a weakly quadratic dependence on wave asymmetry on the incident side. The effect of the relative freeboard on the relationships of wave asymmetries on both sides of LCS is significant: under the same of S_i or A_i, large relative freeboards correspond to small S_t or A_t respectively. This is due to a considerable increase in the intensity of wave breaking as the relative freeboard increased (Blenkinsopp and Chaplin, 2008), consequently more energy is dissipated, which decreases wave nonlinear interactions and generates small wave asymmetries. Figure 3.3.8 shows that wave skewness on the incident side is mostly larger than that on the transmission side, which is mainly due to the decreased wave height and local Ursell number. Small magnitudes of wave asymmetry on both sides of LCBs are

approximately equal, but large magnitudes of wave asymmetry on the incident side correspond to small wave asymmetry on the transmission side. This is because waves with large negative asymmetry has steep front slope and easy to be broken, subsequently leading to small transmitted wave energy. The sign of wave asymmetry changes from negative to positive, corresponding to waves pitching forward to pitching backward (Figure 3.3.1). This is consistent with previous research results over a submerged sand bar on a beach (Herbers et al., 2003). Note that Herbers et al.'s definition of wave asymmetry has the opposite sign to that in the present work and also to that of Elgar and Guza (1985).

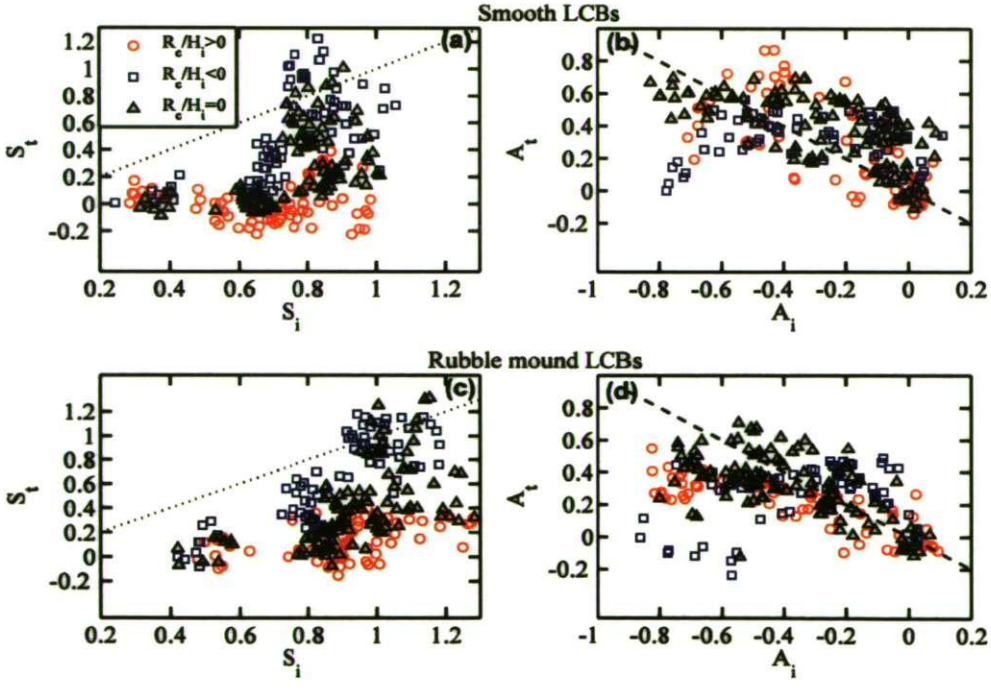

Figure 3.3.8 Relationships of wave asymmetries between both sides of LCS. (a) wave skewness of smooth LCS, (b) wave asymmetry of smooth LCS, (c) wave skewness of rubble mound LCS and (d) wave asymmetry of rubble mound LCS. Dotted line represents $S_i=S_t$ while Dashed line stands for $A_t=-A_i$.

3.4 Bispectral Analysis of Nonlinear Wave Interactions

In the presence of LCS, waves retain sharp crest and flat trough on both sides but change from pitch-forward to pitch-backward, which in turn may change the directions in wave induced sediment transport, consequently modifying the beach morphology after construction of LCS. To better understanding the transformation of wave asymmetries analyzed above, Bispectral analysis (see Appendix C) has been applied here to study the contributions to the wave skewness and asymmetry from the interactions of different wave components, similar as work of Elgar and Guza (1985).

In waves that are initially linear, nonzero wave skewness and asymmetry arises as a result of nonlinear interaction between the frequency constituents of the waves during the shoaling process. Bispectral analysis has been introduced to investigate the contribution of nonlinear interactions between frequency components of wave spectrum by previous researchers (Elgar and Guza, 1985; Doering and Bowen, 1995), since the bispectrum is usually used to detect the secondary forced waves and can apparently show the phase coupling between the primary waves and associated forced waves.

In the DELOS datasets, the generated spectrum initially has only one peak at the primary frequency and keeps the same for cases with negative and zero freeboards, but it evolves to double peaks around the primary frequency for the cases with the positive freeboard due to wave reflections. For the case of the LCB with the negative freeboard (Figure 3.4.1), the

spectrum on the incident side has large peak at the primary frequency f=0.5 Hz and a small peak at the second harmonic frequency f=1.0 Hz, while a broader power spectrum exists on the transmission side, although the primary frequency remains at 0.5 Hz. This is consistent with the investigation by Van der Meer et al. (2005). However, for the case of the LCB with the positive freeboard (Figure 3.4.2), the spectrum on the incident side shows three peaks, which are located at f=0.48 Hz, f=0.6 Hz, and f=1.2 Hz respectively. Transmitted waves are characterised by a broader power spectrum, Peak frequencies are f=0.58 Hz and f=1.1 Hz respectively. In the present work, bispectral analysis is implemented next for the cases of smooth LCB with the negative freeboard (Figure 3.4.1) and positive freeboard (Figure 3.4.2). There are 281 degrees of freedom and the 95% significant level for zero bicoherence is b=0.146 (Haubrich, 1965), and significant nonzero values in the bispectrum are limited to frequencies below 2 Hz. Areas of significant bicoherence indicate frequency pairs (f_1, f_2) that are involved in either sum or difference interactions.

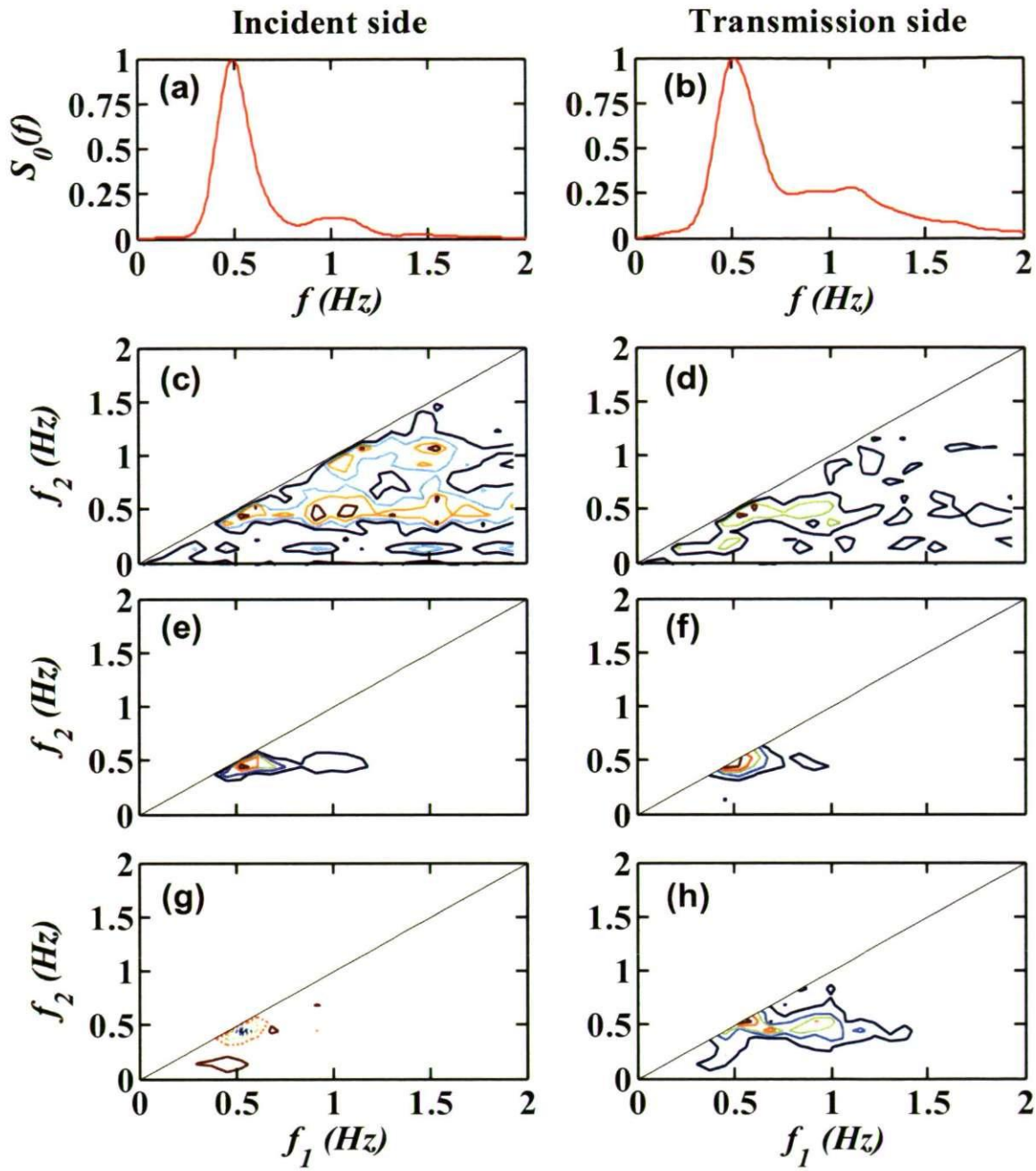

Figure 3.4.1 Normalized Power spectra by the energy of peak wave component (a and b), contours of bicoherence (c and d), contours of real part (e and f) and imaginary part (g and h) of normalized bispectrum on the incident side (left column) and transmission side (right column) of smooth LCS (R_c=-0.05m, H_i=0.13m, h=0.35m, α=0°). The minimum levels of contour plots are (c) 0.15, (d) 0.15, (e) 2e-4, (f) 2e-4, (g) -11e-4 and (h) 0.6e-4. The corresponding intervals of contour levels are 0.1, 0.1, 3e-4, 3e-4, 3e-4, and 1.5e-4 respectively. Dashed contours are negative values and solid ones are positive values.

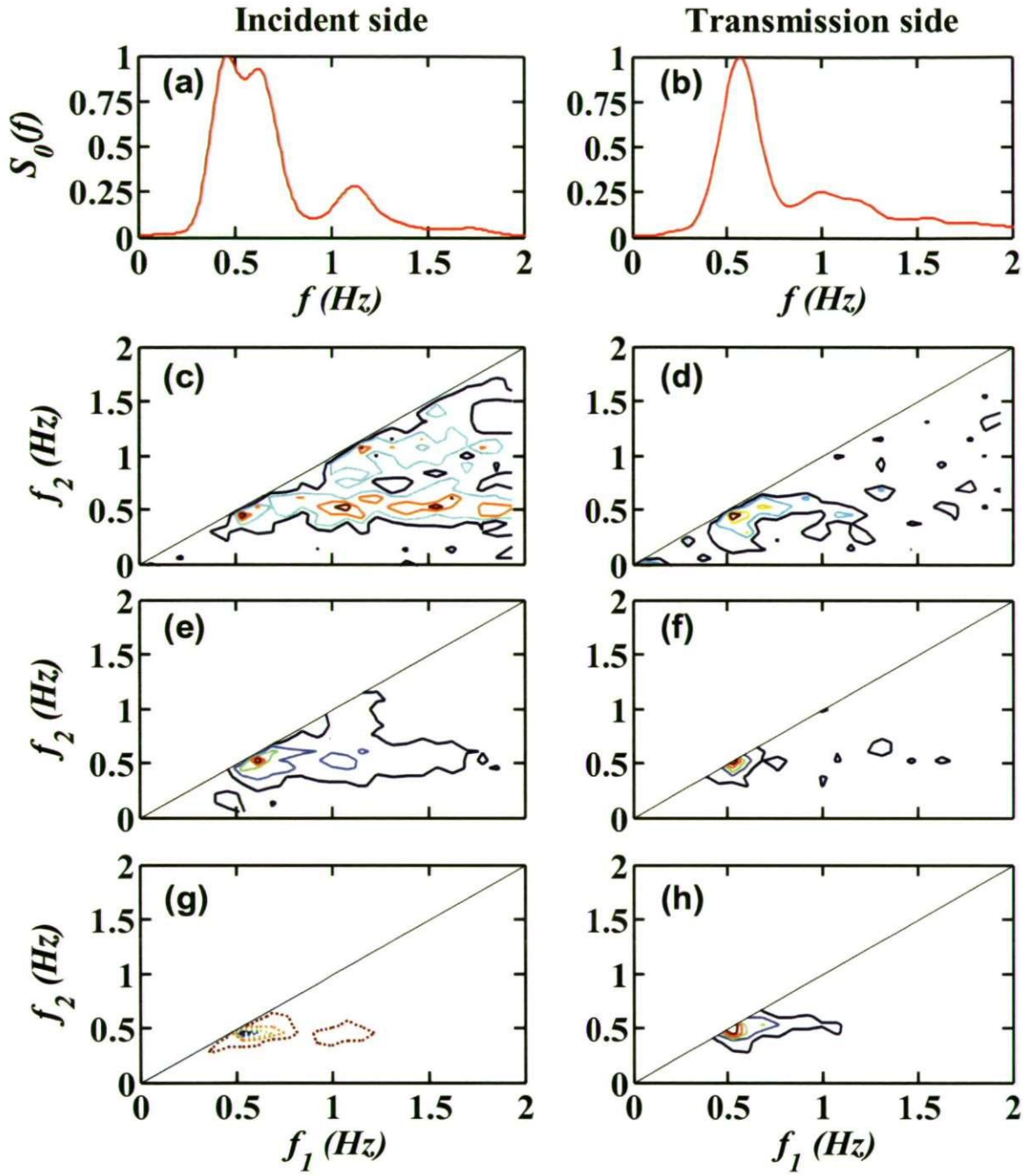

Figure 3.4.2 Normalized Power spectra by the energy of peak wave component (a and b), contours of bicoherence (c and d), contours of real part (e and f) and imaginary part (g and h) of normalized bispectrum on the incident side (left column) and transmission side (right column) of smooth LCS (R_c=0.05m, H_i=0.11m, h=0.25m, a=0°). The minimum levels of contour plots are (c) 0.15, (d) 0.15, (e) 1e-4, (f) 1e-4, (g) -13e-4 and (h) 2e-4. The corresponding intervals of contour levels are 0.1, 0.1, 2e-4, 3e-4, 3e-4, and 3e-4 respectively. Dashed contours are negative values and solid ones are positive values.

The bispectrum was normalised by $E(\eta(t)^2)^{\frac{3}{2}}$. The sign of the real part of bispectrum, $\Re\{B\}$ and imaginary part of bispectrum, $\Im\{B\}$ at frequencies (f_1, f_2) described the sign of the contribution to the overall skewness and asymmetry arising from the nonlinear interactions. The relationships between wave skewness and asymmetry and the bispectrum are defined by Equations (C3) and (C4) in the appendix C. In Figure 3.4.1c, the bicoherence on the incident side indicates strong coupling at the peaks (f_1=0.5 Hz, f_2=0.5 Hz) and (f_1=1.0 Hz, f_2=0.5 Hz) with b=0.35, while on the transmission side (Figure 3.4.1d), the bicoherence indicates strong coupling at the peak (f_1=0.5 Hz, f_2=0.5 Hz) with b=0.35 and frequency pairs (f_1=0.7 Hz, f_2=0.5 Hz) and (f_1=0.9 Hz, f_2=0.5 Hz) with b=0.25. It is obvious that wave nonlinear coupling on the peaks and harmonics on the incident side is greater than that on the transmission side. As shown in Figure 3.4.1e and 8f, on the incident side, $\Re\{B(f_1, f_2)\}$ has a large positive value around the frequency pairs (f_1=0.5 Hz, f_2=0.5 Hz) and also has a small positive value at the frequency pairs (f_1=1.0 Hz, f_2=0.5 Hz); while on the transmission side, $\Re\{B(f_1, f_2)\}$ is positive under the self-self interaction (f_1=0.5 Hz, f_2=0.5 Hz) with large bicoherence. Positive $\Re\{B(f_1, f_2)\}$ of self-self interaction and sum interactions between peak frequency and second harmonic, leads to an overall positive skewness, which is also consistent with that in Figure 3.3.1. Figure 3.4.1g demonstrates that on the incident side, $\Im\{B(f_1, f_2)\}$ is negative around the frequency pairs (f_1=0.5 Hz, f_2=0.5 Hz) with large bicoherence. The large negative $\Im\{B(f_1, f_2)\}$ induced by self-self interaction leads to an overall negative asymmetry although there

are small positive values. However, Figure 3.4.1h shows that $\Im\{B(f_1,f_2)\}$ on the transmission side has large positive values around the frequency pairs (f_1=0.5 Hz, f_2=0.7 Hz) and (f_1=0.5 Hz, f_2=0.9 Hz). The couplings between f_1=0.5 Hz and f_2=0.7 Hz, f_1=0.5 Hz and f_2=0.9 Hz correspond to the difference interactions between f_1= 0.5 Hz and f_3=1.2 Hz, f_1= 0.5 Hz and f_3=1.4 Hz, transferring energy into the spectral valley between 0.5 Hz and 1.4 Hz. The large positive $\Im\{B(f_1,f_2)\}$ induced by difference interactions leads to an overall positive asymmetry.

Comparing with the case with the negative freeboard, the case with the positive freeboard is analyzed and shown in Figure 3.4.2. The bicoherence indicates strong coupling around the peaks (f_1=0.6 Hz, f_2=0.48 Hz) and (f_1=1.2 Hz, f_2=0.48 Hz) with b=0.45 on the incident side and the frequency pairs (f_1=0.58 Hz, f_2=0.52 Hz) with b=0.45 on the transmission side. Figure 3.4.2e and 9f shows that on the incident side, $\Re\{B(f_1,f_2)\}$ is positive around frequency pairs (f_1=0.6 Hz, f_2=0.48 Hz) and (f_1=1.2 Hz, f_2=0.48 Hz), and on the transmission side $\Re\{B(f_1,f_2)\}$ is positive at the frequency pairs (f_1=0.58 Hz, f_2=0.58 Hz) with self-self interaction. Therefore, the large positive $\Re\{B(f_1,f_2)\}$, induced by self-self interaction and interactions between peak frequency and higher frequency, leads to an overall positive skewness. As seen in Figure 3.4.2g, on the incident side, the peak (f_1=0.6 Hz, f_2=0.48 Hz) has negative $\Im\{B(f_1,f_2)\}$ showing a sum interaction between frequencies f_1=0.6 Hz and f_2=0.48 Hz, as well as the sum interaction between frequency pairs (f_1=1.2 Hz, f_2=0.48 Hz). Both sum interactions have large bicoherence. The large

negative $\Im\{B(f_1,f_2)\}$ induced by sum interactions between frequency pairs, leads to an overall positive asymmetry. On the transmission side, Figure 3.4.2h describes positive $\Im\{B(f_1,f_2)\}$ of large magnitude arises from the coupling between f_1=0.58 Hz and f_2=0.52 Hz with b=0.45, corresponding to a difference interaction between f_1=0.58 Hz and f_3=1.1 Hz transferring energy into the spectral valley around the frequency of 0.52 Hz. Large positive $\Im\{B(f_1,f_2)\}$ induced by difference interactions with large bicoherence leads to an overall positive asymmetry.

3.5 Summary

This chapter describes the parameterisation and transformation of wave skewness and asymmetry when waves propagate over smooth and a rubble mound LCS. The analysis was based on measurements collected in the wave basin transmission tests of DELOS project. On the incident side of smooth LCS, wave skewness is positive and increases with increasing Ursell number then stays around the maximum, and wave asymmetry is negative and decays with increasing Ursell number. On the transmission side of smooth LCS, wave skewness shows similar dependence on Ursell number to that on the incident side, but wave skewness is larger than that on the incident side under the same Ursell number, while wave asymmetry is positive and increases rapidly up to a maximum then decays slowly with increasing U_r. Several practical empirical formulae related wave skewness and asymmetry to Ursell number are established using least squares fitting for practical use.

Predictions are in good agreement with measurements. Although relationships between wave asymmetries and Ursell number of rubble mound LCS are similar to those of smooth LCS, wave skewness and asymmetry on the transmission side of rubble mound are smaller than those of smooth LCS under the same Ursell number, although they are both around zero at small Ursell numbers.

Wave skewness on the transmission side of smooth LCS show linear dependence on wave skewness on the incident side, while wave asymmetry on the transmission side display weakly quadratic dependence on wave asymmetry on the incident side. Although wave asymmetries on the transmission side of rubble mound LCS display similar dependence on wave asymmetries on the incident side as that of smooth LCS, the effect of the relative freeboard on the relationships of wave asymmetries between both sides is significant for rubble mound LCS, but not significant for smooth LCS. Wave skewness retains a positive sign on both sides but asymmetry changes from negative on the incident side to positive on the transmission side.

Our bispectral analysis shows that positive skewness and negative asymmetry arises from self-self and sum interactions between frequencies components of wave spectrum; the main contribution to positive asymmetry is due to difference interactions between the two principal components of the wave spectrum on the transmission side of LCS.

Since wave skewness and asymmetry are related to net sediment

transport, the investigations above provide effective ways to predict wave asymmetries, which may help incorporate wave asymmetries into analytic or numerical models of the sediment transport, consequently may help improve the instability of breakwaters and decrease sediment transport.

CHAPTER 4

NUMERICAL MODELLING OF EVOLUTION OF WAVE ASYMMETIES OVER LOW-CRESTED STRUCTURES

The parameterisation and transformation of wave asymmetries over Low-Crested Structures (LCS) in Chapter 3 help us understand the relationship between wave shapes and wave nonlinearity in the presence of coastal structures. However, experimental datasets used in the chapter 3 were limited to areas away from the LCS. Therefore, it is not clear how wave skewness and asymmetry evolve across the LCS, especially above the LCS. It would be helpful for us to look at the whole picture of the evolution of wave asymmetries, from the incident side, over the structural crest to the transmission side of the LCS. This work may enhance our understanding of wave-structure interactions and help to assess the functionality and stability of coastal and flood defence schemes.

The main aim of this chapter is to investigate the evolution of wave skewness and asymmetry over the LCS using the improved RANS-VOF model, as well as briefly interpreting the underlying physics. Laboratory data sets of wave surface elevations, collected in the small scale wave channel tests at the University of Cantabria (UCA) of DELOS project (Appendix D1), are used to verify the numerical results.

This chapter includes seven parts: Firstly previous work on transformation of wave shapes in the nearshore zone is reviewed; it is then followed by a summary of experiments; numerical model implementation and model validation are presented next; along with a comparison of numerical results, measurements and predictions by the empirical formulae derived in chapter 3; subsequently, factors affecting the evolution of wave asymmetries are investigated; the physical interpretations are discussed and finally a brief summary is given.

4.1 Introduction

As mentioned in Chapter 3, the evolution of wave skewness and asymmetry over coastal structures is important to the stability of coastal structures and beach morphology behind coastal structures due to its induced sediment transport (Inman and Bagnold, 1963; Wilson, 1966; Nielsen, 1992; Holmedal and Myrhaug, 2006; Nielsen, 2006; Gonzalez-Rodriguez and Madsen, 2007). Previous research on the cross-shore evolution of wave skewness and asymmetries mainly focused on natural

beaches. Elgar and Guza (1985) found that for waves shoaling across natural beaches, wave skewness increases from around zero up to maximum value from deep water to shallow water and then decreases to near zero in even shallower water. Wave asymmetry decreases from zero as waves shoal, reaching a minimum value slightly shoreward of the skewness maximum, and then slight decreases in wave asymmetry in very shallow water occurs when waves start to break. Doering and Bowen (1995) found that both wave skewness and asymmetry are strongly dependent on local Ursell number (the relative wave height H/h times the relative wavelength λ/h squared, h is water depth) for shoaling and breaking surface gravity waves on natural beaches. For small Ursell numbers, both wave skewness and asymmetry are near zero; for increasing Ursell numbers, wave skewness increases up to maximum value then decreases down to zero, while wave asymmetry simply increase in a negative sense. Herbers et al. (2003) presents the evolution of wave skewness and asymmetry over a submerged sandy bar on the natural beach, by comparing the experimental measurements and numerical results from a Boussinesq model.

Compared with natural beaches, wave propagation over coastal structures gave rise to different wave processes. Previous work on interactions between waves and LCS mainly focused on the prediction of wave transmission and reflection (Van der Meer et al., 2005), overtopping (Zanuttigh et al., 2008), structural stability (Burcharth et al., 2006), Scour (Sumer et al., 2005) and velocity and turbulence fields (Losada et al., 2005). On the other hand, there was plenty of work focused on wave energy transfer in the presence of

coastal structures or sandy bars. Beji and Battjes (1993) examined high frequency energy generations as waves propagated over submerged bars. They interpreted the physical mechanism as the amplification of bound harmonics during the shoaling process and their release in the deeper region, resulting in the decomposition of these finite amplitude waves. In addition, waves satisfy the triplet resonance conditions (Phillips, 1960) on the structural crest, therefore a very rapid flow of energy begins from the primary wave to the higher harmonics. Losada et al. (1997) studied harmonic evolutions of monochromatic waves as they propagate over a porous step under non-breaking conditions. Results showed that the permeability of LCS reduces the amplitude of all the harmonic modes considerably due to the friction of porous media. Also, porous structure increases the effective relative depth and decreases the relative wave height, resulting in a lower Ursell number and a lower chance to generate harmonics. Masselink (1998) investigated the generation of secondary waves on a barred beach using the field measurements. The results showed the decomposition of breaking incident swell into several smaller and shorter waves upon entering the deeper water landward of the bar. The consequent broad wave spectrum results in a decrease in the significant wave period and may further delay the dissipation of wave energy. Sénéchal et al. (2002) found that although wave breaking appears to weaken the strength of nonlinear couplings, the generation of high-frequency energy is hardly affected by wave breaking on a sandy, barred beach. Brossard and Chagdali (2001) and Brossard et al. (2009) found that the decomposition of a wave

above a submerged structure implies a transfer of energy from the fundamental mode towards the bound modes, phase-locked with the fundamental. Downstream the structure, higher free harmonic modes are generated. Currently, there is little work relevant to the evolutions of wave skewness and asymmetry across coastal structures, also the experimental datasets available were insufficient and limited to some areas away from the LCS.

The RANS-VOF model, described in chapter 2, was able to give good predictions of near-field flow around LCS under regular waves (Garcia et al., 2004), velocity and turbulence fields around and within permeable breakwaters (Losada et al., 2005), random wave interaction with submerged permeable structures (Lara et al., 2006) and wave overtopping processes (Losada et al., 2008). It then is employed to investigate the evolution of wave skewness and asymmetry over coastal structures, paying special attention to the area above the structure and behind the structure. Employing the RANS-VOF model helps to overcome the limited experimental datasets for the transformation of wave shapes and enhance our understanding of the effect of coastal structures on the evolution of wave skewness and asymmetry.

4.2 Experiment

Two-dimensional wave transmission tests, conducted in the flume (24.0 m × 0.6 m × 0.8 m) at University of Cantabria, Spain (Appendix D1), were employed to validate results of the RANS-VOF model in this Chapter. Two

rubble-mound low-crested structures of 0.25 and 1.00 m crest width were tested. Both structures keep the same crest elevations from the bottom (0.25 m), front and back slope angles (1V/2H) and porous media. The models had two-layer armour of selected gravel and a gravel core. Armour characteristics are D_{n50}=0.031 m, porosity =0.49 and the core characteristics are D_{n50}=0.046 m, porosity =0.53. A final dissipative beach with 1/20 slope was made of quarry rock with D_{n50}=0.015 m and porosity=0.43.

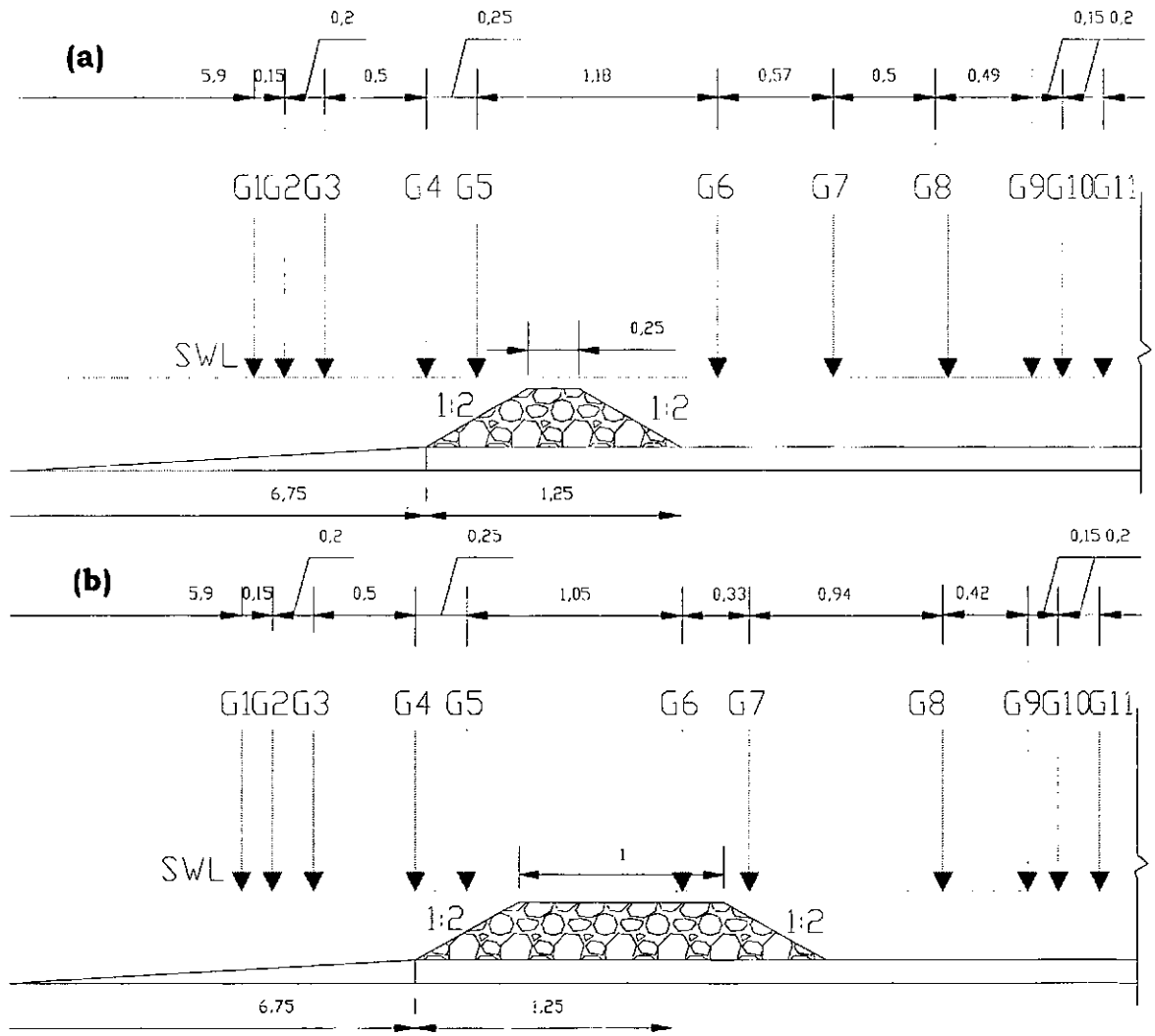

Figure 4.2.1 Installation of wave gauges in the experiments with (a) narrow crest tests and (b) wide crest tests. Unit: m. G1 to G11 represent the surface elevation gauges.

The data used for the present study were measured by 11 resistive free surface gauges to assess free surface evolution, gauges G1 to G3 were installed in front of the LCBs; gauges G4 to G5 were located above the seaward slope of LCBs; gauges G6 was placed on the transmission side for 0.25 m crest width but above the crest and on the leeside slope for 1.00 m crest width instead; gauges G7 to G11 were placed on the transmission side along the flat bottom behind the LCBs. The detailed coordinates of gauges are shown in Figure 4.2.1. Each record was sampled at 30*Hz*. An overall view of test programme in the small-scale wave channel experiments is listed in Table 4.2.1. Experimental set-up and test conditions were described in further detail in Appendix D1.

Table 4.2.1 Overall view of test programmes in wave channel tests

Parameter	Value
H~ H_i (m)	0.04, 0.07, 0.10
T~ T_{pi} (s)	1.6, 2.4, 3.2
L_p (m)	2.53 to 6.17
B (m)	0.25 and 1.0
h (m)	0.3,0.35,0.4

4.3 RANS-VOF Model Implementation

The RANS-VOF model, described in Chapter 2, is used to investigate wave shape changes over LCS. The RANS-VOF model solves the 2D Reynolds Averaged Navier–Stokes equations by decomposing the instantaneous

velocity and pressure fields into the mean and turbulent components. Reynolds stresses are closed with an algebraic non-linear k–ε turbulence model. A PLIC-VOF method was employed to capture free surface.

4.3.1 Model set-up

As can be seen in Figure 4.3.1, the numerical setup includes a permeable LCB (crest width B=1m) located on the bottom of the flume, a 1/20 Plexiglas ramp in front of the LCB and a final dissipative beach with 1/20 slope which was made of quarry rock with D_{n50}=0.015m and porosity, n, is 0.43. The permeable LCB consists of two layers the same as the experiments in Section 4.2 and Appendix D1: an armour layer with the D_{n50}=0.0466 m and n= 0.53; a core layer with the D_{n50}=0.031m and n=0.49. There are two crest widths, B=0.25m and 1.00m, in the present work for investigating the effect of structural crest width. The sponge layer, described by equation (2.2.26), is 8m long (peak wave length at the wave-maker is approximately 3m). The spongy layer absorbs the generated waves directed left and reflected waves from the seaward slope of the LCB.

The computational mesh, designed for the simulation of the experiments described in Section4.2 and Appendix D1, consists of four main regions with different size and functions. As shown in Figure 4.3.1, in the x-direction and without high resolution requirements, the grid size is 0.05m in the sponge layer area and 0.02m around the source region. The grid size is then changed to 0.01m in the vicinity of LCS which is the zone of breaking,

overtopping and strong turbulence generation (local wave length is about 2.5m for T_p=1.6s). On the dissipative beach, the grid size is set to 0.02m again to allow considerable savings of computational time. The grid size in the y-direction is 0.02m from y=0m to y=0.24m (the solid bottom), while in other cells it is 0.01m. The y co-ordinate of the top boundary is 1.0m to avoid numerical instability from the large surface elevation and the splash. The total number of cells is 1150 in the x-direction and 88 in the y-direction.

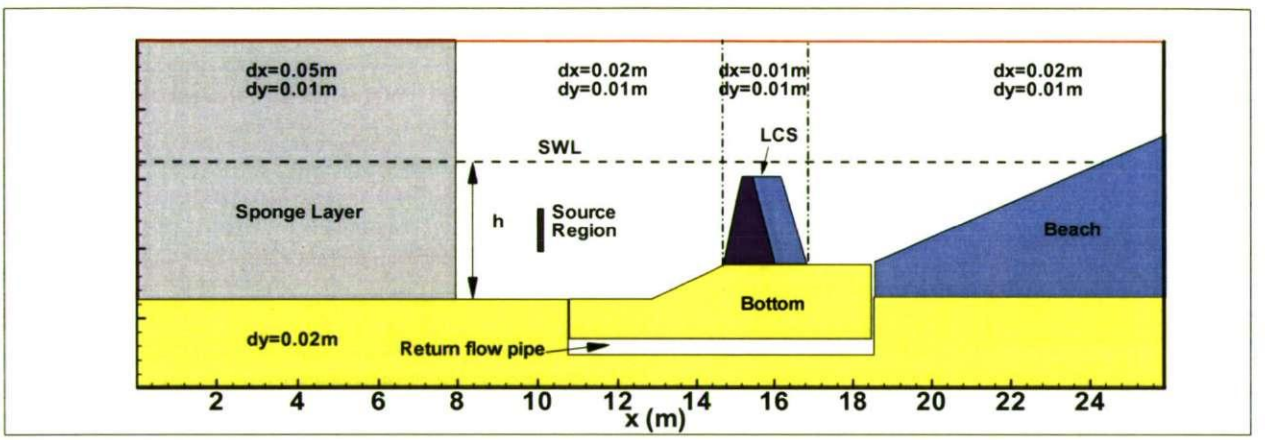

Figure 4.3.1 Sketch of the numerical setup and the computational meshes. Dashed line stands for still water level, SWL, and h represents the water depth.

In the mean flow field, an open boundary, composed of a radiation boundary and an artificial 8m long sponge layer, is specified at the inlet boundary to absorb the reflected waves from LCS; while free-slip boundary condition is applied on the other boundaries. A no-slip condition at the solid boundaries and a zero-stress condition at the free surface were treated. For turbulence field, on the free surface, the zero gradient boundary conditions for turbulence generation were based on the assumption of no turbulence

exchange between the water and air. A log-law distribution of the mean tangential velocity in the turbulent boundary layer is considered near the solid boundary. The initial condition consists of a still water situation with no current and wave motion. A return flow system described in Section 0 was applied. An internal wave-maker developed by Lin and Liu (1999) was located at x =10m and used to generate TMA spectrum (Appendix B). The duration of simulations is in excess of 300 s. According to the rule of thumb for the designation of source region proposed by Lin and Liu (1998), the 0.15m (H) ×0.02m (L) source region is chosen and 0.1m under the still water level.

A total of 48 tests with the different wave conditions and coastal structural geometries are used in this study (Table 4.3.1). Test No. 34 to No. 48 are used to investigate the effect of the randomness in waves on the evolution of wave shapes over LCS. All irregular waves are generated through the internal source region based on the theory of TMA spectrum (Appendix B). Calculation of wave propagation for 300s with cells of 1150×88 requires about 36 CPU hours using a single processor of Intel Core 2 CPU 6600 @ 2.4GHz, 2.4GHz. According to Table 4.3.1, the maximum peak frequency, f_p, is 0.625Hz, and the small water depth is 0.3m. Therefore, the corresponding minimum wavelength is 2.53m. Similarly, the wavelength for f_{max} (about 2Hz in this sudy) is 0.4m. Therefore, there are approximately 250 points for f_p and 40 points for f_{max} above the LCS, and 125 points for f_p and 20 points for f_{max} in front of LCS.

Table 4.3.1 Overall view of numerical simulations of the transformation of wave shapes over LCS

Case No.	Wave type	B (m)	$H \sim H_i$ (m)	$T \sim T_{pi}$ (s)	h (m)	R_c (m)	Porosity (Armor+Core)
1	Regular	1	0.1	1.6	0.4	-0.05	0.53+0.49
2	TMA	0.25	0.1	1.6	0.35	0.0	0.53+0.49
3	TMA	1	0.04	1.6	0.4	-0.05	0.53+0.49
4	TMA	1	0.07	1.6	0.4	-0.05	0.53+0.49
5	TMA	1	0.1	1.6	0.4	-0.05	0.53+0.49
6	TMA	1	0.04	2.4	0.4	-0.05	0.53+0.49
7	TMA	1	0.07	2.4	0.4	-0.05	0.53+0.49
8	TMA	1	0.1	2.4	0.4	-0.05	0.53+0.49
9	TMA	1	0.04	3.2	0.4	-0.05	0.53+0.49
10	TMA	1	0.07	3.2	0.4	-0.05	0.53+0.49
11	TMA	1	0.1	3.2	0.4	-0.05	0.53+0.49
12	TMA	1	0.04	1.6	0.35	0.0	0.53+0.49
13	TMA	1	0.07	1.6	0.35	0.0	0.53+0.49
14	TMA	1	0.1	1.6	0.35	0.0	0.53+0.49
15	TMA	1	0.04	2.4	0.35	0.0	0.53+0.49
16	TMA	1	0.07	2.4	0.35	0.0	0.53+0.49
17	TMA	1	0.1	2.4	0.35	0.0	0.53+0.49
18	TMA	1	0.04	3.2	0.35	0.0	0.53+0.49
19	TMA	1	0.07	3.2	0.35	0.0	0.53+0.49
20	TMA	1	0.1	3.2	0.35	0.0	0.53+0.49
21	TMA	1	0.04	1.6	0.3	0.05	0.53+0.49
22	TMA	1	0.07	1.6	0.3	0.05	0.53+0.49
23	TMA	1	0.1	1.6	0.3	0.05	0.53+0.49
24	TMA	1	0.04	2.4	0.3	0.05	0.53+0.49
25	TMA	1	0.07	2.4	0.3	0.05	0.53+0.49
26	TMA	1	0.1	2.4	0.3	0.05	0.53+0.49
27	TMA	1	0.04	3.2	0.3	0.05	0.53+0.49
28	TMA	1	0.07	3.2	0.3	0.05	0.53+0.49
29	TMA	1	0.1	3.2	0.3	0.05	0.53+0.49
30	TMA	1	0.1	1.6	0.4	-0.05	0.0+0.0
31	TMA	1	0.1	1.6	0.4	-0.05	0.3+0.3
32	TMA	1	0.1	1.6	0.35	0.05	0.53+0.49
33	TMA	1	0.1	1.6	0.35	-0.05	0.53+0.49
34-48	TMA	0.25	0.1	1.6	0.4	-0.05	0.53+0.49

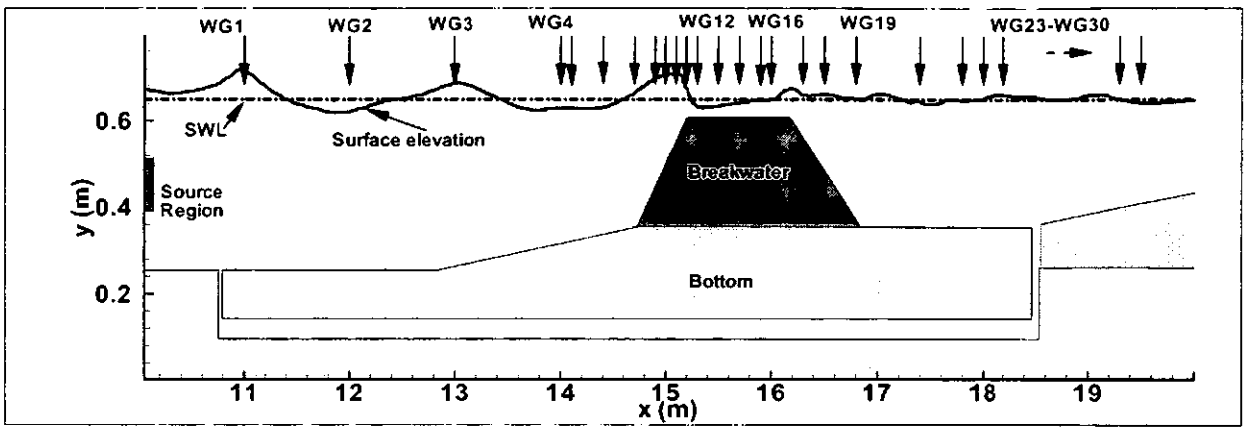

Figure 4.3.2 Overview of 30 numerical gauges (WG1 to WG30). Water depth at x=11m is 0.4 m. Solid line represents calculated surface elevations at *t*=200 s; dash-dotted line stands for still water level.

There are 30 numerical gauges along the cross-shore section of simulation setups, covering the flat bottom and Plexiglas ramp on the incident side, slopes and crest of LCS and flat bottom and permeable beach on the transmission side. The according coordinates of each numerical gauge can be referred to Figure 4.3.2. The outputs have the sample frequency of 40 Hz and consist of VOF values, horizontal and vertical velocities. To exclude the numerical noise and the influence of irregular intervals of sampling (by dynamic time step), the outputs are re-sampled into equal sampling intervals of 0.025s, then filtered using the band pass filter, which has a low limit of 0.2 times peak frequency and a high limit of 5 times peak frequency. This band pass filter ensured that the energy at both the low limit and high limit is less than 1 percentage of the energy at the peak frequency. Since numerical simulation is unstable in the initial several waves arising from the internal wave-maker, the first 10 waves were excluded in following

calculations.

4.3.2 Validation of generated waves

A regular wave propagating over a LCB with a wide crest was generated to investigate the capability of capturing the surface elevations using the RANS-VOF model (Case No.1).

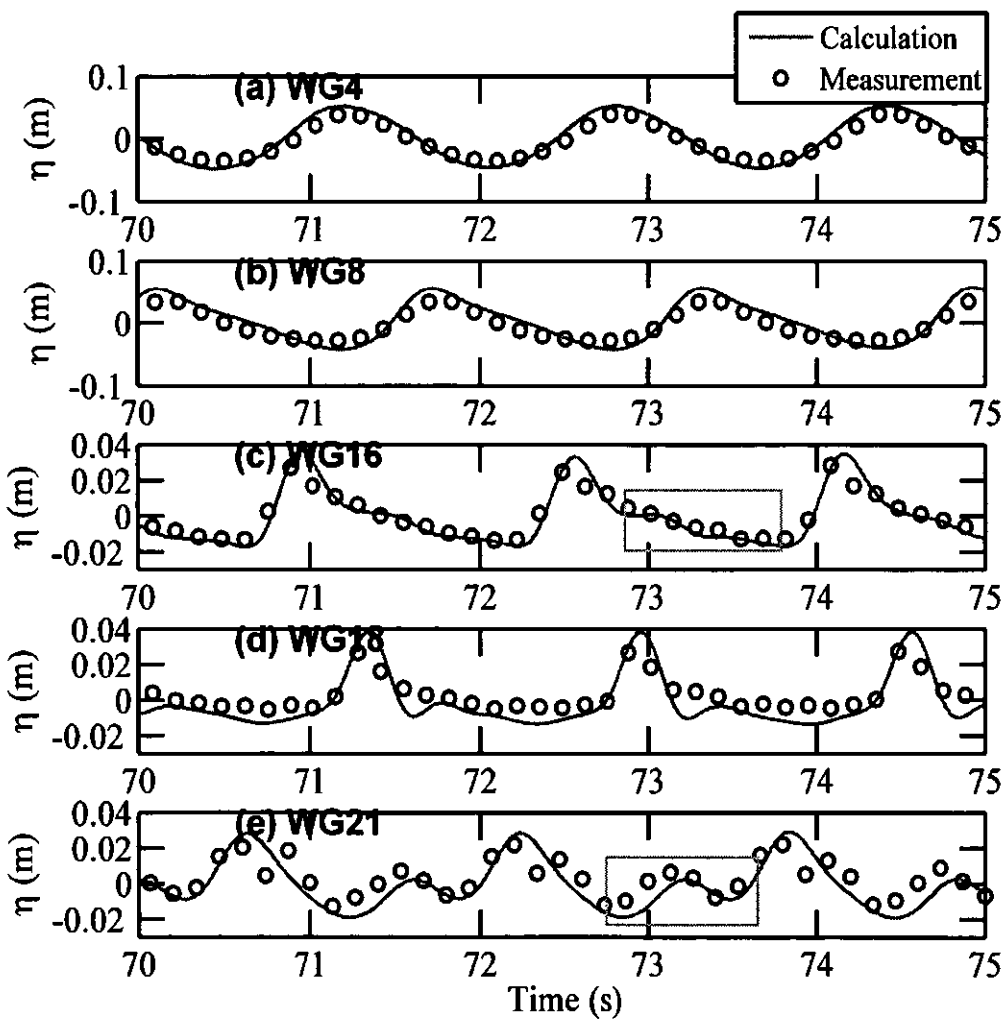

Figure 4.3.3 Comparisons of predicted wave surface elevations and measurements (a) on the incident side, (b) on the seaward slope, (c) on the crest, (d) on the landward slope and (e) on the transmission side of LCS (Case No.1). Coordinates of WGs can be referred in Figure 4.3.2.

As shown in Figure 4.3.3, the cross-shore evolution of wave shapes over a LCB is of importance; waves are all characterized by a peaking of crests, flattening of troughs, a character of positive skewness (Elgar and Guza, 1985), although there are differences in the magnitudes of wave skewness. Waves are characterized by pitching forward from the incident side to the top of the crest, but pitching backward from the top of the crest to the transmission side, corresponding to transfer from negative asymmetry and positive asymmetry. These phenomena are consistent with the results in Section3.3. Measured waves on the incident side were well reproduced through the source region, and all calculated surface elevations are in good agreement with measurements.

The cases with irregular waves generated from the TMA spectrum (see Appendix B) were considered in the present work. Figure 4.3.4 shows the comparisons of calculated power spectrum and measurements in front of and behind the LCB (Case No.8). Results show that the spectrum of measured waves on the incident side (WG4 and WG8) was well reproduced through the source region, and all the calculations are in good agreement with measurements. This indicates that the wave-maker used in the present model is capable of generating accurately the irregular waves for numerical simulations.

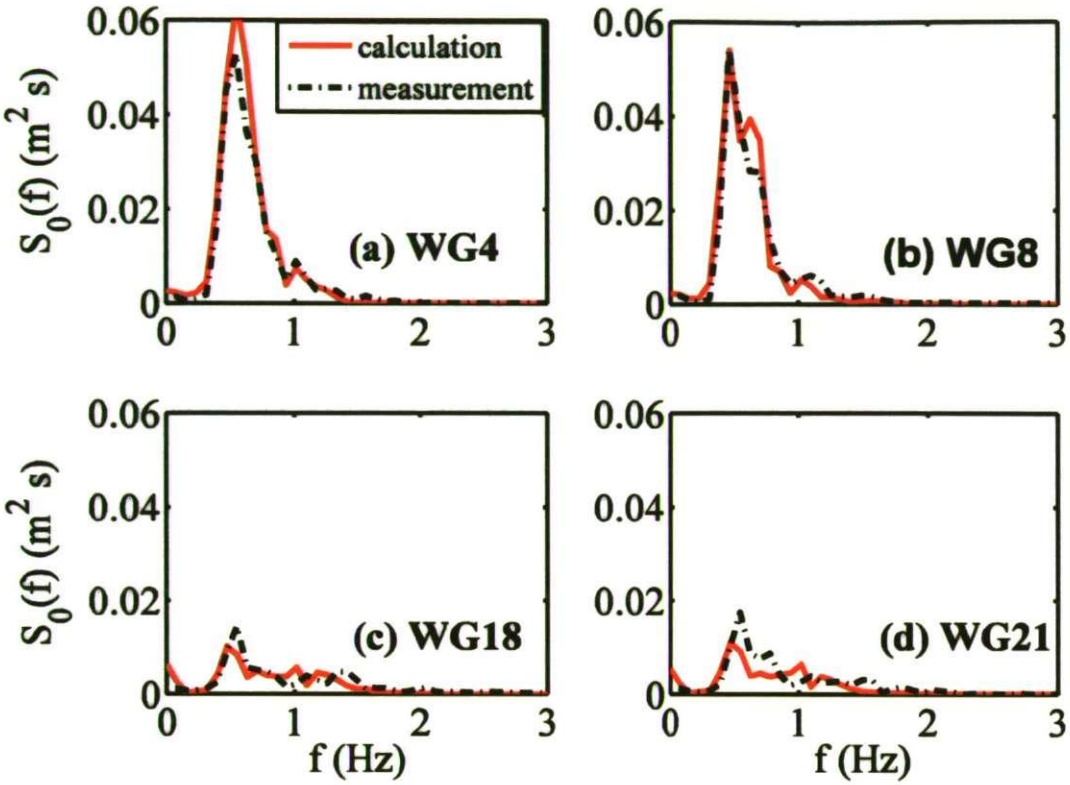

Figure 4.3.4 Comparisons of calculated power spectrum and measurements (Case No.8). Coordinates of WGs can be referred in Figure 4.3.2.

The evolution of wave spectrum is also shown in Figure 4.3.4 with the cut-off frequency equalling 3 *Hz*. The solid and dash-dotted lines represent the calculated and measured spectra respectively. To illustrate the evolutions of the power spectrum, $S_0(f)$, the vertical axes of the graphs (Figure 4.3.4c and Figure 4.3.4d), which correspond to the numerical gauges (WG18 and WG21) on the transmission side, is scaled the same as those of WG4 and WG8. The locations of spectrum peaks and spectrum shape are in good agreement with measurements. Results show that incident wave spectrum has the energy concentrated around the peak frequency and less energy on the higher frequencies (Figure 4.3.4a). The reflected waves from

the LCB contaminate the incident wave spectrum, causing a secondary peak to appear (Figure 4.3.4b). The incident wave energy reduced considerably over LCB and the remaining energy was transferred from the low frequencies to high frequencies, leading to a higher upper tail (Figure 4.3.4c and Figure 4.3.4d). This phenomenon is consistent with that in Van der Meer et al. (2005) and Lara et al. (2006). The spreading of spectrum energy on the high frequencies is well captured by the numerical model, although there is a slight underestimation of spectrum energy around the peak frequency on the transmission side (Figure 4.3.4c and Figure 4.3.4d).

4.3.3 Velocity field around LCS

To further understand the wave transformation over coastal structures, it will be helpful to examine the flow pattern around coastal structures. Figure 4.3.5 presents three snapshots of instantaneous velocity distribution, representing three stages of wave propagating over coastal structures: wave breaking, propagation on the crest and entrance into the transmission side.

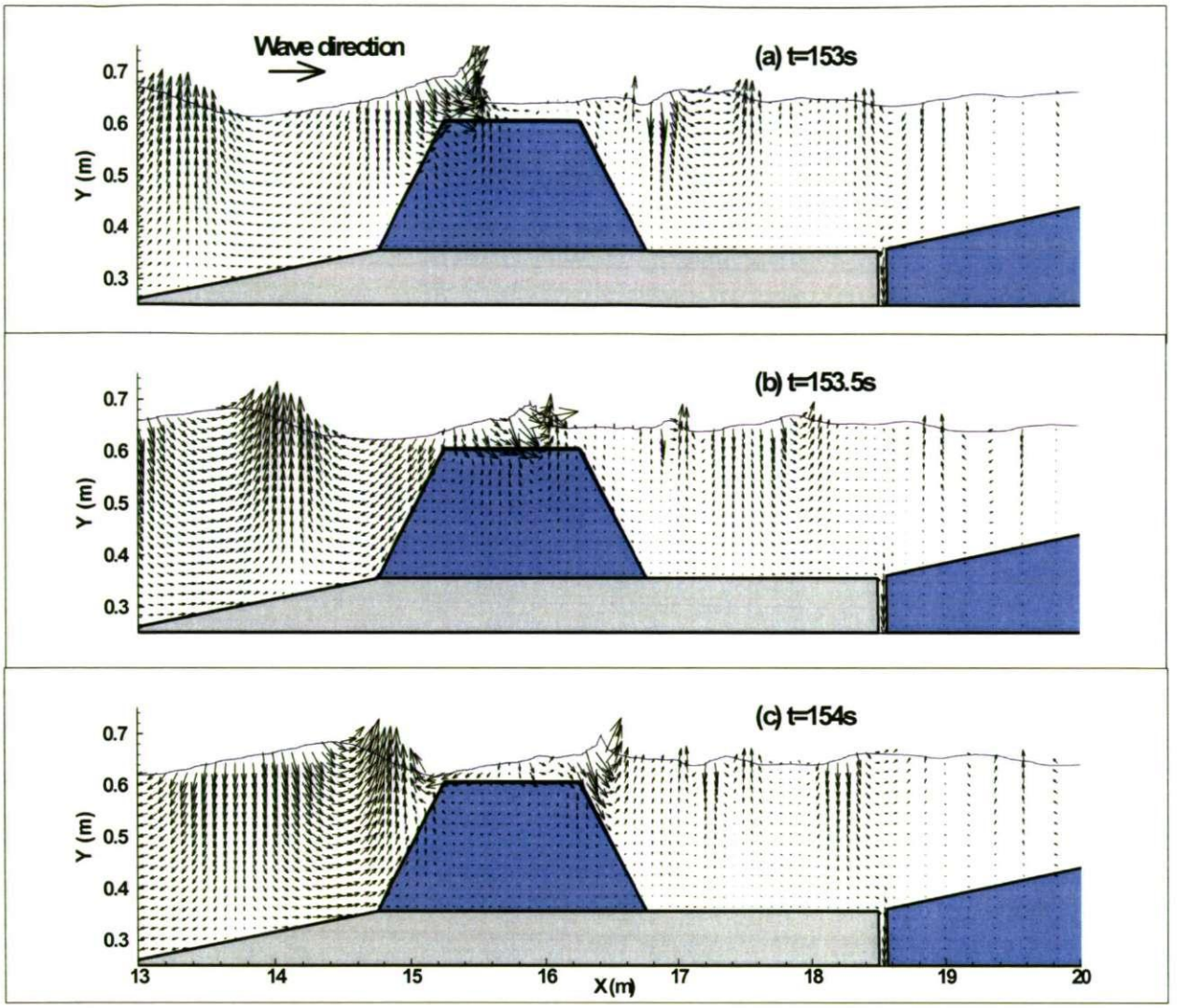

Figure 4.3.5 Snapshot of the flow pattern in the computational domain (shown in Figure 4.3.2). The grey area is the impermeable bottom, while the blue area represents the permeable obstacles. The wave conditions: H=0.07m, T=1.6s, h=0.4m and R_c=-0.05m.

In Figure 4.3.5a, it shows clearly the stage immediately after wave breaking. The velocity field around the seaward edge of the structural crest is very chaotic, with characteristics of both large upward and downward velocities. The velocities on the crest and the leeward slope of coastal structures are around zero, showing there is no wave effect at these areas at this phase. While in Figure 4.3.5b, the waves propagate around the middle of

the structural crest, with small water depth restriction, the velocities, both vertical and horizontal components, remain larger due to energy flux conservation. These large velocities may affect the stability of armour stones on the structural crest. The velocity on the seaward slope of coastal structure is downward and nearly tangent to the slope and there is still no wave effect on the leeward slope of coastal structure. In Figure 4.3.5c, it is obvious that overtopping water with large jet-like velocities enters into the area on the leeward slope of structures, associated with a positive elevation of mean water level. The velocities on the structural crest demonstrate that there is a part of transmitted water flowing back to the incident side of coastal structure, forming a resistance to the incident waves. However, this part of water is very small for Low-Crested Structures.

4.4 Comparisons of Model Results and Measurements

Since the Ursell number is important to wave skewness and asymmetry (Doering and Bowen, 1995; Doering et al., 2000; Elfrink et al., 2006), the parameters related to Ursell number was considered next. Five cases with different wave conditions but the same structural geometry and bottom bathymetry were employed to validate the numerical simulations. These five cases have the wave condtions as: H_i=0.04m, T_{pi}=1.6s and h=0.4m; H_i=0.10m, T_{pi}=1.6s and h=0.4m; H_i=0.07m, T_{pi}=1.6s and h=0.4m; H_i=0.07m, T_{pi}=3.2s and h=0.4m; H_i=0.10m, T_{pi}=1.6s and h=0.3m. In order to compare the calculated wave skewness and asymmetry with measurements, generated wave height and peak period are adjusted to make the calculated

significant wave height and peak frequency at the x=14m the same as the measurements of G1.

Comparisons of wave skewness and asymmetry of wave surface elevation between measurements and numerical calculations are shown in Figure 4.4.1, although the measurement domain is much smaller than the computational domain. For these five cases, calculated wave skewness and wave asymmetry are in good agreement with the measurements both on the incident side and on the transmission side. Numerical calculations and laboratory measurements demonstrate that wave skewness increases slowly in the far field but decreases in the seaward near-field region (consisting of seaward slope and a part of areas in front of the structural toe). It then increases up to the maximum on the structural crest then decreases dramatically down to approximately zero in the leeward near-field region (covering leeward slope and a part of areas behind the structural toe). Wave asymmetry decreases from zero on the incident side, down to the minimum value on the structural crest, and then increases up to positive value in the leeward near-field region of LCS. Finally wave skewness increases and wave asymmetry decreases on the beach behind LCS.

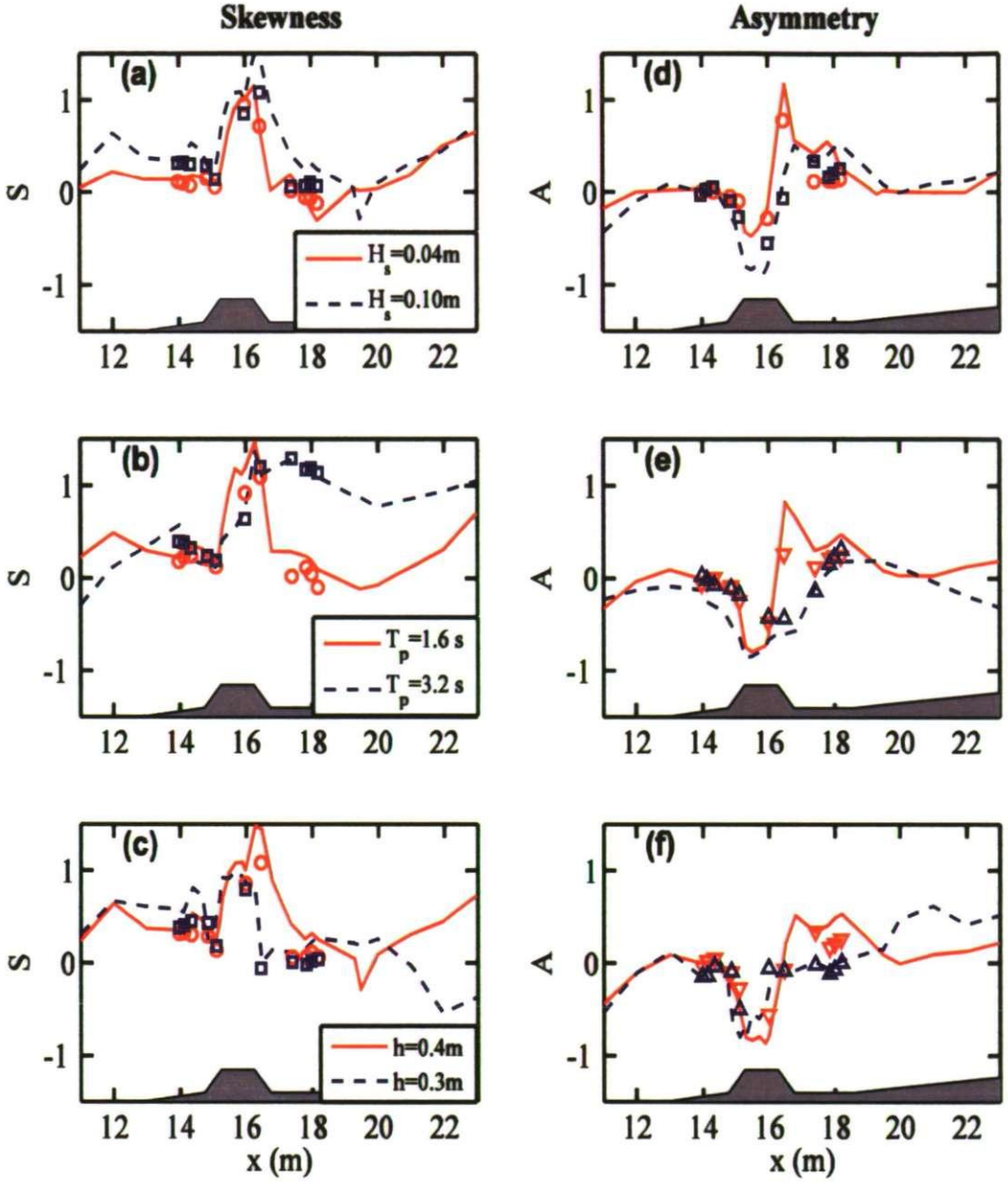

Figure 4.4.1 Comparisons of wave skewness (S) and asymmetry (A) of wave surface elevations between different (a, d) significant wave heights with T_{pi}=1.6s and h_o=0.4m, (b, e) peak wave periods with H_i=0.07m and h_o=0.4m (c, f) water depths at x=11m with H_i=0.10m and T_{pi}=1.6s under the same other wave conditions and structural geometry. Structural crest width B=1.0m. Lines represent numerical results and dots represent measurements. o: measurements associate with solid line, □: measurements associate with dashed line. Grey area represents the LCB and bottom (scaled for aesthetic reason).

Evolutions of wave skewness and asymmetry over LCS described above are similar to those over a submerged sandbar on a natural beach found from the field measurements and predictions in Herbers et al. (2003). Wave skewness is positive on both incident side and transmission side except for the permeable beach, and wave asymmetry is negative on the incident side but changes to positive values on the transmission side instead. This phenomenon is consistent with the results of section 3.3.

4.5 Relationships of Wave Asymmetries and Ursell number

Wave channel tests described in described in Section 4.2 cover larger ranges of wave conditions and structural properties than those in wave basin transmission tests in Section 3.2, as well as more wave gauges around LCS. We next apply the relationships between wave skewness and asymmetry and local Ursell number (see definition in Equation (3.3.3)), derived in Chapter 3, to numerical results and measurements. Results of numerical gauges WG1 to WG7 and Measurements of G1 to G5 are used for comparisons on the incident side, while results of numerical gauges WG19 to WG23 and measurements of G8 to G11 are used for comparisons on the transmission side. Detailed coordinates of numerical gauges and wave gauges can be referred in Figure 4.3.2 and Figure 4.2.1 respectively.

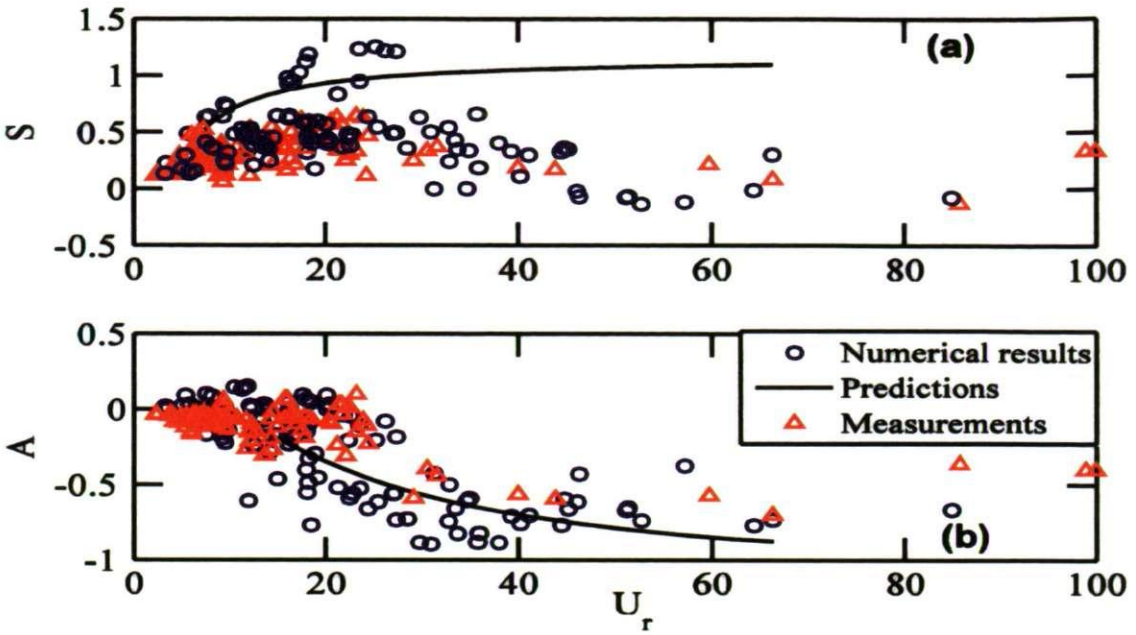

Figure 4.5.1 Relationships of U_r ($U_r=H_sL_m^2/h^3$) and (a) wave skewness and (b) asymmetry in front of LCS. o: the calculated results; Δ: measurements; solid lines: predictions by Equations 3.3.8-3.3.9.

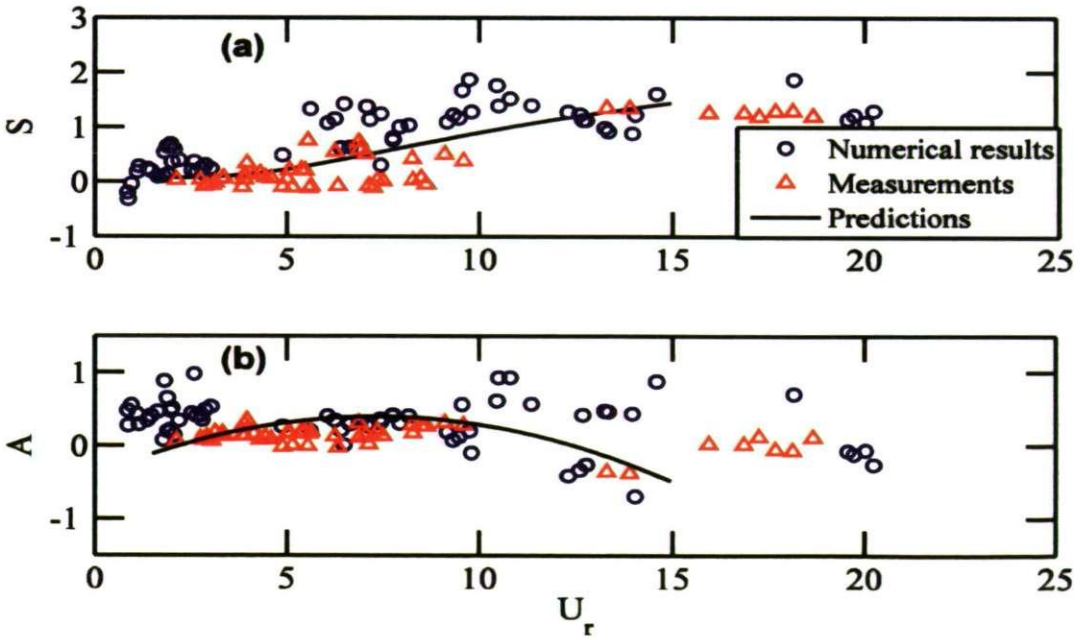

Figure 4.5.2 Relationships of Ursell number, U_r, and (a) wave skewness, S, and (b) wave asymmetry, A, above the flat bottom on the transmission side of LCS. o: the calculated results; Δ: measurements; solid lines: predictions by Equations 3.3.10-3.3.11.

Figure 4.5.1 shows the comparisons of calculations, measurements and predictions by Equations 3.3.8 and 3.3.9 on the incident side of LCS. The relationships between calculated wave asymmetry and local Ursell number are in good agreement with measurements and predictions, but calculated wave skewness is smaller than the predictions although it agrees with measurements. This discrepancy may be due to different reflection coefficients. Both experiments and computational domain in this chapter are 2-Dimension, and waves are reflected normally from LCS. However, experiments for deriving empirical formulae in CHAPTER 3 are 3-Dimension and a large part of reflected waves could escape the area between the inclined structure and the wave generator and get absorbed in the absorbing sidewalls (Kramer et al., 2005). Since reflected waves mainly consist of excited low-frequency wave components, which bring more difference interactions in, therefore, the reflected wave contribute negatively to wave skewness.

Figure 4.5.2 shows the comparisons of calculations, measurements and predictions by Equations 3.3.10-3.3.11 on the transmission side of LCS. The relationships between calculated wave skewness and asymmetry and local Ursell number are in good agreement with measurements and predictions, although the applicable range of Ursell number in Equations 3.3.10-3.3.11 is 1.5-15. Comparing with the observations in Chapter 3, calculations and measurements of this study have large wave period and large water depth, which lead to larger wave height and mean period on the transmission side, consequently large Ursell number. Results of the present study were helpful

to extend the effective ranges of empirical formulae proposed in Chapter 3. It should be noted that the local mean Ursell number becomes to be incredibly large due to extremely small water depths above LCS, thus local mean Ursell number is no longer a suitable parameter to describe wave skewness and asymmetry.

4.6 Factors Affecting the Evolution of Wave Asymmetries

4.6.1 Incident wave height, period and water depth

As shown in Figure 4.4.1a and Figure 4.4.1d, the larger wave height corresponds to larger wave skewness and larger absolute wave asymmetry on both sides of LCS. This is because large waves correspond to large transmitted waves and have large Ursell number, therefore have large wave skewness and absolute wave asymmetry (see Chapter 3).

Figure 4.4.1b and Figure 4.4.1e showed that the effect of wave period on wave skewness is more significant than on wave asymmetry. It is interesting to observe that the variations of wave asymmetries decrease with the increasing wave periods. For the case of T_{pi}=1.6s, the wave skewness and asymmetry dramatically change over LCS, while for the case of T_{pi}=3.2s, the wave skewness and asymmetry have mild changes around LCS. Small wave peak period corresponds to small extent of the effect of LCS. The case of T_{pi}=1.6s decreases the maximum wave skewness to zero in a shorter distance than the case of T_{pi}=3.2s, and the maximum asymmetry of the

former is closer to LCS than that of the latter. This is mainly due to small changes in relative water depth (h/L, h is water depth and L is the wave length) on the rear slope with long wave length, and the decoupling process is strongly dependent on the increasing gradient of relative water depth.

Figure 4.4.1c and Figure 4.4.1f indicated the combined effects of water depth and the freeboard (R_c is 0.05m when h equals 0.3m). On the incident side of LCS, small water depth corresponds to large wave skewness and small negative wave asymmetry. This is consistent with the conclusions of Section3.3: small water depth corresponds to large Ursell number, thus corresponds to larger wave skewness and small negative wave asymmetry. However, small water depth corresponds to nearly zero wave skewness and asymmetry in the leeward near-field region. This is because LCS located in small water depth (h=0.3m) have positive freeboards, which reflect a large part of wave energy and only allow a small part of wave energy to be transmitted and to overtop. This kind of structure finally induces small wave heights and local Ursell number. It should be noted that for the emerged case wave skewness and asymmetry on the top of the crest is mainly calculated based on the free surface inside the porous media. Therefore, it is not recommended here to consider wave skewness and asymmetry on the top of the crest, since the aim of this study is to investigate the mean flow outside the porous media.

4.6.2 Incident wave shapes

Near-shore waves always change shapes under different atmospheric pressure and wind speed. It is important to consider the effect of near-shore incident wave shapes on the evolution of wave skewness and asymmetry, and this will help to understand the wave process approaching the LCS.

To study the effects of incident wave shapes on the evolution of wave skewness and asymmetry across LCS, two cases with different regular wave shapes were investigated, including a positively skewed wave and negatively skewed wave, both pitching forward. These two waves were under the same wave parameters, structural properties and bottom bathymetry. After about 200 wave cycles of the numerical simulations, wave skewness and asymmetry were calculated using numerical outputs of 30 locations across the LCS.

As can be seen in Figure 4.6.1a, the positively skewed wave has sharp crests and flat troughs, but the negatively skewed wave has sharp troughs and flat crests. Both of them pitch forward, a characteristic of steep front face and gentle rear face. The difference of rear face slope induces different magnitude of wave asymmetry, although the front face slope is nearly the same. Figure 4.6.1b shows the evolution of significant wave heights (the average height of the highest one third of the waves) across the LCS. Small variation of wave heights appears in the near field in front of LCS, this is mainly due to the partial standing waves (observed by Garcia et al. 2004 as well) induced by the combination of incident wave and reflected wave from

LCS. Therefore, wave heights around the nodes are smaller than those around the anti-nodes. Wave heights start to decrease after passing the front slope of LCS due to wave breaking. Wave heights continue to decrease down to about one-third of incident wave height since the energy transmitted or overtopped is considerably smaller. It is obvious that the incident wave shapes have little effect on wave heights across the LCS, therefore the conclusion can be drawn that transmission coefficients are not changed by incident wave shapes. Figure 4.6.1c and Figure 4.6.1d show that incident wave shapes have a significant effect on wave asymmetry only on the incident side but they have a significant effect on wave skewness on both the incident side and top of LCS. The incident shapes have less effect on wave skewness and asymmetry on the transmission side. The reason is that wave skewness and asymmetry are adaptive to local water depth in the far field in front of LCS and controlled by local Ursell number (see Chapter 3). Therefore, with the same local water depth and sufficient area of far field in front of LCS, wave asymmetries of different incident wave shapes tend to be the same by this adaptive process.

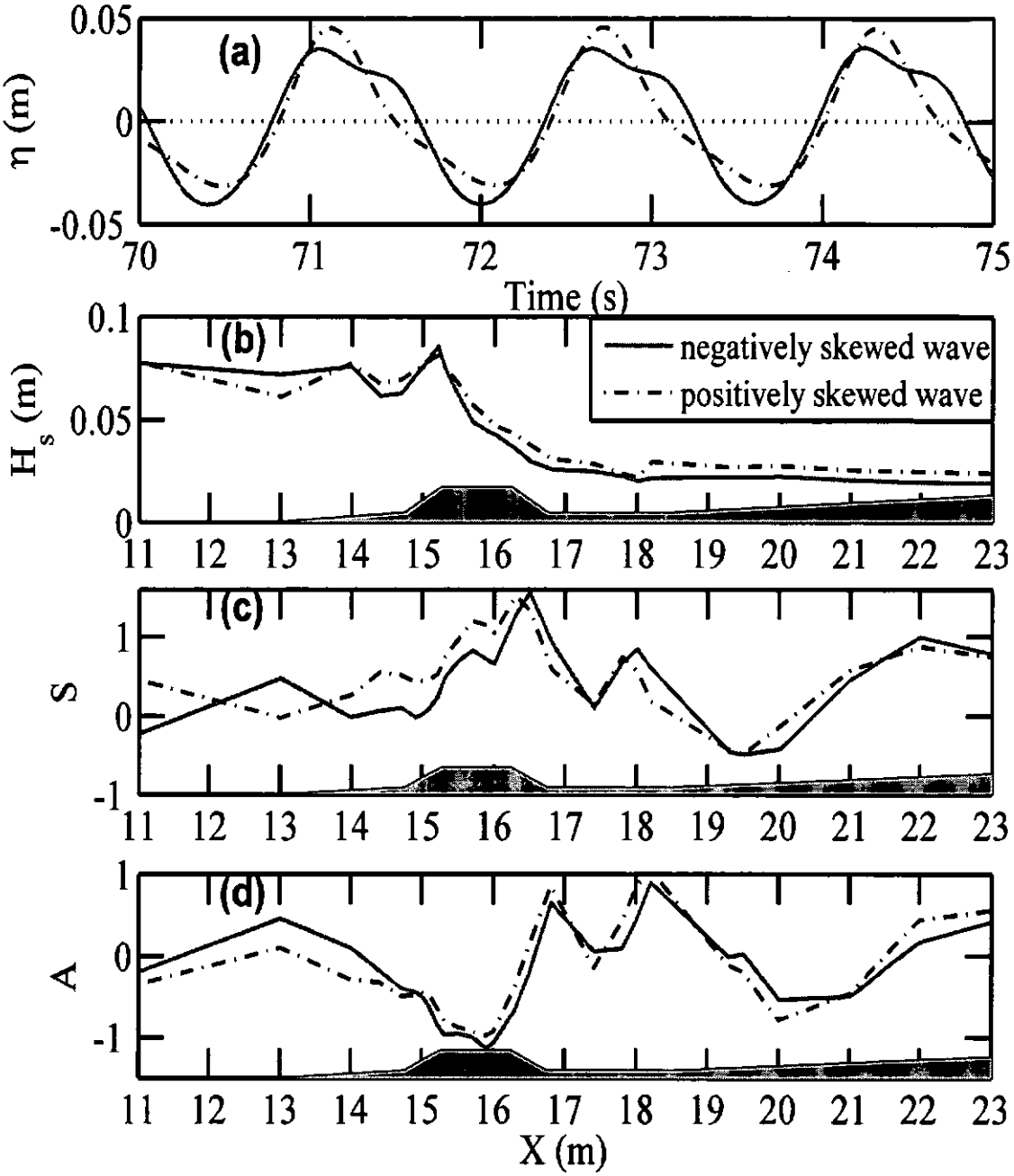

Figure 4.6.1 Effect of incident wave shapes on the evolutions of wave skewness and asymmetry across LCS. (a) Wave profiles at x=11m, (b) significant wave heights, H_s, (c) wave skewness, S, and (d) wave asymmetry, A, under the same wave parameters and structural properties. Grey area represents the LCB and bottom geometry (scaled for aesthetic reason). Negatively skewed wave: S=-0.23, A=-0.19; positively skewed wave: S=0.45, A=--0.35. Source region is located around x=10 m. B=1.0m, R_c= -0.05m.

4.6.3 Randomness in incident waves

With the same wave conditions but random phase angles, 15 cases with irregular waves have been investigated to investigate the effect of wave randomness on wave asymmetries over the breakwater with a narrow crest B=0.25m, H_i=0.10m, T_{pi}=1.6s and h=0.4m at X=11m.

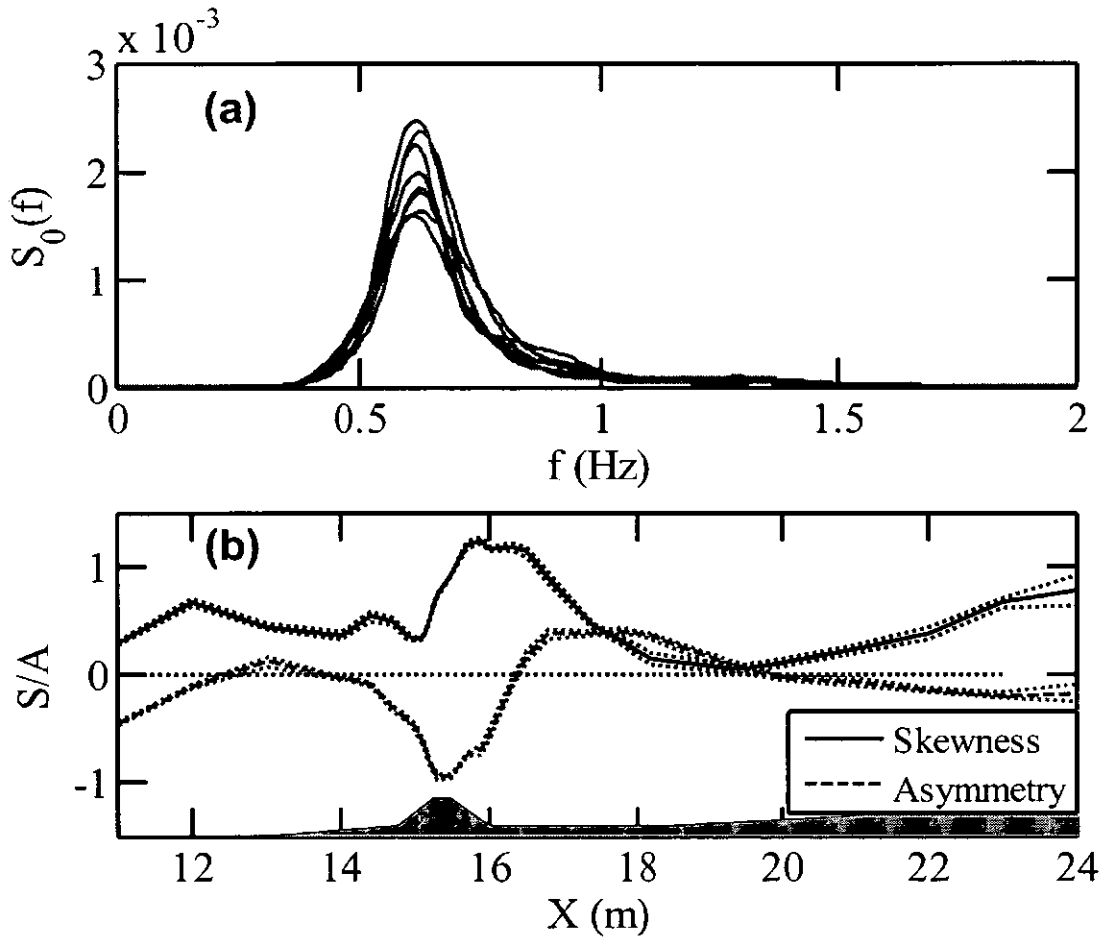

Figure 4.6.2 Effect of the randomness in incident waves on the evolution of wave skewness (*S*) and asymmetry (*A*) over LCS, with the same significant wave height and peak period and structural geometry. (a) Power spectrum, *So(f)*, at x=11m and (b) wave skewness and asymmetry. The dotted line represents the 95% confidence levels of the mean skewness or asymmetry. Grey area represents the LCB and bottom geometry (scaled for aesthetic reason). B=0.25 m, R_c= -0.05 m.

Using the TMA spectrum (see appendix B), Series of time series were generated with wave conditions at x=11m are: significant wave height H_i=0.10m, wave peak period T_{pi}=1.6s and water depth h=0.4m. These time series have the same peak frequency and are only different from the distribution of power spectrum around the peak frequency (Figure 4.6.2a). The mean wave skewness and asymmetry averaged between 10 cases with 95% confidence levels of the mean skewness or asymmetry are shown in Figure 4.6.2b. As can be seen in Figure 4.6.2, the effect of the randomness in irregular waves on both wave skewness and asymmetry across LCS is negligible. This is mainly because wave skewness and asymmetry are dependent on local Ursell number, which is only related to significant wave height, peak frequency and local water depth, rather than the shape of power spectrum (see Chapter 3). Large confidence interval appeared around the shoreline (about x=24m), and this may arise from the numerical errors in dealing with the extremely shallow water, or possibly due to the calculated errors of wave skewness and asymmetry from small significant wave heights.

4.6.4 Relative crest width of LCS

The effect of crest width (B) on wave skewness and asymmetry was investigated through two different crest widths: B=0.25m and B=1.0m, under the same incident wave shapes, H_i=0.10m, T_{pi}=1.6s and h=0.4m at x=11m,

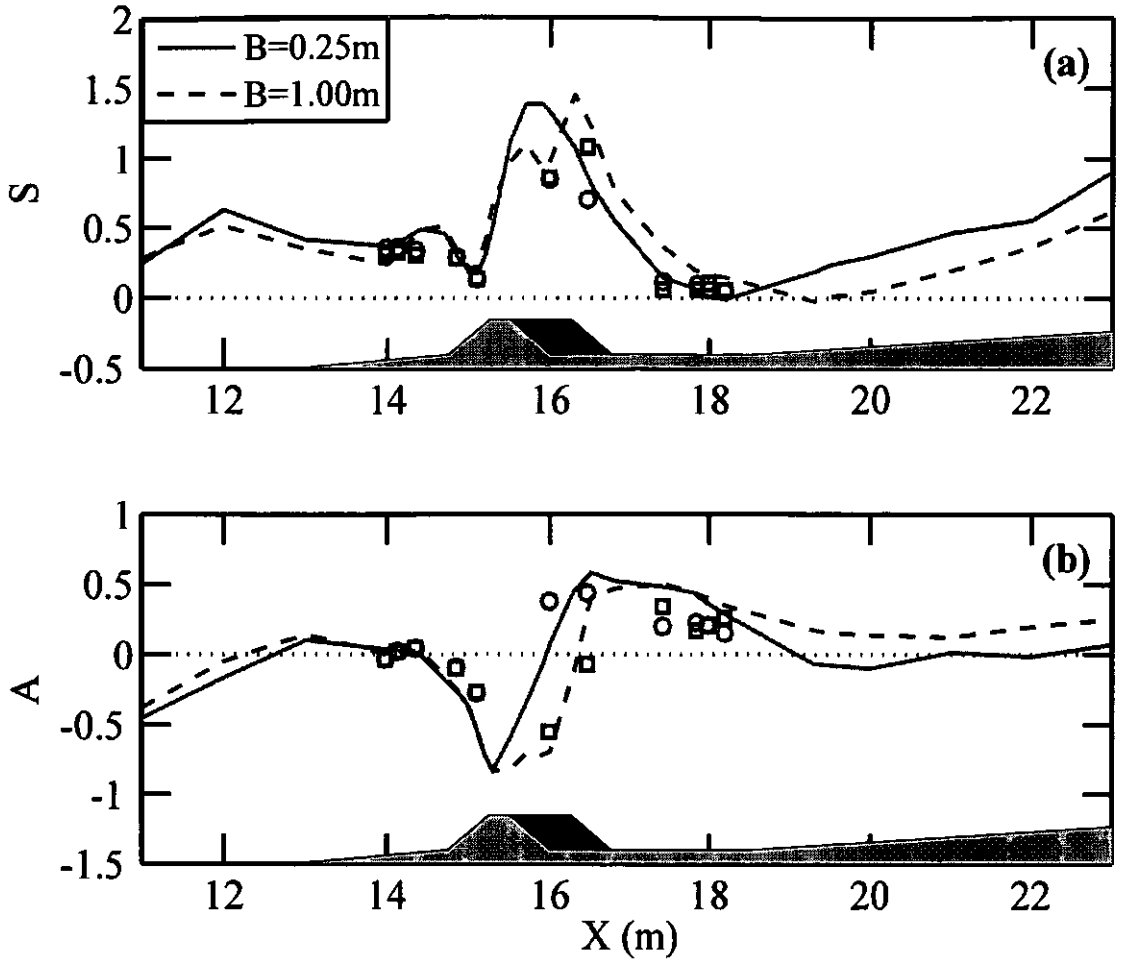

Figure 4.6.3 Effect of relative crest width of LCS on (a) wave skewness (*S*) and (b) asymmetry (*A*) under the same wave conditions. Grey area represents the LCB and bottom geometry (scaled for aesthetic reason). Symbols represent measurements, ○: narrow crest with; □: wide crest with. R_c= -0.05m.

As shown in Figure 4.6.3, both cases display large variations of wave skewness and asymmetry around the LCS. It is interesting to observe that for both crest widths, the point of maximum wave skewness is located around the leeside end of the crest and minimum wave asymmetry appears at the middle of the crest. However, the rate of increase of wave skewness is dependent on the width of the crest. The case with a narrow crest has a

larger rate of increase of wave skewness and asymmetry above the crest than the case with a wide crest. The maximum and minimum wave skewness and asymmetry for these two cases are the same. We can draw a conclusion that wave nonlinear interactions on the crest are developed into saturationfor both crest widths. On the other hand, these two crest widths cause different wave skewness and asymmetry on the transmission side, for example, a wide crest has smaller skewness and larger asymmetry than a narrow crest. This is because large crest width offsets the controlled area by the transmission effect. At the same location on the transmission side, waves propagating over the narrow crest have recovered to a Rayleigh distribution, while waves propagating over the wide crest may be still under the influence of wave transmission effect.

4.6.5 Porosity of LCS

By changing the structural porosity, three cases with different porosities were investigated: zero porosity (γ=0.0), small porosity (γ=0.4) and large porosity (γ=0.53). H_i=0.10m, T_{pi}=1.6s and h=0.4m. As shown in Figure 4.6.4a, significant wave heights decreased slowly when wave propagated in front of LCS, and then increased up to the maximum above the front slope of LCS due to the decreasing water depth. After wave breaking, wave energy dissipated and wave height decayed quickly. Comparing these three cases, the case with zero porosity has the largest wave heights and the case with large porosity has the smallest wave heights above LCS. It is mainly because large porosity of LCS corresponds to large energy dissipation. There is less

energy converting to the potential energy and thus a smaller wave height.

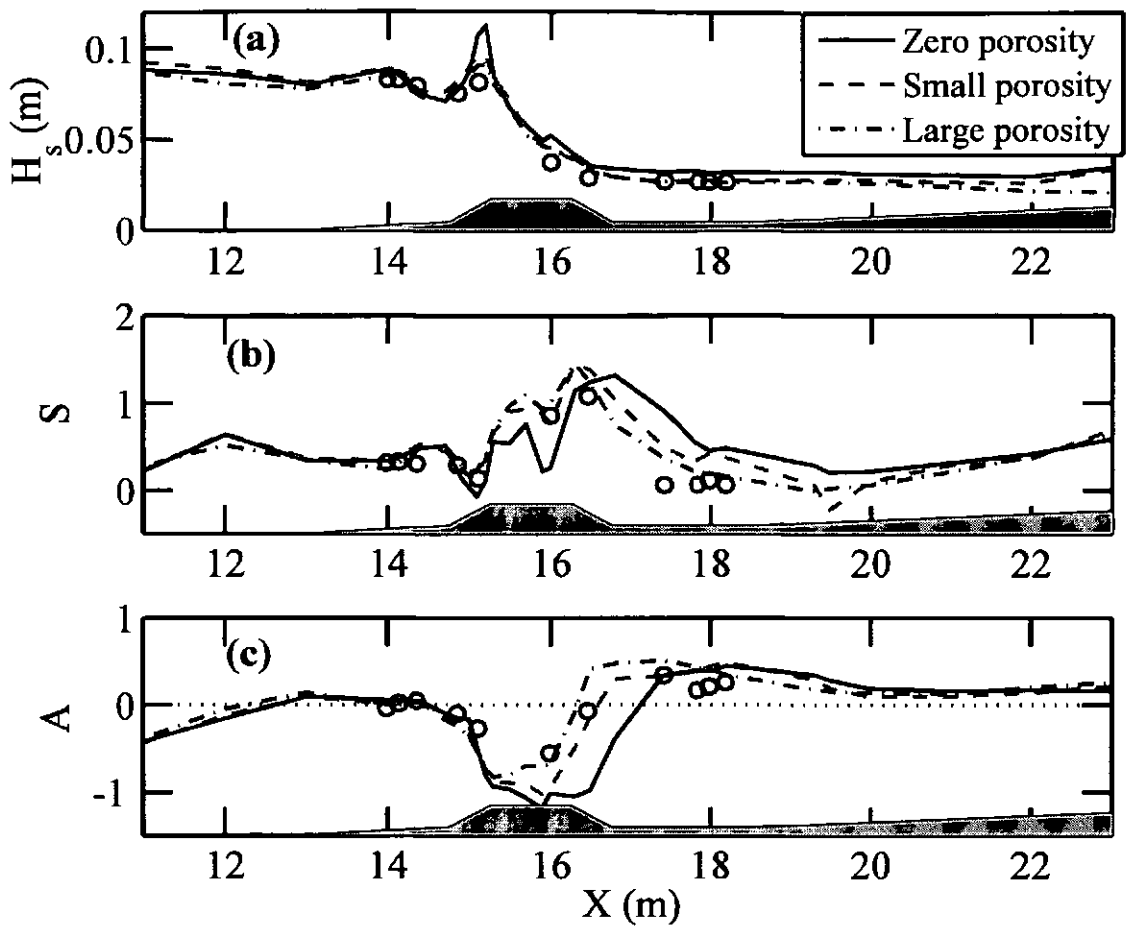

Figure 4.6.4 Effect of structural porosity on the evolution of (a) significant wave height (H_s), (b) wave skewness (S) and (c) wave asymmetry (A) under the same wave conditions and structural geometry. Grey layer only represents the LCB and bottom geometry (scaled for aesthetic reason).○: measurements of the case with large porosity. B=1.0m, R_c= -0.05m.

After examining the significant wave heights, comparisons of wave skewness and asymmetry between these three cases are shown in Figure 4.6.4b and Figure 4.6.4c. For all cases wave skewness increases first then decays on the transmission side of LCS, while wave asymmetry decreases

initially but subsequently increases up to a maximum value.

For the case with large porosity, wave skewness and absolute asymmetry decreases to zero in a shorter distance behind LCS than those for the cases with smaller porosities. The maximum wave skewness and asymmetry of the former is also closer to LCS. Therefore, larger porosity corresponds to smaller extent of the effect of LCS. This can be explained by the work of Losada et al. (1997): Increasing porosity increases the effective water depth (h_{ef}, taking into account the effects of structural permeability). Moreover, due to dissipation in the porous medium, the relative wave height, a/h_{ef}, decreases and the Ursell number decreases as well. Therefore, increasing porosity wave skewness and asymmetry decrease and the chance of harmonic generation is reduced.

4.6.6 Relative freeboards of LCS

Under the same wave conditions, H_i=0.10m, T_{pi}=1.6s and h=0.35m, three cases with different freeboards (R_c=0.05m, 0m and -0.05m) were employed to investigate the effect of relative freeboards on the wave skewness and asymmetry.

As shown in Figure 4.6.5, the effect of relative freeboards on wave skewness and asymmetry is significant on the top of the crest and transmission side but the same does not hold on the incident side. This is expected since the permeability and small freeboards of LCS cause less difference in reflection coefficients. Due to more dissipation inside the

porous media, the case with a positive freeboard has smaller wave energy and subsequently smaller nonlinear interactions over the structural crest. It obviously corresponds to small wave skewness and absolute asymmetry. However, comparing with the case with a negative freeboard, the case with a zero freeboard has larger maximum wave skewness and asymmetry, as well as larger extent of the effect of LCS. The main reason is that the case with a zero freeboard corresponds to a smaller effective water depth on the structural crest. Taking the definition in Losada et al. (1997), the effective water depth on the structural crest is around 0.0108 m for R_c=0 m and 0.0572 m for R_c=0.05m when the linearized friction coefficient equals 5. As mentioned in Chapter 3, wave skewness and asymmetry increase with decreasing water depth and increasing Ursell number. Harmonic generations increase with the decreasing water depth, and therefore they take more time to be released on the transmission side (Losada et al., 1997). As a result, a conclusion can be drawn that coastal structure with around zero freeboard will lead to the maximum wave skewness and asymmetry and large extent of the effect of structures. Coastal structure with a small positive freeboard, however, helps to reduce wave skewness and asymmetry significantly.

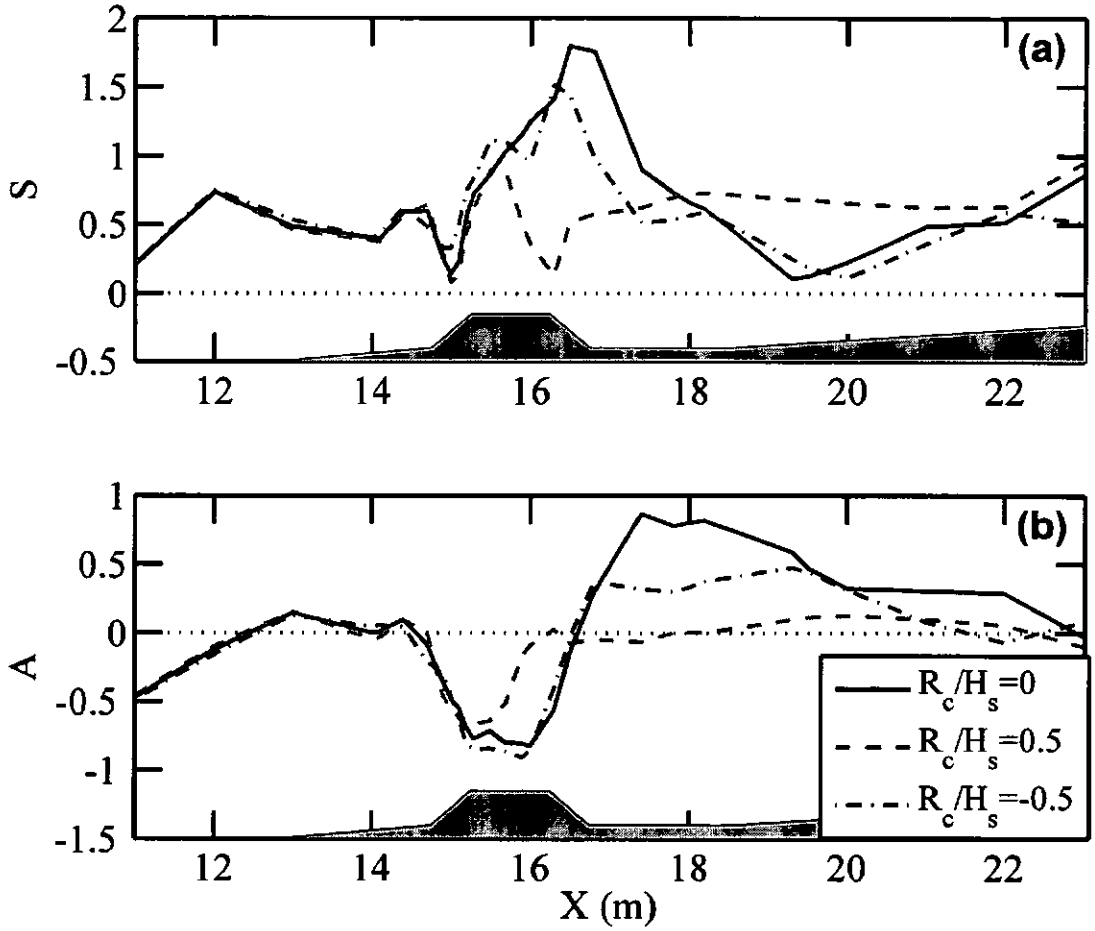

Figure 4.6.5 Effect of relative freeboard on the evolution of (a) wave skewness (*S*) and (b) wave asymmetry (*A*) under the same wave conditions and structural geometry. Grey layer only represents the horizontal location of bottom geometry. B=1.0m.

4.7 Discussions

It has been increasingly recognized that pronounced nonlinear effects in shallow water induce a dramatic transformation of wave shapes from initially symmetric, nearly sinusoidal profiles, to asymmetric, pitched forward profiles characteristic of near-breaking waves. With the presence of LCS,

wave skewness decreases in the seaward near-field region and increases up to the maximum on the structural crest; it then decreases dramatically in the leeward near-field region. Wave asymmetry decreases in the seaward near-field region, down to the minimum value on the structural crest, and then increases up to positive value in the leeward near-field region of LCS.

Elgar and Guza (1985), Doering and Bowen (1995) and Ruessink (1998) concluded that this transformation of wave skewness and asymmetry arises from nonlinear triad interactions in which two primary wave components with frequencies f_1 and f_2 excite a secondary wave component with the sum (f_1+f_2) or difference (f_1-f_2, $f_1>f_2$) frequency. Therefore, Bispectra analysis (See Appendix C) was employed here to examine the nonlinear interactions occurring in the wave propagations over LCS. Kim and Powers (1979) showed that the bi-coherence, $b^2(f_1, f_2)$, represents the fraction of power at frequency f_1+f_2 due to quadratic coupling of the 3 modes (f_1, f_2, and f_1+f_2). The bi-coherence does give an indication of the relative degree of phase coupling between triads of waves (Elgar and Guza, 1985), with b=0 for random phase relationships, and b=1 for a maximum amount of coupling.

As shown in Figure 4.7.1a, in the seaward near-field zone including the seaward slope, there is not only strong coupling in the sum interactions between primary frequency and its harmonics, but also some coupling in the difference interactions between harmonics and low frequencies. These low frequencies may be from the reflected long waves from LCS. However, on the crest the difference interactions diminish and stronger couplings in the sum

interactions between higher harmonics appear (Figure 4.7.1b). In the leeward near-field zone including the leeward slope, difference interactions between harmonics and low frequencies increase gradually, along with decreasing coupling in the sum interactions between primary frequency and its harmonics (Figure 4.7.1c and Figure 4.7.1d). As concluded in Section 3.4, sum interactions (f_1, f_2, f_1+f_2) have positive contributions to wave skewness and negative contributions to wave asymmetry, and the difference interactions (f_1, f_2, f_2-f_1) have a negative contribution to wave skewness and positive contribution to wave asymmetry.

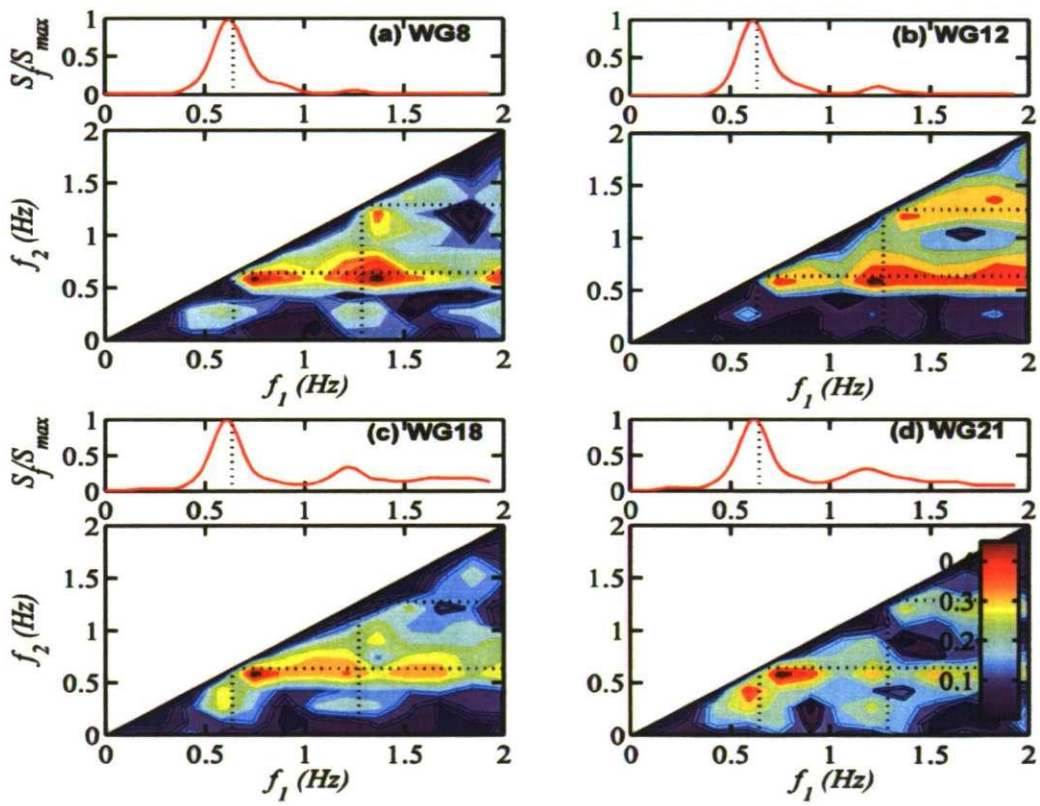

Figure 4.7.1 Normalized power spectrum and bi-coherence, b2(f1, f2), of surface elevations (a) on the front slope (WG8), (b) on the crest (WG12), (c) on the rear slope (WG18) and (d) on the transmission side (WG21). The dotted lines represent the primary frequency and second harmonic.

The nonlinear interactions between primary components and harmonics are consistent with earlier work. Beji and Battjes (1993) found that high frequency energy is generated when waves propagated over submerged bars. They interpreted the physical mechanism as the amplification of bound harmonics during the shoaling process and their release in the deeper region, resulting in the decomposition of these finite amplitude waves. In addition, since waves satisfy the triplet resonance conditions (Phillips, 1960) on the structural crest, a very rapid flow of energy is transferred from the primary wave to the higher harmonics. Brossard and Chagdali (2001) and Brossard et al. (2009) concluded that the decomposition of a wave above a submerged structure implies a transfer of energy from the fundamental mode towards the bound modes, phase-locked with the fundamental.

The effect of sum and difference frequency interaction on wave skewness has been introduced by Crawford (2000), for completeness we will also briefly discuss them here. The difference frequency interaction generates long waves and usually accompanies a group or bound wave response. This group wave is manifested as a depression of the mean surface elevation under the largest waves of the group. Therefore, a peaky wave (positive skewness) in the middle of the group riding on the increasing depressed surface has an increasing negative contribution to wave skewness. In contrast, the sum frequency interaction generates more short waves, corresponding to the release of depressed mean surface elevation. A peaky wave in the middle of the group riding on the increasing elevated surface has an increasing positive contribution to wave skewness.

The effect of the sum and difference frequency interactions on wave asymmetry can be understood physically through the following argument. Sum frequency interaction in front of LCS has a response of short wave generation. Due to the dispersive effect, the short wave propagates slower than the primary wave. The short wave is gradually lagged by the primary wave and appears at the trailing edge of the primary wave (indicated by square in Figure 4.3.3c). Therefore, wave develops as a pitching forward wave, characteristic of sharp front face and gentle rear face. On the crest of LCS, waves propagate at the same velocity in a rather non-dispersive medium due to small water depth, thus wave asymmetry will remain the same. However, when wave propagates into the deep water above the rear slope of LCS, the dispersive effect becomes significant again. Difference frequency interaction dominates this area and generates longer waves. Long wave propagates faster than the primary wave, and it gradually exceeds the primary wave and appears at the leading edge (indicated by square in Figure 4.3.3e). Thus, the wave evolves from pitching forward to pitching backward, characteristic of gentle front face and sharp rear face. It should be noted that the dissipation induced by the continuous shearing after wave breaking, which make the turbulence bore degenerate into small-scale motions with gentle slope of front face (Battjes, 1988), it also contributes to wave evolution from pitching forward to symmetric. Although plunging wave breaking will reduce the wave asymmetry after the breakpoint, the wave has been transformed into a turbulent bore immediately after wave breaking, still characterized by a steep, turbulent front and an area of recirculating flow

between the toe of the front (Battjes, 1988). Therefore, the difference of wave asymmetry before and after wave breaking is small.

In contrast with the evolution of wave skewness and asymmetry on a plane beach in Elgar and Guza (1985), the presence of LCS changes waves from pitch-forward to pitch-backward (corresponding to change the sign of wave asymmetry from negative to positive). The wave skewness has minimum value around the seaward end of the crest and maximum value around the leeward end of the crest of LCS. Wave asymmetry has the minimum above the crest and maximum values on the transmission side. This evolution of wave skewness and asymmetry may affect the directions in wave induced sediment transport, consequently modifying the beach morphology after construction of LCS.

4.8 Summary

A 2-D RANS-VOF model was employed to investigate the evolution of wave skewness and asymmetry of wave surface elevations over LCS. Computed surface elevations and wave asymmetries were in good agreement with laboratory measurements collected in the small scale wave channel tests at the University of Cantabria (UCA). The relationships of calculated skewness and asymmetry and local mean Ursell number agreed reasonably with the predictions of the empirical formulae in Section 3.3. The results of the present study enlarged the validate ranges of mean Ursell number and were helpful to extend the application ranges of empirical formulae.

Our results show that wave skewness increases slowly in the far field but decreases in the seaward near-field region; it then increases up to the maximum on the structural crest then decreases dramatically down to approximately zero in the leeward near-field region. Wave asymmetry decreases from zero on the incident side, down to the minimum value on the structural crest, and then increases up to positive value in the leeward near-field region of LCS. Finally wave skewness increases and wave asymmetry decreases on the beach behind LCS. The presence of LCS changes waves from pitch-forward to pitch-backward (corresponding to change the sign of wave asymmetry from negative to positive). The wave skewness has minimum value around the seaward end of the crest and maximum value around the leeward end of the crest of LCS. Wave asymmetry has the minimum above the crest and maximum values on the transmission side.

Our analysis on factors affecting the evolution of wave skewness and asymmetry shows that large wave height corresponds to large wave skewness and small wave asymmetry on both sides of LCS. Incident wave shapes have a significant effect on wave asymmetry only on the incident side; the negatively skewed wave has the larger free-stream velocity and average overtopping discharge than the positively skewed wave. Rates of increase of wave skewness and asymmetry above the crest increase with the decrease in the crest width. The variations of wave asymmetries decrease with increasing wave periods. Leeward areas with the effect of the structure increase with an increase in the wave peak period and a decrease in the wave porosity. Maximum wave skewness and asymmetry increase with the increase of

structural freeboard from negative ones to zero, but they subsequently decrease with larger positive freeboards. The randomness in irregular waves has little effect on both wave skewness and asymmetry across LCS.

Bispectral analysis shows that the evolution of wave skewness and asymmetry across the LCS can be mainly attributed to difference and sum frequency interactions. There are both sum interactions and difference interactions in the seaward near-field region of LCS, while the sum interactions dominate on the crest and difference interactions dominate in the leeward near-field region of LCS.

This study provides new insights on the role of wave skewness and asymmetry on the breakwaters stability and sediment transport around the structure and on the beaches behind it.

CHAPTER 5

SPATIAL DISTRIBUTION OF WAVE OVERTOPPING WATER BEHIND COASTAL STRUCTURES

The spatial distribution of wave overtopping water behind the structure sets the restriction to the use of the areas behind the coastal defences and determines the consequent damages. Better understanding of the spatial distribution of wave overtopping water is of key importance to the design of sea defences and the placement of roads, walkways, railways, buildings and other infrastructure, even the safety of people. It helps engineers to establish the extent of the hazardous zones behind the structure when overtopping is anticipated.

The aim of this study is to use the RANS-VOF model to investigate the spatial distributions of random wave overtopping over impermeable coastal structures, paying special attention to the effects of wave conditions, structural geometries, and landward ground level on the spatial distribution

of wave overtopping water. This study compares the calculated landward spatial distribution of wave overtopping water with measurements of CLASH project, by Pullen et al (2008) for vertical wall and Lykke Andersen (2006) for 1:2 dike respectively.

This chapter includes six parts: firstly, a concise literature survey on wave overtopping and its distribution is introduced; it is followed by a description of the numerical model implementation; a comparison of numerical results and measurements is given next; along with a semi-analytical model developed to understand the underlying physics of spatial distribution of overtopping water. Factors affecting spatial distribution of overtopping water over coastal structures are analyzed and finally a brief summary is given.

5.1 Introduction

The complexity involved in the wave interaction with LCB has led the majority of investigators to resort to laboratory experiments and field measurements. For example, a database on wave overtopping consisting of more than 10,000 irregular wave overtopping tests collected from more than 160 independent projects or test series was created in the EU project CLASH by van der Meer et al. (2009). Wave overtopping over breakwaters and sea walls was extensively investigated by Jensen and Sorensen (1979) and Owen (1980) respectively, followed by Troch et al. (2004), Briganti et al. (2005), Cáceres et al. (2005), Pullen et al. (2008), and Franco et al. (2009). The work

was extended to the sea dikes by TAW (2002), Schuttrumpf and van Gent (2003) and Li et al. (2004; 2007). Bruce et al. (2009) established the influence of armour type and configuration on overtopping based on small-scale physical model tests. Recent studies were carried out to investigate the influence of wave obliquity and directional spreading on wave overtopping of rubble mound breakwaters by Lykke Andersen and Burcharth (2009) and combined wave overtopping and storm surge overflow of a levee with a trapezoidal cross section by Hughes and Nadal (2009). On the other hand, numerical modelling of wave overtopping has gained popularity recently. Hu et al. (2000) used the non-linear shallow water equations to study wave overtopping. Liu et al. (1999) applied 2D RANS-VOF model, developed by Lin and Liu (1998), to study wave overtopping over porous structures. This model was employed by Losada et al. (2008), Reeve et al. (2008) and Xiao et al. (2009) for the simulation of wave overtopping. In contrast Shao et al (2006) employed the smoothed particle hydrodynamics (SPH) method to investigate the surface wave overtopping. However, previous study on wave overtopping has mainly focused on the overtopping discharge at the overtopping point (Owen, 1980; Troch et al., 2004; Schüttrumpf and Oumeraci, 2005; Bruce et al., 2009; van der Meer et al., 2009), but there is little work on the spatial distribution of wave overtopping water behind the sea defences.

Jensen and Sorensen (1979) presented some results of spatial distribution of wave overtopping discharges behind a vertical wall and

proposed an empirical equation to fit these results. Within the CLASH project, Bruce et al. (2005) and Pullen et al. (2008) collected the spatial distributed overtopping data from both field and laboratory experiments. A relationship between the spatial distribution data and the distance behind the sea defences was established. Their work was only for the vertical wall in the Samphire Hoe and did not consider the effect of landward ground level. Based on the large scale and small scale experiments on rubble mound breakwaters, Lykke Andersen (2006) Lykke Andersen and Burcharth (2006) and Lykke Andersen et al. (2007) proposed a formula which is a function of wave steepness, incident angle, significant wave height and landward ground level, to predict the landward spatial distribution of overtopping water. These formulae were based on experimental data collected by a limited number of buckets in laboratory experiments, and having limited resolution of the spatial distribution. The effect of structural geometry was also not investigated. EurOtop Manual (EurOtop, 2008) recommended a formula slightly different from that in Andersen and Burcharth (2006) to predict the landward spatial distribution of overtopping water. This formula is only valid for rubble mound structures with a slope of approximately 1:2 and for angles of wave attack between 0 and 45. Currently, there is little data on the spatial distribution of wave overtopping water landward of impermeable coastal structures (Bruce et al., 2005) and as a result there is limited guidance on how to parameterize this process.

5.2 RANS-VOF Model Implementation

5.2.1 Set-up of RANS-VOF model

Prior to the applications of the RANS-VOF model to investigate the spatial distribution of overtopping volume, the model was used to examine the overtopping of a smooth impermeable dike with a 1:6 seaward slope, which has also been investigated previously by Li et al. (2004; 2007), Shao et al. (2006), and Ingram et al. (2009).

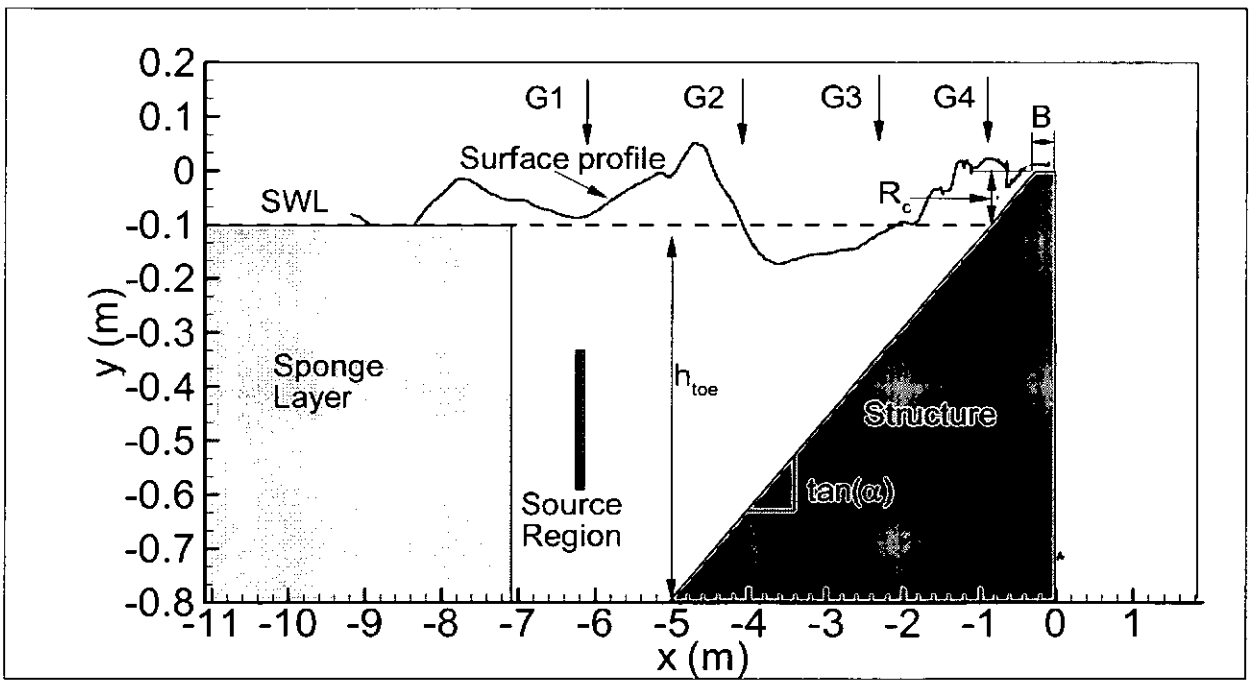

Figure 5.2.1 Sketch of computational domain. G1 to G4 represent the locations of four wave gauges in the experiments; h_{toe} is water depth at the toe of structures; SWL is still water level; R_c, B and tan(α) are the structural freeboard, crest width and seaward slope respectively. The origin of coordinates is at the landward end of structural crest with x for horizontal axis and y for vertical axis.

Figure 5.2.1 shows the setup of numerical simulations. The length of computation domain is 13.0 m × 1.0 m. The geometry of the sea dike includes a seaward slope of 1:6, a crest with a width of 0.3m and a height of 0.8m. An internal wave-maker developed by Lin and Liu (1999) was used to generate regular and irregular waves. The duration of simulations is in excess of 300 s. A radiation boundary, composed of an open boundary and a sponge layer, is specified at the inlet boundary, while a free-slip boundary condition is applied to the solid boundaries. A zero-stress condition is applied at the free surface. Turbulent kinetic energy k and dissipation rate ε are assumed to be a function of distance from the solid surface and have zero gradient at the free surface. h_{toe}=0.7m is water depth at the toe of structures; Rc is the structural freeboard; B is structural crest width; tan(α) is the structural slope; G1 to G4 are surface elevation gauges in the experiments.

5.2.2 Effect of mesh size

The effects of increasing grid resolution on wave induced motions are investigated with three grid levels of 1300×100, 725×85 and 350×40. For grid level of 1300×100, The grid system is uniform with the mesh spacing of Δx_i=0.01 m and Δy_j =0.01 m. For grid level of 725×85, the grid system is non-uniform in both x- and y- directions, presenting a minimum cell size of Δx_i =0.01 m and Δy_j =0.01 m in the vicinity of free surface and coastal structures. For grid level of 350×40, the grid system is non-uniform as well

but the minimum cell size is of Δx_i=0.02 m and Δy_j =0.02 m.

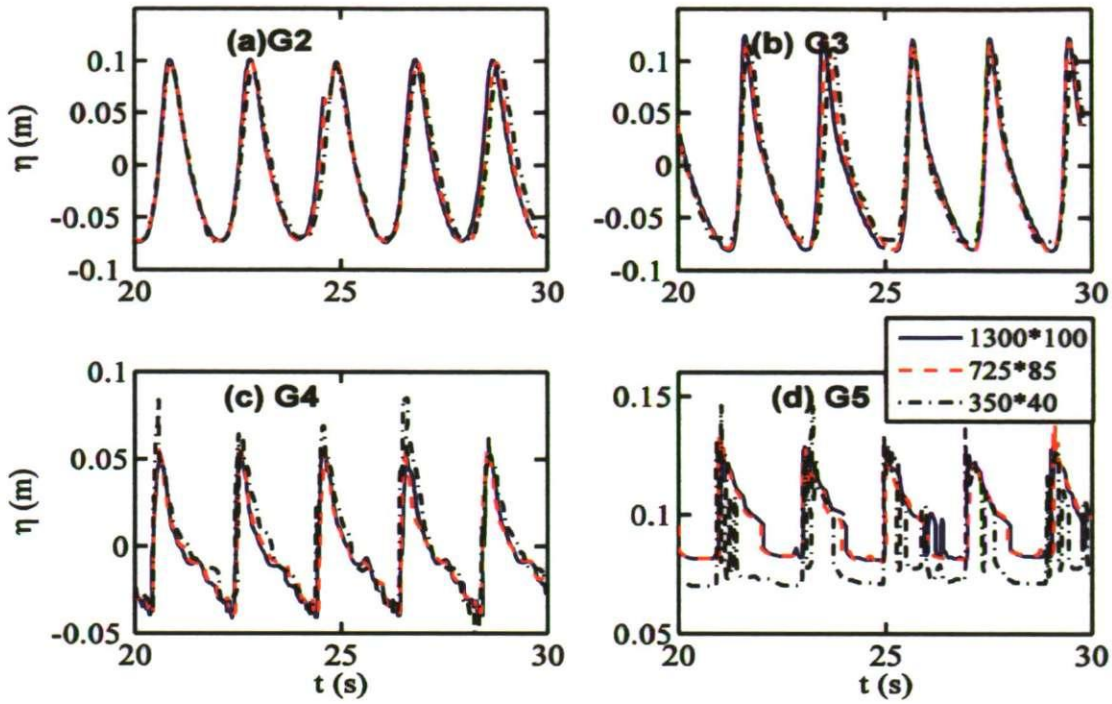

Figure 5.2.2 Effect of mesh size on the predicted surface elevations. H=0.16m, T=2.0s, h=0.7m and R_c=0.1m.

The example of wave overtopping a smooth impermeable dike with a 1:6 seaward slope described by Li et al. (2004) was reinvestigated using the RANS-VOF model. Regular waves with wave height H=0.16 m and wave period T=2.0 s were generated by an internal source region, placed at x=-6.1 m away from the toe of sea dike with a water depth of 0.7 m (Figure 5.2.1). Figure 5.2.2 shows the comparisons of surface elevations between different mesh grid levels. The surface elevation calculated by mesh grid level of

350×40 shows large discrepancy at G4 and G5 from those by other two mesh grid levels, although there is only small underestimation at G2 and G3. This is because the VOF surface capturing scheme with coarse mesh level cannot capture the details of wave breaking, which is the major source of turbulence. It consequently cannot simulate the appropriate turbulence generation and dissipation, leading to incorrect surface elevations. Li et al (2004) also concluded that more detailed physical phenomena of motions can be represented with increased mesh refinement. Since mesh grid levels of 1300×100 and 725×85 has little effect on surface elevations for all wave gauges, a conclusion can be drawn that mesh grid level of 725×85 is fine enough to capture most important processes as other finer grid levels. To save the computational time in the case studies, we next employ the mesh grid level of 725×85 to explore the wave overtopping. Calculation of wave propagation for 300s with cells of 725*85 requires about 30 CPU hours using a single processor of Intel Core 2 CPU 6600 @ 2.4GHz, 2.4GHz.

5.3 Model Validation

5.3.1 Surface elevation

The case of wave overtopping over a 1:6 impermeable dike in Section 5.2.2 can be validated by measurements in Li et al. (2004). Figure 5.3.1 shows that time history of the calculated surface elevation at G2 and G4 are in good agreement with measurements of Li et al (2004), although there is a

discrepancy at G4 between the present model and measured data. This may be due to the 3-D effect of highly nonlinear waves at G4, characterised by a gradual peaking of crests, flattening of troughs and pitching forward to the sea dike.

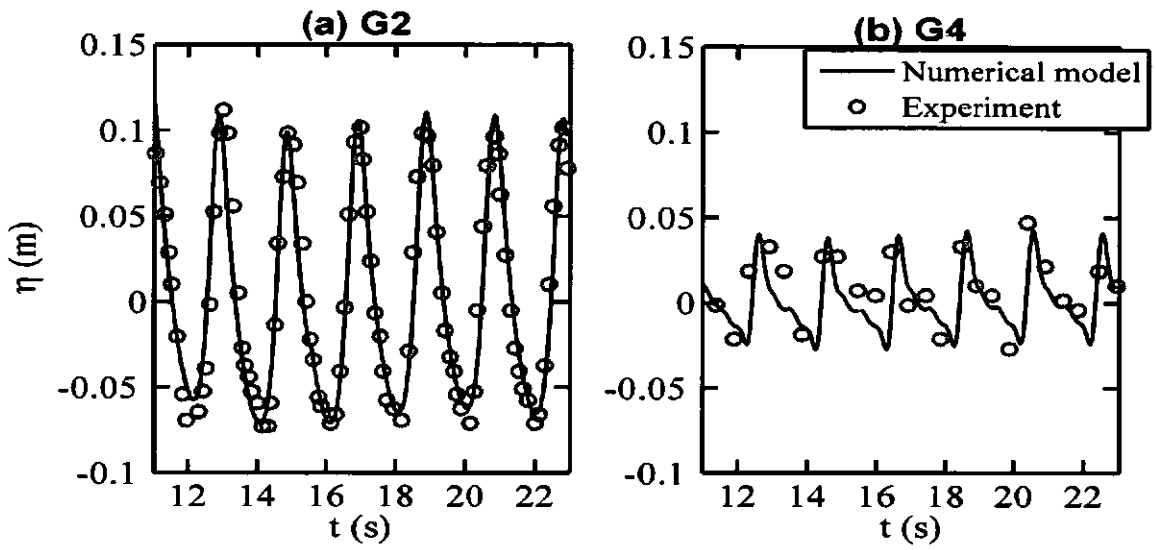

Figure 5.3.1 Calculated surface elevations (solid line) and measured surface elevations of Li et al. (2007) (circles) at (a) G2 and (b) G4. H=0.16m, T=2.0s, h=0.7m and R_c=0.1m.

5.3.2 Average overtopping discharge

Table 5.3.1 lists a total of 35 tests with the different wave conditions and coastal structural geometries used in this study. The outputs of each test case were sampled at 40 Hz for 300-second. There are 3 wave heights, 2 wave periods, 7 structural slopes, 4 relative crest widths, 8 landward ground levels and 3 relative freeboards. Test No. 16 to No. 35 are used to investigate

the effect of the randomness in waves on spatial distribution of overtopping water. All irregular waves are generated through the internal source region using the theory of TMA spectrum (Appendix B).

Table 5.3.1 Overall view of numerical simulations of spatial distribution of overtopping water

Case No.	H_i (m)	T_{pi} (s)	h_{toe} (m)	R_c (m)	B (m)	tan(α)
1	0.14	2.0	0.7	0.1	0.3	1:6
2	0.16	2.0	0.7	0.1	0.3	1:6
3	0.14	1.6	0.7	0.1	0.3	1:6
4	0.16	1.6	0.7	0.1	0.3	1:6
5	0.12	1.6	0.7	0.1	0.3	1:8
6	0.12	1.6	0.7	0.1	0.3	1:4
7	0.12	1.6	0.7	0.1	0.3	1:3
8	0.12	1.6	0.7	0.1	0.3	1:2
9	0.12	1.6	0.7	0.1	0.3	1:1
10	0.12	1.6	0.7	0.1	0.3	Vertical
11	0.16	2.0	0.7	0.15	0.3	1:6
12	0.16	2.0	0.7	0.05	0.3	1:6
13	0.12	1.6	0.7	0.1	0.6	1:6
14	0.12	1.6	0.7	0.1	0.9	1:6
15	0.12	1.6	0.7	0.1	0.0	1:6
16-35	0.12	1.6	0.7	0.1	0.3	1:6

Figure 5.3.2 shows that calculated dimensionless averaged overtopping discharges are in good agreement with the predictions of Equations (A1) and (A3) against the relative freeboards. Calculated dimensionless overtopping discharge is significantly underestimated compared with the predictions for

large relative freeboards. This is probably due to the inability of the model to capture small overtopping volumes, such as spray. Another possible explanation for this underestimation is that the air effect is ignored in the numerical model, since de Waal et al. (1996) and Pullen et al. (2008) found that the increase due to wind is large when the discharge is small and its effect decreases as the discharge increases.

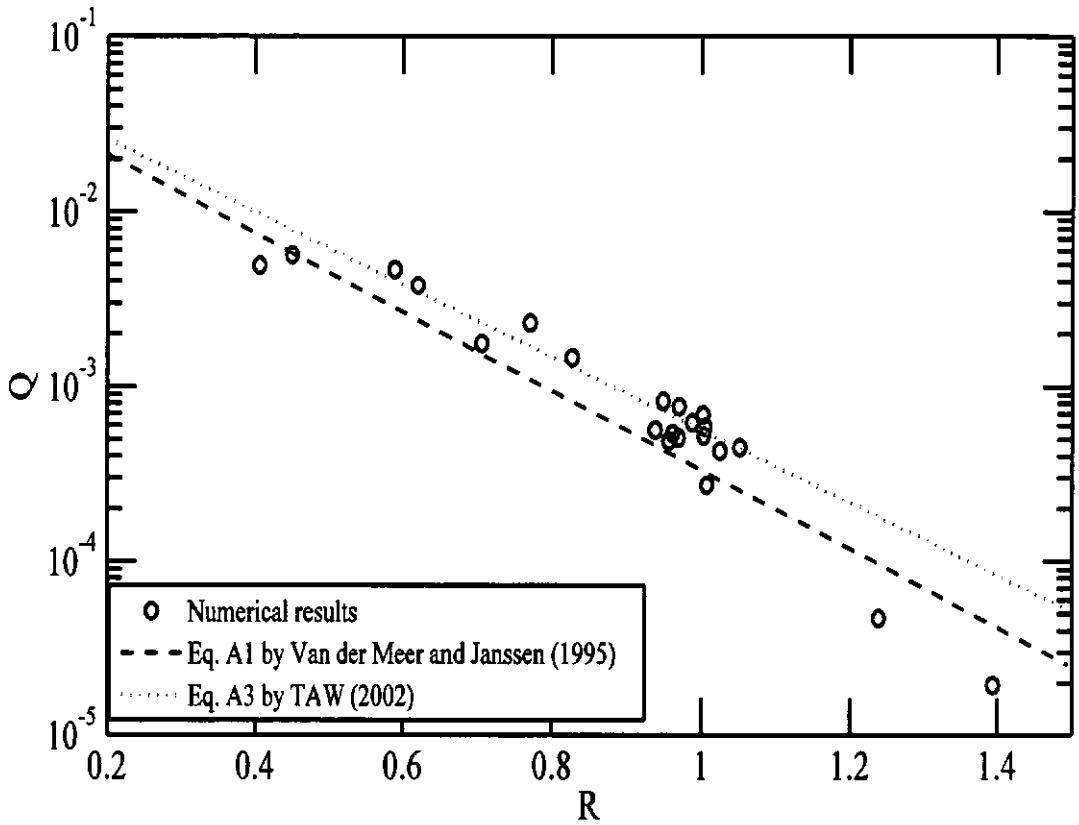

Figure 5.3.2 Comparisons of dimensionless overtopping discharge, $Q=q_{ow}*\sqrt{\tan(\alpha)}/(\xi_p*\sqrt{g*H_s^3})$, against the dimensionless freeboards, $R=R_c/(H_s*\xi_p)$ (ξ_p is surf similarity with the peak period at the toe of structures), between numerical results and empirical formulae.

5.3.3 Landward spatial distribution of overtopping water

Pullen et al (2008) and Lykke Andersen and Burcharth (2006) have measured limited spatial distributions of wave overtopping water for a vertical wall and a sea dike with 1:2 seaward slope. Numerical simulations can provide high resolution results and are much more economical than the associated physical experiments.

As shown in Figure 5.3.3, the proportion of overtopping volume passing the landward location x decays rapidly at first (with distance x from the structure) and then slows with further increase in x away from the structure, so that the bulk of wave overtopping water falls into the area immediately behind the structure. Comparisons of landward spatial distribution of wave overtopping water behind the structure were done for the 1:2 seaward slope case and for a vertical wall, at zero landward ground level. The calculations are in good agreement with the measurements, by Pullen et al (2008) for vertical wall (Figure 5.3.3a) and Lykke Andersen (2006) for the slope of 1:2 (Figure 5.3.3b). The divergence in results for the case with the slope case may be a result of the differing geometry used. Measurements of Lykke Andersen (2006) were for permeable structure with a crest width of 0.17m, and the data was collected in only four chambers; while present work is for impermeable structure with the crest width of 0.3m, and the spatial distribution data of overtopping water has high resolutions.

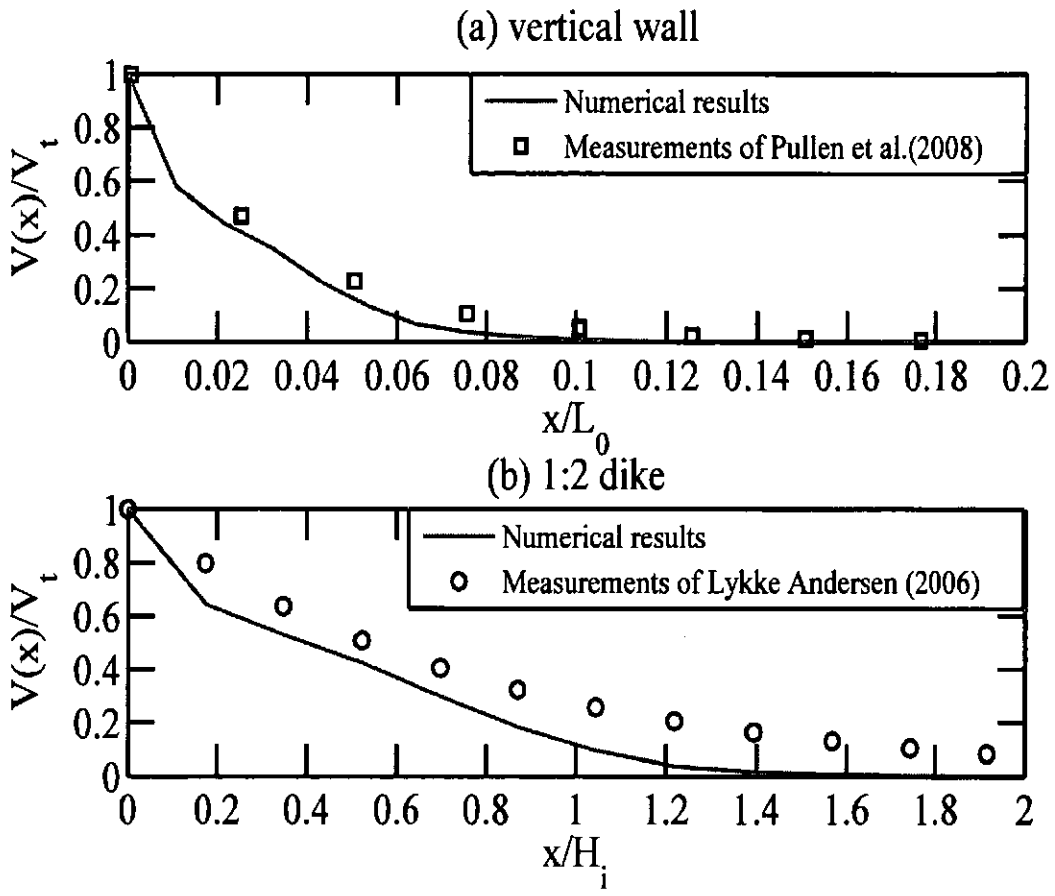

Figure 5.3.3 Comparisons of landward spatial distribution of overtopping water between numerical results and measurements for (a) a vertical wall and (b) a sea dike with the seaward slope of 1:2. $V(x)/V_t$ is the proportion of overtopping volume passing x; V_t is the cumulative overtopping volume; L_0 is deep water wave length with the mean period and H_i is significant wave height at the toe of sea dike; landward ground level h_{meas}=0 for both cases.

5.4 Semi-Analytical Model

It is well known that wave run-up significantly affects the wave overtopping process. For a certain freeboard of coastal structure, the larger the wave run-up height, the larger overtopping volume over the crest is.

Hunt (1959) proposed the following formula for the 2% relative run-up level on impermeable structures:

$$\frac{R_{u2\%}}{H_s} = c_1 * \xi_m \quad for\ \xi_m \le 2.0 \tag{5.4.1}$$

$$\frac{R_{u2\%}}{H_s} = 2.0 * c_1 \quad for\ \xi_m > 2.0 \tag{5.4.2}$$

where c_1=1.5 for irregular wave and 1.0 for regular wave; $R_{u2\%}$ is the run-up that only two percent of the wave run-up values observed will reach or exceed; H_i is significant wave height at the toe of the dike; T_m is mean wave period; $L_0 = gT_m^2/(2\pi)$ is deep water wave length and ξ_m is surf similarity: $\xi_m = \tan(\alpha)/\sqrt{H_i/L_0}$.

It is expected that spatial distribution of wave overtopping water behind the structure is mainly affected by the landward ground level, the horizontal velocity and the layer thickness on the landward end of the dike crest. Schüttrumpf and Oumeraci (2005) derived the general formulae of layer thickness on the dike crest, h_A, at the landward end of the crest (x=0):

$$h_A(x=0) = c_2 * x_Z * (1 - \frac{R_c}{\tan(\alpha) * x_Z}) * \exp(-c_3 \frac{x_C}{B}) \tag{5.4.3}$$

$$x_Z = c_1 * \sqrt{H_i * L_0} \quad if\ \xi_m \le 2.0$$

$$x_Z = c_1 * \frac{2.0 * H_i}{\tan\alpha} \quad if\ \xi_m > 2.0$$

where h_A is the layer thickness on the dike crest; x_Z is horizontal wave run-up length; tan(a) is the structural slope; c_2 =0.168/tana, c_3=0.75 (for irregular wave); g is gravity acceleration.

Schüttrumpf and Oumeraci (2005) found that the variation of the overtopping velocity along the dike crest width is only influenced by bottom friction. The dike crest employed here is relatively short (B=0.30 m) and the surface of the modelled dike was very smooth. Therefore, the velocity changes along the dike crest can be ignored. The horizontal velocity at the landward end of the crest (x=0 m) can be calculated by Equation (10) in Schüttrumpf and Oumeraci (2005):

$$u_{A,50\%} = a_{co} * \frac{\pi * H_i}{T_m} * \sqrt{\frac{R_{u2\%} - R_c}{s_0 * H_i}} \qquad (5.4.4)$$

where a_{co}=0.75; $u_{A,50\%}$ is wave velocity on the structural crest, exceeded by 50% of the incoming waves; $s_0 = \sqrt{H_i / L_0}$ is deep water wave steepness.

The landward trajectory of overtopping water with initial velocity, $u_{A,50\%}$, is treated as free fall and takes the shape of a parabola. The travel distance, $x(y)$, of overtopping water at the elevation of y above the crest is given by:

$$x(y) = u_{A.50\%} * \sqrt{\frac{2(y + h_{meas})}{g - a_{ay}}} + \left(\frac{\partial u_{A.50\%}}{\partial t} - a_{ax} \right) * \frac{y + h_{meas}}{(g - a_{ay})} \quad where\ 0 \le y \le h_A(x = 0) \qquad (5.4.5)$$

where a_{ax} and a_{ay} represent the acceleration induced by the air resistance.

In Equation (5.4.5), assuming the air effect is negligible and the horizontal acceleration of overtopping water is zero, Equation (5.4.5) can be rewritten in a simpler form:

$$x(y) = u_{A,50\%} * \sqrt{\frac{2(y + h_{meas})}{g}} \quad where\ 0 \le y \le h_A(x = 0) \qquad (5.4.6)$$

By dividing the layer thickness on the structural crest, h_A, into 10 units, each unit has the same horizontal velocity and unit height but different elevation y. The proportion of overtopping volume passing landward location x can be calculated from Equations (5.4.3)-(5.4.6).

A case of irregular wave overtopping over a 1:6 sea dike (Case No. 16) was investigated, with H_i=0.12m, T_{pi}=1.6s and the same geometry as shown in Figure 5.2.2. Figure 5.4.1 shows the comparisons of landward spatial distribution of overtopping water between semi-analytical and numerical results and measurements. The semi-analytical landward spatial distribution of overtopping water over a 1:6 dike is in good agreement with the numerical results (Figure 5.4.1a). The general trend of spatial distribution of overtopping water over a 1:2 dike agrees reasonably well with both numerical results and measurements (Figure 5.4.1b). However, the numerical results and measurements tend to spread part of overtopping water into a farther area for both cases. Bearing in mind the assumptions of this semi-analytical model, this is mainly because the velocity used in Equation (5.4.6) is the averaged velocity on the structural crest which 50% of

the incoming waves will exceed. These 50% of waves have larger velocities than $u_{A,50\%}$, consequently, causing the overtopping water to travel farther. Another possible reason is that the significant wave height used in Equations (5.4.3) and (5.4.4), H_i, is approximately the average height of one-third largest waves; therefore, the semi-analytical model ignores the overtopping parts of some individual larger waves, which are able to travel farther.

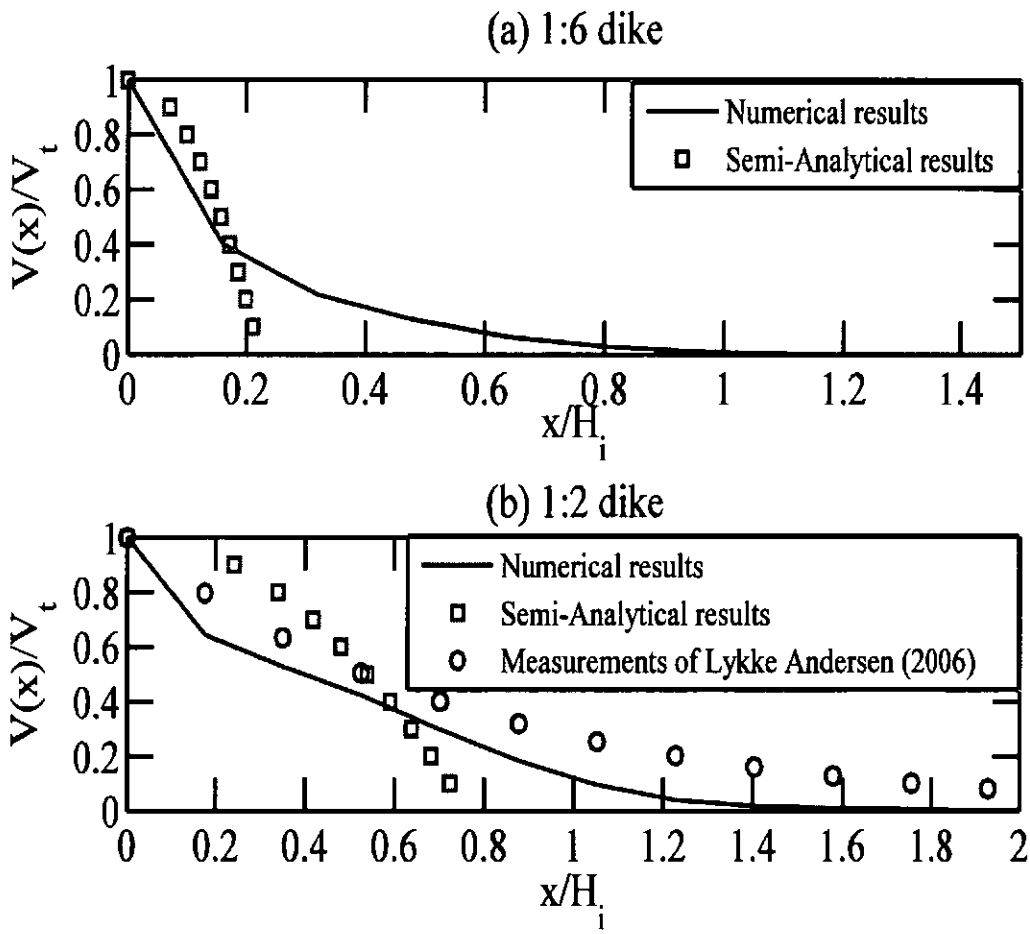

Figure 5.4.1 Comparisons of landward spatial distribution of overtopping water over (a) a 1:6 dike and (b) a 1:2 dike between semi-analytical results, numerical results and measurements. H_i=0.12m.

5.5 Parameter Analysis of Model Results

We will next look at the effects of structural slope, tan(α), incident significant wave height, H_i, mean period of incident wave, T_m, wave randomness, structural relative crest width, B/L_p, structural relative freeboard, R_c/H_i and landward ground level, h_{meas}, on the landward spatial distribution of overtopping water. These parameters were found above to be important in wave overtopping process over coastal structures in the semi-analytical model.

5.5.1 Incident wave condition

It is well known that the relative wave height (wave height divided by water depth) and relative wave length (wave length divided by water depth) are very important to the wave overtopping processes. Large relative height corresponds to large overtopping volume, and larger relative wave length corresponds to a larger phase velocity towards the overtopping point and on the structural crest. The Ursell number, $U_r=H_sL_0^2/h^3$ (H_i is the significant wave height at the toe of structures, L_0 is the deep water wave length with the mean period T_m and h_{toe} is water depth at the toe of structures), can represent the combination effects of wave height and wave length.

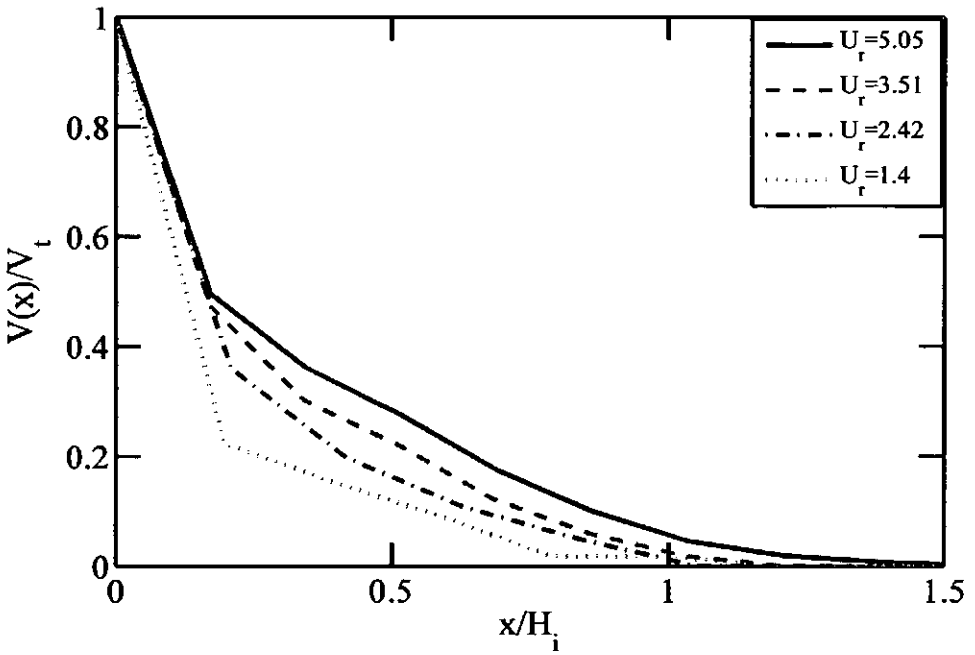

Figure 5.5.1 Effect of Ursell number of incident waves on landward spatial distribution of overtopping water, h_{toe}=0.7m, B=0.3m, $tan(a)$=1:6, R_c=0.1m and h_{meas}=0m.

Figure 5.5.1 shows the influence of Ursell number on landward spatial distribution of wave overtopping water. At the same relative landward distance, the proportion of overtopping water passing x increases with the increasing Ursell number. For small Ursell number, a large part of overtopping water falls into the locations close to the structures, but for large Ursell number it falls into the locations farther away from the structures. It is shown in Figure 5.5.1 that overtopping water mainly falls inside one-quarter of the significant wave height behind the structure for U_r=1.4, while it falls into a larger area, up to one and half significant wave heights behind the structure for U_r=5.05.

5.5.2 Randomness in incident waves

Since random waves are common in real sea states, it is necessary to investigate the effect of wave randomness on the landward spatial distribution of wave overtopping water. The effect of wave randomness was investigated by generating 20 sets of irregular waves, randomly from TMA spectrum with the same significant wave height and peak period at the toe of structures (Case No. 16 to No. 35). The simulation time is 300s, approximately 200 waves. The geometry and boundary conditions are also the same for all these 20 cases.

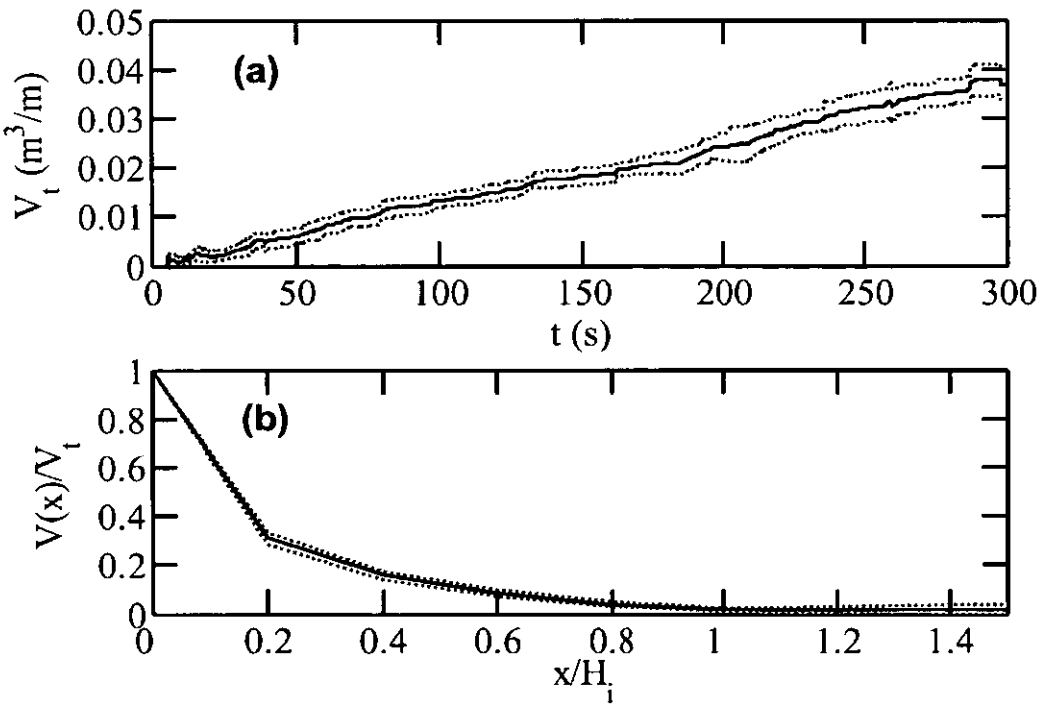

Figure 5.5.2 Effect of wave randomness on (a) cumulative overtopping volume (V_t) and (b) landward spatial distribution of overtopping water. Solid line represents the expected value and the dashed lines show the 95% confidence levels of the expected value. H_i=0.12m, T_{pi}=1.6s, h_{toe}=0.7m, R_c=0.1m, B=0.3m and h_{meas}=0m.

Figure 5.5.2 shows the effect of randomness on cumulative overtopping volume and landward spatial distribution of overtopping water for the first 200 waves. The maximum standard deviation is 0.004 (expected value μ=0.037) for the cumulative volume, and is 0.04 (expected value μ=0.31) for the proportion of overtopping water passing x. Therefore, the effect of wave randomness on the overtopping discharge and landward spatial distribution is not significant, although the effect of randomness on cumulative overtopping volume is larger than on landward spatial distribution of overtopping water. A conclusion could be drawn that spatial distribution of wave overtopping is mainly dependent on the parameters of peak wave components (e.g. H_i and T_{pi}).

5.5.3 Seaward slope of the structure

Types of breaking waves, such as spilling, plunging, collapsing and surging, occur on the coast depending on the surf similarity, consisting of incident wave steepness and bottom slope (Battjes, 1974). Wave energy reflected from the coast is also dependent on the surf similarity. Therefore, seaward structural slopes associate with wave reflection coefficients, wave breakers and wave run-ups on the seaward slopes. An investigation of the effect of structural slopes on landward spatial distribution of wave overtopping water will be presented next.

Seven cases with structural slopes of 1:8, 1:6, 1:4, 1:3, 1:2, 1:1 and a

vertical wall are examined respectively. All cases (Case No. 5 to No. 10 and No. 16) have the same generated waves from an internal wave maker and the same freeboards. As shown in the Figure 5.5.3, the proportion of wave overtopping volume passing x increases as the structural slope increases from 1:8 to 1:3, but it decreases as the slope increases further from 1:3 to a vertical wall. All the proportion of wave overtopping water decreases exponentially with distance x away from the structure.

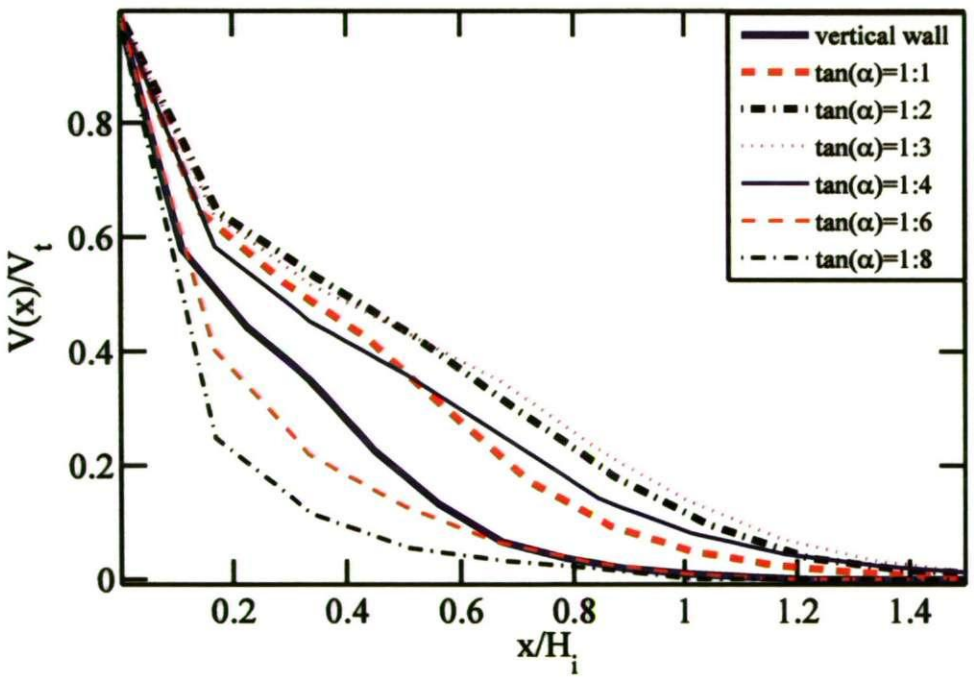

Figure 5.5.3 Effect of structural seaward slope, tan(α), on the landward spatial distribution of overtopping water. H_i=0.12m, T_{pi}=1.6s, h_{toe}=0.7m, R_c=0.1m, B=0.3m and h_{meas}=0m.

The effect of structural seaward slopes on spatial distribution of overtopping water is not monotonic and can be explained as following: For

milder slope, wave breaker is likely to be a spilling or plunging breaker and wave reflection coefficient is small. The wave loses more energy to breaking but has less wave energy reflected. For steeper slope, wave tends not to break, or has a surging breaker; wave reflection coefficient is large, and standing waves can also be formed. Wave energy is mainly reflected and has less wave energy dissipated due to wave breaking. The combination of wave breaking and reflection on the seaward slopes affects the horizontal velocity and layer thickness on the crest, which are key parameters for the landward spatial distribution shown in Equation (5.4.6). For example, the case with the slope of 1:8 has much energy dissipated due to wave breaking, and the case with the slope of 1:3 has little energy dissipated due to wave breaking and little energy reflected by structures, therefore, the sum of kinetic energy and potential energy on the crest of the latter case is larger than that of the former case. Wave overtopping water of the case with the slope of 1:3, therefore, travels farther than the case with the slope of 1:8. This is consistent with the conclusion in Sunamura and Okazaki (1996) that the reflection coefficient increases as the breaker type changes from spilling to collapsing through plunging, corresponding to increasing the structural slopes.

5.5.4 Relative crest width of the structure

The relative crest width of the structure, defined as the ratio of the crest width, B, to the deep water wave length, L_p, is significant to the layer

thickness and velocity on the structural crest (Schüttrumpf and Oumeraci, 2005). Therefore, it can be expected that the landward spatial distribution of overtopping water is dependent on the relative crest width based on semi-analytical model.

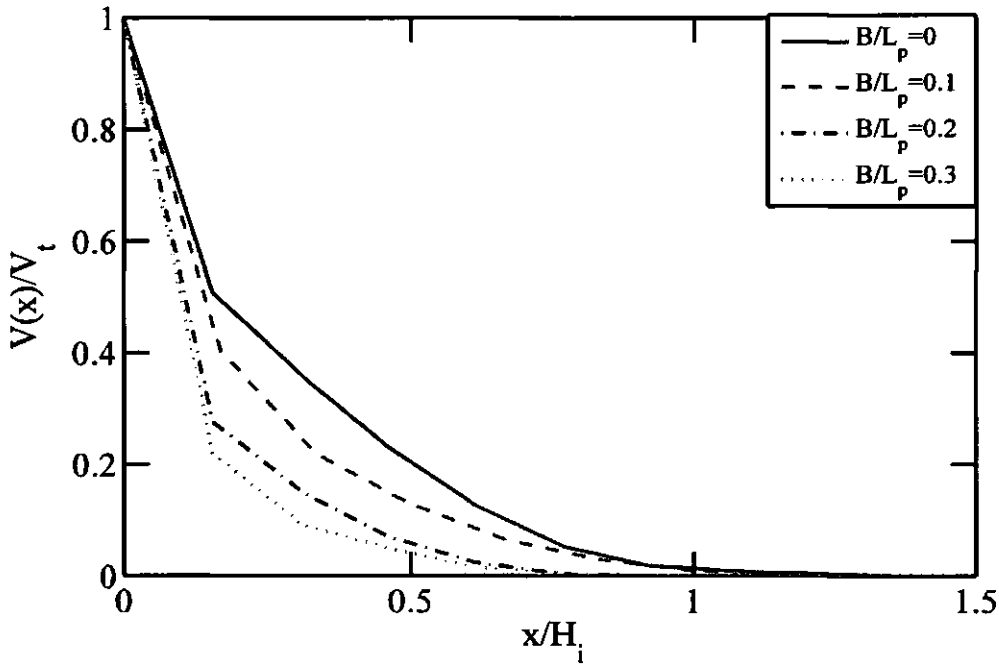

Figure 5.5.4 Effect of the relative structural crest width, B/L_p, on the landward spatial distribution of overtopping water. H_i=0.12m, T_{pi}=1.6s, h_{toe}=0.7m, $tan(a)$=1:6, R_c=0.1m and h_{meas}=0m.

Figure 5.5.4 shows the spatial distribution of wave overtopping water against relative landward distance, x/H_i. With the same incident wave conditions (H_i=0.12m, T_{pi}=1.6s) and the same geometry, the proportion of wave overtopping volume passing x increases significantly as decreasing the relative crest width from 0.3 to 0. This is because large relative crest width

leads to large deductions of velocity and layer thickness on the structural crest due to the friction and the deformation of the overtopping tongue at the crest of the dike (Schüttrumpf and Oumeraci, 2005). The larger the relative crest width, the more significant the effect of friction and the deformation of the overtopping tongue is. Therefore, for the same velocity and layer thickness on the seaward end of structural crest (x=-B), large relative crest width corresponds to a smaller velocity and less layer thickness on the landward end of structural crest (x=0m). Small velocity and layer thickness result in small travel distance of overtopping water.

5.5.5 Relative freeboard of the structure

Structural freeboard relative to significant wave height at the toe of structures, R_c/H_i, is significant to the velocity and layer thickness on the structural crest, according to Equation (5.4.3) and Equation (5.4.4).

Figure 5.5.5 shows that the effect of relative structural freeboards on landward spatial distribution of wave overtopping water is significant. For a certain landward location, the proportion of wave overtopping volume passing x decreases as increasing relative structural freeboards. For example, the majority of overtopping water travels about one significant wave height away from structures for relative freeboard of 0.94, but it travels farther behind structures, up to 1.6 times the significant wave height for a relative freeboard of 0.32. This is mainly due to the horizontal velocity on the crown

crest. Due to the gravity effect, large relative freeboard requires more potential energy to overtop the crest; therefore, the kinetic energy will decrease. Small kinetic energy corresponds to small horizontal velocity on the crown crest. Therefore, large relative freeboard leads to small travel distance of overtopping water.

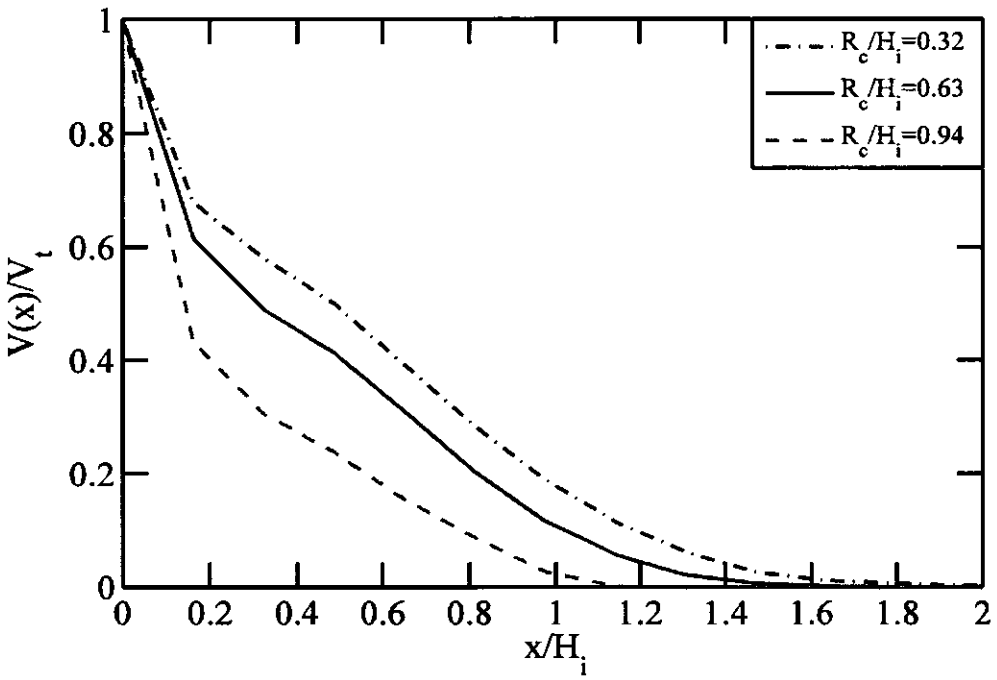

Figure 5.5.5 Effect of relative structural freeboard, R_c/H_i, on landward spatial distribution of overtopping water. H_i=0.16m, T_{pi}=2.0s, h_{toe}=0.7m, h_{meas}=0m, B=0.3m and tan(α)=1:6.

5.5.6 Landward ground level

It can be expected that the spatial distribution of overtopping water depends on the landward ground level, h_{meas}. As discussed in Section 5.4, the trajectory of overtopping volume is in a parabolic type, therefore, we can

estimate that if the overtopping volume is dropped into $x=\sqrt{\frac{2(y+0)}{g}}$ m at h_{meas}=0m, then it will fall into $x=\sqrt{\frac{2(y+0.1)}{g}}$ at h_{meas}=0.1m instead (Figure 2.3.5). Figure 5.5.6 shows the effect of landward ground level on landward spatial distribution of overtopping water as a function of relative landward distance.

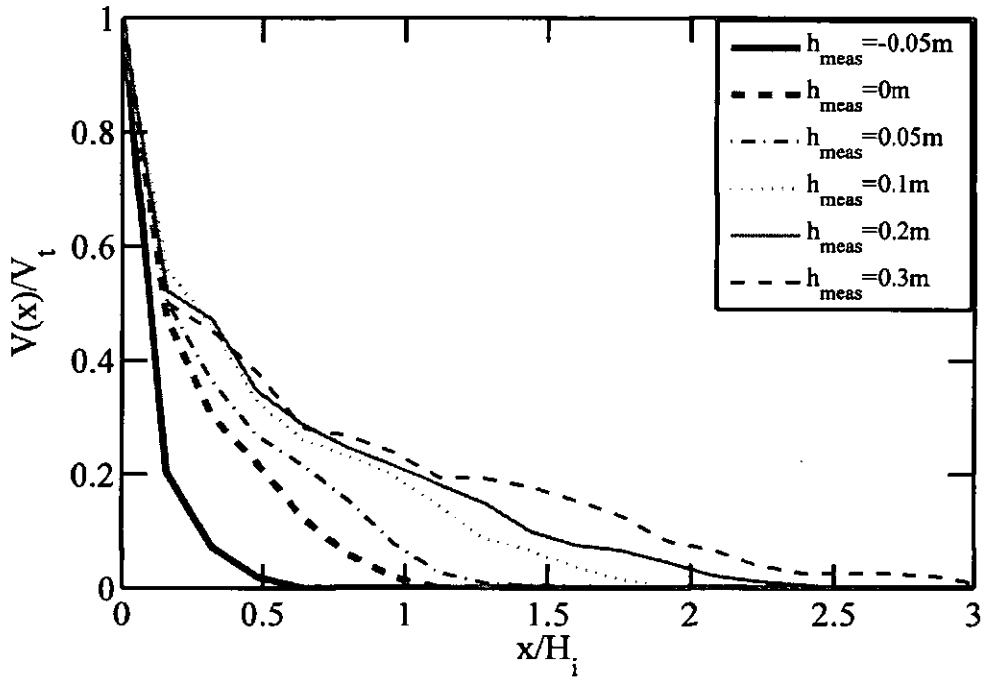

Figure 5.5.6 Effect of landward ground level, h_{meas}, on the landward spatial distribution of wave overtopping water. H_i=0.12m, T_{pi}=1.6s, h_{toe}=0.7m, R_c=0.1m, tan(α)=1:6 and B=0.3m.

It is interesting to observe that for the same wave conditions and structural geometry, spatial distribution of wave overtopping water is strongly dependent on h_{meas}. The proportion of wave overtopping volume

passing x increases with increasing the landward ground level, h_{meas}. The overtopping water even reaches to a distance up to three times bigger than significant wave height for h_{meas}=0.3 m, while it only splashes down in the area of half the significant wave height from structures for h_{meas}=-0.05 m. However, our results show the overestimation in the proportion of wave overtopping water falling into the area with x slightly bigger than zero, comparing with the predictions by Lykke Andersen (2006). This is mainly due to the small overtopping discharge for this case, similar to a nappe (in hydro-engineering refers to the sheet of water over-topping) clinging to the landward face of the weir with very low water heads. It can be expected that the proportion of wave overtopping water falling into the area immediately behind the structure decreases with increasing the overtopping discharge, such as decrease relative freeboard (Figure 5.5.5).

5.6 Summary

Spatial distribution of irregular wave overtopping water behind impermeable coastal structures was investigated using the RANS-VOF model. We have demonstrated that the calculated average overtopping discharges agree well with predictions by Van der Meer and Janssen (1995) and TAW (2002). Calculated landward spatial distributions of wave overtopping water are in good agreements with the measurements by Pullen et al (2008) for a vertical wall and Lykke Andersen (2006) for a dike with the slope of 1:2. The

proportion of wave overtopping water decreases exponentially with the distance away from the structure, corresponding to the bulk of wave overtopping water falling into areas immediately behind the structure.

A semi-analytical model was derived to extract the governing parameters involving the spatial distribution of wave overtopping water behind coastal structures. This semi-analytical model related the landward spatial distribution of wave overtopping water to the landward ground level, the velocity and layer thickness on the crest. The semi-analytical landward spatial distribution of overtopping water agrees reasonably well with both numerical results and measurements. Parameter analysis found that negatively skewed waves have the larger cumulative overtopping volume and average overtopping discharge than positively skewed waves. For the same incident wave conditions, the proportion of wave overtopping volume passing a location increases with increasing structural slope from 1:8 to 1:3, but it decreases with increasing the slope from 1:3 to vertical wall. The proportion of wave overtopping water passing a location increases with increasing Ursell number of incident waves and the landward ground level, but decreases with increasing relative structural freeboard and the relative crest width. The effect of wave randomness is negligible on both cumulative overtopping volume and landward spatial distribution of wave overtopping water.

CHAPTER 6

CONCLUSIONS AND FUTURE WORK

6.1 Conclusions

6.1.1 Main findings

This PhD work has successfully investigated the transformation of wave shapes over Low-Crested Structures (LCS) and the spatial distribution of the overtopping water behind coastal structures, by employing the improved 2D RANS-VOF model and state-of-the-art experimental datasets.

The first part of this work presents the results of an investigation of the transformation of wave skewness and asymmetry as waves propagate over low-crested breakwaters, (LCBs), based on an analysis of measurements collected in the DELOS project. The local Ursell number, calculated by mean period rather than peak period, is identified as a key parameter affecting wave skewness and asymmetry around LCS. This work then established a set of empirical formulae using least squares regression for both smooth and

rubble mound LCBs, relating wave skewness and asymmetry to local Ursell number. Predicted wave skewness and asymmetry are in good agreement with measurements. Further study shows that wave skewness on both sides of LCBs is linearly correlated for rubble mound LCBs but weakly correlated for smooth LCBs. Wave asymmetry on both sides of LCBs has a weakly quadratic correlation. The effect of the relative freeboard on the relationships of wave asymmetries between both sides is significant for rubble mound LCBs, but the same does not hold for smooth LCBs.

RANS-VOF model is firstly introduced to investigate wave skewness and asymmetry over over Low-Crested Structures. Numerical results are in good agreement with laboratory measurements collected in the small scale wave channel tests at the University of Cantabria (UCA) and the predictions made by the empirical formulae derived in this thesis. In the presence of LCS, positive wave skewness decreases in the seaward near-field region and increases rapidly up to the maximum on the structural crest. It then decreases dramatically in the leeward near-field region. Negative wave asymmetry decreases in the seaward near-field region, down to the minimum value on the structural crest, and then increases up to positive value in the leeward near-field region of LCS.

The Bispectral Analysis in this work helps us understand that wave nonlinear interactions, including sum interaction and difference interaction, strongly contribute to wave skewness and asymmetry. That is, sum interaction contributes positively to wave skewness but negatively to wave

asymmetry, while difference interaction negatively contributes to wave skewness but positively contributes to wave asymmetry. The underlying physics of large variations of wave shapes in the vicinity of coastal structures is that: both sum interactions and difference interactions are significant in the seaward near-field region, while the sum interactions dominate on the structural crest but difference interactions dominate in the leeward near-field region of LCS.

Parameter analysis shows that larger wave heights correspond to greater wave skewness and smaller wave asymmetry on both sides of LCS. Incident wave shapes have a significant effect on wave skewness and asymmetry but only on the incident side. Rates of increasing wave skewness and asymmetry above the crest increase with decreasing structural crest width. The variations of wave asymmetries above structures decrease with increasing wave periods. The extent of the effect of structures, however, increases with an increasing wave peak period and a decreasing structural porosity. Maximum wave skewness and asymmetry increase with the increase of structural freeboard from negative values to zero, but they subsequently decrease with larger positive freeboards. The randomness in irregular waves has an insignificant effect on both wave skewness and asymmetry across LCS.

The second part of this work presents results of the spatial distribution of the overtopping water behind impermeable coastal structures, using the RANS-VOF model. Calculated average overtopping discharges agree well with

predictions by Van der Meer and Janssen (1995) and TAW (2002). The calculated spatial distributions of wave overtopping water behind the structure are in good agreement with the measurements by Pullen et al (2008) for a vertical wall and Lykke Andersen and Burcharth (2006) for a 1:2 seaward slope of the dike. A semi-analytical model, relating the landward spatial distribution of wave overtopping water to the landward ground level, and the velocity and layer thickness on the crest, was derived. The semi-analytical landward spatial distribution of overtopping water agrees reasonably well with both numerical results and experimental measurements. This finding can lead researchers to target these parameters and produce more detailed guidelines for protecting the properties that are sheltered by coastal structures in the future.

Parameter analysis shows that for the same incident wave conditions, the proportion of wave overtopping water passing a landward location increases initially with the increase in the seaward slope of the structure from 1:8 to 1:3, but it subsequently decreases with steeper slopes (from 1:3 to vertical). The proportion of wave overtopping water passing a location increases with Ursell number of the incident waves and landward ground level, but decreases with increasing relative structural freeboard and structural crest width. The effect of wave randomness is negligible on landward spatial distribution of wave overtopping water.

6.1.2 Recommendations

The local Ursell number, known as a measure of wave nonlinearity, is identified as a key parameter affecting wave skewness and asymmetry around LCS. The flow depth and flow velocities at the leeward end of structural crests, as well as the landward ground levels, are also proved to be governing parameters of landward spatial distribution of wave overtopping,

The derived empirical formulae, which relate wave skewness and wave asymmetry to local wave conditions, provide effective ways to predict wave skewness and asymmetry directly and accurately. The predicted wave skewness and asymmetry can be subsequently incorporated into analytic or numerical models of sediment transport. The semi-analytical model of the landward spatial distribution of overtopping water also provides a useful means to approximately estimate the spatial distribution of overtopping water behind coastal structures, before running high-cost experiments or complex numerical simulations. This estimation can offer a general concept of spatial distribution of overtopping water and will give an idea of the ranges of hazard zones expected in a specific setup.

The sequence of random waves with typical parameters, such as significant wave height and peak period, has no significant effect on the transformation of wave skewness and asymmetry over LCS and on the landward spatial distribution of overtopping water over an impermeable structure. This finding will give engineers more confidence when using

significant wave height and peak period only to investigate the transformation of random wave shapes and random wave overtopping.

As mentioned in the introduction, wave skewness and wave asymmetry are directly related to sediment transport. The proportion of wave overtopping water passing a certain landward location can also be used to define the location and area of hazardous zones behind the structure for the scenarios when overtopping is anticipated. As a result, controlling the wave asymmetries is an effective means of controlling the net sediment transport, and controlling the proportion of the overtopping water passing a certain landward location helps to reduce the extent of the hazardous zones behind the structure. The findings of this study along with the economic considerations can be used to propose guidelines for future practical engineering applications.

- Building a toe berm or a shallow foreshore in front of the structure can reduce incident wave heights and peak periods by forcing wave breaking. This will result in smaller wave skewness and asymmetry, wave overtopping discharge and the size of the hazardous area behind the defences.

- Using a relatively small positive freeboard and a relatively small structural crest in addition to a large structural porosity, could cause smaller wave skewness and asymmetry, as well as smaller extent of the effect of structures.

- Adopting a large relative crest and freeboard, and a high ground level

for placing landward properties, as well as trying to avoid seaward slopes of 1:2 and 1:3. This could cause a small proportion of the overtopping water passing a certain landward location and a smaller hazardous area behind the defences.

6.2 Future Work

More experimental data for wave transformation over coastal structures and landward spatial distribution of wave overtopping water is needed to enhance our understanding and verify the main findings of the present work.

The present 2D RANS-VOF model simulates both the turbulence field and mean flow field very well in the whole domain except at the breaking point. This is due to the fact that gravity-wave breaking is essentially a three-dimensional process and the k-ε turbulence model always overestimates the turbulence level around the breaking point (Lin and Liu, 1998). At the same time, this model ignores the air effect above the free surface and as a result, the trapped air bubbles inside the water and splashes in the air are not fully treated. Also, the velocities and pressure at the free surface need to be linearly extrapolated. These approximations are one of the possible causes for the discrepancy between numerical results and measurements in the present work. Therefore, more work should be done in the improvements of the numerical model. These improvements may consist of taking account of the air effect and considering the 3D effect in wave breaking and overtopping, as well as employing a dynamic Sub-Grid-Scale (SGS) turbulence model

which helps to capture the wave-induced small-scale turbulent flows.

The present study shows that the local effect of LCS on the transformation of wave shapes is significant. However, only a qualitative analysis on variations of wave shape has been done so far. A quantitative analysis on the extent of the effect of structures on variations of wave shape will be needed for practical applications in the future.

The future work should also cover the impact and redistribution of overtopping water after touching the landward ground. It is expected that the impact of the overtopping water on the landward ground level and the redistribution of overtopping water are of importance to landward scour research and the landward drainage scheme. In addition, the spatial distribution of wave overtopping water over a permeable coastal structure, which is more common in the practical applications, still needs to be addressed.

APPENDIX A

EMPIRICAL FORMULAE FOR OVERTOPPING DISCHARGE

A combination of storm surge and large waves may cause overtopping of such structures like breakwaters, dikes, seawalls, etc., leading to damage to and flooding of the area behind the structure. Overtopping is defined as the water volume passing over the crest of structures per unit length in a unit time. The average discharge, q, has the unit of $m^3/m/s$.

A1 Formulae of Van der Meer and Janssen (1995)

Another commonly used formula for calculating wave overtopping discharge is derived by Van der Meer and Janssen (1995).

For breaking waves (plunging): $\xi_p<2$

$$\frac{q}{\sqrt{g*H_s^3}} = \frac{0.06}{\sqrt{\tan\alpha}} * \xi_p * \exp(-5.2 * \frac{R_c}{\xi_p * H_s * \gamma_r * \gamma_b * \gamma_h * \gamma_\beta}) \qquad \text{(A1)}$$

For non-breaking waves (surging): $\xi_p>2$

$$\frac{q}{\sqrt{g*H_s^3}} = 0.2*\exp(-2.6*\frac{R_c}{H_s*\gamma_r*\gamma_b*\gamma_h*\gamma_\beta}) \quad \text{(A2)}$$

Where α is the slope of the front face of the structure, R_c is the structural freeboard, H_s significant wave height ($=H_{1/3}$) at the toe of the slope and L_{op} being the deep water wave length $gT^2_p/(2\pi)$. $\xi_p = \frac{\tan\alpha}{\sqrt{H_s/L_{op}}}$. The coefficients γ_b, γ_h, γ_r, and γ_β are introduced to take into account the influence of a berm, shallow foreshore, roughness and oblique wave attach. All these coefficients are 1.0 in present work.

A2 Formulae of TAW (2002)

(EurOtop, 2007) recommends the formulae to probability design and prediction proposed by TAW (2002) for breaking and non-breaking waves ($\xi_{m-1,0}<5$):

$$\frac{q}{\sqrt{g*H_{m0}^3}} = \frac{0.067}{\sqrt{\tan\alpha}}*\gamma_b*\xi_{m-1,0}*\exp(-4.75*\frac{R_c}{\xi_{m-1.0}*H_{m0}*\gamma_b*\gamma_f*\gamma_\beta*\gamma_v}) \quad \text{(A3)}$$

With a maximum of: $\frac{q}{\sqrt{g*H_{m0}^3}} = 0.2*\exp(-2.6*\frac{R_c}{H_{m0}*\gamma_f*\gamma_\beta})$

The formulae to deterministic design and prediction:

$$\frac{q}{\sqrt{g*H_{m0}^3}} = \frac{0.067}{\sqrt{\tan\alpha}}*\gamma_b*\xi_{m-1,0}*\exp(-4.3*\frac{R_c}{\xi_{m-1.0}*H_{m0}*\gamma_b*\gamma_f*\gamma_\beta*\gamma_v}) \quad \text{(A4)}$$

With a maximum of: $\frac{q}{\sqrt{g*H_{m0}^3}} = 0.2*\exp(-2.3*\frac{R_c}{H_{m0}*\gamma_f*\gamma_\beta})$

Where α is the slope of the front face of the structure, R_c is the structural freeboard, H_{m0} is the energy spectrum based significant wave height at the toe of the slope and $T_{m-1,0}$ being the mean energy wave period, $L_{m-1,0}=gT^2_{m-1,0}/(2\pi)$. $\xi_{m-1.0} = \frac{\tan\alpha}{\sqrt{H_{m0}/L_{m-1.0}}}$. The coefficients γ_b, γ_f, γ_β, and γ_v are introduced to take into acount the influence of a berm, permeability and roughness of or on the slope, oblique wave attach and a vertical wall on the slope respectively. All these coefficients are 1.0 in present work.

APPENDIX B

TMA SPECTRUM

TMA spectrum is developed to incorporate finite depth effects into the JONSWAP spectrum. Bouws et al. (1985) apply the transformation factor, $\Phi(\omega_h)$, derived by Kitaigorodskii et al. (1975), to the JONSWAP spectrum and present the TMA spectrum as $S(\omega)=S_0(\omega)^* \Phi(\omega_h)$, where $S_0(\omega)$ is the JONSWAP spectrum and $\omega_h = 2\pi f\sqrt{h/g}$

The transformation factor, $\Phi(\omega_h)$ is calculated as following (Kitaigorodskii et al., 1975):

$$\phi(\omega_h) = \left[\frac{k(\omega,h)^{-3} \frac{\partial}{\partial\omega} k(\omega,h)}{k(\omega,\infty)^{-3} \frac{\partial}{\partial\omega} k(\omega,\infty)} \right]_{\omega_h=\omega\sqrt{h/g}} \qquad \text{(B1)}$$

The JONSWAP spectrum, described in Hasselmann et al., (1973), can be expressed in following form:

$$S_0(\omega) = \frac{\alpha g^2}{\omega^5} \exp(-1.25\left(\frac{\omega_p}{\omega}\right)^4)\gamma^{-(\omega-\omega_p)^2/(2\sigma^2\omega_p^2)} \qquad \text{(B2)}$$

Wave data collected during the JONSWAP experiment were used to determine the values for the constants in Equation (B2):

$$\gamma=3.3;\ \alpha = 0.076\left(\frac{U_{10}^2}{Fg}\right)^{0.22};\quad \omega_p = 22\left(\frac{g^2}{U_{10}F}\right)^{1/3};\quad \sigma = \begin{cases} 0.07 & \omega \le \omega_p \\ 0.09 & \omega > \omega_p \end{cases}$$

where F is the distance from a lee shore, called the fetch, or the distance over which the wind blows with constant velocity. U_{10} is the mean wind speed at 10 meters above the sea water level. These two constants were modified to generate the target significant wave height and peak period.

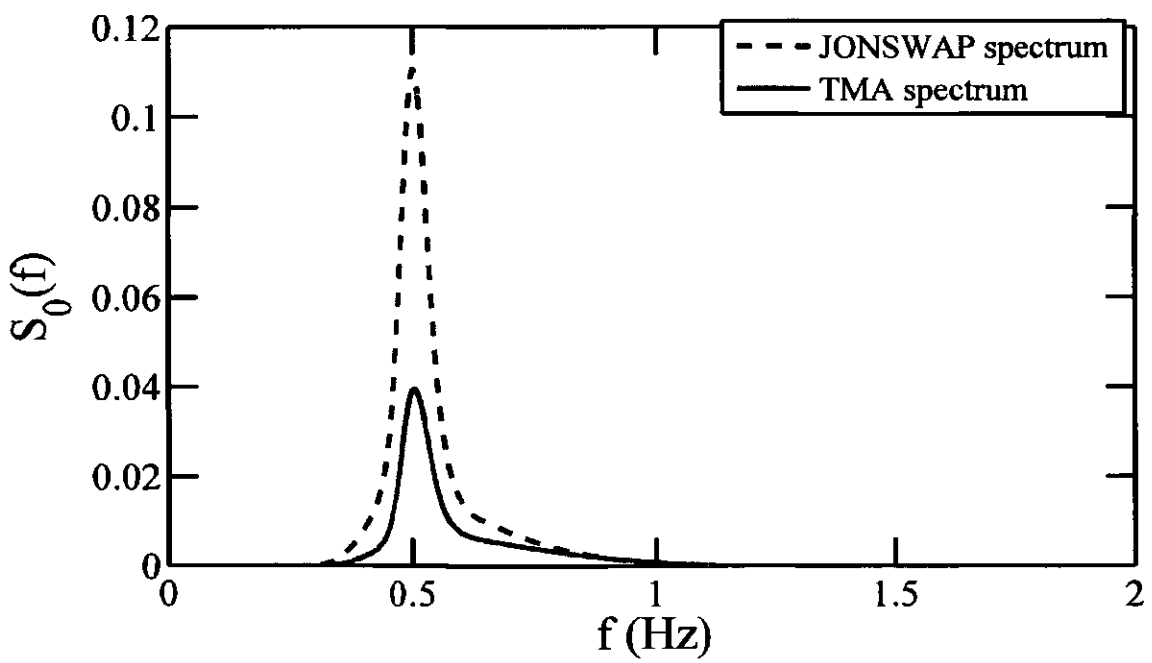

Figure B1 JONSWAP spectrum and TMA spectrum for H_s=0.16m, T_p=2.0s, h=0.7m and U_{10}=10m/s, F=3.3km.

Figure B1 is an example of a TMA spectrum which indicates clearly the effect of water depth of the magnitude as well as the shape of the JONSWAP spectrum.

When the time series or TMA spectrum of irregular waves are available, the Fast Fourier Transformation (FFT) is then employed to obtain the angular frequency, ω_i, the amplitude, a_i, and the phase, P_{si}, of the wave components, which is necessary for internal source functions (see equation (2.2.36))

For time series,

$$\omega_i = \frac{i * f_s * \pi}{n} \tag{B3}$$

$$a_i = \frac{|FFT(\eta(t))_i|}{N} \tag{B4}$$

$$P_{si} = \arctan\left(\frac{imag\left[FFT(\eta(t))_i\right]}{real\left[FFT(\eta(t))_i\right]}\right) \tag{B5}$$

Where $\eta(t)$ is the time series data, f_s is the sampling frequency of $\eta(t)$, N is the number of points in time series, n is the number of points of FFT, and i is the frequency line number, or array index, of the FFT of $\eta(t)$.

For TMA spectrum, the amplitude vector of i-th target wave component, a_i is:

$$a_i = \sqrt{2 * S(\omega_i) * \Delta\omega_i} \qquad \text{(B6)}$$

where $\Delta\omega_i$ is the frequency interval and the phase vector, ω_i is the vector used in generating TMA spectrum (Equations (B1) and (B2)), P_{si}, can be generated randomly.

APPENDIX C

BISPECTRAL ANALYSIS

C1 Descriptions

The digital complex bispectral estimate $B(f_1, f_2)$ for discretely sampled data can be interpreted in terms of Fourier coefficients, (Haubrich, 1965; Kim and Powers, 1978), as

$$B(f_1, f_2) = E[A(f_1)A(f_2)A^*(f_3)] \qquad \text{(C1)}$$

where $E[\ ]$ denotes an expected value, $A(f)$ denotes a complex Fourier coefficient, while the asterisk represents a complex conjugate. f_i (i=1, 2, 3) are wave frequencies and conventionally $f_3=f_1+f_2$. For example, if $B(0.59, 0.59)=0.5$, this indicates a self-self interaction at frequency $f=0.59$ coupling to energy at frequency $f=1.18$ Hz.

In the work of Kim and Powers (1978), the normalized magnitude of the bispectrum was used to define the bicoherence, b.

$$b^2(f_1,f_2)=\frac{|B(f_1,f_2)|^2}{E[|A_{f1}A_{f2}|^2]E[|A_{f_1+f_2}|^2]} \quad \text{(C2)}$$

Elgar and Guza (1985) concluded that the bicoherence does represent the relative degree of phase coupling between triads of waves. For example, with b=1 for full coupling, and b=0 for random phase relationships. Significant peaks in bicoherence identify two frequencies of the three in an interacting triad contributing significant energy to the time series.

Hasselman et al. (1963) and Elgar and Guza (1985) indicated that the mean cube or third moments of a stationary random time series, denoted here by $\eta(t)$, can be related to the integral of the parts of the bispectrum if f_1 is greater than f_2. For example, wave skewness, S, can be expressed as

$$S=\frac{\sum\sum\Re\{B(f_1,f_2)\}}{E(\eta(t)^2)^{3/2}} \quad \text{(C3)}$$

Similarly, wave asymmetry, A, was defined as the integral of the imaginary part of the bispectrum (Elgar and Guza, 1985)

$$A=\frac{\sum\sum\Im\{B(f_1,f_2)\}}{E(\eta(t)^2)^{3/2}} \quad \text{(C4)}$$

Where $\Im\{\}$ and $\Re\{\}$ denote the imaginary and real parts of the bispectrum respectively.

C2 Benchmark of Bispectral Analysis

To check the validity of bispectral analysis code and the sign of skewness and asymmetry, the pitch-backward saw-tooth (steep rear faces and gently sloping front faces, but crests and troughs of equal amplitudes) waves are used, see Figure C1.

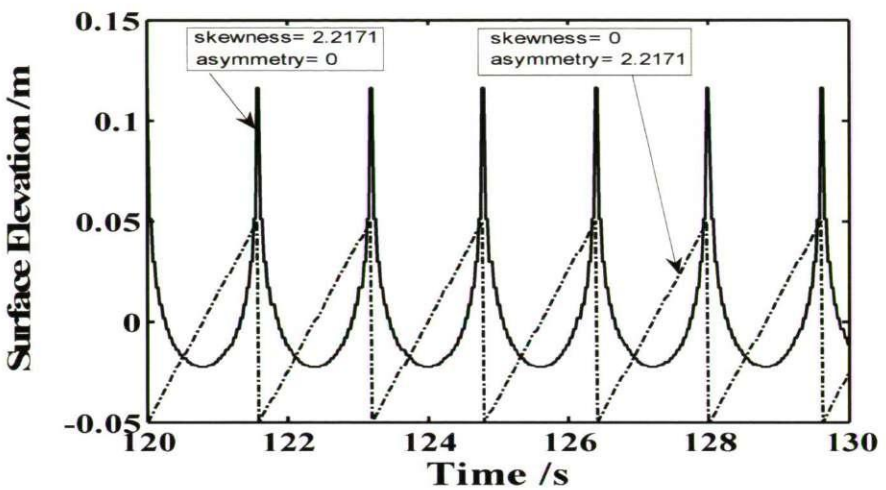

Figure C1 Surface elevations of a saw-tooth wave (dashed line, Skewness=0, Asymmetry=2.2171) and its Hilbert transform (solid line, Skewness=2.2171, Asymmetry=0).

While a 'stokes wave' shape (broad, low troughs and narrow, tall crests but symmetric front and back faces) has zero asymmetry and positive skewness. The different wave shape and characteristics come from the 90 degree phase difference, which also reflect the phase relationship between the primary frequency and the phase-locked harmonics, although they have identical power spectra.

The Higher-Order Spectral Analysis (*HOSA*) code was employed in this study, with 1024-point Fourier Transform, 512-point hanning window and 50% overlap. The sample frequency of data is 40 Hz. Data is 800 seconds long. The real part of bispectrum is zero and the image part of bispectral is positive, and the sum value is 2.2171, see Figure C2. It is easy to find that the primary frequency f1 is 0.625 Hz, and the peaks of image part of bispectrum are (f_1, f_1), ($2f_1$, f_1), ($3f_1$, f_1), ($4f_1$, f_1), ($2f_1$, $2f_1$), ($2f_1+f_1$, $2f_1$). The results above show that this HOSA code can describe the bispectrum efficiently.

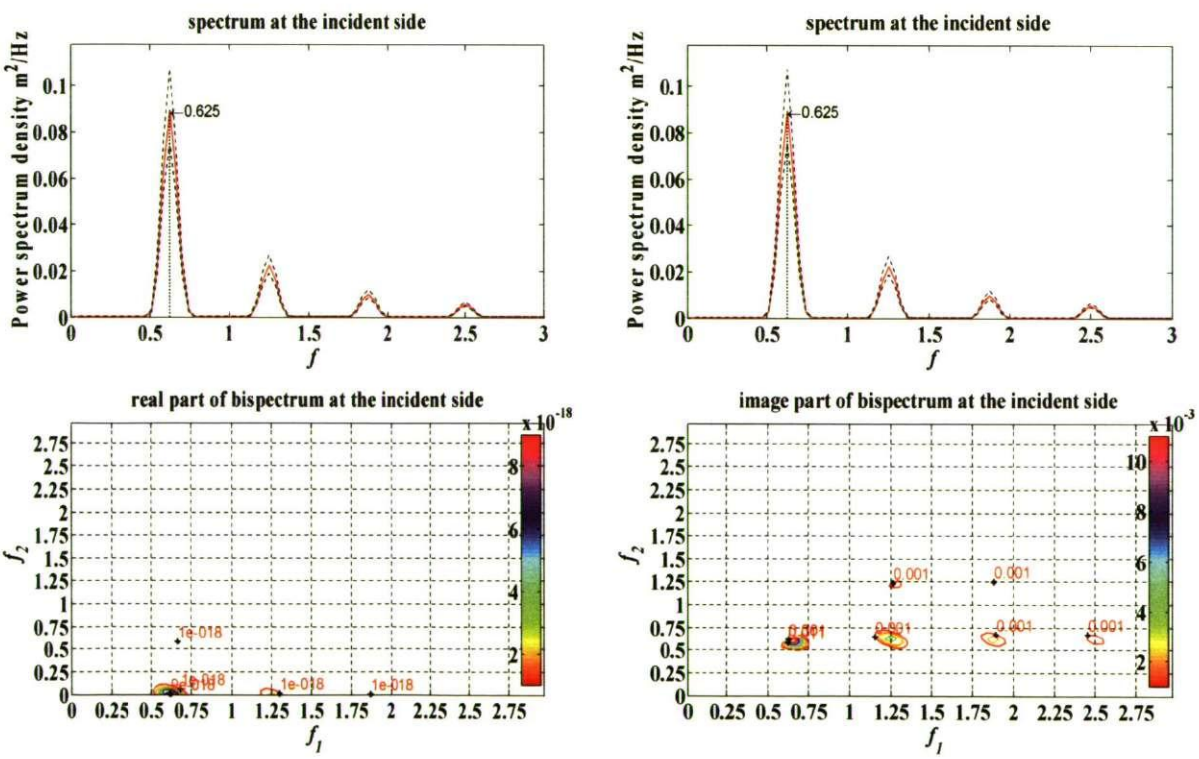

Figure C2 Bispectrum of pitch-backward saw-tooth time series. Left panel is the real part of bispectrum, while right panel is the image part of bispectrum

APPENDIX D

EXPERIMENTS

D1 Two-Dimensional Wave Transmission Tests

Two-dimensional wave transmission tests were conducted in the small-scale channel flume at University of Cantabria, Spain (Figure D1), within the EU-funded DELOS project. Detailed descriptions about this project can be found in Kramer *et al.* (2005) and DELOS website (http://www.delos.unibo.it/). The wave and current flume is 24 m long, 0.60 m wide and 0.80 m high. The piston–type wave-maker has two attached free surface wave gauges integrated in an Activc Wave Absorption System (AWACS ®) that allows the absorption of reflected waves from the model. The wave-maker and the rear absorbing beach occupy 4 m at one of the ends of the flume.

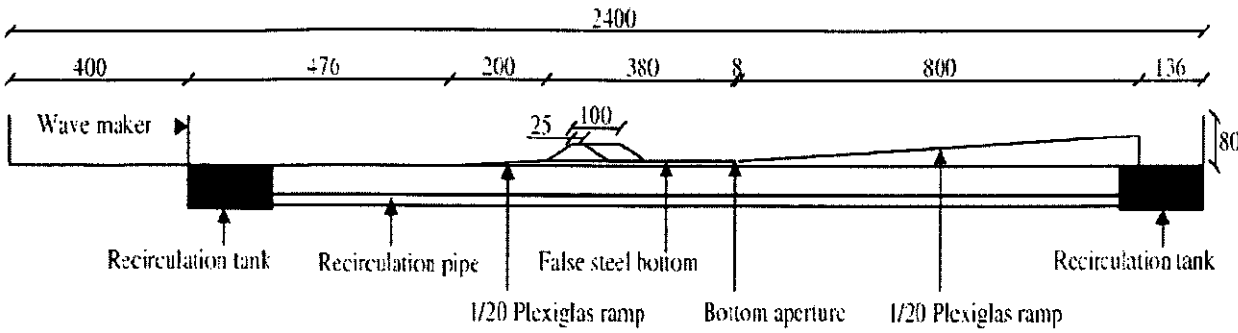

Figure D1 Experimental set-up (Kramer et al., 2005). Distances in centimetres

The low crested structure model was built over a 3.8-m long stainless steel horizontal false bottom. In the frontal foot of the rubble, a Plexiglas ramp with 1V / 20 H slope connected the false bottom with the bottom of the flume. Two rubble-mound low-crested structures of 0.25 and 1.00 m crest width were tested. Crest elevation from the bottom (0.25 m), front and back slope angles (1V/2H) and rubble characteristics were maintained constant for both structures. The models had two-layer armour of selected gravel and a gravel core. The core characteristics are D_{n50}=0.031 m, porosity =0.49 and Armour characteristics are D_{n50}=0.046 m, porosity =0.53. A final dissipative beach with 1/20 slope was made of quarry rock with D_{n50}=0.015 m and porosity=0.43.

The data used for the present study were measured by 11 resistive free surface gauges to assess free surface evolution. Gauges G1 to G3 are installed in front of LCS. Gauges G4 to G5 are located above the seaward slope of LCS. Gauge 6 is above the crest and Gauge 7 is on the leeside slope

for 1.00 m crest width, while both gauges G6 and G7 are placed on the transmission side for 0.25 m crest width instead. Gauges G8 to G11 were placed on the transmission side along the flat bottom behind the LCS. The detailed coordinates of gauges are shown in Figure 4.2.1. Each record was sampled at 30*Hz*. The rubble mound LCS were tested for three different water depths of 0.3 m, 0.35 m and 0.4 m, corresponding to three different freeboards (-0.05 m, 0 m and 0.05 m). There are three incident wave heights (0.04 m, 0.07 m and 0.10 m) and three wave periods (1.6 s, 2.4 s and 3.2 s). Table D1 presents a summary of the relevant small-scale channel tests (only G1 and G8 are shown). Experimental set-up and test conditions were described in further detail in Kramer et al. (2005).

Table D1 Summary of the relevant small-scale channel tests

Test No.	Test set-up					Gauge G1						Gauge 8					
	B (m)	Duration (s)	H_i (m)	T_{pi} (s)	h (m)	H_s(m)	T_p(s)	T_{mean}(s)	Ur	S	A	H_s(m)	T_p(s)	T_{mean}(s)	U_r	S	A
50	0.25	480	0.1	1.6	0.4	0.09	1.53	1.13	14.39	0.41	-0.05	0.05	1.55	0.94	10.39	0.08	0.16
116	0.25	480	0.1	1.6	0.35	0.09	1.63	1.11	16.10	0.47	-0.15	0.03	1.61	0.92	7.06	0.07	0.26
223	1	800 (reg)	0.1	1.6	0.4	0.08	1.60	1.56	18.02	0.33	-0.12	0.03	1.60	0.83	1.91	0.03	0.54
255	1	480	0.04	1.6	0.4	0.03	1.59	1.11	5.93	0.12	-0.03	0.02	1.59	0.73	3.97	0.03	0.07
260	1	480	0.07	1.6	0.4	0.06	1.55	1.11	10.11	0.21	-0.08	0.03	1.57	0.70	5.83	0.03	0.09
264	1	480	0.1	1.6	0.4	0.08	1.59	1.14	14.63	0.35	-0.03	0.03	1.52	0.75	6.08	0.03	0.29
268	1	720	0.04	2.4	0.4	0.03	2.20	1.43	10.92	0.15	-0.03	0.02	2.28	0.85	8.28	0.06	0.13
272	1	720	0.07	2.4	0.4	0.05	2.28	1.39	21.42	0.23	-0.06	0.02	2.35	0.78	13.97	0.34	0.34
276	1	720	0.1	2.4	0.4	0.08	2.24	1.39	28.57	0.33	-0.06	0.03	2.35	0.87	16.85	0.73	0.31
280	1	960	0.04	3.2	0.4	0.03	3.10	1.66	20.24	0.24	-0.08	0.02	3.18	1.02	15.84	0.75	0.00
284	1	960	0.07	3.2	0.4	0.07	3.10	1.60	52.80	0.52	-0.14	0.03	3.10	1.05	33.39	1.35	-0.36
289	1	960	0.1	3.2	0.4	0.07	3.10	1.59	53.01	0.52	-0.14	0.03	3.18	1.07	34.59	1.34	-0.38
320	1	480	0.04	1.6	0.35	0.03	1.63	1.07	13.42	0.12	-0.04	0.03	1.64	1.55	17.28	-0.07	0.02
323	1	480	0.07	1.6	0.35	0.06	1.63	1.10	24.59	0.26	-0.05	0.04	1.63	1.39	23.25	-0.05	0.27
326	1	480	0.1	1.6	0.35	0.09	1.64	1.10	33.86	0.47	-0.15	0.01	11.38	1.09	223.23	-0.07	0.17
329	1	720	0.04	2.4	0.35	0.03	2.35	1.45	28.03	0.12	-0.05	0.03	2.35	2.12	33.88	0.04	0.08
332	1	720	0.07	2.4	0.35	0.06	2.40	1.43	53.04	0.21	-0.04	0.02	2.48	1.83	24.89	0.54	0.25
335	1	720	0.1	2.4	0.35	0.08	2.40	1.40	74.39	0.30	0.01	0.01	2.48	1.34	15.11	1.38	0.42
338	1	960	0.04	3.2	0.35	0.03	2.58	1.60	28.52	0.27	-0.03	0.02	3.25	2.68	61.94	0.18	0.04
342	1	960	0.07	3.2	0.35	0.05	2.58	1.56	53.26	0.47	-0.05	0.02	3.25	1.81	46.00	1.12	-0.12
346	1	960	0.1	3.2	0.35	0.07	2.58	1.51	77.05	0.63	-0.07	0.01	3.33	1.31	35.31	1.85	-0.38
365	1	480	0.04	1.6	0.3	0.03	1.61	1.02	12.72	0.14	-0.04	0.02	1.61	1.45	11.53	0.01	0.06
367	1	480	0.07	1.6	0.3	0.06	1.61	1.03	21.48	0.34	-0.11	0.04	1.61	1.62	20.01	0.13	0.01
369	1	480	0.1	1.6	0.3	0.09	1.63	1.07	32.94	0.47	-0.26	0.07	1.63	1.82	41.61	0.15	-0.08
371	1	720	0.04	2.4	0.3	0.03	2.20	1.42	24.48	0.06	0.03	0.02	2.48	1.97	34.20	-0.02	-0.06
373	1	720	0.07	2.4	0.3	0.06	2.40	1.40	52.23	0.16	0.07	0.05	2.48	2.12	66.72	-0.01	-0.16
375	1	720	0.1	2.4	0.3	0.08	2.40	1.40	76.30	0.33	0.10	0.07	2.48	2.34	100.37	0.00	-0.25
377	1	960	0.04	3.2	0.3	0.03	2.58	1.55	28.14	0.18	0.06	0.03	3.18	2.48	60.15	0.03	-0.12
379	1	960	0.07	3.2	0.3	0.05	2.58	1.51	50.59	0.38	0.07	0.04	3.18	2.61	105.65	0.00	-0.23
381	1	960	0.1	3.2	0.3	0.07	2.58	1.45	76.46	0.57	0.03	0.07	3.25	2.85	175.73	0.03	-0.41

D2 Wave Basin Transmission Tests

Data was obtained from oblique three-dimensional wave transmission tests in the multidirectional wave basin (18.0 m × 12.0 m × 1.0 m) at Aalborg University, Denmark), within the EU-funded DELOS project. Detailed descriptions about this project can be found in Wang (2003), Kramer *et al.* (2005) and DELOS website (http://www.delos.unibo.it/).

A smooth mound Low-Crested Breakwater, and a rubble mound Low-Crested Breakwater, were tested. The cross-section and layouts of smooth and rubble mound LCS including positions of gauges are given in Figure D2. The rubble mound structure was 25 cm high with a crest width of 10 cm and it was built of quarry rock. The cross-section consisted of a bottom layer, a core and an outer armour layer with the detailed characteristics: W_{50}=0.269 kg, D_{n50}=0.0466m and a grading of D_{85}/D_{15}=1.25, see the cross-section scheme at the top and left hand-side of Figure D2. The smooth structure had gentler slopes than the rubble mound structure, which is also the case in reality. The seaward slope was 1:3 and the leeward slope 1:2. The structure height was 0.30m and the crest width 0.20m. The structures were placed on a horizontal plateau, which was 0.16m higher than the bottom of the basin. This created a larger depth in front of the wave generator and made it possible to generate very steep and breaking waves in front of the structure, see Figure D3. Reflection from the rear wall of the basin was minimised using 1:5 rubble beach.

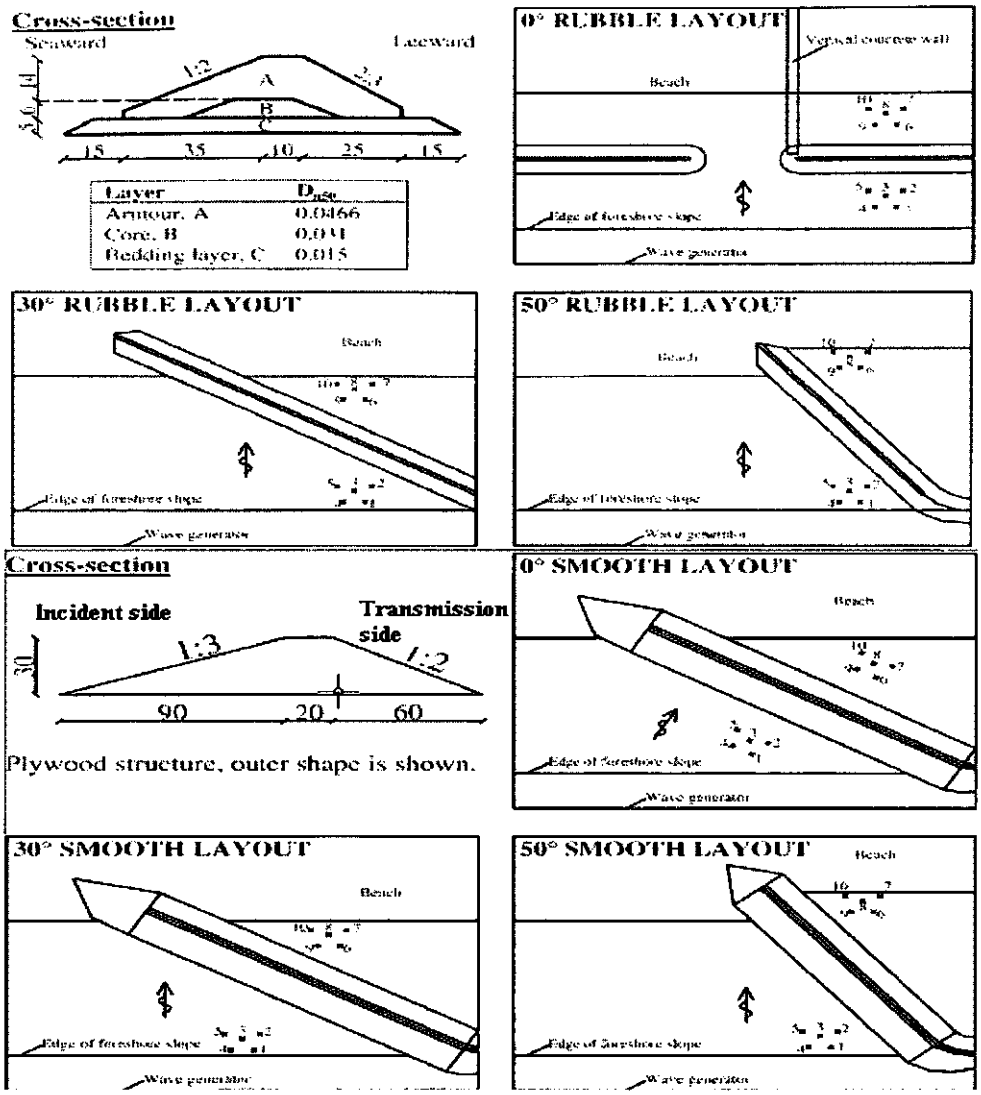

Figure D2 Cross-section and layouts of rubble mound and smooth LCS including positions of gauges, 'x' marks the position of wave gauges (Kramer et al., 2005).

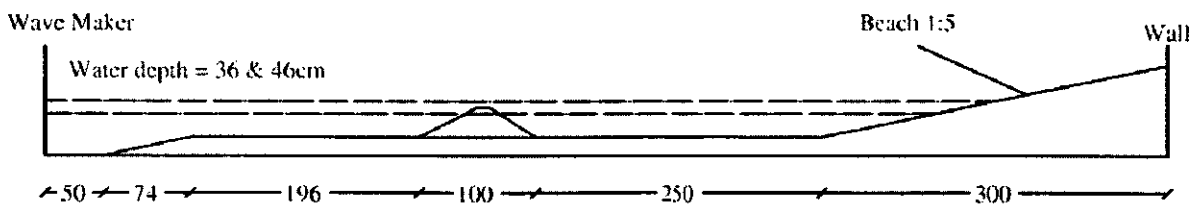

Figure D3 Bottom topography for 0° rubble mound layout (Kramer et al., 2005). Units in cm

The target irregular 3D waves were generated using the directional

spectrum, $S(\omega)$, which describes the distribution of the wave energy in both the spatial and frequency domains. $S(\omega)$ is expressed as a product of the unidirectional wave spectrum $S_0(\omega)$ (described in equation (B2)) and a spreading function $D(\theta,\omega)$, that is, $S(\theta,\omega) = S_0(\omega) * D(\theta,\omega)$.

D(θ,f) is the spreading function that characterises the distribution of wave energy in wave propagation directions from 0 to 2π. Even though the wave energy can be distributed in different direction, the total energy in wave field should remain constant. It is defined by $\int_0^{2\pi} D(\theta, f)d\theta = 1$. The Cosine-power or $\cos^{2s}$ spreading function is as following (Mitsuyasu et al., 1975):

$$D(\theta, f) = \frac{2^{2s'-1}}{\pi} \frac{\Gamma^2(s'+1)}{\Gamma(2s'+1)} \cos^{2s'}\left[\frac{\theta-\theta_0}{2}\right] \qquad \text{(D1)}$$

where θ = wave propagation angle, θ_0 =main wave propagation direction, Γ=Gamma function, s' is a function of wave frequency. In experiments, a constant value of s'=50 was used in 3D wave generation.

Layouts of breakwaters with 0°, 30° and 50° relative to the wave generator were used to cover a large range of wave incident angles. Table D2 and Table D3 presents a summary of 168 wave basin transmission tests over a smooth LCS and rubble mound LCS respectively (only G2 and G7 are shown). Each record was sampled at 40Hz and was 90-second long. The observations were measured from ten fixed gauges, five of them located on the incident side and other five gauges located on the transmission side of LCS (Figure D2).

Table D2 Wave basin transmission tests on Smooth LCS

	Test set-up					Gauge 2						Gauge 7					
Test No.	Layout	R_c (m)	h (m)	H_i (m)	T_{pi} (s)	H_s (m)	T_p (s)	T_{mean} (s)	U_r	S	A	H_s (m)	T_p (s)	T_{mean} (s)	U_r	S	A
1	0	0	0.3	0.08	1.6	0.09	1.53	1.37	15.08	0.66	-0.07	0.05	1.58	1.05	3.30	0.02	0.38
2	0	0	0.3	0.11	1.88	0.13	2.05	1.43	23.93	0.99	-0.45	0.06	1.90	1.17	6.76	0.31	0.55
3	0	0	0.3	0.14	2.12	0.17	2.18	1.48	33.35	0.83	-0.76	0.07	2.05	1.31	10.43	0.61	0.44
4	0	0	0.3	0.08	1.13	0.07	1.16	1.09	6.03	0.34	0.03	0.03	1.19	0.76	0.79	0.04	-0.08
5	0	0	0.3	0.11	1.33	0.10	1.31	1.19	11.13	0.64	-0.01	0.04	1.35	0.89	1.94	0.03	0.13
6	0	0	0.3	0.14	1.5	0.13	1.53	1.23	16.56	0.87	-0.11	0.06	1.55	1.03	4.15	0.24	0.31
7	0	0	0.3	0.14	2.12	0.17	2.18	1.54	36.70	0.74	-0.80	0.08	2.05	1.23	12.53	0.53	0.59
8	0	0	0.3	0.14	1.5	0.14	1.53	1.25	17.42	0.97	-0.15	0.07	1.58	1.07	5.15	0.22	0.43
9	0	0.05	0.25	0.07	1.5	0.09	1.48	1.28	19.28	0.69	-0.06	0.03	1.51	0.84	1.81	-0.14	0.11
10	0	0.05	0.25	0.09	1.7	0.11	1.58	1.31	23.77	0.97	-0.18	0.04	1.65	1.01	3.75	0.04	0.47
11	0	0.05	0.25	0.11	1.88	0.13	2.18	1.40	32.30	0.96	-0.45	0.05	1.77	1.11	5.95	0.22	0.60
12	0	0.05	0.25	0.07	1.06	0.06	1.09	1.04	7.78	0.29	-0.02	0.02	1.11	0.62	0.36	0.09	-0.06
13	0	0.05	0.25	0.09	1.2	0.09	1.37	1.14	13.21	0.53	0.00	0.02	1.26	0.71	0.96	0.01	-0.04
14	0	0.05	0.25	0.11	1.33	0.11	1.37	1.14	16.39	0.75	-0.10	0.03	1.42	0.84	1.96	0.00	0.12
15	0	-0.05	0.35	0.09	1.7	0.12	1.65	1.46	15.71	0.68	-0.12	0.07	1.71	1.07	4.54	0.26	0.46
16	0	-0.05	0.35	0.13	2.04	0.18	2.01	1.57	28.66	0.87	-0.49	0.09	1.97	1.20	8.53	0.72	0.41
17	0	-0.05	0.35	0.17	2.33	0.21	2.23	1.62	36.91	0.88	-0.72	0.09	2.23	1.39	12.23	0.89	0.08
18	0	-0.05	0.35	0.09	1.2	0.09	1.30	1.15	6.40	0.37	0.05	0.06	1.30	0.84	1.37	0.09	0.12
19	0	-0.05	0.35	0.13	1.44	0.14	1.40	1.26	12.80	0.72	-0.01	0.07	1.55	1.00	3.09	0.36	0.34
20	0	-0.05	0.35	0.17	1.65	0.18	1.55	1.30	18.51	0.93	-0.24	0.10	1.60	1.12	6.44	0.59	0.32
21	30	0	0.3	0.08	1.6	0.10	1.42	1.29	13.81	0.60	-0.04	0.04	1.51	0.90	2.54	0.00	0.31
22	30	0	0.3	0.11	1.88	0.13	1.55	1.34	20.08	0.76	-0.42	0.05	1.77	1.05	4.49	0.29	0.56
23	30	0	0.3	0.11	1.88	0.14	1.93	1.41	24.02	0.78	-0.42	0.04	1.77	1.02	3.68	0.17	0.54
24	30	0	0.3	0.11	1.88	0.13	1.65	1.35	21.01	0.94	-0.39	0.05	1.83	1.11	5.41	0.34	0.55
25	30	0	0.3	0.14	2.12	0.17	2.09	1.48	32.69	0.80	-0.71	0.05	1.97	1.13	6.63	0.47	0.60
26	30	0	0.3	0.08	1.13	0.08	1.06	1.02	5.72	0.40	0.02	0.03	1.19	0.72	0.74	0.03	-0.11
27	30	0	0.3	0.11	1.33	0.11	1.31	1.14	11.56	0.65	-0.01	0.04	1.37	0.83	1.89	-0.06	0.09
28	30	0	0.3	0.11	1.33	0.12	1.28	1.12	11.46	0.69	-0.05	0.04	1.35	0.81	1.52	-0.01	0.14
29	30	0	0.3	0.11	1.33	0.11	1.35	1.15	11.46	0.65	-0.01	0.04	1.35	0.85	2.12	0.05	0.16
30	30	0	0.3	0.14	1.5	0.14	1.38	1.17	15.29	0.79	-0.13	0.05	1.40	0.90	3.11	0.09	0.35
31	30	0	0.3	0.14	2.12	0.16	2.18	1.48	32.16	0.85	-0.70	0.06	2.09	1.20	9.35	0.63	0.60
32	30	0	0.3	0.14	1.5	0.14	1.40	1.16	15.44	0.81	-0.07	0.05	1.44	0.90	3.47	0.10	0.34
33	30	0	0.3	0.14	1.5	0.15	1.44	1.18	16.41	0.84	-0.03	0.05	1.51	0.90	3.53	0.15	0.43
34	30	0	0.3	0.14	1.5	0.15	1.40	1.18	16.27	0.86	-0.09	0.05	1.46	0.89	3.33	0.05	0.38
35	30	0.05	0.25	0.07	1.5	0.10	1.46	1.25	18.70	0.60	0.05	0.03	1.46	0.81	1.48	-0.09	0.10
36	30	0.05	0.25	0.09	1.7	0.12	1.44	1.28	25.27	0.75	-0.20	0.03	1.65	0.94	3.18	-0.05	0.31
37	30	0.05	0.25	0.11	1.88	0.13	2.05	1.37	31.81	0.85	-0.45	0.04	1.77	1.02	4.12	0.04	0.51
38	30	0.05	0.25	0.11	1.88	0.14	2.01	1.41	37.46	0.80	-0.46	0.04	1.90	1.00	4.12	-0.05	0.43
39	30	0.05	0.25	0.11	1.88	0.13	1.60	1.29	28.18	0.84	-0.50	0.04	1.80	1.03	5.12	0.14	0.64
40	30	0.05	0.25	0.07	1.06	0.07	1.02	0.98	7.19	0.35	0.01	0.02	1.16	0.61	0.32	0.17	-0.03
41	30	0.05	0.25	0.09	1.2	0.09	1.23	1.06	11.53	0.53	0.01	0.02	1.19	0.68	0.80	0.03	-0.14

Continued

Test set-up						Gauge 2						Gauge 7					
Test No.	Layout	R_c (m)	h (m)	H_i (m)	T_{pi} (s)	H_s (m)	T_p (s)	T_{mean} (s)	U_r	S	A	H_s (m)	T_p (s)	T_{mean} (s)	U_r	S	A
42	30	0.05	0.25	0.11	1.33	0.12	1.35	1.13	17.82	0.69	-0.07	0.03	1.38	0.79	1.64	-0.05	0.05
43	30	-0.05	0.35	0.09	1.7	0.12	1.55	1.35	12.76	0.65	-0.12	0.06	1.63	1.01	3.44	0.20	0.34
44	30	-0.05	0.35	0.13	2.04	0.17	2.05	1.49	23.61	0.74	-0.45	0.07	1.86	1.11	5.48	0.65	0.40
45	30	-0.05	0.35	0.13	2.04	0.17	1.90	1.53	26.26	0.75	-0.43	0.06	1.97	1.10	5.21	0.53	0.49
46	30	-0.05	0.35	0.13	2.04	0.17	1.97	1.50	24.53	0.78	-0.49	0.08	1.97	1.20	7.75	0.71	0.41
47	30	-0.05	0.35	0.17	2.33	0.21	2.28	1.65	38.60	0.75	-0.74	0.09	2.18	1.33	10.53	0.98	0.18
48	30	-0.05	0.35	0.09	1.2	0.10	1.22	1.07	5.69	0.41	0.03	0.05	1.23	0.79	1.36	0.13	-0.02
49	30	-0.05	0.35	0.13	1.44	0.14	1.38	1.20	11.51	0.70	-0.06	0.06	1.46	0.90	2.42	0.17	0.38
50	30	-0.05	0.35	0.13	1.44	0.14	1.31	1.19	10.93	0.70	-0.07	0.05	1.42	0.86	2.18	0.13	0.25
51	30	-0.05	0.35	0.13	1.44	0.14	1.38	1.21	11.68	0.68	-0.05	0.07	1.46	0.98	3.35	0.18	0.34
52	30	-0.05	0.35	0.17	1.65	0.19	1.51	1.22	15.99	0.91	-0.27	0.07	1.77	1.05	4.31	0.48	0.46
53	50	0	0.3	0.08	1.6	0.11	1.55	1.31	15.21	0.62	-0.17	0.03	1.60	0.82	1.44	0.03	0.23
54	50	0	0.3	0.11	1.88	0.15	1.77	1.36	23.95	0.82	-0.43	0.04	1.83	0.98	3.09	0.15	0.26
55	50	0	0.3	0.11	1.88	0.14	1.74	1.39	23.95	0.86	-0.37	0.03	1.71	0.91	2.23	0.14	0.19
56	50	0	0.3	0.11	1.88	0.14	1.80	1.38	23.89	0.75	-0.47	0.04	1.77	1.04	4.02	0.23	0.41
57	50	0	0.3	0.14	2.12	0.17	1.90	1.44	31.63	0.81	-0.51	0.04	1.90	1.06	4.45	0.23	0.45
58	50	0	0.3	0.08	1.13	0.07	1.07	0.99	5.13	0.39	0.00	0.02	1.16	0.62	0.37	0.09	-0.06
59	50	0	0.3	0.11	1.33	0.12	1.31	1.10	10.63	0.69	-0.09	0.03	1.38	0.74	0.90	0.05	0.06
60	50	0	0.3	0.11	1.33	0.11	1.35	1.10	9.91	0.62	-0.04	0.03	1.40	0.72	0.66	-0.01	0.09
61	50	0	0.3	0.11	1.33	0.11	1.40	1.11	10.54	0.70	-0.11	0.04	1.42	0.79	1.48	0.04	0.12
62	50	0	0.3	0.14	1.5	0.15	1.51	1.19	16.75	0.85	-0.28	0.04	1.55	0.91	1.94	0.13	0.31
63	50	0	0.3	0.14	2.12	0.16	1.97	1.49	32.32	0.77	-0.51	0.04	1.97	1.04	4.35	0.21	0.29
64	50	0	0.3	0.14	1.5	0.14	1.51	1.22	17.47	0.77	-0.28	0.04	1.65	0.86	1.82	0.23	0.21
65	50	0	0.3	0.14	1.5	0.15	1.48	1.18	16.39	0.84	-0.32	0.04	1.58	0.85	1.81	0.23	0.19
66	50	0	0.3	0.14	1.5	0.15	1.46	1.19	17.01	0.82	-0.31	0.04	1.58	0.87	1.83	0.25	0.17
67	50	0.05	0.25	0.07	1.5	0.11	1.51	1.22	19.68	0.63	-0.18	0.01	1.48	0.66	0.45	-0.22	-0.03
68	50	0.05	0.25	0.09	1.7	0.14	1.68	1.27	28.54	0.76	-0.37	0.02	1.63	0.80	1.25	-0.18	0.07
69	50	0.05	0.25	0.11	1.88	0.17	1.65	1.28	35.79	0.80	-0.48	0.02	1.68	0.88	2.02	-0.05	0.28
70	50	0.05	0.25	0.11	1.88	0.16	1.71	1.29	34.46	0.95	-0.37	0.02	1.71	0.81	1.17	-0.19	0.08
71	50	0.05	0.25	0.11	1.88	0.16	1.77	1.30	34.89	0.73	-0.52	0.03	1.68	0.93	2.69	-0.01	0.30
72	50	0.05	0.25	0.07	1.06	0.08	1.00	0.90	6.47	0.38	0.03	0.01	1.19	0.52	0.09	0.01	-0.08
73	50	0.05	0.25	0.09	1.2	0.10	1.31	1.01	11.19	0.55	-0.05	0.01	1.26	0.55	0.21	0.11	-0.08
74	50	0.05	0.25	0.11	1.33	0.13	1.42	1.09	17.33	0.72	-0.16	0.02	1.35	0.68	0.52	-0.06	-0.04
75	50	-0.05	0.35	0.09	1.7	0.12	1.58	1.37	13.71	0.61	-0.05	0.05	1.65	0.88	2.14	0.15	0.13
76	50	-0.05	0.35	0.13	2.04	0.16	1.97	1.54	25.10	0.76	-0.42	0.06	2.09	1.09	4.42	0.37	0.37
77	50	-0.05	0.35	0.13	2.04	0.16	1.86	1.47	22.01	0.84	-0.38	0.05	1.97	1.03	3.14	0.25	0.23
78	50	-0.05	0.35	0.13	2.04	0.17	1.86	1.49	24.61	0.79	-0.52	0.07	1.90	1.10	5.23	0.51	0.56
79	50	-0.05	0.35	0.17	2.33	0.20	2.23	1.56	32.72	0.84	-0.62	0.07	2.28	1.15	6.15	0.73	0.50
80	50	-0.05	0.35	0.09	1.2	0.09	1.08	1.05	5.12	0.39	-0.01	0.05	1.16	0.73	1.12	0.21	-0.01
81	50	-0.05	0.35	0.13	1.44	0.14	1.38	1.21	11.59	0.62	-0.08	0.05	1.42	0.82	1.72	0.13	0.12
82	50	-0.05	0.35	0.13	1.44	0.14	1.28	1.17	10.47	0.68	-0.02	0.04	1.48	0.77	1.14	0.09	0.07
83	50	-0.05	0.35	0.13	1.44	0.14	1.40	1.20	11.16	0.64	-0.09	0.06	1.40	0.90	2.40	0.06	0.14
84	50	-0.05	0.35	0.17	1.65	0.19	1.60	1.26	17.56	0.81	-0.24	0.06	1.65	0.97	2.77	0.28	0.35

Table D3 Wave basin transmission tests on Rubble Mound LCS

	Test set-up					Gauge 2						Gauge 7					
Test No.	Layout	R_c (m)	h (m)	H_i (m)	T_{pi} (s)	H_s (m)	T_p (s)	T_{mean} (s)	U_r	S	A	H_s (m)	T_p (s)	T_{mean} (s)	U_r	S	A
1	0	0	0.25	0.08	1.6	0.11	1.58	1.26	21.13	0.88	-0.31	0.05	1.53	1.03	5.50	0.42	0.54
2	0	0	0.25	0.11	1.88	0.14	1.65	1.30	29.80	1.11	-0.48	0.06	1.65	1.10	8.77	0.96	0.51
3	0	0	0.25	0.14	2.12	0.14	2.01	1.40	36.09	1.12	-0.58	0.06	2.09	1.20	11.28	1.13	0.32
4	0	0	0.25	0.08	1.13	0.06	1.07	0.98	6.59	0.42	0.03	0.03	1.16	0.75	1.55	0.07	-0.09
5	0	0	0.25	0.11	1.33	0.10	1.38	1.08	13.64	0.87	-0.18	0.05	1.38	0.93	4.13	0.13	0.37
6	0	0	0.25	0.14	1.5	0.12	1.48	1.14	19.31	0.92	-0.40	0.05	1.48	0.97	5.38	0.38	0.44
7	0	0	0.25	0.14	2.12	0.14	2.01	1.39	35.43	1.15	-0.59	0.07	2.05	1.21	11.84	1.31	0.25
8	0	0	0.25	0.14	1.5	0.14	1.51	1.16	22.58	0.89	-0.41	0.06	1.51	0.99	6.29	0.51	0.47
9	0	0.05	0.2	0.07	1.5	0.10	1.60	1.13	24.48	0.93	-0.45	0.03	1.58	0.98	4.60	0.20	0.33
10	0	0.05	0.2	0.09	1.7	0.12	1.63	1.18	32.57	1.01	-0.61	0.03	1.71	1.04	6.04	0.28	0.29
11	0	0.05	0.2	0.11	1.88	0.13	1.68	1.23	39.60	0.97	-0.68	0.03	1.90	1.07	7.25	0.40	0.31
12	0	0.05	0.2	0.07	1.06	0.06	1.07	0.93	9.74	0.48	0.07	0.02	1.13	0.85	1.86	-0.03	-0.05
13	0	0.05	0.2	0.09	1.2	0.08	1.09	0.94	13.37	0.86	0.01	0.02	1.30	0.88	2.61	-0.09	0.13
14	0	0.05	0.2	0.11	1.33	0.10	1.44	1.00	18.58	0.91	-0.29	0.03	1.38	0.89	3.51	0.12	0.24
15	0	-0.05	0.3	0.09	1.7	0.10	1.51	1.35	15.70	0.79	-0.03	0.06	1.55	1.19	6.86	0.61	0.43
16	0	-0.05	0.3	0.13	2.04	0.14	1.90	1.38	23.45	1.17	-0.38	0.08	1.97	1.26	10.78	1.04	0.16
17	0	-0.05	0.3	0.17	2.33	0.15	2.13	1.45	28.64	1.13	-0.57	0.09	2.23	1.36	13.60	1.15	-0.15
18	0	-0.05	0.3	0.09	1.2	0.08	1.19	1.07	6.66	0.44	0.02	0.05	1.22	0.93	2.76	-0.02	0.05
19	0	-0.05	0.3	0.13	1.44	0.12	1.44	1.21	14.01	0.76	-0.06	0.07	1.46	1.07	5.62	0.52	0.43
20	0	-0.05	0.3	0.17	1.65	0.16	1.58	1.26	20.34	1.01	-0.25	0.08	1.60	1.13	8.13	0.89	0.19
21	30	0	0.25	0.08	1.6	0.11	1.46	1.23	19.88	0.93	-0.11	0.04	1.53	1.02	4.65	0.09	0.22
22	30	0	0.25	0.11	1.88	0.13	1.65	1.24	24.82	1.19	-0.25	0.05	1.74	1.08	6.35	0.33	0.33
23	30	0	0.25	0.11	1.88	0.13	1.60	1.19	21.84	1.24	-0.32	0.04	1.90	1.06	5.71	0.29	0.27
24	30	0	0.25	0.11	1.88	0.13	1.71	1.26	26.00	1.21	-0.31	0.05	1.74	1.10	7.11	0.33	0.33
25	30	0	0.25	0.14	2.12	0.13	1.86	1.27	27.53	1.24	-0.63	0.06	2.01	1.14	8.69	0.69	0.36
26	30	0	0.25	0.08	1.13	0.08	1.16	1.01	8.63	0.53	-0.01	0.03	1.25	0.78	1.62	0.16	-0.06
27	30	0	0.25	0.11	1.33	0.12	1.31	1.08	15.57	0.83	-0.11	0.04	1.40	0.93	3.87	0.03	0.04
28	30	0	0.25	0.11	1.33	0.12	1.28	1.08	15.94	0.86	-0.13	0.04	1.42	0.88	2.89	0.08	0.08
29	30	0	0.25	0.11	1.33	0.11	1.31	1.10	16.05	0.79	-0.18	0.05	1.28	0.90	3.86	0.15	0.01
30	30	0	0.25	0.14	1.5	0.14	1.35	1.11	19.99	1.00	-0.27	0.05	1.42	0.98	5.21	0.24	0.22
31	30	0	0.25	0.14	2.12	0.13	1.93	1.27	27.23	1.23	-0.66	0.06	2.05	1.14	9.00	0.70	0.37
32	30	0	0.25	0.14	1.5	0.14	1.46	1.14	21.25	0.98	-0.26	0.05	1.51	0.97	5.10	0.30	0.24
33	30	0	0.25	0.14	1.5	0.14	1.44	1.16	22.23	1.01	-0.24	0.05	1.53	1.00	5.74	0.20	0.26
34	30	0	0.25	0.14	1.5	0.14	1.46	1.13	21.26	1.01	-0.25	0.06	1.53	1.01	6.09	0.21	0.30
35	30	0.05	0.2	0.07	1.5	0.09	1.42	1.17	25.69	0.97	-0.16	0.04	1.55	1.09	8.06	-0.04	0.15
36	30	0.05	0.2	0.09	1.7	0.11	1.51	1.17	28.74	1.12	-0.25	0.03	1.71	1.09	7.81	0.15	0.22
37	30	0.05	0.2	0.11	1.88	0.12	1.65	1.18	32.98	1.19	-0.34	0.03	1.77	1.07	7.13	0.34	0.17
38	30	0.05	0.2	0.11	1.88	0.11	1.58	1.14	27.40	1.21	-0.36	0.03	1.77	1.06	6.65	0.32	0.13
39	30	0.05	0.2	0.11	1.88	0.12	1.77	1.22	34.75	1.18	-0.32	0.03	1.83	1.05	6.92	0.25	0.17
40	30	0.05	0.2	0.07	1.06	0.06	1.14	0.95	10.12	0.50	-0.03	0.03	1.10	0.97	4.27	0.12	0.01
41	30	0.05	0.2	0.09	1.22	0.09	1.22	1.02	17.63	0.81	-0.21	0.03	1.31	0.93	3.93	0.05	-0.10

Continued

	Test set-up					Gauge 2						Gauge 7					
Test No.	Layout	R_c (m)	h (m)	H_i (m)	T_{pi} (s)	H_s (m)	T_p (s)	T_{mean} (s)	U_r	S	A	H_s (m)	T_p (s)	T_{mean} (s)	U_r	S	A
42	30	0.05	0.2	0.11	1.33	0.11	1.35	1.08	24.98	0.90	-0.25	0.03	1.35	0.94	3.94	0.00	0.05
43	30	-0.05	0.3	0.09	1.7	0.10	1.55	1.31	15.25	0.90	-0.12	0.06	1.55	1.12	5.84	0.29	0.31
44	30	-0.05	0.3	0.13	2.04	0.13	1.80	1.36	20.97	1.11	-0.55	0.08	1.83	1.18	8.38	0.75	0.34
45	30	-0.05	0.3	0.13	2.04	0.13	1.80	1.33	20.28	1.13	-0.63	0.07	1.97	1.21	7.99	0.74	0.32
46	30	-0.05	0.3	0.13	2.04	0.14	1.80	1.36	21.42	1.18	-0.48	0.08	1.90	1.23	10.28	0.76	0.32
47	30	-0.05	0.3	0.17	2.33	0.16	2.23	1.44	29.83	0.96	-0.86	0.09	2.18	1.27	11.59	1.09	-0.01
48	30	-0.05	0.3	0.09	1.2	0.09	1.16	1.04	6.84	0.52	0.02	0.05	1.19	0.82	2.03	0.29	-0.05
49	30	-0.05	0.3	0.13	1.44	0.13	1.37	1.14	13.34	0.85	-0.11	0.07	1.38	1.02	4.83	0.24	0.27
50	30	-0.05	0.3	0.13	1.44	0.13	1.35	1.12	12.18	0.81	-0.07	0.06	1.38	0.99	4.03	0.19	0.20
51	30	-0.05	0.3	0.13	1.44	0.13	1.38	1.16	13.88	0.83	-0.08	0.07	1.40	1.04	5.58	0.26	0.28
52	30	-0.05	0.3	0.17	1.65	0.15	1.51	1.21	17.96	1.05	-0.23	0.08	1.77	1.13	7.51	0.52	0.38
53	50	0	0.25	0.08	1.6	0.09	1.46	1.20	15.71	0.97	-0.04	0.04	1.55	1.03	5.11	0.06	0.34
54	50	0	0.25	0.11	1.88	0.11	1.71	1.23	21.01	1.19	-0.43	0.05	1.77	1.05	5.90	0.39	0.30
55	50	0	0.25	0.11	1.88	0.11	1.55	1.21	20.30	1.23	-0.39	0.05	1.77	1.11	6.64	0.44	0.29
56	50	0	0.25	0.11	1.88	0.12	1.71	1.21	21.52	1.28	-0.45	0.05	1.77	1.04	6.38	0.32	0.36
57	50	0	0.25	0.14	2.12	0.13	1.97	1.28	27.63	1.16	-0.75	0.05	1.90	1.08	6.86	0.60	0.34
58	50	0	0.25	0.08	1.13	0.08	1.09	1.01	8.70	0.56	0.02	0.03	1.28	0.77	1.57	0.12	-0.04
59	50	0	0.25	0.11	1.33	0.11	1.25	1.07	14.50	0.89	-0.05	0.04	1.38	0.85	2.89	0.02	0.11
60	50	0	0.25	0.11	1.33	0.10	1.28	1.06	13.37	0.87	-0.02	0.04	1.38	0.85	2.44	-0.07	-0.01
61	50	0	0.25	0.11	1.33	0.11	1.28	1.08	14.08	0.85	-0.08	0.05	1.42	0.93	4.08	0.09	0.18
62	50	0	0.25	0.14	1.5	0.13	1.38	1.09	17.70	1.06	-0.25	0.05	1.65	0.97	4.64	0.25	0.30
63	50	0	0.25	0.14	2.12	0.13	2.05	1.30	27.00	1.10	-0.80	0.05	2.05	1.12	6.70	0.72	0.24
64	50	0	0.25	0.14	1.5	0.13	1.44	1.09	17.88	1.06	-0.26	0.05	1.51	0.87	3.43	0.39	0.20
65	50	0	0.25	0.14	1.5	0.13	1.37	1.07	16.94	1.09	-0.28	0.05	1.60	0.89	3.47	0.38	0.20
66	50	0	0.25	0.14	1.5	0.13	1.42	1.11	18.19	1.12	-0.23	0.05	1.58	0.91	3.84	0.40	0.23
67	50	0.05	0.2	0.07	1.5	0.08	1.38	1.12	20.04	1.01	-0.05	0.04	1.51	1.16	9.58	-0.06	0.14
68	50	0.05	0.2	0.09	1.7	0.10	1.46	1.11	22.93	1.25	-0.23	0.03	1.55	1.05	7.03	0.08	0.25
69	50	0.05	0.2	0.11	1.88	0.11	1.60	1.10	24.84	1.28	-0.51	0.03	1.80	1.09	7.60	0.32	0.33
70	50	0.05	0.2	0.11	1.88	0.10	1.65	1.11	23.88	1.26	-0.52	0.03	1.77	1.14	7.99	0.27	0.33
71	50	0.05	0.2	0.11	1.88	0.11	1.60	1.14	26.71	1.27	-0.48	0.03	1.71	1.04	6.72	0.28	0.26
72	50	0.05	0.2	0.07	1.06	0.07	1.06	0.95	10.33	0.57	0.03	0.02	1.11	0.94	3.29	0.09	0.01
73	50	0.05	0.2	0.09	1.2	0.09	1.22	1.00	16.60	0.88	-0.05	0.03	1.28	1.00	4.55	0.05	-0.09
74	50	0.05	0.2	0.11	1.33	0.10	1.30	1.03	20.12	0.97	-0.14	0.03	1.35	0.99	4.80	-0.07	0.03
75	50	-0.05	0.3	0.09	1.7	0.10	1.60	1.29	14.10	0.91	-0.22	0.06	1.65	1.18	7.03	0.31	0.39
76	50	-0.05	0.3	0.13	2.04	0.13	1.93	1.41	22.71	1.01	-0.63	0.07	2.01	1.23	9.27	0.77	0.40
77	50	-0.05	0.3	0.13	2.04	0.13	1.83	1.37	21.54	1.08	-0.57	0.07	1.90	1.24	8.82	0.72	0.32
78	50	-0.05	0.3	0.13	2.04	0.14	1.90	1.38	23.43	1.06	-0.75	0.08	1.90	1.22	9.47	0.82	0.44
79	50	-0.05	0.3	0.17	2.33	0.16	2.23	1.48	31.48	0.91	-0.85	0.08	2.18	1.25	9.72	1.04	0.11
80	50	-0.05	0.3	0.09	1.2	0.09	1.14	1.03	6.58	0.49	0.03	0.05	1.22	0.94	3.02	0.26	-0.02
81	50	-0.05	0.3	0.13	1.44	0.13	1.35	1.13	12.43	0.87	-0.11	0.06	1.55	1.04	4.69	0.16	0.25
82	50	-0.05	0.3	0.13	1.44	0.12	1.31	1.10	10.96	0.83	-0.07	0.06	1.46	1.03	4.31	0.19	0.21
83	50	-0.05	0.3	0.13	1.44	0.13	1.31	1.14	13.05	0.89	-0.11	0.07	1.42	1.06	5.56	0.21	0.24
84	50	-0.05	0.3	0.17	1.65	0.15	1.51	1.18	17.24	1.06	-0.37	0.07	1.55	1.06	5.92	0.63	0.39

REFERENCES

Allsop, N.W.H., Bruce, T., Pearson, J., Alderson, J.S. and Pullen, T., 2003. Violent wave overtopping at the coast: when are we safe?, Proceedings of the International Conference on Coastal Management, Thomas Telford, London, pp. 54-69.

Allsop, W., Bruce, T., Pearson, J. and Besley, P., 2005. Wave overtopping at vertical and steep seawalls. *Proceedings of the ICE - Water Maritime and Energy*, 158(3): 103 - 114

Ashgriz, N. and Poo, J.Y., 1991. FLAIR: Flux line-segment model for advection and interface reconstruction. *Journal of Computational Physics*, 93(2): 449-468.

Austin, M., Masselink, G., O'Hare, T. and Russell, P., 2009. Onshore sediment transport on a sandy beach under varied wave conditions: Flow velocity skewness, wave asymmetry or bed ventilation? *Marine Geology*, 259(1-4): 86-101.

Avgeris, I., Karmbas, T.V. and Prinos, P., 2004. Boussinesq modelling of wave interaction with porous submerged breakwaters. In: Smith, J.M. (Editor), the 29th International Conference on Coastal Engineering. ASCE, National Civil Engineering Laboratory, Lisbon, Portugal.

Bagnold, R.A., 1966. An approach to the sediment transport problem from general physics. *US Geological Survey Professional Paper*, 422-I: 37.

Bailard, J.A. and Inman, D.L., 1981. An energetics bedload model for a plane sloping beach: local transport. *Journal of Geophysical Research*, 86(C3): 2035-2043.

Battjes, J.A., 1988. Surf-Zone Dynamics. *Annual Review of Fluid Mechanics*, 20: 257-293.

Bear, J., 1972. *Dynamics of fluids in porous media*. Elsevier Science, New York.

Beji, S. and Battjes, J.A., 1993. Experimental Investigation of Wave-Propagation over a Bar. *Coastal Engineering*, 19(1-2): 151-162.

Beji, S. and Battjes, J.A., 1994. Numerical-Simulation of Nonlinear-Wave Propagation over a Bar. *Coastal Engineering*, 23(1-2): 1-16.

Beseley, P., 1999. Overtopping of Seawalls—Design and Assessment Manual. R&D Technical Report W 178, Environment Agency, Bristol,

Blenkinsopp, C.E. and Chaplin, J.R., 2008. The effect of relative crest submergence on wave breaking over submerged slopes. *Coastal Engineering*, 55(12): 967-974.

Bouws, E., Gunther, H., Rosenthal, W. and Vincent, C.L., 1985. Similarity of the Wind Wave Spectrum in Finite Depth Water 1. Spectral Form. *J. Geophys. Res.*, 90.

Bowen, A.J., 1980. Simple models of nearshore sedimentation; beach profiles and longshore bars. In: McCann, S.B. (Editor), The Coastline of Canada. Geological Survey of Canada, pp. 1-11.

Briganti, R., Bellotti, G., Franco, L., De Rouck, J. and Geeraerts, J., 2005. Field

measurements of wave overtopping at the rubble mound breakwater of Rome-Ostia yacht harbour. *Coastal Engineering*, 52(12): 1155-1174.

Brossard, J. and Chagdali, M., 2001. Experimental investigation of the harmonic generation by waves over a submerged plate. *Coastal Engineering*, 42(4): 277-290.

Brossard, J., Perret, G., Blonce, L. and Diedhiou, A., 2009. Higher harmonics induced by a submerged horizontal plate and a submerged rectangular step in a wave flume. *Coastal Engineering*, 56(1): 11-22.

Bruce, T., Pullen, T., Allsop, N.W.H. and Pearson, J., 2005. How far back is safe? Spatial distributions of wave overtopping. Telford, London, Proc. Coastlines, Seawalls and Breakwaters, ICE. Thomas Telford, London.

Bruce, T., van der Meer, J.W., Franco, L. and Pearson, J.M., 2009. Overtopping performance of different armour units for rubble mound breakwaters. *Coastal Engineering*, 56(2): 166-179.

Burcharth, H.F., Kramer, M., Lamberti, A. and Zanuttigh, B., 2006. Structural stability of detached low crested breakwaters. *Coastal Engineering*, 53(4): 381-394.

Caceres, I., Sanchez-Arcilla, A., Zanuttigh, B., Lamberti, A. and Franco, L., 2005. Wave overtopping and induced currents at emergent low crested structures. *Coastal Engineering*, 52(10-11): 931-947.

Causon, D., Ingram, D., Mingham, C., Zang, J., Hu, K. and Zhou, J.G., 2000. Numerical simulation seawall overtopping, Proc. of the 27th International Conference on Coastal Engineering, Sydney, Australia, pp. 2086–2099.

Chorin, A.J., 1968. Numerical Solution of the Navier-Stokes Equations. *Mathematics of Computation*, 22(104): 745-762.

Chorin, A.J., 1969. On the Convergence of Discrete Approximations to the Navier-Stokes Equations. *Mathematics of Computation*, 23(106): 341-353.

Christensen, E.D. and Deigaard, R., 2001. Large eddy simulation of breaking waves. *Coastal Engineering*, 42(1): 53-86.

Christou, M., Swan, C. and Gudmestad, O.T., 2008. The interaction of surface water waves with submerged breakwaters. *Coastal Engineering*, 55(12): 945-958.

Cornish, V., 1898. On sea beaches and sandbanks. *The Geographical Journal*, 11(5): 528-543.

Cox, D.T., Kobayashi, N. and Kreibel, D.L., 1994. Numerical model verification using SUPERTANK data in surf and swash zones. In: Sánchez-Arcilla, A., M.C.F. Stive and N.C. Kraus (Editors), Coastal Dynamics '94: Proceedings International Conference on the Role of Large Scale Experiments in Coastal Research. American Society of Civil Engineers, Barcelona, Spain, pp. 248–262.

Crawford, A.M., 2000. Field observations of linear transition ripple migration and wave orbital velocity skewness. PhD thesis Thesis, Memorial Univeristy of Newfoundland, Newfoundland.

Crawford, A.M. and Hay, A.E., 2001. Linear transition ripple migration and wave orbital velocity skewness: Observations. *Journal of Geophysical Research-Oceans*, 106(C7): 14113-14128.

Cruz, E.C., Isobe, M. and Watanabe, A., 1997. Boussinesq equations for wave transformation on porous beds. *Coastal Engineering*, 30(1-2): 125-156.

Dalrymple, R.A., Knio, O., Cox, D.T., Gesteira, M. and Zou, S., 2001. Using a Lagrangian Particle Method for Deck Overtopping. In: Billy, L.E. and J.M. Hemsley (Editors). ASCE, pp. 110.

de Waal, J.P., Tönjes, P. and Van der Meer, J.M., 1996. Overtopping of sea defences. In: Edge, B.L. (Editor), Proceedings of the Twenty-fifth International Conference on Coastal Engineering. ASCE, Orlando, Florida, USA, pp. 2216–2229.

Delnoij, E., Kuipers, J.A.M. and van Swaaij, W.P.M., 1988. Numerical simulation of

bubble coalescence using a volume of fluid (vof) model, the 3rd International Conference on Multiphase Flow, Lyon, France.

Diskin, M.H., Vajda, M.L. and Amir, I., 1970. Piling-up behind low and submerged permeable breakwaters. *Journal of the Waterways. Harbors and Coastal Engineering Division*, 96(2): 359–372.

Doering, J.C. and Bowen, A.J., 1995. Parametrization of orbital velocity asymmetries of shoaling and breaking waves using bispectral analysis. *Coastal Engineering*, 26: 15-33.

Doering, J.C., Elfrink, B., Hanes, D.M. and Ruessink, G., 2000. Parameterization of velocity skewness under waves and its effect on cross-shore sediment transport. In: Edge, B.L. (Editor), Proceedings of the 27th International Conference of Coastal Engineering, Sydney, Australia, pp. 1383-1397.

Dong, P. and Zhang, K., 1999. Two-phase flow modelling of sediment motions in oscillatory sheet flow. *Coastal Engineering*, 36(2): 87-109.

Dong, P. and Zhang, K., 2002. Intense near-bed sediment motions in waves and currents. *Coastal Engineering*, 45(2): 75-87.

Dongeren, A.R.V. and Svendsen, I.A., 1997. Absorbing-Generating Boundary Condition for Shallow Water Models. *Journal of Waterway, Port, Coastal, and Ocean Engineering*, 123(6): 303-313.

Drake, T.G. and Calantoni, J., 2001. Discrete particle model for sheet flow sediment transport in the nearshore. *Journal of Geophysical Research*, 106(C9): 19859–19868.

Du, Y.L., Pan, S.Q. and Chen, Y.P., 2010. Modelling the effect of wave overtopping on nearshore hydrodynamics and morphodynamics around shore-parallel breakwaters. *Coastal Engineering*, doi: 10.1016/j.coastaleng.2010.04.005.

Elfrink, B., Hanes, D.M. and Ruessink, B.G., 2006. Parameterization and simulation of near bed orbital velocities under irregular waves in shallow water. *Coastal Engineering*, 53: 915-927.

Elfrink, B., Rakha, K.A. and Deigaard, R., 1999. Effect of near-bed velocity skewness on cross shore sediment transport, Proc. Coastal Sediments'99, Long Island, NY, pp. 33-47.

Elgar, S. and Guza, R.T., 1985. Observations of Bispectra of Shoaling Surface Gravity Waves. *Journal of Fluid Mechanics*, 161: 425-448.

Elgar, S., Guza, R.T., Raubenheimer, B., Herbers, T.H.C. and Gallagher, E.L., 1997. Spectral evolution of shoaling and breaking waves on a barred beach. *J. Geophys. Res.*, 102(C7): 15797-15805.

EurOtop, 2007. Wave Overtopping of Sea Defences and Related Structures — Assessment Manual, Eds: Pullen, T., Allsop, N. W. H., Bruce, T, Kortenhaus, A., Schuttrumpf, H., Van der Meer, J., www.overtopping-manual.com

EurOtop, 2008. Wave Overtopping of Sea Defences and Related Structures — Assessment Manual, Eds: Pullen, T., Allsop, N. W. H., Bruce, T, Kortenhaus, A., Schuttrumpf, H., Van der Meer, J., www.overtopping-manual.com

Flaten, G. and Rygg, O.B., 1991. Dispersive shallow water waves over a porous sea bed. *Coastal Engineering*, 15(4): 347-369.

Franco, L., Geeraerts, J., Briganti, R., Willems, M., Bellotti, G. and De Rouck, J., 2009. Prototype measurements and small-scale model tests of wave overtopping at shallow rubble-mound breakwaters: the Ostia-Rome yacht harbour case. *Coastal Engineering*, 56(2): 154-165.

Fuhrman, D.R., Bingham, H.B. and Madsen, P.A., 2005. Nonlinear wave-structure interactions with a high-order Boussinesq model. *Coastal Engineering*, 52(8): 655-672.

Fuhrman, D.R., Fredsøe, J. and Sumer, B.M., 2009. Bed slope effects on turbulent wave boundary layers: 2. Comparison with skewness, asymmetry, and other

effects. *J. Geophys. Res.*, 114.
Gallagher, E.L., Elgar, S. and Guza, R.T., 1998. Observations of sand bar evolution on a natural beach. *J. Geophys. Res.*, 103(C2): 3203-3215.
Garcia, N., Lara, J.L. and Losada, I.J., 2004. 2-D numerical analysis of near-field flow at low-crested permeable breakwaters. *Coastal Engineering*, 51(10): 991-1020.
Goda, Y., 2009. A performance test of nearshore wave height prediction with CLASH datasets. *Coastal Engineering*, 56(3): 220-229.
Gonzalez-Rodriguez, D. and Madsen, O.S., 2007. Seabed shear stress and bedload transport due to asymmetric and skewed waves. *Coastal Engineering*, 54(12): 914-929.
Gotoh, H., Shao, S.D. and Memita, T., 2004. SPH-LES model for numerical investigation of wave interaction with partially immersed breakwater. *Coastal Engineering Journal*, 46(1): 39-63.
Greaves, D., 2004. Simulation of interface and free surface flows in a viscous fluid using adapting quadtree grids. *International Journal for Numerical Methods in Fluids*, 44(10): 1093-1117.
Greaves, D.M., 2006. Simulation of viscous water column collapse using adapting hierarchical grids. *International Journal for Numerical Methods in Fluids*, 50(6): 693-711.
Greaves, D.M., 2007. Viscous waves and wave-structure interaction in a tank using adapting quadtree grids. *Journal of Fluids and Structures*, 23(8): 1149-1167.
Gunbak, A.R., Gokce, T. and Guler, I., 1990. Erosion and protection of Samandag Breakwater, J. Coastal Research, Proc. of Skagen Symposium, pp. 753-771.
Haas, K.A., Check, L.A. and Hanes, D.M., 2008. Modeling the Effects of Wave Skewness and Beach Cusps on Littoral Sand Transport. *Journal of Coastal Research*, 24(sp3): 141-149.
Hasselman, K., Munk, W. and MacDonald, G., 1963. Bispectra of ocean. waves. In: Rosenblatt, M. (Editor), Time Series Analysis. Wiley, pp. 125-139.
Hasselmann, K., Barnett, T.P., Bouws, E., Carlson, H., Cartwright, D.E., Enke, K., Ewing, J.A., Gienapp, H., Hasselmann, D.E., Kruseman, P., Meerburg, A., Mller, P., Olbers, D.J., Richter, K., Sell, W. and Walden., H., 1973. Measurements of wind-wave growth and swell decay during the Joint North Sea Wave Project (JONSWAP). *Ergnzungsheft zur Deutschen Hydrographischen Zeitschrift Reihe*, 8(12): 95.
Haubrich, R.A., 1965. Earth noise, 5 to 500 Millicycles per second. 1.Spectral stationarity, normality and nonlinearity. *Journal of Geophysical Research*, 70(6): 1415-1427.
Hedges, T.S. and Reis, M.T., 1998. Random wave overtopping of simple sea walls : a new regression model. *Proceedings of the Institution of Civil Engineers. Water, maritime and energy*, 130(1): 1-10.
Herbers, T.H.C., Orzech, M., Elgar, S. and Guza, R.T., 2003. Shoaling transformation of wave frequency-directional spectra. *Journal of Geophysical Research-Oceans*, 108(C1): 3013.
Hieu, P.D. and Tanimoto, K., 2006. Verification of a VOF-based two-phase flow model for wave breaking and wave-structure interactions. *Ocean Engineering*, 33(11-12): 1565-1588.
Hirt, C.W. and Nichols, B.D., 1981. Volume of fluid (VOF) method for the dynamics of free boundaries. *Journal of Computational Physics*, 39(1): 201-225.
Hoefel, F. and Elgar, S., 2003. Wave-Induced Sediment Transport and Sandbar Migration. *Science*, 299(5614): 1885-1887.
Holmedal, L.E. and Myrhaug, D., 2006. Boundary layer flow and net sediment transport beneath asymmetrical waves. *Continental Shelf Research*, 26(2): 252-268.

Hsiao, S.-C., Liu, P.L.F. and Chen, Y., 2002. Nonlinear water waves propagating over a permeable bed. *Proceedings of the Royal Society of London. Series A: Mathematical, Physical and Engineering Sciences*, 458(2022): 1291-1322.

Hsu, T.-J. and Hanes, D.M., 2004. Effects of wave shape on sheet flow sediment transport. *J. Geophys. Res.*, 109.

Hsu, T.J., Sakakiyama, T. and Liu, P.L.F., 2002. A numerical model for wave motions and turbulence flows in front of a composite breakwater. *Coastal Engineering*, 46(1): 25-50.

Hu, K., Mingham, C.G. and Causon, D.M., 2000. Numerical simulation of wave overtopping of coastal structures using the non-linear shallow water equations. *Coastal Engineering*, 41(4): 433-465.

Hubbard, M.E. and Dodd, N., 2002. A 2D numerical model of wave run-up and overtopping. *Coastal Engineering*, 47(1): 1-26.

Hughes, S.A. and Nadal, N.C., 2009. Laboratory study of combined wave overtopping and storm surge overflow of a levee. *Coastal Engineering*, 56(3): 244-259.

Ichikawa, T., 1967. Scouring damages and vertical wall breakwaters of Tagonoura port. *Coastal Engineering in Japan,*, 10: 95-101.

Ilegbusi, O.J., 1989. Turbulent boundary layer on a porous flat plate with severe injection at various angles to the surface. *International Journal of Heat and Mass Transfer*, 32(4): 761-765.

Ingram, D.M., Gao, F., Causon, D.M., Mingham, C.G. and Troch, P., 2009. Numerical investigations of wave overtopping at coastal structures. *Coastal Engineering*, 56(2): 190-202.

Inman, D.L. and Bagnold, R.A., 1963. Littoral processes. In: Hill, M.N. (Editor), The sea. Interscience, New York, pp. 529–533.

Janssen, C.M., Hassan, W.N., Wal, R.v.d. and Ribberink, J.S., 1997. Grain-size influence on sand transport mechanisms. In: Thornton, E.B. (Editor), the 3rd International Conference on Coastal Dynamics. ASCE, Plymouth, UK, pp. 58-67.

Jensen, O.J. and Sorensen, T., 1979. Overspilling/overtopping of rubble-mound breakwaters. Results of studies, useful in design procedures. *Coastal Engineering*, 3: 51-65.

Johnson, H., Wilkens, J., Parsons, A. and Chesher, T., 2010. Guidance for outline design of nearshore detached breakwaters on sandy macro-tidal coasts.SC0600026/R1 Environment Agency,

Johnson, H.K., Karambas, T.V., Avgeris, I., Zanuttigh, B., Gonzalez-Marco, D. and Caceres, I., 2005. Modelling of waves and currents around submerged breakwaters. *Coastal Engineering*, 52(10-11): 949-969.

Karambas, T.V. and Koutitas, C., 1992. A breaking wave propagation model based on the Boussinesq equations. *Coastal Engineering*, 18(1-2): 1-19.

Karambas, T.V. and Koutitas, C., 2002. Surf and Swash Zone Morphology Evolution Induced by Nonlinear Waves. *Journal of Waterway, Port, Coastal, and Ocean Engineering*, 128(3): 102-113.

Karim, M.F. and Tingsanchali, T., 2006. A coupled numerical model for simulation of wave breaking and hydraulic performances of a composite seawall. *Ocean Engineering*, 33(5-6): 773-787.

Keulegan, G.H. and Carpenter, L.H., 1958. Forces on cylinders and plates in an oscillating fluid. *Journal of Research of the National Bureau of Standards*, 60: 423-440.

Kim, Y.C. and Powers, E.J., 1978. Digital Bispectral analysis of self-excited fluctuation spectra. *Physics of Fluids*, 21(8): 1452-1453.

Kim, Y.C. and Powers, E.J., 1979. Digital bispectral analysis and its applications to nonlinear wave interactions. *IEEE transactions on plasma science*, PS-7(2): 120-

131.
King, D.B., 1990. Studies in oscillatory flow bed load sediment transport. Ph.D. Thesis, University of California, San Diego.
Kitaigorodskii, S.A., Krasitskii, V.P. and Zaslavskii, M.M., 1975. On Phillips' theory of equilibrium range in the spectra of wind-generated waves. *Journal of Physical Oceanography*, 5: 410-420.
Kobayashi, N., Cox, D.T. and Wurjanto, A., 1990. Irregular Wave Reflection and Run-Up on Rough Impermeable Slopes. *Journal of Waterway Port Coastal and Ocean Engineering-Asce*, 116(6): 708-726.
Kobayashi, N., Otta, A.K. and Roy, I., 1987. Wave Reflection and Run-Up on Rough Slopes. *Journal of Waterway, Port, Coastal, and Ocean Engineering*, 113(3): 282-298.
Kobayashi, N. and Wurjanto, A., 1989. Wave transmission over submerged breakwaters. *Journal of Waterway Port Coastal and Ocean Engineering-Asce*, 115(5): 662-680.
Koshizuka, S., Tamako, H. and Oka, Y., 1995. A particle method for incompressible viscous flow with fluid fragmentation. *Comput. Fluid Dynamics*, 4: 29-46.
Kramer, M., Zanuttigh, B., van der Meer, J.W., Vidal, C. and Gironella, F.X., 2005. Laboratory experiments on low-crested breakwaters. *Coastal Engineering*, 52(10-11): 867-885.
Lara, J.L., Garcia, N. and Losada, I.J., 2006. RANS modelling applied to random wave interaction with submerged permeable structures. *Coastal Engineering*, 53(5-6): 395-417.
Larsen, J. and Dancy, H., 1983. Open boundaries in short wave simulations -- A new approach. *Coastal Engineering*, 7(3): 285-297.
Launder, B.E., Reece, G.J. and Rodi, W., 1975. Progress in the development of a Reynolds-stress turbulence closure. *Journal of Fluid Mechanics*, 68(03): 537-566.
Launder, B.E. and Spalding, D.B., 1974. The numerical computation of turbulent flows. *Computer Methods in Applied Mechanics and Engineering*, 3(2): 269-289.
Li, T., Troch, P. and De Rouck, J., 2004. Wave overtopping over a sea dike. *Journal of Computational Physics*, 198(2): 686-726.
Li, T., Troch, P. and Rouck, J.D., 2007. Interactions of breaking waves with a current over cut cells. *Journal of Computational Physics*, 223(2): 865-897.
Lillycrop, W.J. and Hughes, S.A., 1993. Scour Hole Problems Experienced by the Corps of Engineers; Data Presentation and Summary.CERC-93-2, US Army Engineer Waterways Experiment Station, Coastal Engineering Research Center,, Vicksburg, MS.,
Lin, P.Z. and Liu, P.L.-F., 2000. A user's manual for a breaking wave model, School of civil and environmental engineering, Cornell University, New York,
Lin, P.Z. and Liu, P.L.F., 1998. A numerical study of breaking waves in the surf zone. *Journal of Fluid Mechanics*, 359: 239-264.
Liu, P.L.F., Lin, P.Z., Chang, K.A. and Sakakiyama, T., 1999. Numerical modeling of wave interaction with porous structures. *Journal of Waterway Port Coastal and Ocean Engineering*, 125(6): 322-330.
López, J., Hernándezb, J., Gómezb, P. and Faura, F., 2005. An improved PLIC-VOF method for tracking thin fluid structures in incompressible two-phase flows. *Journal of Computational Physics*, 208(1): 51-74.
Losada, I.J., Lara, J.L., Christensen, E.D. and Garcia, N., 2005. Modelling of velocity and turbulence fields around and within low-crested rubble-mound breakwaters. *Coastal Engineering*, 52(10-11): 887-913.
Losada, I.J., Lara, J.L., Guanche, R. and Gonzalez-Ondina, J.M., 2008. Numerical analysis of wave overtopping of rubble mound breakwaters. *Coastal*

Engineering, 55(1): 47-62.

Losada, I.J., Patterson, M.D. and Losada, M.A., 1997. Harmonic generation past a submerged porous step. *Coastal Engineering*, 31(1-4): 281-304.

Lu, L., Li, Y.-c., Teng, B. and Chen, B., 2008. Numerical simulation of turbulent free surface flow over obstruction. *Journal of Hydrodynamics, Ser. B*, 20(4): 414-423.

Lykke Andersen, T., 2006. Hydraulic Response of Rubble Mound Breakwaters. Scale Effects - Berm Breakwaters. Ph.D Thesis, Aalborg University.

Lykke Andersen, T. and Burcharth, H.F., 2006. Landward Distribution of Wave Overtopping for Rubble Mound Breakwaters, Proceedings of the First International Conferece on the Application of Physical Modelling to Port and Coastal Protection. IAHR, Porto, Portugal, pp. 401-411.

Lykke Andersen, T. and Burcharth, H.F., 2009. Three-dimensional investigations of wave overtopping on rubble mound structures. *Coastal Engineering*, 56(2): 180-189.

Lykke Andersen, T., Burcharth, H.F. and Gironella, F.X., 2007. Single Wave Overtopping Volumes and their Travel Distance for Rubble Mound Breakwaters, The 5th International Conference on Coastal Structures, Venice, Italy.

Madsen, P.A., Bingham, H.B. and Liu, H.U.A., 2002. A new Boussinesq method for fully nonlinear waves from shallow to deep water. *Journal of Fluid Mechanics*, 462(-1): 1-30.

Madsen, P.A., Bingham, H.B. and Schäffer, H.A., 2003. Boussinesq-type formulations for fully nonlinear and extremely dispersive water waves: derivation and analysis. *Proceedings of the Royal Society of London. Series A: Mathematical, Physical and Engineering Sciences*, 459(2033): 1075-1104.

Markle, D.G., 1986. Stability of rubble-mound breakwater and jetty toes; survey of field experience. REMR-CO-1, U.S. Army Corps Engineers. Coastal Engineering research center, Vicksburg, Miss.,

Masselink, G., 1998. Field investigation of wave propagation over a bar and the consequent generation of secondary waves. *Coastal Engineering*, 33(1): 1-9.

Minikin, R.R., 1950. *Winds, Waves and Maritime Structures.* Charles Griffin, London.

Mitsuyasu, H., Tasai, F., Suhara, T., Mizuno, S., Ohkusu, M., T.Honda and Rikiishi, K., 1975. Observations of the Directional Spectrum of Ocean Waves Using a Cloverleaf Buoy. *Journal of Physical Oceanography*, 5: 750-760.

Nielsen, P., 1992. *Coastal bottom boundary layers and sediment transport.* Advanced Series on Ocean Engineering, Vol. 4. World Scientific, Singapore, 324 pp.

Nielsen, P., 2006. Sheet flow sediment transport under waves with acceleration skewness and boundary layer streaming. *Coastal Engineering*, 53(9): 749-758.

Nielsen, P. and Callaghan, D.P., 2003. Shear stress and sediment transport calculations for sheet flow under waves. *Coastal Engineering*, 47(3): 347-354.

Oppenheim, A.V. and Schafer, R.W., 1998. *Discrete-Time Signal Processing,* . Prentice-Hall, Upper Saddle River, New Jersey.

Oumeraci, H., 1994a. Review and analysis of vertical breakwater failures -- lessons learned. *Coastal Engineering*, 22(1-2): 3-29.

Oumeraci, H., 1994b. Scour in front of vertical breakwaters —review of problems Proceedings of International Workshop on Wave Barriers in Deep Waters, Port and Harbour Research Institute, Yokosuka, pp. 281–307.

Owen, M.W., 1980. Design of sea walls allowing for wave overtopping, Report EX. 924. Hydraulics Research Station, Wallingford, UK.

Pan, S., Vincent, C.E., Li, M., Fernando, P.T., Zhu, Y., O'Connor, B.A., Taylor, T.J., Dolphin, T.J. and Bacon, J.C., 2005. Effect of shore parallel breakwaters on coastal morphology under storm conditions. In: Allsop, N.W.H. (Editor), International Coastlines, Structures & Breakwaters Conference. Thomas Telford Ltd, London, pp. 10.

Parker, B. and Youngs, D.L., 1992. Two and three dimensional Eulerian simulation of fluid flow with material interfaces. *Atomic Weapons Establishment, Aldermaston.*

Peregrine, D.H., 1967. Long waves on a beach. *Journal of Fluid Mechanics*, 27: 815-827.

Petit, H.A.H., Tönjes, P., Gent, M.R.A.v. and Bosch, P.v.d., 1994. Numerical Simulation and Validation of Plunging Breakers Using a 2D Navier-Stokes Model. In: Edge, B.L. (Editor), the 24th International Conference on Coastal Engineering. American Society of Civil Engineers, Kobe, Japan, pp. 511-524

Phillips, O.M., 1960. On the dynamics of unsteady gravity waves of finite amplitude. *J. Fluid Mech.*, 9 193-217.

Puleo, J.A., Holland, K.T., Plant, N.G., Slinn, D.N. and Hanes, D.M., 2003. Fluid acceleration effects on suspended sediment transport in the swash zone. *J. Geophys. Res.*, 108(C11): 3350.

Pullen, T., Allsop, W., Bruce, T. and Pearson, J., 2008. Field and laboratory measurements of mean overtopping discharges and spatial distributions at vertical seawalls. *Coastal Engineering*, 56(2): 121-140.

Raubenheimer, B., Guza, R.T. and Elgar, S., 1996. Wave transformation across the inner surf zone. *J. Geophys. Res.*, 101(C11): 25589-25597.

Raubenheimer, B., Guza, R.T., Elgar, S. and Kobayashi, N., 1995. Swash on a gently sloping beach. *J. Geophys. Res.*, 100(C5): 8751-8760.

Reeve, D.E., Soliman, A. and Lin, P.Z., 2008. Numerical study of combined overflow and wave overtopping over a smooth impermeable seawall. *Coastal Engineering*, 55(2): 155-166.

Rider, W.J. and Kothe, D.B., 1998. Reconstructing Volume Tracking. *Journal of Computational Physics*, 141(2): 112-152.

Rodi, W., 1980. Turbulence models for environmental flows. In: Knollmann, W. (Editor), Prediction methods for turbulent flows. Hemisphere Publ. Corp, London, pp. 259-350.

Ruessink, B.G., 1998. Bound and free infragravity waves in the nearshore zone under breaking and nonbreaking conditions. *J. Geophys. Res.*, 103(C6): 12,795–12,805.

Ruessink, B.G., van den Berg, T.J.J. and van Rijn, L.C., 2009. Modeling sediment transport beneath skewed asymmetric waves above a plane bed. *J. Geophys. Res.*, 114(C11): C11021.

Sakakiyama, T. and Liu, P.L.F., 2001. Laboratory experiments for wave motions and turbulence flows in front of a breakwater. *Coastal Engineering*, 44(2): 117-139.

Schäfer, H.A., Madsen, P.A. and Deigaard, R., 1993. A Boussinesq model for waves breaking in shallow water. *Coastal Engineering*, 20(3-4): 185-202.

Schüttrumpf, H. and Oumeraci, H., 2005. Layer thicknesses and velocities of wave overtopping flow at seadikes. *Coastal Engineering*, 52(6): 473-495.

Schuttrumpf, H. and van Gent, M.R.A., 2003. Wave Overtopping at Seadikes. In: Jeffrey, A.M. (Editor). ASCE, pp. 36.

Seabrook, S.R. and Hall, K.R., 1998. Wave transmission at submerged rubblemound breakwaters, Proceedings of the Coastal Engineering Conference. Proceedings of the 1998 26th International Conference on Coastal Engineering, ICCE-98. ASCE, Copenhagen, Denmark, pp. 2000-2013.

Seelig, W.N., 1980. Two-Dimensional Tests of Wave Transmission and Reflection Characteristics of Laboratory Breakwaters., COASTAL ENGINEERING RESEARCH CENTER FORT BELVOIR VA,

Sénéchal, N., Bonneton, P. and Dupuis, H., 2002. Field experiment on secondary wave generation on a barred beach and the consequent evolution of energy dissipation on the beach face. *Coastal Engineering*, 46(3): 233-247.

Shao, S.D., Ji, C., Graham, D.I., Reeve, D.E., James, P.W. and Chadwick, A.J., 2006.

Simulation of wave overtopping by an incompressible SPH model. *Coastal Engineering*, 53(9): 723-735.

Shih, T.-H., Zhu., J. and Lumley, J.L., 1996. calculation of wall-bounded complex flows and free shear flows. *International Journal for Numerical Methods in Fluids*, 23(11): 1133-1144.

Shiraishi, N., Numata, A. and Hase, N., 1960. The effect and damage of submerged breakwater in Niigata coast. *Coastal Engineering in Japan,*, 3: 89–99.

Silvester, R. and Hsu, J.R.C., 1997. *Coastal stabilization*. World Scientific, Singapore.

Stokes, G.G., 1847. On the theory of oscillatory waves. *Transactions of the Cambridge Philosophical Society*, 8: 441-455.

SUMER, B.M. and Freds¢e, J., 2002. *The Mechanics of Scour in the Marine Environment*. Advanced Series on Ocean Engineering, Vol. 17. World Scientific Publishing Co. Pte. Ltd.

Sumer, B.M., Fredsøe, J., Lamberti, A., Zanuttigh, B., Dixen, M., Gislason, K. and Di Penta, A.F., 2005. Local scour at roundhead and along the trunk of low crested structures. *Coastal Engineering*, 52(10-11): 995-1025.

Sumer, B.M., Whitehouse, R.J.S. and Tørum, A., 2001. Scour around coastal structures: a summary of recent research. *Coastal Engineering*, 44(2): 153-190.

TAW, 2002. Technical Report on Wave run-up and Wave Overtopping at Dikes, Eds: Meer, J.W.v.d., Technical Advisory Committee for Flood Defence, The Netherlands, www.tawinfo.nl.

Titov, V.V. and Synolakis, C.E., 1995. Modeling of Breaking and Nonbreaking Long-Wave Evolution and Runup Using VTCS-2. *Journal of Waterway, Port, Coastal, and Ocean Engineering*, 121(6): 308-316.

Titov, V.V. and Synolakis, C.E., 1998. Numerical Modeling of Tidal Wave Runup. *Journal of Waterway, Port, Coastal, and Ocean Engineering*, 124(4): 157-171.

Troch, P., Geeraerts, J., Van de Walle, B., De Rouck, J., Van Damme, L., Allsop, W. and Franco, L., 2004. Full-scale wave-overtopping measurements on the Zeebrugge rubble mound breakwater. *Coastal Engineering*, 51(7): 609-628.

van der A, D.A., O'Donoghue, T. and Ribberink, J.S., 2010. Measurements of sheet flow transport in acceleration-skewed oscillatory flow and comparison with practical formulations. *Coastal Engineering*, 57(3): 331-342.

Van der Meer, J. and Janssen, J.P.F.M., 1995. Wave run-up and wave overtopping at dikes. In: Kobayashi, N. and Z. Demirbilek (Editors), Wave forces on inclined and vertical structures. ASCE, pp. 1-27.

Van der Meer, J.W., 1987. Stability of breakwater armour layers -- design formulae. *Coastal Engineering*, 11(3): 219-239.

Van der Meer, J.W., Briganti, R., Zanuttigh, B. and Wang, B.X., 2005. Wave transmission and reflection at low-crested structures: Design formulae, oblique wave attack and spectral change. *Coastal Engineering*, 52(10-11): 915-929.

Van der Meer, J.W., Regeling, E. and de Waal, J.P., 2000. Wave Transmission: Spectral Changes and Its Effects on Run-Up and Overtopping. In: Edge, B.L. (Editor), Proceedings of the 27th International Conference of Coastal Engineering, Sydney, Australia, pp. 2156-2168.

Van der Meer, J.W. and Stam, C.J.M., 1992. Wave Runup on Smooth and Rock Slopes of Coastal Structures. *Journal of Waterway, Port, Coastal, & Ocean Engineering*, 118(5): 534-550.

van der Meer, J.W., Verhaeghe, H. and Steendam, G.J., 2009. The new wave overtopping database for coastal structures. *Coastal Engineering*, 56(2): 108-120.

Van Gent, M.R.A., 1994. The modelling of wave action on and in coastal structures. *Coastal Engineering*, 22(3-4): 311-339.

Wang, B., 2003. Oblique wave transmission at low-crested structures. MSc. Thesis

Thesis, Institute for Water Education.

Wang, B.X., Otta, A.K. and Chadwick, A.J., 2007. Transmission of obliquely incident waves at low-crested breakwaters: Theoretical interpretations of experimental observations. *Coastal Engineering*, 54(4): 333-344.

Wei, G., Kirby, J.T. and Sinha, A., 1999. Generation of waves in Boussinesq models using a source function method. *Coastal Engineering*, 36(4): 271-299.

Wilson, K.C., 1966. Bed-load transport at high shear stress. *Journal of the Hydraulic Division*, 92: 49-59.

Xiao, H., Huang, W. and Tao, J., 2009. Numerical modeling of wave overtopping a levee during Hurricane Katrina. *Computers & Fluids*, 38(5): 991-996.

Youngs, D.L., 1982. Time-dependent multi-material flow with large fluid distortion. In: Morton, K.W. and J.J. Baines (Editors), Numerical Methods for Fluid Dynamics. Academic Press, pp. 273-285.

Zanuttigh, B., Martinelli, L. and Lamberti, A., 2008. Wave overtopping and piling-up at permeable low crested structures. *Coastal Engineering*, 55(6): 484-498.

Zanuttigh, B. and van der Meer, J.W., 2008. Wave reflection from coastal structures in design conditions. *Coastal Engineering*, 55(10): 771-779.

Zou, Q.-P., Hay, A.E. and Bowen, A.J., 2003. Vertical structure of surface gravity waves propagating over a sloping seabed: Theory and field measurements. *J. Geophys. Res.*, 108(C8): 3265.